

Characterization and modification of a buffer-gas-cell

for rapid extraction of short-lived isotopes for
use in gas-phase chemistry experiments at TASCA

Dissertation
zur Erlangung des akademischen Grades
Doktor der Naturwissenschaften (Dr. rer. nat.)
im Promotionsfach Chemie

am Fachbereich Chemie, Pharmazie, Geographie und Geowissenschaften
der **Johannes Gutenberg-Universität Mainz**



JOHANNES GUTENBERG
UNIVERSITÄT MAINZ

von

Stefan Alexander William Götz
geb. in Wiesbaden-Dotzheim

Mainz, 2021

1. Gutachter:

2. Gutachter:

Tag der mündlichen Prüfung: 11.03.2022

Contents

Declaration	VI
List of Tables	VII
List of Figures	XIV
<hr/>	
1 Abstract	1
<hr/>	
2 Zusammenfassung	2
<hr/>	
3 Introduction	3
<hr/>	
4 Theory	7
4.1 Introduction in SHE research	7
4.1.1 Stability of superheavy elements	7
Liquid Drop Model	8
The nuclear Shell Model	8
4.1.2 Production of SHEs in nuclear fusion reactions	11
4.1.3 Experimental techniques	13
One-atom-at-the-time experiments	13
Chemical separation	15
Detection	15
4.1.4 Chemical properties of SHEs	16
Chemistry experiments with SHEs	17
Liquid-phase experiments	18
Gas-phase experiments	18
4.2 Experimental Methods	21
4.2.1 The buffer-gas-cell	23
Slowing down of ions in gas	25
Neutralization	26
Molecule formation	27
Ion mobility in static electric fields	28
Inhomogeneous RF electric fields	29
4.2.2 The gas chromatographic method	30
Basics of gas chromatographic transport	32
Isothermal gas chromatography	32

	The adsorption enthalpy and the diffusion coefficient	34
	Monte Carlo Simulation	35
4.2.3	Gas-flow kinetics	37
	Diffusion	38
<hr/>		
5	Scope of the current work	40
<hr/>		
6	Experimental setup	42
6.1	Off-line measurements with recoil-ion sources	42
6.1.1	^{225}Ac recoil-ion source	43
6.1.2	^{223}Ra recoil-ion source	45
6.2	On-line measurements behind a recoil separator	46
6.2.1	Beam production	47
	Experiments at MARS - The K500 cyclotron	47
	Experiments at TASCAs - The UNILAC	48
6.2.2	Targets	49
	Physical vapor deposition	49
	Molecular plating	49
6.2.3	Physical separators	50
	MARS	51
	TASCAs	52
6.2.4	Focal Plane Detector	53
6.3	Buffer-gas-cell	53
6.3.1	DC Cage	55
6.3.2	RF funnel	55
6.4	COMPACT detector array	57
6.5	COMPACT data acquisition systems	57
6.6	Gas handling system	59
<hr/>		
7	Instrumental development	60
7.1	Transition electrode	60
7.2	MiniCOMPACT	61
7.2.1	Design of the miniCOMPACT	63
7.2.2	Basic characterization of the miniCOMPACT as detector unit for non-volatile elements	64
	Study of the signal noise	64
<hr/>		
8	Optimization of the the experimental parameters of the BGC	67
8.1	Simulations	67
8.1.1	Estimation of the stopping distribution of fusion products inside the BGC	67

Simulation results	68
Discussion	71
8.2 Measurement methods	73
8.2.1 Measurement of the extraction efficiency	73
8.2.2 Measurement of the extraction time	74
8.3 Experimental analysis of the BGC parameters	75
8.3.1 Optimization of the DC gradient on the electrode system	76
Result	76
Discussion	77
8.3.2 Optimization of the RF amplitude	78
Result	78
Discussion	79
8.3.3 Influence of the voltage difference between last funnel electrode and transition electrode	79
Results	79
Discussion	81
<hr/>	
9 Off-line experiments at GSI	85
9.1 Extraction efficiency measurement	85
9.1.1 Result	85
9.1.2 Discussion	89
9.2 Extraction time measurement	90
9.2.1 Result	90
9.2.2 Discussion	91
9.3 Summary	93
<hr/>	
10 On-line chemistry experiments	95
10.1 On-line chemistry experiments behind the MARS spectrometer	96
10.1.1 Experiments behind MARS	96
10.1.2 Focal plane measurements behind MARS	98
Result	98
Discussion	98
10.1.3 Extraction efficiency measurements behind the MARS separator	99
Result	100
Discussion	101
10.2 On-line chemistry experiments behind the gas-filled separator TASCA	102
10.2.1 Experiments behind TASCA	102
10.2.2 Analyses of the obtained experimental data	103
10.2.3 Focal plane measurements behind TASCA	105
Results	107

Discussion	107
10.2.4 Extraction efficiency measurement behind the gas-filled separator TAsCA	109
Result	109
Discussion	110
10.2.5 Summary	112
<hr/>	
11 Future Perspectives	114
11.1 Chemical experiments of superheavy nuclei	114
11.2 Chemistry beyond Fl	114
11.3 Summary	116
<hr/>	
A Appendices	118
A.1 Stopping Distribution Simulations	118
A.2 HIVAP: MARS experimente	119
A.3 HIVAP: TAsCA experimente	121
A.4 Study of the recoil release probability	122
<hr/>	
B Bibliography	126
<hr/>	
C Curriculum vitae	143

Declaration

Hiermit erkläre ich, dass ich diese Arbeit selbstständig verfasst und keine anderen, als die darin angegebenen Hilfsmittel und Hilfen benutzt habe. Diese Arbeit wurde weder als Ganzes, noch in Teilen als Prüfungsarbeit für eine staatliche oder andere wissenschaftliche Prüfung eingereicht. Insbesondere nicht als Dissertation bei einer anderen Fakultät oder einem anderen Fachbereich.

Bensheim, den 04.11.2021

List of Tables

Tab. 4.1:	Summary of transactinide isotopes investigated in gas-phase chemical experiments. The respective half-lives were taken from [69]. The production rate is based on a target thickness of 0.8 mg cm^{-2} and a beam intensity of $3 \cdot 10^{12}$ particles per second. As an introduction, the review articles [23, 45] will give a general overview over gas-phase chemistry experiments.	20
Tab. 6.1:	Parameters of the used ^{223}Ra and ^{225}Ac recoil-ion sources, which were used for the efficiency measurements. E_α is the α -particle energy and I the intensity of the corresponding line; b_α the branching ratio for alpha decay and P_{release} is the recoil release probability from the source surface. The α activity (A) and the effective release rate (\dot{N}^{tot}), which is needed for efficiency determination of both sources is given. Data were taken from [139].	44
Tab. 6.2:	Conditions for the MP of $^{144,147}\text{Sm}$ and ^{165}Ho targets.	50
Tab. 6.3:	Decay properties of the nuclides used for the calibration of the DSSD and PSSD	54
Tab. 6.4:	Optimum parameters for the operation of the gas stop cell. . .	55
Tab. 6.5:	Main parameters for the extraction time measurement	59
Tab. 8.1:	Target information for the experiments at MARS and TASCA.	68
Tab. 8.2:	Kinetic energies of the fusion evaporation residues in front of the entrance window to the BGC.	69
Tab. 9.1:	BGC efficiency studied with the recoil-ion sources ^{223}Ra and ^{225}Ac , together with the efficiencies for the extraction, transport, and detection. ϵ_{det} has been taken from [49] and ϵ_{extr} can be deduced from Equation 9.1. \dot{N}_{det} is calculated with Equation 8.10 and the transport times are $t_1 = 75 \text{ ms}$ (detector 1) and $t_2 = 160 \text{ ms}$ (detector 16). The He flow rate was $0.04 \text{ mbar L s}^{-1}$ and the pressure inside the BGC was 30 mbar. The funnel amplitude was $120 \text{ V}_{\text{pp}}$	89

Tab. 10.1:	List of the used ^{152}Gd , ^{165}Ho , and $^{144,147}\text{Sm}$ targets. The target composition and thickness as well as the backing thickness are given. The targets were prepared by Thermal Evaporation (TE) [155] or Molecular Plating (MP) [191].	95
Tab. 10.2:	List of experiments with ^{40}Ar ion beams as described in this thesis. The cross sections σ_{HIVAP} were calculated with HIVAP [41, 195], at the lab-frame ion beam energy in the center of the target E_{COT} . The E_{CN} is the kinetic energy of the CN if formed at ion beam energy E_{COT} . The three right-most columns indicate nuclear properties of the produced EVRs: energy of the most intense α -line ($E_{\alpha 1}$) [196], branching for α -decay (b_{α}) [196], and half-life $T_{1/2}$ [196]. The energy loss was calculated with SRIM-2013 [193]	97
Tab. 10.3:	Measured experimental efficiency ϵ_{exp} for the given astatine and mercury radionuclides in comparison to the calculated extraction efficiency, ϵ_{calc} . N_{win} is the fraction of ions that passes through the entrance window, and ϵ_{stop} is the stopping efficiency for these ions inside the BGC as calculated with SRIM for ^{199}At and ^{182}Hg ions with kinetic energies of 40 MeV impinging on a $3.5\ \mu\text{m}$ -thick titanium foil. ϵ_{BGC} is the extraction efficiency of the BGC as measured in the off-line studies. ϵ_{calc} is the product of ϵ_{BGC} , N_{win} and ϵ_{stop} , which is in good agreement with ϵ_{exp}	101
Tab. 10.4:	List of experiments with ^{48}Ca beams as described in this paper. The cross sections σ_{HIVAP} were calculated with HIVAP [41, 195], at the given E_{COT} . The data for E_{α} , b_{α} and $T_{1/2}$ are taken from the Evaluated Nuclear Structure File (ENSDF) database [196]. The energy loss was calculated with SRIM-2013 [193].	104
Tab. 10.5:	Summary of the measured number of counts in the $^{48}\text{Ca} + ^{165}\text{Ho}$ reaction in the TASCAs FP at E_{COT} 273 MeV and 244 MeV. The projectile dose was $1.3(1) \cdot 10^{14}$ for $E_{\text{COT}} = 273\ \text{MeV}$ and $1.2(2) \cdot 10^{14}$ for $E_{\text{COT}} = 244\ \text{MeV}$	107
Tab. 10.6:	Calculated extraction efficiencies using the multiple-peak fit analysis from subsection 10.2.2 for the data obtained with the mini-COMPACT for A) $E_{\text{COT}} = 244\ \text{MeV}$ and B) $E_{\text{COT}} = 273\ \text{MeV}$. The overall efficiencies ϵ_{exp} of the BGC-miniCOMPACT system for the respective Fr radioisotopes are compared to the theoretically expected efficiencies ϵ_{calc} (for further details see subsection 10.1.3).	111

List of Figures

Fig. 3.1:	Periodic table of the chemical elements as of 2015. The color scheme divides naturally-occurring and synthetic elements, with the latter mainly populating the lower regions of the table. . .	4
Fig. 3.2:	Comparison of maximum cross sections for heavy and super-heavy elements produced in cold fusion and hot fusion reactions. The figure was adopted from [18].	5
Fig. 4.1:	Deviation of the liquid drop model from experimental data as a function of the neutron number and proton number for all known isotopes based on the AME2003 [32].	9
Fig. 4.2:	Energies of single-particle in a hamonic-oscillator and square-well potentials. The latter split the second set of levels by the spin-orbital term to produce the experimental observed shell gaps. In addition, the multiplicities and their sums are given. .	10
Fig. 4.3:	Nilsson model, which describes the nuclear energy levels of a modified harmonic-oscillator potential as a function of the deformation of the nucleus. The graph is adapted from [37]. .	11
Fig. 4.4:	Schematic illustration of the fusion evaporation reaction towards creation of an ER.	12
Fig. 4.5:	Relativistic (solid line) and nonrelativistic (dashed line) radial distribution of the 7s valence electrons in Db. Figure taken from [42].	17
Fig. 4.6:	A shematic diagram of the Berkley Gas-filled Separator. The Beam enters the apparatus from the left. Adapted from [87]. .	21
Fig. 4.7:	Schematic outline of the Gas-filled Recoil Ion Separator. Figure was adopted from [65].	22
Fig. 4.8:	Schematic outline of the Dubna Gas-Filled Recoil Separator. Adapted from [80].	23
Fig. 4.9:	Part of the nuclear map with the shell correction energy from microscopic-macroscopic model calculations (in blue) showing the regions of stronger binding around $Z = 108$ and 114 and $N = 162$ and 184 . figure based on date from [94].	24

Fig. 4.10:	Left: RF gradient field produced by a series of ring electrodes with RF equipotential lines indicated [100]. Right: Simulation for the ion motion in a gas-filled RF funnel by W. Plaß. The figure is taken from [114].	30
Fig. 4.11:	Schematic figure of the chromatographic principle.	31
Fig. 4.12:	Schematic representation of the IC method and the form of its typical obtained chromatogram. Figure adapted from [18] . . .	34
Fig. 4.13:	Microscopic model of the adsorption process of a molecule in a column to describe exponential probability distribution $\rho(\eta)$. Taken from [128]	37
Fig. 5.1:	Production rate of SHEs folded with an 1 s-extraction-delay. The delay is due to the needed extraction time of the current used setups. The lines are added to guide the eye.	41
Fig. 6.1:	Schematic overview of the setup. In A) (black square) the setup for the on-line measurements is shown. The ER ions (1) passing through the entrance window (2) enter the BGC. For the off-line measurements B) (blue square), the respective recoil-ion source (3) is installed inside the BGC. Ions will be guided to the exit by a DC cage (4). In the funnel-structure (5), an RF field prevents the ions from hitting the wall. The ER ions were transferred via the transition electrode into the transport line. The α -decay was registered in the COMPACT detector array (8). The laminar gas-flow was generated by a diaphragm pump (9).	43
Fig. 6.2:	Photograph of the used source cone at the end of the linear-motion feedthrough. This type of source cone was used for both recoil-ion sources.	44
Fig. 6.3:	Experimental setup for the molecular plating of the ^{225}Ac recoil-ion source.	44
Fig. 6.4:	The ^{225}Ac decay chain for the ^{225}Ac recoil-ion source. The half-life and the decay mode (yellow: α -decay; blue: β^- -decay) is given. Data were taken from [139].	45
Fig. 6.5:	The ^{227}Ac decay chain for the ^{223}Ra recoil-ion source. The origin source was ^{227}Ac . The half-life and the decay mode (yellow: α -decay; blue: β^- -decay) is given. Data were taken from [139].	46
Fig. 6.6:	Experimental setup for the production of the ^{223}Ra recoil-ion source.	46

Fig. 6.7:	α -decay spectra of the extracted ^{225}Ac (A) and ^{223}Ra (B) ions and their decay products. The energy resolution in the α -spectrum was about 70 keV (FWHM) for ^{223}Ra and about 90 keV (FWHM) in the case of ^{225}Ac	47
Fig. 6.8:	Schematic overview of the Cyclotron Institute facility. The beamline that was used for the experiments at the Cyclotron Institute behind the MARS spectrometer is clearly shown, while all other branches have been blurred. Figure is modified from [153].	48
Fig. 6.9:	Schematic overview of the GSI UNILAC and ECR source [154].	49
Fig. 6.10:	Schematic view of the MARS spectrometer. The subscripts on each of the quadrupole or dipole magnets indicate the focusing plane of the magnet. The incoming beam from the K500 cyclotron enters the target chamber (TC) from the left side. The flight trajectory of the ERs to the detector chamber (DC) are also shown [148, 162].	51
Fig. 6.11:	A schematic layout of a TASCA. The primary beam (1) from the UNILAC passes through a rotating target wheel (2). The separator TASCA consists of one dipole (D) magnet, where unwanted nuclear reaction products and unreacted primary beam (3) are separated from EVRs and subsequently focused by means of two quadrupole (Q) magnets. At the exit of TASCA, a entrance window (4) separates the low-pressure region in TASCA from the high-pressure region in the BGC (5). The figure was adopted from [68].	52
Fig. 6.12:	The DC cage structure in a schematic view. The DC cage consists of 5 ring segments, which were connted to an RF-/DC-mixing board. The system is fixed to the entrance flange via four ceramic spacers.	56
Fig. 6.13:	The RF funnel structure in a schematic view with the 40 ring electrode plates and the ceramic spacers between adjacent plates. The left side shows the complete funnels with the ceramic spacers (green). On the right side, a half-cut of the funnel structure is shown. The contour of the last funnel ring electrode is complete shown (blue).	56

Fig. 6.14:	Schematic of the COMPACT array. The flow direction is marked. The bottom and top half-array is shown in full, including the detectors, with the 1 st and 16 th labeled. B) Enlarged view of the last section of the COMPACT array. Only the last part of the top half-array - containing the top detectors facing the bottom detectors and leaving a gap of 0.05 mm to form the rectangular chromatography channel - is shown towards the end of the array.	57
Fig. 6.15:	Schematic overview of the electronics for the efficiency and transport time measurements with the BGC is shown. On the top, the analogue signal processing is shown. For a detailed description see text. The dashed box shows the process for the extraction time measurements.	58
Fig. 7.1:	Enlarged schematic view of the TE. Only the last funnel electrodes and the conical shape of the TE are shown. The TE represents the entrance into the Teflon transport line. The Teflon tube inside the metal tube is not shown.	61
Fig. 7.2:	Measured distribution of adsorbed ²¹⁷ At along an Au-covered COMPACT detector.	63
Fig. 7.3:	Photo of the miniCOMPACT in the open vacuum chamber directly behind the BGC exit. At the end of the miniCOMPACT, the Swagelok [®] connector is shown.	63
Fig. 7.4:	A) Half-section view of the miniCOMPACT in its mounting flange (1). Only the bottom of the miniCOMPACT array with the 8 PIN diodes (2) is shown. B) Schematic of the coupling section of the miniCOMPACT array to the RF-funnel. The bottom half of the mounting flange (1) with the first three PIN diodes (2), the entrance nozzle (3) and the last funnel electrode (4, red contour) are shown. The distance between the last funnel electrode and the miniCOMPACT entrance is enlarged by a factor of 10 for a better overview. The opening diameter of the nozzle is 3 mm and converging to a diameter of 0.6 mm to match the pitch between the detectors in the miniCOMPACT.	65
Fig. 7.5:	Schematic view of the custom made flanges with the miniCOMPACT. The outer flange (1) with the extraction nozzle connects the funnel exit with miniCOMPACT entrance. The outer flange holds the ceramic plate (2) in which the miniCOMPACT sits. The inner flange (3) is used to press the ceramic plate on the outer flange.	66

Fig. 7.6:	Achievable mean signal noise on the miniCOMPACT with the parameters from Table 6.4 (A) without RF from the funnel and (B) with RF on the funnel.	66
Fig. 8.1:	Schematic picture of the BGC with the used geometrical parameters for the determination of the number of ions which were stopped inside BGC.	70
Fig. 8.2:	Stopping positions for ^{205}At ions simulated by the computer program TRIM in consideration of a $4.1\ \mu\text{m}$ -thick Ti entrance window and 50 mbar He buffer gas.	71
Fig. 8.3:	Dependence of the simulated stopping efficiency from the Ti entrance window thickness for (A) At, Pb and Hg and (B) for Fr ions.	72
Fig. 8.4:	Timing diagram for the measurement of the extraction time t_{extr} . A) shows the applied voltage on the source in dependence of the time and B) give an overview of the trajectory of the recoil-ions. In C) the chromatogram in the COMPACT detectors is shown.	75
Fig. 8.5:	Extraction efficiency of ^{219}Rn from the BGC as function of the DC gradient (∇_{DC}) applied on the electrode system.	77
Fig. 8.6:	Extraction efficiency of ^{219}Rn from the BGC as a function RF amplitude of the RF funnel for 22, 39 and 60 mabr helium pressure inside the BGC.	78
Fig. 8.7:	Investigation of the influence of $\Delta V_{\text{transition}}$ on the extraction efficiency of ^{219}Rn without TE (A) and with TE (B) for a \hat{U}_{RF} of $120 V_{\text{PP}}$ at 796 kHz, $p_{\text{cell}} = 30\ \text{mbar}$ and a gradient of $8\ \text{V cm}^{-1}$	80
Fig. 8.8:	Long-term achievable ^{219}Rn signal stability on the COMPACT detector with TE (blue circles) or without TE (red circles).	81
Fig. 8.9:	Investigation of the influence of the pressure on the extraction efficiency of ^{219}Rn ions on the BGC setup with TE.	82
Fig. 9.1:	α -decay spectra of the extracted daughters of ^{221}Fr (A) and ^{219}Rn (B) ions and their decay products measured with COMPACT.	86
Fig. 9.2:	Distribution patterns from the MCS of ^{221}Fr in pure He gas in the Teflon transport line. The pressure inside the Teflon capillary was about 40 mbar. The value of $-\Delta H_{\text{ads}}^{\text{Teflon}}$ represents a lower limit, see text for a detailed discussion.	87

Fig. 9.3:	Distribution patterns of ^{219}Rn in pure He gas (A) in the Teflon transport line and (B) on the Au-covered COMPACT detector array. The pressure inside the Teflon transport line and inside the COMPACT detector array was about 40 mbar. The solid line in Figure 9.3B represents experimental data. The gray bar histograms are the results of Monte Carlo simulations using the values for ΔH_{ads} (^{219}Rn) indicated in the panels. For adsorption on Teflon, panel A, the value of -24 kJ/mol gives the best agreement; no substantial change is observed for values up to -30 kJ/mol. The value for adsorption on gold in panel B is taken from [187].	88
Fig. 9.4:	Number of ^{215}Po α decays as function of the delay between ion source release and the arrival at the PIN diodes of the COMPACT array.	91
Fig. 9.5:	Extraction time t_{extr} from the BGC (source \rightarrow COMPACT detector) and transport times t_{trans} of the ion packet through the transport line. t_{cell} was calculated with Equation 9.2. . . .	92
Fig. 10.1:	Typical α -spectra measured with the FP-detector for fusion products in ^{40}Ar -induced reactions on (A) ^{152}Gd , (B) ^{165}Ho and (C) ^{147}Sm . The respective particle doses is shown in each of the figures.	99
Fig. 10.2:	Typical α spectra with COMPACT-detector for fusion products in ^{40}Ar -induced reactions on (A) ^{165}Ho and (B) ^{147}Sm	100
Fig. 10.3:	Sum α -spectrum on the first three miniCOMPACT detector pairs of the $^{48}\text{Ca} + ^{165}\text{Ho}$ reaction at $E_{\text{COT}} = 273$ MeV. The measurement time was 60 min.	105
Fig. 10.4:	Influence of the different variance ω_2 values on the low energy tailing of a simulated α -peak.	106
Fig. 10.5:	Calibration spectrum of the miniCOMPACT with an ^{225}Ac recoil-ion source. The peaks were fitted with an asymmetric double sigmoidal (Asym2Sig) function from Equation 10.1. . .	106
Fig. 10.6:	Alpha spectra recorded in the FP measurement at TASCA (A) at $E_{\text{COT}} = 273$ MeV and (B) at $E_{\text{COT}} = 244$ MeV. Dominant lines are labeled.	108
Fig. 10.7:	Experimental data (sum α spectrum, see Figure 10.3) simulated with multiple asymmetric double sigmoidal fits. The enveloping curve around the experimental data is the sum of the individual simulated peaks from the multiple fit analysis for the respective nuclides.	110

Fig. 10.8:	The relative peak areas from the FP spectra (see Table 10.6) compared to the relative peak area as determined by the multiple fit analysis.	111
Fig. 11.1:	Estimated half-lives of isotopes in the region of the heaviest elements. Based on data from [209, 210]. Figure taken from [211].	116
Fig. A.1:	HIVAP predictions for the excitation functions for the $^{152}\text{Gd}(^{40}\text{Ar}, \text{xn})^{192-x}\text{Pb}$ reaction. Data was taken from [219].	119
Fig. A.2:	HIVAP predictions for the excitation functions for the $^{147}\text{Sm}(^{40}\text{Ar}, \text{xn})^{187-x}\text{Hg}$ reaction. Data was taken from [219].	120
Fig. A.3:	HIVAP predictions for the excitation functions for the $^{165}\text{Ho}(^{40}\text{Ar}, \text{xn})^{205-x}\text{At}$ reaction. Data was taken from [219].	121
Fig. A.4:	HIVAP predictions for $5n$ - to $9n$ -evaporation channels of the fusion reaction $^{165}\text{Ho} + ^{48}\text{Ca}$. Data was taken from [219].	121
Fig. A.5:	HIVAP predictions for $p\alpha n$ -evaporation channels of the fusion reaction $^{165}\text{Ho} + ^{48}\text{Ca}$. Data was taken from [219].	122
Fig. A.6:	HIVAP predictions for αxn -evaporation channels of the fusion reaction $^{165}\text{Ho} + ^{48}\text{Ca}$. Data was taken from [219].	123
Fig. A.7:	Schematic view of the organic deadlayer on the ^{225}Ac recoil-ion source. In a) the kinetic energy of ^{219}Rn is high enough to penetrate the deadlayer and ^{219}Rn can leave the recoil-ion source. In the case that the kinetic energy is not high enough (b)) only the α -particle can leave the recoil-ion source.	124
Fig. A.8:	Setup (schematic) for the determination of P_{release} of ^{221}Fr	124
Fig. A.9:	Detected alpha rates for ^{221}Fr with 'open' and shielded detector. The rates were determined by successive measurements with measurement times of 30 s. The detector was shielded at the time t_{move} . The ^{221}Fr α -rate from the implanted recoils on the detector has to be extrapolated from the exponential fit.	125

Efficient gas-filled recoil thermalization chambers are the most common interfaces for a variety of sophisticated chemical experiments with superheavy elements. They can be installed directly behind a target or alternatively behind a recoil separator. Despite limitations of this gas-flow-based transfer of the thermalized reaction products from the Buffer-Gas-Cell (BGC) to the chemical experiment, they are widely used due to their high extraction efficiency. The flow rate-dependent extraction speed has so far limited access to nuclides with a half-life of less than about one second. The novel approach in this thesis presents a fast extraction with an extraction time of a few tens of ms and the first successful transportation of non-volatile elements such as francium (Fr) to the detection unit. For this purpose, a BGC with superimposed electrical fields (direct current and radio frequency) was coupled with the gas-phase chromatography setup COMPACT for the first time. A further development of the well-known COMPACT detector, the so-called miniCOMPACT detector, was introduced and the efficient coupling for the rapid extraction of non-volatile elements was achieved. The achieved extraction time of less than 55 ms is almost ten times faster than with previous gas-flow-based transfer techniques with comparable extraction efficiencies. In addition, the BGC was characterized extensively with established methods with regard to its extraction efficiency and extraction time. ^{223}Ra and ^{225}Ac recoil ion sources providing ^{219}Rn and ^{221}Fr were used for this experiments.

In addition, the novel coupling of the newly developed miniCOMPACT and the BGC with superimposed electrical fields was successfully characterized in on-line experiments with Hg, Fr and At isotopes. These experiments allowed the chemical study of short-lived α -decaying radioisotopes in ^{40}Ar - and ^{48}Ca -induced fusion reactions. In the context of this study, extraction efficiencies of more than 23% could be achieved, which is in the same order of magnitude as for the recoil ion sources. This work confirms the applicability of this novel coupling in the area of the heaviest elements under the difficult conditions of low production rates and short half-life. It paves the way for chemical experiments beyond flerovium (Fl), which is currently the heaviest element accessible for chemical experiments.

Die Anwendung von effizienten, gasgefüllten Thermalisationskammern sind die am häufigsten verwendeten Schnittstellen für eine Vielzahl von anspruchsvollen chemischen Experimenten mit superschweren Elementen. Sie können direkt hinter dem Target oder alternativ hinter einem Rückstoßseparator installiert werden. Trotz Limitierungen dieser auf Gasfluss basierten Überführung der thermalisierten Reaktionsprodukte von der Gas-Stopp-Zelle hin zum chemischen Experiment, finden sie aufgrund ihrer hohen Extraktionseffizienz eine breite Anwendung. Die flussratenabhängige Extraktionsgeschwindigkeit limitiert bisher ein Zugang zu Nukliden mit einer Halbwertszeit von kleiner als etwa einer Sekunde. Der neuartige Ansatz in dieser Arbeit präsentiert eine schnelle Extraktion mit einer Extraktionszeit von einigen zehn ms und den ersten erfolgreichen Transport von nicht flüchtigen Elemente wie beispielsweise Francium (Fr) hin zur Detektoreinheit. Hierfür wurde zum ersten Mal eine Gas-Stopp-Zelle mit überlagerten elektrischen Feldern (Gleichstrom und Hochfrequenz) mit dem Gasphasenchromatographieaufbau COMPACT gekoppelt. Hierfür wurde eine Weiterentwicklung des bekannten COMPACT-Detektors, dem sogenannten miniCOMPACT-Detektor, eingeführt, womit die effiziente Kopplung zur schnellen Extraktion von nicht-flüchtigen Elementen gelang. Die erzielte Extraktionszeit von unter 55 ms ist fast um einen Faktor zehn schneller als mit bisherigen auf Gasfluss basierten Überführungstechniken bei vergleichbaren Extraktionseffizienzen. Zusätzlich wurde die Gas-Stopp-Zelle bezüglich ihrer Extraktionseffizienz und Extraktionsgeschwindigkeit ausführlich mit etablierten Methoden charakterisiert. Hierfür kamen ^{223}Ra - und ^{225}Ac -Rückstoßionenquellen, welche ^{219}Rn und ^{221}Fr lieferten, zum Einsatz.

Darüber hinaus wurde die neuartige Kopplung dieses Systems bestehend aus dem weiterentwickelten miniCOMPACT und der Gas-Stopp-Zelle mit überlagerten elektrischen Feldern erfolgreich in On-line Experimenten mit Hg-, Fr- und At-Isotopen charakterisiert. Diese Experimente erlaubten die chemische Studie von kurzlebigen α -zerfallenden Radioisotopen in ^{40}Ar - und ^{48}Ca -induzierten Fusionsreaktionen. Im Rahmen dieser Studien konnten Extraktionseffizienzen von mehr als 23% erreicht werden, welche in der gleichen Größenordnung liegen wie für die Rückstoßionenquellen. Diese Arbeit bestätigt die Anwendbarkeit dieser neuartigen Kopplung im Bereich der schwersten Elemente unter den erschwerten Bedingungen der geringen Produktionsraten und der kurzen Halbwertszeit. Sie ebnet somit den Weg für chemische Experimente jenseits von Flerovium, welches das derzeit schwerste für chemische Experimente zugängliche Element ist.

In the following section a brief summary of the introduction in the field of SHEs, which are based on the concepts described in the next chapter, is given.

The year 2019 marked a special anniversary year for physics, chemistry, and biology as the UNESCO and United Nations General Assembly proclaimed 'The International Year of the Periodic Table (IYPT2019) [1, 2]. The Periodic Table of the Elements (PTE) was published by the Russian chemist Dmitri Ivanovich Mendeleev and presented for the first time a illustration of the periodic trends of all known 63 elements until that point in time [3]. Since that time, many scientists have expanded the PTE by discovering and synthesizing of 'new' elements up to the present day. The modern layout was established by American chemist Horace Groves Deming [4] in 1923 and completed in its final shape by the American chemist Glenn Seaborg, who suggested in the 1950's that the actinides, like the lanthanides, belonged in their own separate row below the main group elements [5]. The PTE is structured such as to reflect the periodic trends of the elements, with the groups containing chemically similar elements. The 7th period of the PTE was closed by the recognition of the four missing elements with the atomic numbers $Z=113$, $Z=115$, $Z=117$, and $Z=118$ in 2015. These were named nihonium (Nh, $Z=113$), moscovium (Mc, $Z=115$), tennessine (Ts, $Z=117$), and oganesson (Og, $Z=118$), respectively [6–8]. The 7th period (excluding Fr, Ra and Ac) belongs to the TransActiNide (TAN, $Z>103$) elements, also known as Super-Heavy Elements (SHE). The modern periodic table as of 2015 is shown in Fig. 3.1. The first 92 elements all occur naturally, and technetium (Tc, $Z=43$) and promethium (Pm, $Z=61$) were discovered in 1945 after having first been synthesized, because they are the lightest elements with no stable isotopes. Neptunium (Np, $Z=93$) and plutonium (Pu, $Z=94$) are found only in trace amounts [9] since their half-lives are short compared to the age of the Earth. Uranium (U, $Z=92$) is the heaviest element which has been found in large quantities in nature, since it is extremely long-lived (^{238}U , $T_{1/2} = 4.468 \cdot 10^9$ years) with a half-life that is almost as long as the age of the Earth. The elements from americium (Am, $Z=95$) up to oganesson have only been synthesized in nuclear reactions.

The experimental investigation of the SHEs helps to understand the limits of nuclear stability and the properties of the SHEs, such as the half-life, decay properties, shape and structure properties and much more. Such scientific knowledge leads to a better understanding of chemical or physical concepts at this region of the nuclear chart that is difficult to access. The experiments with SHEs are challenging, since the number of available atoms drops drastically to few atoms per day or week.

Periodic Table of Chemical Elements

1 IA																	18 VIIIA	
1	H 1776																	He 1895
2	Li 1817	Be 1797											B 1808	C 1694	N 1772	O 1747	F 1866	Ne 1898
3	Na 1807	Mg 1755											Al 1825	Si 1824	P 1669	S Ancient	Cl 1774	Ar 1894
4	K 1807	Ca 1808	Sc 1879	Ti 1791	V 1830	Cr 1797	Mn 1755	Fe 1755	Co 1751	Ni 1751	Cu Ancient	Zn 1746	Ga 1875	Ge 1886	As Ancient	Se 1817	Br 1826	Kr 1898
5	Rb 1861	Sr 1790	Y 1878	Zr 1789	Nb 1801	Mo 1781	Tc 1937	Ru 1844	Rh 1803	Pd 1803	Ag 1817	Cd 1863	In 1863	Sn Ancient	Sb Ancient	Te 1783	I 1811	Xe 1898
6	Cs 1860	Ba 1808	La-Lu Lanthanide	Hf 1923	Ta 1802	W 1783	Re 1925	Os 1803	Ir 1803	Pt 1735	Au Ancient	Hg 1861	Tl Ancient	Pb 1400	Bi 1898	Po 1898	At 1940	Rn 1900
7	Fr 1939	Ra 1898	Ac-Lr Actinide	Rf 1964	Db 1967	Sg 1974	Bh 1981	Hs 1984	Mt 1982	Ds 1994	Rg 1994	Cn 1996	Nh 2003	Fl 1999	Mc 2003	Lv 2000	Ts 2009	Og 2002
	<div style="display: flex; justify-content: space-between;"> <div> <p>■ Natural Element</p> <p>■ Artificial Element</p> </div> <div> <p>Liquid Chem.</p> <p>Gas-Chem.</p> </div> </div>																	
	La 1839	Ce 1803	Pr 1885	Nd 1885	Pm 1945	Sm 1879	Eu 1901	Gd 1880	Tb 1843	Dy 1886	Ho 1867	Er 1842	Tm 1879	Yb 1878	Lu 1907			
	Ac 1899	Th 1829	Pa 1913	U 1789	Np 1940	Pu 1940	Am 1944	Cm 1944	Bk 1949	Cf 1950	Es 1952	Fm 1952	Md 1955	No 1958	Lr 1961			

Fig. 3.1.: *Periodic table of the chemical elements as of 2015. The color scheme divides naturally-occurring and synthetic elements, with the latter mainly populating the lower regions of the table.*

The liquid drop model proposed by the theoretical physicist George Gamow (1930) [10] and described by the Bethe–Weizsäcker mass formula in 1935 by the German physicist Carl Friedrich von Weizsäcker [11] predicts short spontaneous fission half-lives for elements with $Z \geq 103$. However, the appearance of closed nuclear shells resulting in a stabilization of SHEs [12]. These quantum mechanical nuclear shells counter the Coulomb force of the protons and prevent the disintegration of the nucleus. When taking this shell-stabilization into account, SHEs with enhanced stability against spontaneous fission around the deformed doubly magic isotope ^{270}Hs ($Z = 108$, $N = 162$) can be found [13].

The artificial syntheses of elements beyond Pu is straightforward by the bombardment of Pu with neutrons. Neutron-rich isotopes undergo an β^- -decay into a nucleus with an higher Z . This way of production of heavier elements than Pu is limited to fermium (Fm, $Z = 100$), due to very fast spontaneous fission of the heavy Fm isotopes which do not undergo β^- -decay. To circumvent this problem, elements beyond Fm are produced at accelerators, where charged particles are accelerated to energies large enough to overcome the Coulomb repulsion thus enabling fusion with a heavy element as target material. The production of SHEs is often classified in their significantly different excitation energy E^* of the Compound Nucleus (CN) when formed at the beam-energy corresponding to the fission barrier. E^* is a critical parameter for the survival probability of the CN. The first type of typical target–projectile combinations, the so-called cold fusion reactions, allowed the discovery of elements with $Z = 107$ –113. The cold fusion reaction use Pb and Bi targets and medium heavy beams and produce CNs at E^* around 10–20 MeV [14]. The syntheses of Nh

via ^{70}Zn and ^{209}Bi currently marks the end of this reaction path.

The production cross sections for these SHEs ranges from 15 nb for the production of rutherfordium (Rf, $Z = 104$) [15, 16] to 0.022 pb for the production of Nh [17]. The cold fusion reactions result in neutron-deficient compound nuclei, and the probability that the system survives against fission is relatively low. The second target–projectile combination type, the hot fusion reaction, irradiates targets from ^{238}U to ^{249}Cf with C to S beams. These fusion reactions lead to a larger fusion cross section along with a lower survival probability due to a higher E^* of the CN. The resulting CN of the hot fusion reaction has an E^* around 30–50 MeV (evaporating 3–5 neutrons). The slope of the cross sections for the cold fusion decrease to the same extent as for the hot fusion. Subsequent elements ($Z = 113$ –118) synthesized in "hot" fusion reactions between doubly-magic ^{48}Ca ¹ and actinide targets show cross sections at a stable level of a few pb. These target-projectile combinations are more mass and charge asymmetric and show a reduced Coulomb barrier with a greater initial excitation energy than the cold fusion reactions.

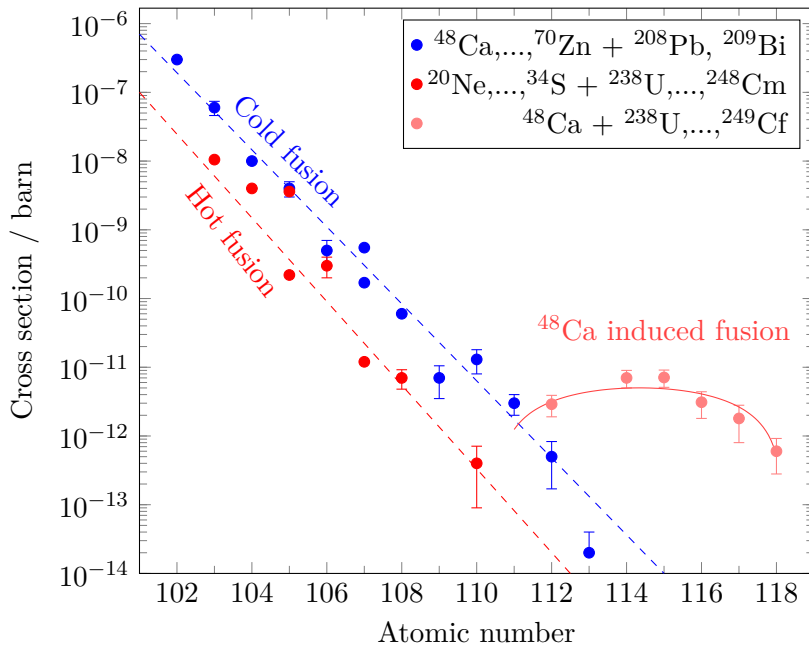


Fig. 3.2.: Comparison of maximum cross sections for heavy and superheavy elements produced in cold fusion and hot fusion reactions. The figure was adopted from [18].

In Fig. 3.2 the cross section for both types of reactions as function of Z is shown. Here, the use of doubly magic ^{48}Ca projectiles with actinide targets leads to a lower E^* of the CN and thus improved the CN survival probability. The cross sections measured in ^{48}Ca -induced production of transactinides is significantly higher compared to other projectile-target combinations. The Joint Institute for Nuclear

¹Nuclei with "magic" neutron number and "magic" proton number are called "doubly magic" and are especially stable against decay.

Research (JINR) in Dubna, Russia used ^{48}Ca induced reactions to discover the elements Fl–Og [19].

From the experimentalist’s point of view, experiments in the upper end of the nuclear chart are always a challenge, since the number of available atoms drops drastically to few atoms per day and below. The cross sections drop from about 10 000 pb to less than 1 pb from Rf to Og, which leads to a production rate decrease ranging from 4 min^{-1} down to 1 month^{-1} [20]. Only single atoms are available requiring one-atom-at-a-time experiments [21, 22]. The main interest in chemical experiments with SHEs is on the study of their chemical behavior relative to that of their lighter homologs [18, 23]. Deviations from trends established by lighter group members are expected due to the influence of relativistic effects, which increase $\propto Z^2$ [24]. The relativistic effects influence the energetic position of the respective atomic orbitals and lead to significant change in the chemical properties of the transactinide elements. This has an immediate implication on the Bohr radius (a_0). The relativistic mass of an electron m_{rel} can be calculated by

$$m_{\text{rel}} = \frac{m_0}{\sqrt{1 - (v/c)^2}} \quad (3.1)$$

where m_0 is the electron rest mass, v is the velocity of the electron and c the speed of light. After substituting the relativistic mass into the equation for the effective Bohr radius a_{rel} , this can be written as

$$a_{\text{rel}} = a_0 \cdot \sqrt{1 - (v/c)^2} \quad . \quad (3.2)$$

The effective Bohr radius decreases with increasing electron velocity. For Og = 118, $v \approx 0.86 \cdot c$, the 1s electron will have 86% of the speed of light. Taking this electron speed into account in Eq. 3.2 leads to shrinking in the effective Bohr radius by 51%. This leads to an orbital contraction and stabilization of the spherical s and $p_{1/2}$ electron orbitals. This orbital contraction is called direct relativistic effect. The indirect relativistic effect based on the expansion of outer d and f orbitals, due to the more efficient screening of spherical s and $p_{1/2}$ shells against the nuclear charge, so that the outer orbitals are energetically destabilized [24, 25]. Therefore, for SHEs some deviations from trends of lighter homologues within one group of the PTE can be expected, due to strong influence of relativistic effects on the chemical properties ².

²based on the influence of the relativistic effect on the valence electrons

The PTE currently contains 118 elements, where the lightest element is hydrogen and the heaviest element is named oganesson. The chemistry of SHEs provides a deeper insights into our understanding of the nucleus and the electronic structure at its limits. With the discovery of the first artificial elements, there are intricate questions, which drive the research of SHEs. The quest to answer the questions what is the heaviest element, which can exist and what are its chemical properties, is a strong driving force to develop new techniques for the production and investigation of such elements. The following chapter deals with a brief introduction to the field of SHEs with its key aspects such as stability, production, detection and chemical properties.

4.1 Introduction in SHE research

4.1.1 Stability of superheavy elements

With the introduction of the PTE in 1869 by the Russian chemist D. Mendeleev only one constituent of the nuclear matter, the still unknown proton, was considered. After the discovery of the proton by the New Zealand-British physicist Ernest Rutherford in 1913 and the neutron by the British physicist James Chadwick¹ in 1932, the field nuclear physics was born. A model for the nucleus could be developed, where the protons and neutrons were held together in the small and dense nucleus by strong short-range nuclear cohesive forces. The Coulomb force between positively charged protons leads to an instability of the nucleus with increasing Z , but can be compensated by the addition of neutrons up to a certain limit.

The driving force to expand the chart of nuclides. A number of theoretical calculations were made and expanded the PTE all the way up to elements 172 and 173 [26–28]. This high atomic number leads to a binding energy of the electrons in the 1s orbital at $2m_e c^2$. This in turn results in that the electron reaches the negative-energy continuum. This circumstance cannot be treated by theory and therefore it symbolizes the current end of the PTE. However, the study of nuclear properties, such as nuclear decay and nuclear reactions is s closely linked to the stability of a nucleus.

¹He studied under Ernest Rutherford and won the 1935 Nobel Prize in Physics for this discovery of the neutron.

Liquid Drop Model

A measure for the magnitude of the stability of a nucleus is the binding energy. In the 1940s, the most successful model for describing the properties of a given nucleus was the liquid drop model, which was proposed by G. Gamow [10]. In 1935, the German physicist C. F. von Weizsäcker further developed this simple model after the discovery of the neutrons. By treating the nucleus as an incompressible, uniformly charged fluid, Weizsäcker made first attempts to formulate the liquid drop model. The binding energy is described by the 'semi-empirical mass formula' (Eq. 4.1) that successfully predicts the binding energies in nuclei.

$$B(N, Z) = a_{\text{vol}}A - a_{\text{surf}}A^{\frac{2}{3}} - a_{\text{coul}}\frac{Z^2}{A^{\frac{1}{3}}} - a_{\text{asym}}\frac{(N - Z)^2}{A} \pm \delta_{\text{pair}} \quad (4.1)$$

In Eq. 4.1 N , Z , and A are the neutron, proton and mass numbers, respectively. The constants $a_{\text{vol}} \approx 16$ MeV, $a_{\text{surf}} \approx 18$ MeV, $a_{\text{coul}} \approx 0.7$ MeV, $a_{\text{asym}} \approx 93$ MeV and $a_{\text{pair}} \approx 11$ MeV are empirically determined. The first represents the attractive nuclear force between nucleons, this nuclear energy is proportional to the volume. The second term describes the surface energy and corrects the assumption made in the first term, where every nucleon interacts with the same number of other nucleons, and is proportional to the surface area. The a_{coul} term is the Coulomb term which accounts for the potential energy of protons. The asymmetry energy is described by the a_{asym} and considers the Pauli principle. The last term includes the pairing energy due to the pairing of protons with protons and neutrons with neutrons [29]. The model's triumph came from explaining the phenomenon of nuclear fission (Bohr and Wheeler, 1939) [30, 31].

The mass M of the respective nucleus can be calculated by means of the binding energy $B(N, Z)$.

$$M = N(m_{\text{n}}) + Z(m_{\text{p}}) - \frac{B(N, Z)}{c^2} \quad (4.2)$$

In Eq. 4.2, N and Z are the number of protons and neutrons, respectively, while m_{n} and m_{p} are the neutron and proton mass, respectively. The liquid-drop model neglects any shell effects on the binding energies and therefore heavy elements beyond $Z = 104$ would undergo fission with very short half-lives due their coulomb repulsion. Without the considering of stabilizing effects of closed nuclear shells, elements beyond atomic number 104 could not exist.

The nuclear Shell Model

The heaviest elements have only a low stability against spontaneous fission and α decay, due to their large number of protons. The stability of a nucleus is connected to its respective binding energy (see Sec. 4.1.1). The Eq. 4.1 describes the binding energy

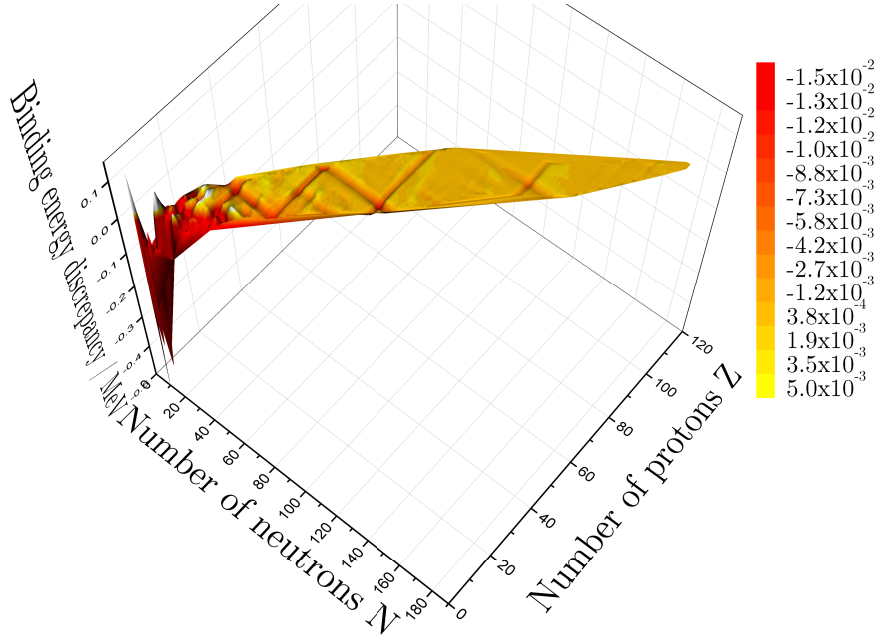


Fig. 4.1.: Deviation of the liquid drop model from experimental data as a function of the neutron number and proton number for all known isotopes based on the AME2003 [32].

of nuclides in macroscopic calculations. The stability and therefore the existence of SHEs is owed to nuclear structure effects, which prevents the fission of the nucleus. This phenomenon is shown in Fig. 4.1, where the shell structure is shown by the pits at closed nuclear shells. The existence of shell structure was already noticed in the early 1930s. First approaches to correct the deviation between the experimental data and the calculated data from the semi-empirical mass formula did not succeed. It took nearly two decades before the German-born American theoretical physicist Maria Göpert Mayer coupled the nucleon spin to its motion within a modified square well potential in 1950 [33, 34]. This quantum mechanical interpretation forms the basis for the 'shell model', since the nucleus will have fine energy levels and exists in stationary states (orbitals). Mayer together with the physicists Eugene Paul Wigner (atomic nucleus and the elementary particles) and Johannes H. D. Jensen (nuclear shell model) were honored in 1963 with the Nobel Prize in Physics for their contribution in unrelated work to the nuclear shell model [35]. The energy levels, associated multiplicities and magic numbers calculated from a harmonic-oscillator potential well including a spin-orbit coupling are shown in Fig. 4.2. The Swedish physicist Sven Gösta Nilsson calculated shell correction energies to extend the shell model to deformed nuclei. Therefore, a deformed nuclear potential with the consideration of the density of single-particle energy levels within the nucleus [36] was added, since the nuclear shell model fails in describing the non-spherical nuclei. The basic formulation of the shell model does not account for the stabilizing effects for nuclides near the closed shells, since in a quantum mechanical description spherical systems

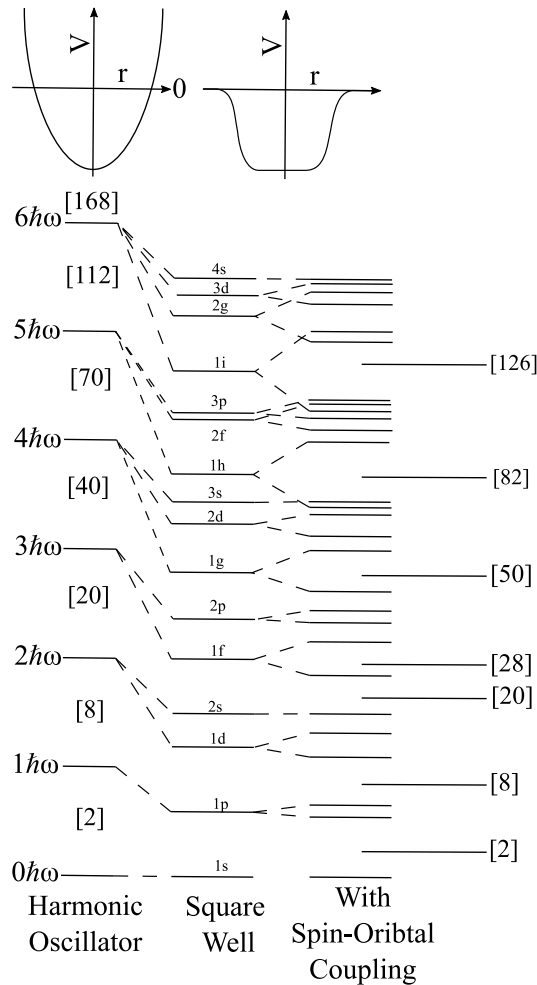


Fig. 4.2.: *Energies of single-particle in a harmonic-oscillator and square-well potentials. The latter split the second set of levels by the spin-orbital term to produce the experimental observed shell gaps. In addition, the multiplicities and their sums are given.*

cannot rotate collectively. In the Nilsson model, the harmonic oscillator potential is modified with an anisotropy to change oscillator frequency along all three Cartesian axes. The rotational bands follow the same $J(J+1)$ pattern of energies as in rotating molecules. The energy splitting as a function of deformation is shown in Fig. 4.3. A large gap between energy levels at $\epsilon = 0$ indicates a particle number at which there is a shell closure and an increase of the deformation results in a shift in energy for the associated energy level. The nuclear shells occur in the regions where there are the fewest single particle levels, this means that the shell-correction energy tends to lower the ground-state masses of nuclei with magic or near-magic numbers. At a deformation of about $\epsilon \approx 0.6$, there is a cross-over of the Nilsson states, the existing shell gaps vanish and new gaps occur.

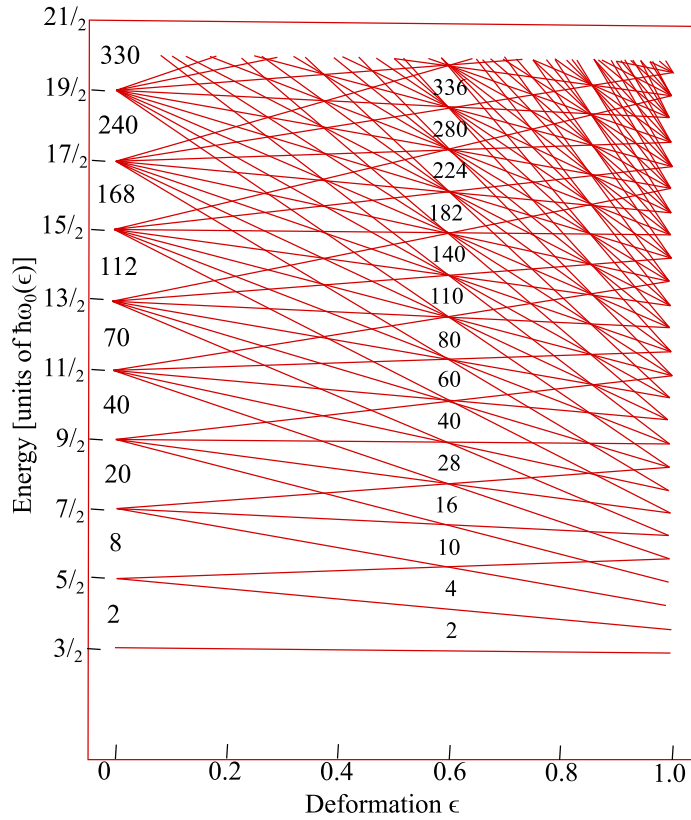


Fig. 4.3.: Nilsson model, which describes the nuclear energy levels of a modified harmonic-oscillator potential as a function of the deformation of the nucleus. The graph is adapted from [37].

4.1.2 Production of SHEs in nuclear fusion reactions

As mentioned in Chap. 3, all elements heavier than U do not occur in nature² because their half-lives are short compared with the age of the Earth. All elements beyond U have to be produced artificially and the most straight forward way is to bombard an element such as U with neutrons and allow the neutron-rich isotopes to β^- -decay into a element with $Z + 1$ (${}^A_Z X \rightarrow {}^A_{Z+1} X'$)³. The heaviest element which can be produced by such a process is Fm ($Z = 100$), since all heavier Fm isotopes do not decay by β^- -emission but by fission. To circumvent this problem, heavier elements than Fm can only be produced in nuclear fusion reactions and are investigated in one-atom-at-a-time experiments [22]. There are two types of fusion reactions, cold fusion and hot fusion (Chap. 3), according to their excitation energy E^* of the compound nucleus.

In general the production probability for a nuclide in a nuclear reaction is described

²except for trace amounts of Np and Pu

³Es ($Z = 99$) and Fm were first detected in the debris of the 1952 Ivy Mike hydrogen bomb test [38].

as Evaporation Residue (ER) cross section σ_{ER} (see Eq. 4.3) and is written as the product of the capture cross section σ_{cap} , the probability for the formation of a compound nucleus P_{CN} , and the survival probability W_{surv} .

$$\sigma_{\text{ER}} = \sigma_{\text{cap}} \cdot P_{\text{CN}} \cdot W_{\text{surv}} \quad (4.3)$$

There were several aproches to describe the fusion reaction as a multi stage process. In a first model, the Danish physicist Niels Bohr suggest an entrance channel and an exit channel (1936) [39], where the entrance channel describes the approach of the accelerated projectile to the stationary target, to form a highly excited compound nucleus. The exit channel on the contrary describes the de-excitation to the Evaporation Residue (ER) nucleus [40]⁴. In later models a third stage was introduced, dividing the entrance channel into two separate stages.

The detection of an ER is an incontrovertible evidence that the accelerated projectile

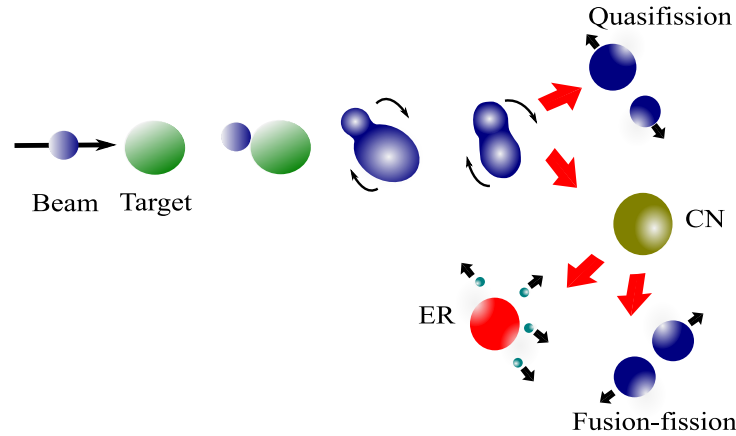


Fig. 4.4.: *Schematic illustration of the fusion evaporation reaction towards creation of an ER.*

fused with the target to a compound nucleus, which survived against fission. As shown in Fig. 4.4, the formation of an ER takes place, if the bombarding energy is sufficient to overcome the Coulomb repulsion [42]. In a first step, the accelerated projectile collides with the stationary target to form a dinuclear transition state, which is called "system in capture" and described by the σ_{cap} ⁵. The excited transition state undergoes shape and energy equilibration, unless the system reseparates via quasifission into a projectile-like fragment and a target-like fragment after a brief interaction. The quasifission hinders the formation of the intended compound nucleus. The quasifission occurs with a higher probability in symmetric combination of projectile and target nucleus and also at higher energies, where the transition state evolves after nucleon transfer takes place. In the case of a strongly asymmetric

⁴R. Bass studied the nuclear potential (Bass Fusion Barrier) on the basis of the liquid drop model, which later was named after him [41].

⁵depends on the center of mass energy, the Coulomb barrier and the angular momentum

nuclear combination, the system may merge into a compound nucleus ($P_{\text{CN}\approx 1}$). The compound nucleus then deexcites via particle and γ ray emission to reach the final ER. In the case that the fission barrier is higher than the excitation energy⁶, the excited compound nucleus most often undergoes fission within 10^{-14} s. The deexciting survival probability is described by W_{surv} . The survival probability during the deexcitation or the compound nucleus can be calculated within a statistical framework. In this model, the survival probability (see Eq. 4.4) depends only on the ratio of the probability of the neutron evaporation and the the probability of fission and neutron evaporation. The probability for neutron evaporation and fission is determined by the partial width Γ_i , where the index marks neutron (n) and fission (f) and hence realization probability (P_{xn}), where the compound nucleus evaporates exactly x neutrons.

$$W_{\text{surv}} = P_{xn} \prod_{i=1}^x \left(\frac{\Gamma_n}{\Gamma_n + \Gamma_f} \right) \quad (4.4)$$

The statistical analysis of the decay of the compound nucleus in the statistical framework has the largest inaccuracy in Eq. 4.3, around a factor 3 [43].

4.1.3 Experimental techniques

Fast chemical separations to study chemical and physical properties of short-lived radioactive nuclides have a long history in the SHE field. The difficulties in the production and rapid chemical separation of only a few single atoms of SHEs from unwanted side products lead to the development and introduction of unique separation methods. The first transuranium elements up to Md ($Z = 101$) were identified by chemical means and from there on physical methods prevailed. Nevertheless, rapid gas-phase chemistry was important for the claim of the discovery Rf ($Z = 104$) and Db ($Z = 105$) [42, 44, 45]. Today the fastest chemical gas-phase separations allow the investigation of nuclides of SHEs with half-lives of less than 1 s. Due to the low production rates and short half-lives, chemistry experiments must be performed on the one-atom-at-a-time scale. Experiments with transactinide elements can be broken down into the following basic steps: (i) synthesis of the transactinide element, (ii) fast transport of the synthesized to the chemical apparatus and (iii) preparation of a sample and detection via nuclear spectroscopy.

One-atom-at-the-time experiments

The low production yields of SHEs demand efficient methods to perform chemical experiments with only one atom at a time. A further problem of the availability of

⁶The expected excitation energy E^* is the sum of center of mass energy E_{CM} and the Q-value of the reaction $E^* = E_{\text{CM}+Q}$

only a single atom is that the law of mass action⁷ is not valid anymore, since a single atom can not exist in two different states at the same time. Another consequence is that the reaction time $t_{1/2}$ becomes too slow in laboratory experiments. The reaction time for a elementary reaction of the second order ($E_1 + E_2 \rightleftharpoons E_3 + E_4$) is given by

$$t_{1/2} = \frac{1}{k_1 C_0} \quad (4.5)$$

where k_1 is the forward reaction rate constant and $C_0 = [E_1] = [E_2]$ is the starting concentration of E_1 and E_2 . With a decreasing of the starting concentration beyond the tracer scale ($C_0 < 10^{10}$), the reaction time is increased by a factor of 10^{10} . Therefore, reactions between two single atoms cannot be observed on the time scale of laboratory experiments. The reaction between a single atom⁸ and a reactant in macroscopic scale ($E_{\text{single}} + E_{\text{macro}} \rightleftharpoons E_{\text{single}}E_{\text{macro}}$) can be understood as reaction of first order⁹. The change in the concentration with time can be written as

$$-\frac{d[E_{\text{single}}]}{dt} = k[E_{\text{single}}][E_{\text{macro}}] = k'[E_{\text{single}}] \quad (4.6)$$

with $[E_{\text{macro}}] \approx 1$ the reaction rate constant, which can be coupled with the concentration $[E_{\text{macro}}]$ to a conditional rate constant. The reaction time for a reaction of pseudo first order can be written as

$$t_{1/2} = \frac{\ln 2}{k} \quad (4.7)$$

The reaction time is independent from the initial concentration. The reaction in [Eq. 4.6](#) is important for chemical experiments¹⁰ in the liquid-phase. Nevertheless, chemical experiments can be only performed, if the half-live of the investigated nuclide is in the same order as the reaction time ([Eq. 4.7](#)). On this basis, chemical experiments with SHEs can only be performed with isotopes with half-lives of at least a second or larger. If the half-life is around seconds, there are fast chemical techniques, which will be briefly presented in [Sec. 4.1.4](#).

The chemical investigation of single short-lived atoms of transactinide elements is one of the most challenging tasks, since only single atoms are available for such experiments. All the techniques like synthesis, rapid transport, chemical isolation, and detection of the radioactive decay have to be optimized in order to push those experiment forward to heavier transactinide elements. The coupling of chemical systems to recoil separators allowed to conduct on-line chemical experiments. The chemical investigation of SHEs can be divided into four steps: (i) synthesis of the

⁷The law of mass is only valid in macroscopic framework, where elements were in the the order of trace scale (10^{-10} mole; $1 \text{ mol} = 6.02210476 \cdot 10^{23}$ atoms) available.

⁸With a short half-life, since with a stable or long-lived nuclide any radiochemical techniques can be used for single-atom chemistry.

⁹here is no significant consumption of the reactant in macroscopic scale ($[E_{\text{macro}} \approx 1]$)

¹⁰Hydrolysis and complexation

ER in fusion reactions (Sec. 4.1.2), (ii) fast extraction of the synthesized ER to the subsequent chemical apparatus (see Sec. 6.3), (iii) fast chemical separation of the desired ER and (iv) detection of the ER via characteristic decay properties. In the context of this work, the second step with the introduction of a new coupling of a BGC with electric fields to the chemical system COMPACT is of particular importance. The production rate of ERs is proportional to the target thickness¹¹ and the beam intensity. The useable thickness of the target is also limited by the recoil range of the formed compound nucleus ($< 1 \text{ mg cm}^{-2}$) [42]. In addition, the target backing and the target restrict the beam intensity, since the target has to withstand the high beam intensity. Due to the repulsive Coulomb force between the accelerated projectile and the stationary target, the projectile needs a high enough energy to overcome the fusion barrier with a small impact parameter (central collision). At higher impact parameters elastic and inelastic scattering takes place. During inelastic scattering, the probability of capture of the projectile by the target nucleus and a further CN formation is suppressed and transfer reactions dominate. Transfer reactions lead to a huge amount of different nuclei and together with the elastically scattered target material, which have to be separated from the desired ER. Therefore, highly efficient and selective separation techniques are needed. Since the half-lives of SHE decrease with increasing atomic number, fast separation methods must be used for SHE experiments.

Chemical separation

From the lighter elements like Rf ($T_{1/2}(^{261}\text{Rf}) = 78 \text{ s}$) to the heavier elements like Fl ($T_{1/2}(^{289}\text{Fl}) = 1.9 \text{ s}$), speed becomes increasingly important. The separation system must be selective enough to study chemical properties as well as to separate undesired by-products of the nuclear reaction, which could interfere with the detection of transactinide nuclei. Therefore, the speed and selectivity is important for the required sensitivity for the chemical separation. The consequence of chemical experiments at the one-atom-at-a-time scale is that the studied nuclide must be subjected to a repetitive partition experiment to ensure statistical significance, since the law of mass action is no longer valid. The desired nuclide cannot exist simultaneously in different forms and participate in the chemical equilibrium. For this reason, the concentration or partial pressure has to be replaced by the probability to find an atom in one state or another. The individual probabilities can be deduced from chromatography experiments.

Detection

After the separation and preparation of a sample, the unambiguous identification of the separated nuclei is the most important part of the whole experiment. The

¹¹This assumption is only valid as long as the entire excitation function is in the target.

identification of the separated nuclei via their characteristic nuclear decay signature is the only possibility to unambiguously detect the presence of these nuclei. For this reason, the prepared samples must be suitable for the subsequent high resolution α -particle and SF-spectroscopy. The detection of characteristic decay chains of the transactinide nuclei prove the presence of the desired nuclei in the sample. Therefore, every event is registered together with its time information. This allows the determination of energy and time correlations between the mother-daughter α - α - or α -sf decay sequences.

4.1.4 Chemical properties of SHEs

The PTE (Chap. 3), introduced by Dmitri Mendeleev and independently by the German chemist Lothar Meyer in 1869¹², is for modern chemists an essential tool to summarize and compare the chemical properties of all currently known elements. The elements were placed by their electronic configuration in the valance shell and hence by their proton number even through this was not yet known at that time. Since the introduction of the PTE it is a fundamental part to verify the validity of the PTE. During the last decades, the chemical studies of transactinides expand our knowledge of chemical properties of the heaviest elements and they were used for the validating the PTE. The chemistry of the SHEs share similar chemical properties in dependence on the reactivity of the valence electron configuration with the lighter homologues in the same column in the PTE up to the present day [47]. This is not self-evident, since the chemical properties of the heaviest elements can differ from the light homologues due to relativistic effects. The electronic structure in the valence shell of SHEs is influenced by relativistic effects. The relativistic velocity¹³ (see Eq. 3.1) of the inner and outer electrons due to the high nuclear charge is responsible for contraction of the s and $p_{1/2}$ orbitals and a better shielding of the nuclear charge, so that the outer orbitals (d and f) are more expanded and destabilized [25, 42, 48]. In Fig. 4.5, the relativistic contraction of the $7s$ atomic orbital of Db ($Z = 105$) is shown. Here, the large s -wave probability is shifted closer to the nucleus due to the relativistic effect. Therefore, first chemical differences in the properties of SHEs can be observed in chemical adsorption experiments in the gas-phase. Detail studies at the Joint Institute for Nuclear Research in Dubna (Russia) and the GSI Helmholtzzentrum für Schwerionenforschung GmbH in Darmstadt (Germany) with Fl were able to show that Fl forms a metal-metal bond on a gold surface, however with a significantly lower bond strength than the lighter homologue Pb ($Z = 82$) [49]. Similarly, Cn ($Z = 112$) reacts with the gold surface much weaker than its homologue Hg ($Z = 80$) due to relativistic effects on the valence electron shell [50]. The prediction of chemical properties by theoretical quantum-chemical methods are

¹²In his book 'Die modernen Theorien der Chemie' (1864), he introduced the concept of atoms and molecules together with a first version of a PTE [46].

¹³The relativistic velocities cause an increase in the electron mass.

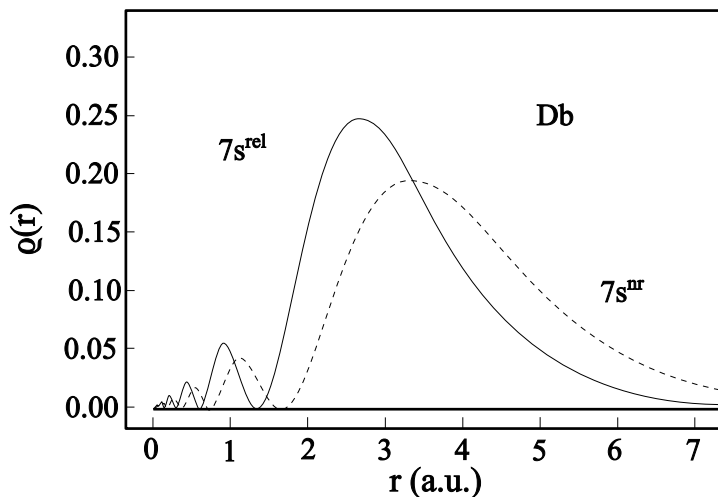


Fig. 4.5.: *Relativistic (solid line) and nonrelativistic (dashed line) radial distribution of the 7s valence electrons in Db. Figure taken from [42].*

essential for a better understanding of the chemical behavior of SHEs. Nevertheless, the theoretical methods need input from the experimental side to improve and validate their models. In the last decades a symbiotic relationship between both fields has developed.

As mentioned in [Sec. 4.1.1](#), the stability of SHEs decreases with increasing the nuclear charge due to the Coulomb force of the protons. Therefore, the production cross section and production rate drops significantly at a maximum of one atom per week [20]. The first transuranium elements were identified by chemical means. In the last decades this shifted completely to the nuclear physics field due to the very short half-lives. In the last years, the hunt for new elements were brought to a halt, since the limits of performance of the state-of-the-art is reached.

Chemistry experiments with SHEs

The chemical experiments presented in this section provide important information about the chemical properties of the transactinide elements. Under the restrictions of chemistry with single atoms, only a limited number of chemical properties can be investigated experimentally. The formation of chemical compounds and their volatility was studied in gas-phase chromatography experiments, where the adsorption behavior and retention times were investigated. On the other hand, the formation of complexes with transactinide elements in aqueous solutions and the behavior of these complexes were investigated by using liquid-phase chromatography and liquid-liquid extraction experiments. The obtained results of these experiments can only be compared directly with the behavior of lighter homologues if they were determined in the same experiment. The interpretation of the experimental results is based on the determination of analogies to the lighter homologues. Many important

properties, such as the ionic radius and the stability of the oxidation states, can only be determined indirectly. A further difficulty arises from the fact that the structure of the transactinide molecule is not accessible with classic spectroscopy methods and this information remains hidden. For the physicochemical quantities, like adsorption enthalpy or sublimation enthalpy, empirical models are used and the interpretation of these data is a difficult venture.

Liquid-phase experiments

In the liquid-phase chemistry the hydrolysis, complex formation and the stability of oxidation states of SHEs were studied. The manual liquid-liquid separation methods were used to study the chemical properties of Rf [51–53] and Db [54]. Here the complex formation, determined from the distribution coefficient (K_d) with halide anions on a cation exchange column was compared with lighter homologues. The separation procedure was time intensive, since every single sampling step needs around 30 s and manual separation techniques become impractical. A breakthrough was made with the introduction of automated column separations and faster sampling times and higher reproducibility could be achieved. The ARCA (Automated Rapid Chemistry Apparatus) was used to study the F^- complex formation of cationic species of Zr, Hf and Rf [55]. The transactinides Rf ($Z = 104$), Db ($Z = 105$) and Sg ($Z = 106$) have been chemical separated with the ARCA setup. The last element, which has been investigated in liquid-phase chemistry experiments is Sg, produced at the GSI Helmholtzzentrum für Schwerionenforschung with the reaction $^{22}Ne + ^{248}Cm$. The formation of oxides, oxide halides and hydroxide halides in the liquid-phase were investigated with the synthesized $^{265}Sg^{14}$ [57, 58] and compared with the lighter group-6 elements. Until today, no chemical experiments in the liquid-phase were performed with elements beyond Sg. Experiments in the liquid-phase are limited to productions rates around one atom per hour and half-lives of order of several seconds [42]. Some isotopes for elements Mt ($Z = 109$), Ds ($Z = 110$) and Rg ($Z = 111$) are relatively long-lived, but cannot be produced directly, but are formed in α -decay chains of heavier precursors.

Gas-phase experiments

Chemistry experiments are difficult to conduct since the production rate and the short half-lives limit these experiments to isotopes with half-lives no shorter than 1 s [45]. The liquid-phase chemistry experiments feasibility depends on the difficulty to produce them with a rate that would allow these experiments. Until today, experiments in the gas-phase are an efficient method to investigate chemical properties or to perform chemical separations. The gas-phase experiments assumes that the high kinetic energy of ERs is decreased to thermal energies in a so called Recoil

¹⁴ ^{265}Sg has two states with half-lives of about 9 and 16 s [56].

Transfer Chambers (RTC) [59]. The RTC can be connected straightforward with a capillary directly to a gas chromatographic system [42, 45]. Another advantage of this approach is that gas-phase separation procedures are fast and efficient and can be performed continuously in contrast to liquid-phase experiments.

The separation of transactinide elements in the gas-phase were established by I. Zvára *et al.* in Dubna (Russia) [60, 61] and involved first chemical studies of volatile Rf, Db, and Sg (oxy)halides. The chemical behavior of transactinide compounds from Rf up to Bh were studied in detail in on-line gas chromatography experiments with the On-Line Gas chromatography Apparatus (OLGA), which allowed the α -spectrometric measurement of ERs and was a breakthrough in the field of the *in situ* detection of volatile reaction products on the single atom scale [62]. This technique was developed by Gäggeler *et al.* [62]. In 1992, the Berkley group adapted the improved version of OLGA II and constructed the Heavy Element Volatility Instrument (HEVI) [63], which used a continuous on-line gas chromatography system to separate halide complexes according to their volatility¹⁵. In 2002, U. Kirbach *et al.* developed the first thermochromatographic detector for the on-line measurements of SHE, the Cryo-Thermochromatographic Separator (CTS). An improved version, the Cryo On-Line Detector (COLD), was successfully applied by Ch. E. Düllmann *et al.* for the first chemical investigation of HsO₄ [64]. The Cryo On-Line Multidetector for Physics And Chemistry of Transactinides (COMPACT) detection system [13] was constructed by A. Yakushev *et al.* particular for chemistry experiments with HsO₄ and was also used to conduct chemical experiments with Sg(CO)₆ [65] and Fl [49]. The chemical behavior of such complexes were studied with the thermochromatography technique. In contrast to the classic chromatography, the chromatogram is not measured at the end of the separation column, but during the separations steps. Due to the short half-lives, a fraction of the transactinide elements will decay inside the column. The results were compared with calculations from microscopic models for gas chromatography. Monte Carlo simulations are of particular importance in gas chromatography experiments with transactinides.

The *in situ* formation of a volatile compound, like halides, oxyhalides, oxide hydroxides, and oxides were studied with transactinide elements up to group 7. The very volatile tetroxide molecule is the species of choice for elements of group 8 [13, 64]. The successful syntheses of the volatile Sg hexacarbonyl complexes [65] arises perspectives for further studies with carbonyls of group 6–9 [66]. The heaviest element which was studied with gas-phase chromatography is Fl. Recent gas-phase thermochromatography experiments with the elements Cn [67] and Fl confirm that both elements are volatile atoms due to their closed and quasi-closed electron ground-shell configurations, $6d^{10}7s^2$ and $7s^2 7p_{1/2}^2$, respectively [68]. But with the current state-of-the-art technique the elements Mt, Ds, and Rg ($Z = 109 - 111$) cannot be investigated. The low production rates due to the low cross sections and short

¹⁵The retention time is meant by the terminus volatility.

half-lives make it not feasible to conduct gas-phase experiments. The production probability of ^{48}Ca induced fusion reactions is peaked around Fl ($Z = 114$) and Mc ($Z = 115$) with a cross section in the range of almost ten pb and drops significantly with increasing Z . For these elements a fast and efficient technique is required to get access to elements beyond Fl. First attempts with Nh were performed at the Dubna Gas-Filled Recoil Separator, but no information on the chemical form of Nh (atomic vs. NhOH) and decay chains have been published yet. The longest lived isotope of Mc and beyond are too short for chemical investigation with the current state-of-the-art.

Another important factor for a potential gas-phase investigation is the volatility of these elements, since the gas chromatography needs volatile species for the transport from the RTC to the gas chromatography column [42, 45, 49]. In Tab. 4.1, the current scientific knowledge about the chemical investigation of transactinide elements with gas-phase experiments were summarized.

Tab. 4.1.: Summary of transactinide isotopes investigated in gas-phase chemical experiments. The respective half-lives were taken from [69]. The production rate is based on a target thickness of 0.8 mg cm^{-2} and a beam intensity of $3 \cdot 10^{12}$ particles per second. As an introduction, the review articles [23, 45] will give a general overview over gas-phase chemistry experiments.

Isotope	Half-life (s)	Reaction	σ	Production rate	Investigated species	Ref.
^{261}Rf	65_{-10}^{+10}	$^{248}\text{Cm} + ^{18}\text{O}$	5_{-2}^{+3} nb	1.5 min^{-1}	RfCl_4 , RfBr_4 RfOCl_2	[70, 71]
^{262}Db ^{263}Db	34_{-2}^{+2} 27_{-7}^{+10}	$^{249}\text{Bk} + ^{18}\text{O}$	6_{-3}^{+3} nb 10_{-4}^{+6} nb	2 min^{-1} 3 min^{-1}	DbBr_5 , DbCl_5 , DbOCl_3	[72, 73]
^{265}Sg ^{266}Sg	10_{-8}^{+20} 21_{-12}^{+20}	$^{248}\text{Cm} + ^{22}\text{Ne}$	380_{-70}^{+90} pb 60_{-29}^{+106} pb	8 h^{-1} 1 h^{-1}	SgO_2Cl_2 , $\text{SgO}_2(\text{OH})_2$, $\text{Sg}(\text{CO})_6$	[57, 65, 74–76]
^{267}Bh	17_{-6}^{+14}	$^{249}\text{Bk} + ^{22}\text{Ne}$	58_{-15}^{+33} pb	1.2 h^{-1}	BhO_3Cl	[77]
^{269}Hs ^{270}Hs	16_{-6}^{+6} 9_{-4}^{+4}	$^{248}\text{Cm} + ^{26}\text{Mg}$	7_{-3}^{+3} pb 3_{-1}^{+2} pb	3 d^{-1} 1.5 d^{-1}	HsO_4	[13, 64]
^{283}Cn	4_{-1}^{+1}	$^{238}\text{U} + ^{48}\text{Ca}$	3_{-2}^{+4} pb	1.5 d^{-1}	Cn	[78, 79]
^{284}Nh	$0.93_{-0.14}^{+0.14}$	$^{243}\text{Am} + ^{48}\text{Ca}$	$8.5_{-3.7}^{+6.4}$ pb	2.8 d^{-1}	Nh, (NhOH)	[80, 81]
^{285}Nh	$3.3_{-1.1}^{+1.1}$		$1.5_{-0.9}^{+1.4}$ pb	0.8 d^{-1}		
^{287}Fl ^{288}Fl ^{289}Fl	$0.48_{-0.09}^{+0.16}$ $0.69_{-0.11}^{+0.17}$ $1.9_{-0.4}^{+0.7}$	$^{244}\text{Pu} + ^{48}\text{Ca}$	$3.6_{-1.7}^{+3.4}$ pb $1.7_{-1.1}^{+2.5}$ pb $5.3_{-2.1}^{+3.6}$ pb	1.8 d^{-1} 0.9 d^{-1} 2.7 d^{-1}	Fl	[49, 82, 83]

4.2 Experimental Methods

The artificial elements heavier than Fm ($Z = 100$) were produced in nuclear fusion reactions using particle accelerators. A first approach to perform chemical experiments to probe the structure of the PTE (see Fig. 4.9) was to thermalize the nuclear reaction products in a gas-filled recoil chamber¹⁶ direct behind the target. In the recoil chamber also the majority of the unwanted side products from transfer reaction and interaction of the beam with impurities or target assembly were thermalized. In addition, a plasma is created inside the recoil chamber. An important factor to perform chemistry experiments with SHEs is a fast transfer of the reaction products from the targets to the chemistry setup. Therefore, the aerosol transport technique is a well-established method to transfer short-lived isotopes with half-lives of few seconds [62, 84]. The thermalized reaction products were picked up by carrier gas seeded with aerosol particles since the non-volatile fusion products attach on the surface of such aerosol particles. An alternative approach is the in-situ formation of highly volatile species and the transfer of these species to the downstream experimental setup. This method was successful used in the chemical investigation of Hs in the form HsO_4 . A draw-back of both techniques are that there is no selectivity between the desired and unwanted reaction products. An unambiguous identification of the nuclides of interest is not possible without a chemical setup with a high separation factor. The presence of a plasma due to the intense projectile beam behind the target destroys the needed aerosol particles or volatile species for the transportation. This results in a drastic drop in the transport efficiency at high beam intensities. This can be overcome by the combination of a gas-jet with a physical recoil separator [85, 86]. The physical pre-separation was established with the Berkeley Gas-filled

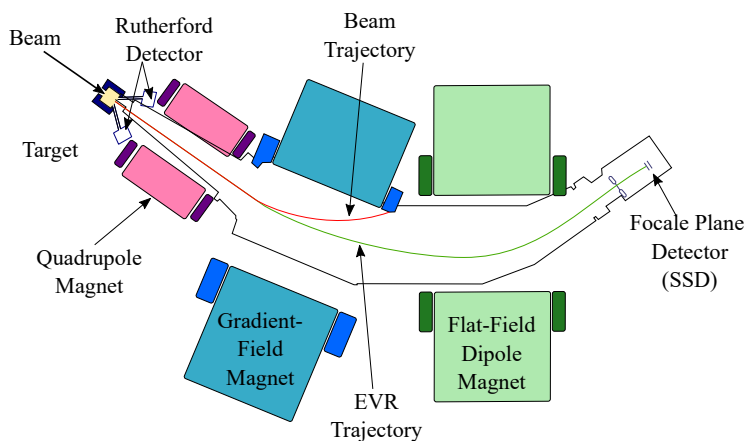


Fig. 4.6.: A schematic diagram of the Berkeley Gas-filled Separator. The Beam enters the apparatus from the left. Adapted from [87].

Separator (BGS, see Fig. 4.6) at LBNL, Berkeley, CA, where also the first Recoil

¹⁶For experiments without a preseparator, the terminus recoil chamber is used for a gas-filled cell.

of the ERs. The advantage that the fusion evaporation products were produced and separated in-flight allows the straightforward connection to a gas-phase chemistry setup like COMPACT, where the chemistry separation and detection were performed simultaneously. This approach provides access to gas-phase chemistry experiments with Fl ($Z = 114$), which is the heaviest element that had its chemical properties studied. The current state-of-the-art technique is limited to isotopes with half-lives around 1 s [45, 49]. In the recent years, a number of efforts have been made to

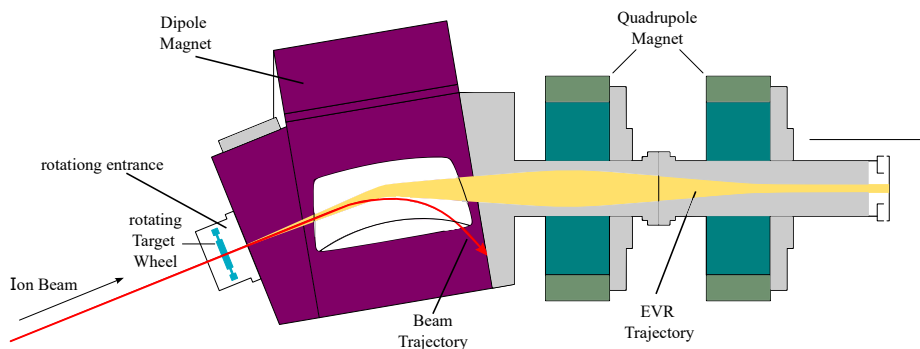


Fig. 4.8.: *Schematic outline of the Dubna Gas-Filled Recoil Separator. Adapted from [80].*

push the limit further towards short-lived isotopes, which are accessible through hot fusion reactions. One of these methods is vacuum chromatography. Vacuum chromatography exploits the molecular flow regime with fast particle velocities. Since the absence of gas, the particles have to be stopped by implantation. Afterwards, the particles are subsequently released from a hot surface. These techniques need an α -particle detector that operates in a high-temperature regime [89, 90]. In the work presented here, an extended BGC with a superimposed DC and RF electric guiding field will be used [91–93].

4.2.1 The buffer-gas-cell

The production of SHEs in fusion-evaporation reactions requires primary beam energies in the range of 5–6 MeV/u to overcome the Coulomb repulsion, which results in recoil energies around tens of MeV. The recoil energy of the ER exceeds the energy acceptance of the chemical setup. BGC, also referred as ion gas-catchers are a suitable tool to stop and thermalize fast recoil-ions. The basic idea of the BGC is to slow down and thermalize initially energetic recoil-ions from nuclear reactions in He gas. Ions are transported by the carrier gas out of the BGC and injected through a differentially pumped electrode system to the high vacuum section of the isotope separator for further experiments. During the stopping process, the charge state is constantly changed in charge exchange collisions [91, 95]. In pure He buffer gas the ions can reach a 2^+ charge state, since the second ionization potential for most elements is below the first ionization potential of He. However impurities like

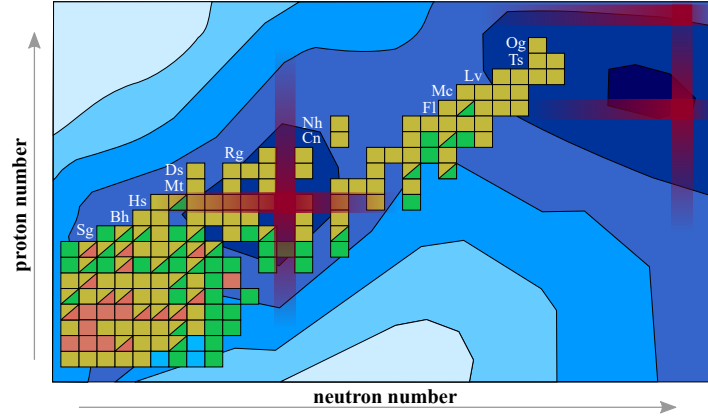


Fig. 4.9.: Part of the nuclear map with the shell correction energy from microscopic-macroscopic model calculations (in blue) showing the regions of stronger binding around $Z = 108$ and 114 and $N = 162$ and 184 . figure based on data from [94].

H_2 , N_2 , O_2 or H_2O in sub-ppm level reduce the charge state to 1^+ or even lead to neutralization. Modern BGCs use de Laval nozzles to extract ions from the BGC. It is used to accelerate a gas passing through it in the axial direction to form a supersonic gas-jet [92, 96, 97].

This method of transforming high-energy nuclear reaction products into low-energy ion beams was pioneered in the early 1980s in so-called IGISOL (Ion Guide Isotope Separator On-Line) systems, for use with light-ion fusion-evaporation reactions where recoil energies are small (<100 keV/u; for heavy ions often less than a few keV/u) [95]. Since no chemical process is involved, the extraction time of such a BGC is in the range of several ms. This opens access to short-lived nuclei. A first demonstration of this technique was the extraction and investigation of ^{188m}W ($T_{1/2} = 5.5$ ms) in 1985 [98]. With the success of the transportation and thermalization of low-energy products, this technique was quickly adapted to fission and heavy-ion fusion-evaporation reactions. With the introduction for use at in-flight separators, the higher recoil energies require higher stopping powers of the BGC, which results in larger stopping volumes. The rapid extraction times could no longer be guaranteed and require electric-field guidance of the ions for a fast and efficient extraction. The initial kinetic energies of the incoming product beam are reduced with degraders or the entrance window down to around 1 MeV/u, since the size of the gas volume has a direct influence on the extraction time. The size of the BGC and the gas pressure depend on the energy distribution of the entering ions. The main disadvantage of the BGC is that the extraction efficiency depends on the incoming ion beam intensity. The reason for this observation is the creation of high density ion-electron pairs during the thermalization process. The resulting charge density screens the electric field and leads to an increase of the lateral distribution of the slowed ions [92, 93, 99]. The impurity of the buffer gas is another parameter, which negatively influences the

extraction efficiency since the neutralization or molecule formation leads to isotope losses. At thermal energies the ions cannot be neutralized in collisions with the buffer gas. The neutralization happens due to impurities in the buffer gas. The technical development has focused on removing impurities down to sub-ppb levels [93, 100–102]. The introduction of the cryogenic BGC improved the purity due to freezing out the impurities [97].

The BGCs employ one of two basic designs. The first design consists of a simple gas-filled chamber, which used gas-flow to extract the ions. This design is used for the aforementioned RTCs. Here, the extraction efficiency is high but the extraction time is limited by the gas-flow. The second design contains a buffer gas-filled chamber, exit nozzle and an electrode structure to generate DC and RF fields for a fast ion extraction. The advantage is that this reduces significantly the extraction time and increases the efficiency, but RF systems are extremely complex. Numerous ion-transport methods utilizing electric fields and respective electrode structures have been explored in order to improve the transport times inside large volume BGCs. The ion-motion in gas will be discussed in the next sections.

Slowing down of ions in gas

The stopping power of the BGC and the range of the ions is determined the dimension of the chamber and the operation pressure at a given kinetic energy of the pre-separated ions from the physical recoil separator. The ions lose energy in elastic and inelastic collisions if they pass through matter. The ions experience atomic and nuclear interactions with the penetrated matter. The atomic collisions are dominating and are of statistical nature. The mean energy loss $\langle \Delta E \rangle$ of an ion in a layer of gas Δx at a defined energy E is given by the formula

$$\frac{\langle \Delta E \rangle}{\Delta x} = NS(E) \quad . \quad (4.8)$$

The kinetic energy is lost in collisions of N atoms with the linear stopping power $S(E) = -dE/dx$. The term $\frac{dE}{dx}$ is the rate at which energy is lost as the ion moves through the gas. With a decrease of the ion velocity the stopping power increases. In the 1930s much research has been carried out to determine the stopping power and H. A. Bethe established the first equations for the stopping power. The Bethe formula describes the energy loss for a given charge state:

$$-\frac{dE}{dx} = \frac{4\pi e^4 Z^2}{m_0 v^2} \rho_N B \quad (4.9)$$

with the ion's atomic number Z and velocity v , m_0 is the rest mass of an electron, ρ_N is the density of the gas and B is a parameter dependent on the medium and ion

velocity:

$$B = Z \left[\ln \frac{2m_0v^2}{I} - \ln \left(1 - \frac{v^2}{c^2} \right) - \frac{v^2}{c^2} \right] \quad (4.10)$$

Here, Z is the atomic number of the gas, I is the average energy for ionization of the gas, and c is the speed of light. The Eq. 4.9 has an elastic and an inelastic contribution [103]. The elastic collisions have a minor contribution to the total energy loss at kinetic energies over 1 MeV/u. The inelastic stopping power function have a maximum at a few MeV/u due to the mean ionisation. As the particle comes to rest, the charge is reduced due to electron pickup and energy loss goes to zero. The characteristic stopping power of an ion through the gas as function of the path length is described by the Bragg curve. The range R of a particle through the gas is dependent on the stopping power and is given by the differential equation:

$$R = \int_{E_0}^0 \frac{dE}{-dE/dx} \quad (4.11)$$

where E_0 is the initial kinetic energy of the ion and $-dE/dx$ is the energy loss function of the ion [104].

Neutralization

BGCs filled with noble gasses like helium are good devices to preserve charged species. The high ionization potential of He prevents charge-exchange processes between the ions of interest and the buffer gas He, which leads to a relatively long ion survival time. Together with the use of high-density in the range of atmospheric pressure, as it is used with the RTC at TASCAs (see Chap. 3), make BGCs to an attractive approach to thermalize radioactive ions after their production and transfer into a chemistry experimental setup. Depending on the volume of such a BGC, extraction times will range from ms (with electric field) to several seconds (only gas-flow). The dimensions of the BGC are rather limited, as is the obtained efficiency due to the neutralization of the primary ions [105].

The transferred ions from the target station into the BGC, the ions collide with the buffer gas and eventual impurity molecules during their residence time inside the BGC. All these collisions and interactions eventually lead to a neutralization or formation of molecular ions. The reaction mechanism for the neutralization of the ions X^+ can be described as three-body ion recombination [101, 105]



and the reaction rate depends on the He gas pressure and the density of electrons in the BGC. The three-body recombination coefficient α together with the number of created ions (electron pairs, EP) N_{EP} the charge density n in dependency of the

time t can be written with the time constant $\tau = 1/\sqrt{N_{\text{EP}} \cdot \alpha}$ as

$$n(t) = \sqrt{\frac{N_{\text{EP}}}{\alpha} \frac{\exp(2t/\tau) - 1}{\exp(2t/\tau) + 1}} . \quad (4.13)$$

The equilibrium density $n = n_{\text{ion}} = n_{\text{electron}}$ is given by

$$n = \sqrt{\frac{N_{\text{EP}}}{\alpha}} . \quad (4.14)$$

The neutralization of molecular ions (X^+M) by means of dissociative recombination needs only a two-body interaction with the electrons and is a fast interaction process [101, 105]



where the characteristic recombination time τ is described with the electron density n_{electron} as

$$\tau = \frac{1}{\alpha n_{\text{electron}}} . \quad (4.16)$$

Typical values for α are in the range of $10^{-7} - 10^{-5} \text{ cm}^3 \text{ s}^{-1}$ [101] and combined with an electron concentration of around 10^7 cm^{-3} within the BGC, the characteristic recombination time is in the same order of magnitude of the extraction or residence time of the ions inside the BGC (10 – 1000 ms) [101, 105].

Molecule formation

In addition to neutralization reactions, gas-phase chemical ion-molecule reactions are commonly observed as reactions between an ion X^+ and impurity molecule M . In the case that the buffer gas purity is not guaranteed, molecular formation may become a significant loss mechanism, which drastically reduces the extraction efficiency of the desired ions [101, 106]. The main reaction leading to the formation of molecules is an association reaction



where the transitional state X^+M^* is not stable; however, it can be stabilized [107] in the presence of buffer gas atoms (He)



The dynamics of the bimolecular reaction can be described by a reaction rate constant k_2 and the differential equation

$$\frac{d[X]}{dt} = -k_2[M] \quad (4.19)$$

where $[X]$ and $[AB]$ define the concentration of the ions X^+ and molecules M . An impurity concentration of 1 ppm (parts per million) at typical BGC pressures of 50 mbar results in $[M]$ of 10^{12} atoms cm^{-3} . The time constant τ can be calculated with the Eq. 4.20.

$$\tau = \frac{1}{k_2[M]} \quad (4.20)$$

The reaction time for the formation of molecules is $\tau = 7.5$ ms with an assumed impurity level around 1 ppm. This is a factor 2 faster than the extraction time. From this follows that for a high extraction efficiency, it is essential to reduce impurities and every effort to achieve this goal is justified.

Ion mobility in static electric fields

High-energy beams after in-flight separation require larger stopping volumes, which in turn leads to a delay in the extraction of the ions. Due to the longer residence time, the losses of ions will be increased not only due to the limited lifetime but also due to charge exchange of the ions with the impurities and diffusion to the walls. Since there are ions present, electric fields can be used to accelerate the extraction. The drift velocity v_d of an ion in gas is directly related to its ion mobility K and the strength of the electrical field E :

$$v_d = K \frac{p \cdot T_0}{p_0 \cdot T} E \quad (4.21)$$

where K is the ion mobility ($\text{cm}^2 \text{V}^{-1} \text{s}^{-1}$), E is the electric field (V cm^{-1}), p is the operating pressure (mbar), T_0 is the standard temperature (273 K), p_0 is the standard pressure (1013 mbar), and T is the operating temperature (K). For heavy ions in He buffer gas, the reduced mobility is $k_0 = 20 \text{ cm}^2 \text{V}^{-1} \text{s}^{-1}$ and if a DC gradient of 10 V cm^{-1} is applied, the calculated drift velocity of the heavy ion in 100 mbar He buffer gas is around 20 m s^{-1} [108]. Once the ion motion is damped by the gas, the ion follows the line produced by the applied DC voltage directly. Since the electric field terminates at the end wall of the BGC, it is necessary to employ high enough gas flow to ensure to overcome the electric force at the nozzle. The electric field applied to the BGC is important for the ion velocity in the gas and influences the extraction time out of the BGC. The extraction time can be influenced by the dragging force of the applied electric field, since the ion mobility is constant at fixed gas pressure and temperature. Nevertheless, the applied field gradient is limited by the Paschen's law

[109].

Inhomogeneous RF electric fields

The problem by using only static electric fields to extract ions out from the BGC is to locate the point charge in the vicinity of the gas cell exit, where the gas-flow can surpass the drift motion. If this is not the case, the ion motion will terminate at the electrodes. The National Superconducting Cyclotron Laboratory (NSCL) group of the Michigan State University (MSU) used a flower-shaped electrode, which emulates a $\Phi \propto -1/r$ potential [110]. Here r is the distance to the nozzle exit. In another approach, the cathode, which is used in a static electric field, is replaced by a series of ring electrodes. A RF voltage is applied to these electrodes in addition to a DC gradient. The idea is based on the fundamental principle of the RF quadrupole ion trap from W. Paul¹⁸ (1953) [111]. This technique was adapted by the Tokyo group in their RF-hopper approach in the early 1970s [112]. In 1997 on the IGISOL workshop in Dubna, M. Wada proposed the first RF funnel for the transportation of thermal ions in a large BGC [91]. The confining force of an inhomogeneous RF-field in vacuum can be described by the pseudo-potential V_{eff} :

$$V_{\text{eff}} = \frac{e}{4m\omega^2} E_0^2 \quad (4.22)$$

where e is the elementary charge, m is the mass of the ion, ω is the frequency of the RF, and E_0 is the electric field strength, respectively. Since the ions have to stop before they can be extracted, the presence of the buffer gas damps the motion of the ions by collisions and results in a lower effective potential $V_{\text{eff,damp}}$ from Eq. 4.22:

$$V_{\text{eff,damp}} = \frac{\omega^2}{\omega^2 + \delta^2} V_{\text{eff}} \quad (4.23)$$

where the damping factor δ is defined by the ion's mobility K as:

$$\delta = \frac{e}{mK} \quad (4.24)$$

Wada expressed the repelling force F_{RF} in a quadrupole field created by a pair of adjacent electrodes as

$$F_{\text{RF}} = -mK^2 \frac{V_{\text{Funnel}}^2}{d^3} \left(\frac{r}{d} \right) . \quad (4.25)$$

Here, d is half of the electrode spacing, V_{Funnel} is the applied RF amplitude [108]. This repelling force decreases as the distance from the electrode structure increases

¹⁸W. Paul was honored with the Nobel Prize in Physics in 1989 for this work

and also decreases in the presence of buffer gas [108, 113]:

$$\langle F_{\text{vac}} \rangle = -\frac{e^2}{2m\omega^2} \left(E \frac{dE}{dx} \right) \quad (4.26)$$

where $\langle F_{\text{vac}} \rangle$ is the average force action on charge particles in an inhomogeneous RF field; in the presence of gas, it is reduced to

$$\langle F_{\text{damp}} \rangle = \langle F_{\text{vac}} \rangle \frac{1}{1 + \left(\frac{e}{Km\omega} \right)^2} \quad (4.27)$$

From Eq. 4.27 follows that the repelling force is proportional to the square of the mass and inversely proportional to the square of the gas pressure.

The ions are dragged towards the Funnel exit by the electrostatic force F_{DC} created by a DC gradient. For the given electric field strength E_0 , the electric field force on an ion with the velocity v can be deduced by:

$$F_{\text{DC}} = qE_0 - \frac{qv}{K} \quad (4.28)$$

The repulsive force of the RF field is a local phenomenon and is shown in Fig. 4.10. BGCs with RF-funnel structure are found nowadays in several other BGCs as all

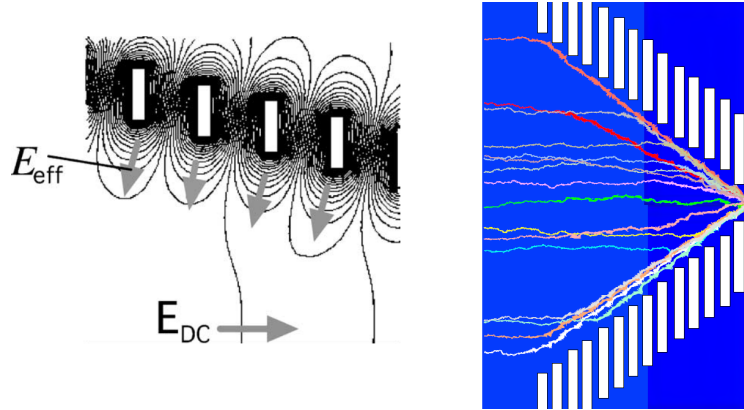


Fig. 4.10.: *Left: RF gradient field produced by a series of ring electrodes with RF equipotential lines indicated [100]. Right: Simulation for the ion motion in a gas-filled RF funnel by W. Plaß. The figure is taken from [114].*

parts of the funnel can be produced with ultra-high-vacuum components [108]. This makes the RF-funnel a suitable tool for chemistry experiments.

4.2.2 The gas chromatographic method

During the last decades chemical methods have been used to separate the desired transactinide nuclei, which were synthesized in fusion evaporation reactions, from unwanted byproducts. The gas-phase separation technique has the advantage that the procedure is fast, efficient and can be performed continuously and is also par-

ticularly suitable for one atom-at-the-time experiments with transactinide nuclei. Gas chromatography separation experiments were particularly important for the chemical investigation of most of the transactinide elements (see Sec. 4.1.4). In these experiments special chromatography systems were used, where the chromatography column is simultaneously used to detect the ERs via their characteristic nuclear decay properties. Examples for this are the chromatography and detection systems COLD and COMPACT detector. The gas-phase chemistry experiments are based on the fundamental principle of adsorption and desorption, or in other words, of the distribution coefficient between the mobile phase and the stationary phase¹⁹. The chromatographic principle is shown in Fig. 4.11. The chromatographic separation of

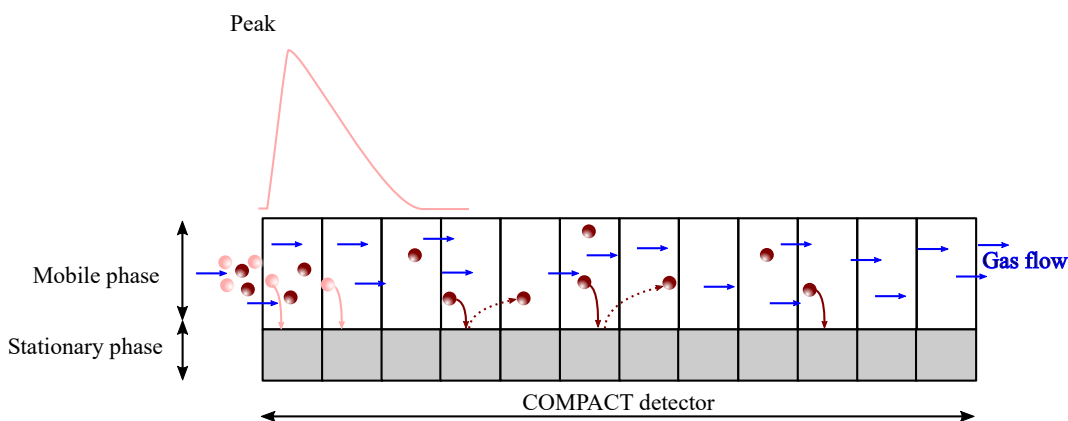


Fig. 4.11.: Schematic figure of the chromatographic principle.

the transactinide elements in the column takes place due to the repeated adsorption and desorption in the stationary phase. The phenomena that occur during gas adsorption on the surface of the solid are very varied due to the variety of surface structures [115]. A distinction is made between physisorption and chemisorption. The physisorption is based on the relatively weak Van der Waals interactions between adsorbate²⁰ and adsorbent²¹. The interaction is an electrostatic attraction of a permanent or induced dipole moment of two species. The adsorption depends on the gas pressure and is reversible. In comparison with chemisorption, where the electronic structure of the adsorbed atoms/molecules is changed, physisorption does not result in changes to the electronic structure. The categorisation of an adsorption as physisorption or chemisorption depends principally on the adsorption enthalpy. The adsorption enthalpy $\Delta H_{\text{ads}} \approx -20 \text{ kJ mol}^{-1}$ for the physisorption is in the same order of magnitude as the enthalpy of condensation [116, 117].

The chemisorption is based on chemically binding forces, and the adsorbate is bound to certain sites of the adsorbent. The chemisorption is mostly irreversible and can lead to the dissociation of molecules. The adsorption enthalpy $\Delta H_{\text{ads}} > 50 \text{ kJ mol}^{-1}$

¹⁹The stationary phase is the detector surface, which can be covered with gold (Au) or quartz (SiO_2).

²⁰The atoms on the surface.

²¹The detector surface.

is much larger and comparable to the reaction enthalpy. The adsorption kinetics is dependent on the temperature. The reaction rate decreases with a decrease of the temperature of the adsorbent. In extreme cases of physisorption or chemisorption there is possibility that both phenomena can occur simultaneously.

Gas-phase chemistry experiments are based on the principle of gas-solid chromatography and can be divided into two techniques to obtain thermochemical data of transactinide elements: (i) thermochromatography (TC) and (ii) isothermal chromatography (IC). In the present work only IC was used and on this account, the following discussion refers only a brief description of this method.

Basics of gas chromatographic transport

When transporting tracer amounts of transactinide elements through a chromatographic column, the relationship between the migration speed of the particle and experimental parameters is essentially determined by the adsorption enthalpy ΔH_{ads} on the column material. The adsorption enthalpies are determined in this work exclusively by the IC. In the following paragraphs the basics for determining thermodynamic state functions are briefly discussed. In order to describe the extraction processes in chromatographic columns correctly, the basic steps that determine the transport process must be known. In the simplest case, it is an adsorption-desorption process without changing the chemical state²² of the extracted species [118, 119]. This section concludes with the determination of the aforementioned adsorption enthalpy by Monte Carlo simulations (see Sec. 4.2.2), which give access to this quantity.

Isothermal gas chromatography

In the IC, the temperature along the column is kept constant and the volatile species are transported through the chromatography column with a carrier gas. A closer examination of the Height Equivalent to a Theoretical Plate (HETP) [118, 119] in Fig. 4.11 shows that the distribution of transactinide atoms in the stationary (c_{stat}) and mobile phase (c_{mob}) is described by the distribution coefficient k_a :

$$k_a = \frac{c_{\text{stat}}}{c_{\text{mob}}} . \quad (4.29)$$

The migration distance z_A by the individual transactinide element within the column is a function of the processing time t_R ²³, the column surface area (a_z)²⁴ and flow

²²For example oxidation state in the mobile phase and stationary phase.

²³Equivalent to the retention time.

²⁴Column area per unit length [cm^2/cm]

rate (Q) of the carrier gas:

$$z_A = \frac{Qt_R}{a_z k_a} . \quad (4.30)$$

Eq. 4.30 shows that k_a can be written as:

$$k_a = \frac{Qt_R}{z_A a_z} . \quad (4.31)$$

The separation of two different elements is described by their retention time. Therefore, they travel at different apparent velocities in the mobile phase, causing them to separate. The retention time is an important coefficient of performance and can be understood in the framework of molecular kinetics, where the atom spends a sum of the random elementary adsorption residence times which accompany each adsorption event. The retention time (Eq. 4.32) in an isothermal column with the temperature T_c depends on the mean desorption time for a first order reaction $\tau_a = \tau_0 \exp\left(\frac{\Delta H_{\text{ads}}}{RT_c}\right)$ and the number $Z_z = \frac{v_0 z a_z}{4Q}$ of adsorption-desorption events on the way [120–125]:

$$t_R = \frac{z_A T_0 a_z}{Q} \sqrt{\frac{R}{2\pi m T_c}} \tau_0 \exp\left(\frac{\Delta H_{\text{ads}}}{RT_c}\right) . \quad (4.32)$$

In Eq. 4.32, the mean speed $\bar{v} = \sqrt{\frac{8RT}{\pi M}}$ from the Maxwell-Boltzmann distribution, the z coordinate along the column, and the period of the adsorbate oscillation τ_0 ²⁵ is used [120–125].

IC is a technique where the adsorbate comes in contact with the adsorbent under constant temperature. Depending on the temperature of the column and the adsorption interaction of the species with the column surface, they travel slower through the length of the column than the carrier gas. The varying of the isothermal temperature gives an integral chromatogram [18, 42, 45] and the characteristic quantity determined by IC (see Fig. 4.12) is the temperature at which half of the introduced nuclides are detected at the exit of the column ($T_{50\%}$) and at this point the retention time is equal to the half-life of the radionuclide contained in the species. The extraction of 50% indicates the inversion point of the breakthrough curve. The yield of the species at the exit of the column changes within a small interval of isothermal temperatures from zero to maximum yield. The measuring of extraction yield as a function of the temperature is shown in Fig. 4.12. The IC is a well suited technique for the continuous separation of short-lived transactinide elements in on-line experiments [18, 42, 49]. However, there are some disadvantages concerning the determination of ΔH_{ads} . In order to determine the temperature $T_{50\%}$, a measurement sufficiently

²⁵The reciprocal of vibrations of the adsorbent lattice with a characteristic Debye's phonon frequency [126].

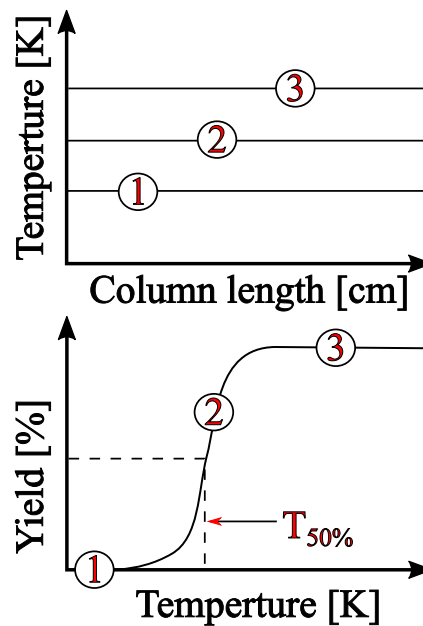


Fig. 4.12.: Schematic representation of the IC method and the form of its typical obtained chromatogram. Figure adapted from [18]

above and below this temperature is required, but this temperature is unknown a priori. Therefore, several experiments at different isothermal temperatures have to be conducted, which requires long measurement series below $T_{50\%}$ to demonstrate that transactinide elements or compounds are retained in the column at a certain temperature.

The adsorption enthalpy and the diffusion coefficient

In gas adsorption chromatography, the adsorption enthalpy is usually studied. The desorption of a atom or molecule from the column surface requires overcoming an attraction due to adsorption forces, since the adsorbed particle in the potential minimum must be raised. A physisorbed particle oscillates in its relatively flat potential well and can leave the surface again after some time simply because of these oscillations. The Frenkel equation (Eq. 4.33), an Arrhenius-like expression, can be used to deduce the temperature dependent mean time (τ_a) an atom spends on a surface.

$$\tau_a = \tau_0 \exp\left(-\frac{\Delta H_{\text{ads}}}{RT_c}\right) \quad (4.33)$$

Here, the activation energy is similar to the adsorption enthalpy ΔH_{ads} . The Frenkel equation (Eq. 4.33) clarifies that with a decrease of the temperature the mean time an atom spends adsorbed on the surface increases. From the Frenkel equation, the

temperature dependent Arrhenius-like adsorption rate (k_a) can be derived in the form [116, 117]

$$k_a = A \exp\left(-\frac{\Delta H_{\text{ads}}}{RT_c}\right) = \underbrace{\frac{a_z l_c}{t_\lambda Q} \exp\left(\frac{\Delta S_{\text{ads}}^\circ}{R}\right)}_A \exp\left(-\frac{\Delta H_{\text{ads}}}{RT_c}\right) \quad (4.34)$$

in a column with the length l_c . Here, $\Delta S_{\text{ads}}^\circ$ and t_λ correspond to the standard entropy change and mean radioactive lifetime of the transactinide nuclide. The use of models in the microscopic framework allows the simulation of the transit of an atom or molecule through a column, and $-\Delta H_{\text{ads}}$ on the column surface can be deduced by using Eq. 4.33 connecting the average adsorption time to the phonon vibration frequency ($1/\tau_0$) via a Boltzmann factor containing $-\Delta H_{\text{ads}}$. This thermochemical quantity is characteristic for atom-surface interaction and is independent from experimental conditions, such as gas-flow rate or temperature gradient [121–124].

In the following discussion, the diffusion is related to non-volatile atoms or molecule compounds on the column surface. The diffusion leads to a broadening of the peaks in the isothermal chromatogram. For Standard Temperature and Pressure (STP) conditions an adsorbed particle can diffuse on the order of $0.1 \mu\text{m}$ across the column surface due to the concentration gradient (dc/dt) along the gas channel. The diffusion is described by the 2nd Fick's law²⁶ in absence of any chemical reactions as differential equitation. The mean squared diffusional displacement $\langle z_D \rangle^2$ of molecules, the time of diffusion t and the mutual diffusion coefficient $D_{1,2}$ are related by

$$\langle z_D \rangle^2 = 2D_{1,2}t \quad (4.35)$$

The diffusion coefficient $D_{1,2}$ is described in dependence of the pressure p and temperature t by the semi-empirical Gilliland's equation [127]

$$D_{1,2} = \frac{0.0044T^{2/3}}{p[(M_1/\rho_1)^{1/3} + (M_2/\rho_2)^{1/3}]^2} \left(\frac{1}{M_1} + \frac{1}{M_2}\right)^{2/2} \text{ cm}^2 \text{ s}^{-1} \quad (4.36)$$

where ρ_1 and ρ_2 are the density of the diffusing gas or carrier gas and M_1 , M_2 are the molecular weights of the diffusing gas and carrier gas, respectively. The diffusion of a transactinide element under STP conditions with common carrier gases from Eq. 4.36 is around $0.01 - 0.1 \text{ cm}^2 \text{ s}^{-1}$ [128].

Monte Carlo Simulation

Monte Carlo simulations are often used when problems cannot be solved analytically or can only be solved with great effort. Here, a very large number of similar random simulations are performed to solve the central issue by using the numerical probability

²⁶Fick's second law predicts how diffusion causes the concentration c to change with respect to time t : $\frac{dc}{dt} = D_{1,2} \frac{d^2c}{dx^2}$, where $D_{1,2}$ is the diffusion coefficient in one dimension and x is the position

theory. The methods for calculating thermodynamic state functions presented in [Sec. 4.2.2](#) are based on the experimental determination of a deposition temperature. The adsorption within the chromatographic column is not selective but occurs in an adsorption area on the column surface. The attempt to derive the information of the adsorption enthalpy by the solution of differential equations is difficult. Therefore, the movement of a particle is described as a result of numerous collisions with the column surface, where the just-desorbed particle diffuses through the column by random free jumps until it hits the surface again and adsorbs on it. Based on this principle, the adsorption distribution is predicted by Monte Carlo simulations and compared with the experimental results. A microscopic model of gas chromatography was proposed by Zvara [\[121\]](#), on the basis of which gas chromatographic experiments can be simulated with the Monte Carlo method. The code from Zvara *et al.* allows to determine the expected yield of a volatile species for given adsorption enthalpy and isothermal temperature. A detailed description of the proposed model by Zvara is given in [\[121, 128\]](#). In this section, only the basic aspects and equations will be discussed.

The mean adsorption residence time of a particle in the adsorbed state is a random variable and is given by the Frenkel equation (see [Eq. 4.33](#)). The Frenkel equation shows a strong temperature dependence. With a weak interaction between the adsorbate and the surface of $\Delta H_{\text{ads}} \approx 25 \text{ kJ mol}^{-1}$ at STP conditions, the mean adsorption residence time is $\tau_{\text{a}} = 10^{-18} \text{ s}$. The mean adsorption residence time increases to $\tau_{\text{a}} = 1 \text{ s}$ already at temperature of 100 K.

According to the molecular gas theory, the mean flow velocity v_1 in a given section of the column is determined by the time τ_{a} and the number of collisions with the column surface. In an open cylindrical column with the column area (a_z), the number of collisions between a molecule and the wall at a given carrier gas-flow rate Q results in

$$Z_z = \sqrt{\frac{2\pi RT_c}{M}} \cdot \frac{a_z}{Q} \quad . \quad (4.37)$$

The distance that a molecule travels by random free jumps after successive collisions with the surface can vary within wide limits (see [Fig. 4.13](#)). Short shifts in the order of $1/Z_z$ (after a collision with the surface) have a high probability, for large jumps there is a small but non-zero probability. An approximation is used for the probability in the Zvara model. In the simplified physical model, the molecule that hits the wall generally experiences a series of adsorption-desorption processes without changing the coordinates. This series is interrupted by large jumps η which have an exponential probability distribution ($\rho(\eta)$) [\[121–124\]](#).

$$\rho(\eta) = \frac{1}{\bar{\eta}} \exp\left(-\frac{\eta}{\bar{\eta}}\right) \quad (4.38)$$

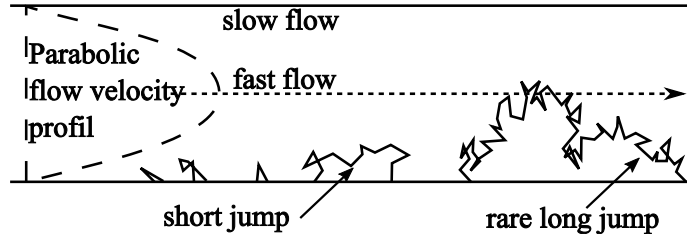


Fig. 4.13.: *Microscopic model of the adsorption process of a molecule in a column to describe exponential probability distribution $\rho(\eta)$. Taken from [128]*

The effective mean length of the jumps $\bar{\eta}$ at high laminar carrier gas velocities is obtained from the mass flow velocity and the diffusion coefficient $D_{1,2}$, which can be calculated using Gilliland's equation Eq. 4.36:

$$\bar{\eta} = \frac{11Q}{48\pi D_{1,2}} \quad . \quad (4.39)$$

The adsorption residence probability $\rho(\tau_a)$ for a random number of collisions in a series is given by

$$\rho(\tau_a) = \frac{1}{Z_z \bar{\eta} \bar{\tau}_a} \exp\left(-\frac{\tau_a}{\bar{\tau}_a \bar{\eta} Z_z}\right) \quad . \quad (4.40)$$

The path of a real particle through the column will be described by a series of jumps in the Monte Carlo simulation. After each jump, the total extraction time (total retention time in the mobile and stationary phase) is compared with the actual duration of the chromatographic experiment for the given particle. This depends on the time when the particle enters the chromatography column, the half-life of the used nuclide and, if applicable, the time it takes to pass through the chromatography column. This series of jumps is repeated until either the molecule decays inside the column due to its finite lifetime or it reaches the end of the column and the last coordinate of the particle is saved in the chromatogram. Afterwards, the process begins with the simulation of a new particle.

4.2.3 Gas-flow kinetics

Gas-flow kinetics play an important role in the description of effects in chromatography or in the BGC. They help to understand complex processes such as the diffusion coefficient or the viscosity. Both phenomena are part of the discussion of the Monte Carlo simulation. In the following section, the most important quantities of gas flow kinetics are briefly presented, which are then also used to characterize the buffer gas cell. Turbulence should be avoided in chromatography as well as in the extraction of ions from an BGC. In the gas chromatography, turbulent flow profiles have a significant negative impact on the separation performance. Turbulence are an important phenomenon, which is relevant for gas cells. The gas-flow can become

turbulent, if the gas cell has inner shapes, which caused excessive kinetic energy in parts of a gas-flow. This leads to a loss of desired ions since an ion is stopped inside a vortex, where it cannot reach the gas cell exit anymore, or the ion can collide with the gas cell surface and is lost. Both effects lead to a drop in the extraction efficiency and should be avoided if possible. Such phenomena may become problematic especially in larger gas cells with high buffer gas-flow rates. The same phenomena also occur in the following detector unit. The dimensionless Reynolds number (Re) [129] provides a simple way to calculate the level of turbulence. The equation describes if flow conditions lead to laminar or turbulent flow. The Reynolds number is given by [130, 131]

$$Re = \frac{\rho_m v L}{\eta} \quad . \quad (4.41)$$

where ρ_m is the mass density of the gas, v is the gas velocity, L is the length of the gas cell, and η_{vis} is the gas specific dynamic viscosity. The specific dynamic viscosity for the typically used buffer gas He is $\eta_{vis} = 20 \mu\text{Pa s}$ [132].

A laminar flow occurs when the Reynolds number is below a critical value of approximately $Re < 120$. At larger Reynolds numbers a vortex behind objects occurs and if the Reynolds number increases to several thousands the flow starts to be fully turbulent [130, 131].

Diffusion

The diffusion of atoms and ions in the buffer gas volume or gas duct is an important parameter as it is responsible for one of the significant ion loss mechanisms in a gas cell or peak broadening in the chromatographic detector unit. In the following a brief overview about the diffusion phenomenon is given. The diffusion of a particle due to a concentration gradient dc/dx is described by the 1st Fick's law.

$$J(x) = -D \frac{dc}{dx} \quad (4.42)$$

where D is the diffusion coefficient and $J(x)$ is the flux of atoms. The diffusion of a particle takes place until the difference in concentration as the cause of the diffusion is reduced. The change in concentration in a volume element $V = A\Delta s$ over time is given by

$$\frac{dc}{dx} = \frac{A}{V} [J_x(s) - J_x(s + \Delta s)] \quad (4.43)$$

with the area A , where the ions diffuse through, and s the coordinate of the area. By assuming a constant diffusion coefficient D , Eq. 4.43 can be simplified to the 2nd

Fick's law

$$\frac{dc}{dt} = D \frac{d^2c}{dx^2} \quad . \quad (4.44)$$

The solution of this differential equation is a normal distribution [116, 117],

$$p(x, t) = \frac{N}{2A\sqrt{\pi Dt}} \exp\left(-\frac{x^2}{4Dt}\right) \quad (4.45)$$

with the standard deviation,

$$\sigma(t) = \sqrt{2D_0t} \quad . \quad (4.46)$$

In the last years, the focus on the research of SHE is shifting since the synthesis of new heavier elements is technically complex. The low production rate and low half-lives pushes the experimental setups to their limits. In chemical experiments with SHE, the coupling of an RTC with a chemical gas-phase chromatography system has developed over the years into a very powerful and universally applicable method. A well established technique to study chemical properties of transactinides is to measure their interaction strength with heterosurfaces. Current experimental setups involve the synthesis of the element under study in nuclear fusion reactions, followed by thermalization in a gas-filled volume. This is either mounted directly behind the target [18, 74] or behind a physical preseparator [49, 59, 85]. Extraction from this chamber is the most time-consuming step in many contemporary setups of this type, and requires about 1 s or more. Furthermore, chemistry setups are typically coupled to these gas-filled chambers via plastic tubing. In case of strong interactions of the elements with the surface of these tubes, they adsorb on the surface and decay there before reaching the subsequent detection system. This approach allowed the study of volatile species of the transactinide elements including Sg(CO)₆ [65], HsO₄ [64] or elemental Cn [133] to Fl [82], which are the heaviest elements, whose chemical properties have been studied. The radioisotope ²⁸⁴Nh is available as the daughter of ²⁸⁸Mc (moscovium, $Z = 115$) and would in principle allow similar experiments with Nh [80, 81]. Looking beyond, to heavier elements, such extraction times from the RTC are significantly longer than the half-lives of readily accessible radioisotopes of all elements with $Z > 114$ ($t_{1/2} < 200$ ms) via ⁴⁸Ca-induced nuclear reactions. Exceptions are ²⁸⁹Mc and ²⁹⁰Mc, but the production of these radioisotopes is only possible with ²⁴⁹Bk-targets, which are rarely available. Consequently, no chemical studies with moscovium or even heavier elements have been performed to date. Less volatile species were extracted from the gas-filled volume and carried over reactive surfaces by the aerosol-jet technique, including (oxy)halides of Rf, Db, Sg, and Bh [45]. For chemical studies of elements beyond Fl or Nh, which are short-lived and are expected to be reactive [134–136], these limitations need to be overcome. In the case, if we take into account production rates and the half-lives of SHEs, which are accessible via fusion-evaporation reactions, there is an experimentally inaccessible area with state-of-the art techniques (see Fig. 5.1). Similar challenges are present in neighboring fields, including nuclear and atomic physics studies of short-lived exotic nuclei. A successful technique to forward these to a variety of experimental setups is by coupling using Buffer-Gas-Cells (BGC) with superimposed electrical

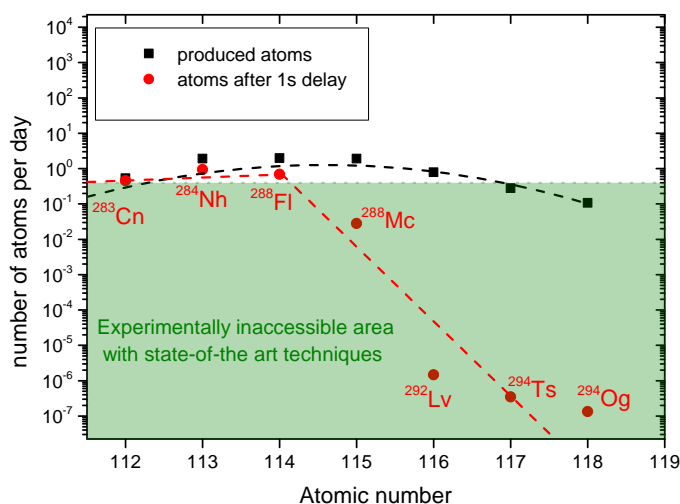


Fig. 5.1.: Production rate of SHEs folded with an 1 s-extraction-delay. The delay is due to the needed extraction time of the current used setups. The lines are added to guide the eye.

fields providing very short extraction times down to milliseconds [108]. To explore the applicability of the BGC technique in the field of chemical studies of the heaviest elements, we present here exploratory studies on the combination of a BGC with state-of-the-art chemistry setups suitable for studies of transactinide elements.

For the gas-chromatographic studies of non-volatile elements like Fr, a newly developed miniCOMPACT was introduced. Such a system should be comprehensively characterized in accordance with the current methods and strategies. This includes the characterization of the extraction efficiency together with the extraction time and the influence of all operating conditions on the extraction characteristics. The development of a suitable interface for connecting the chemistry setups to the BGC is a prerequisite for its practical use.

This work presents the first successful coupling of the COMPACT detector to a BGC with superimposed electrical fields and the first extraction of elements in the ionic stage. So far, this method has been limited to volatile elements in the neutral state. The extracted ions neutralize with their first wall collisions in the novel miniCOMPACT and are then accessible for gas-chromatographic studies. Based on this, this work additionally presents the first extraction of the non-volatile Fr. The here presented system of the BGC with the COMPACT detector proves the efficiency to get access to elements beyond Fl with short half-lives within the extraction time of several ms.

The experiments introduced in the present thesis are divided into two parts:

- I. off-line measurements with α -recoil-ion sources and
- II. on-line measurements conducted at the GSI Helmholtzzentrum für Schwerionenforschung in Darmstadt (Germany) and at the Cyclotron Institute at Texas A&M University, Collage Station, TX (USA)

This chapter first discusses the setup for the off-line measurements with the ^{225}Ac (Sec. 6.1.1) and ^{223}Ra (Sec. 6.1.2) recoil-ion sources followed by the setup for the on-line measurements (Sec. 6.2). The chapter concludes with a detailed overview of the BGC (Sec. 6.3) and the detector array (Sec. 6.4). In on-line experiments the BGC was directly connected behind the recoil preseparator (see Fig. 6.1A). The produced ER ions entered the BGC through a thin Ti entrance window (a few microns thick) and were stopped by collision with the He buffer gas. During off-line experiments, the respective recoil-ion source mounted on a linear motion feedthrough replaced the recoil separator and the entrance window (see Fig. 6.1B). The thermalized ions were accelerated by the applied electric field gradient of the BGC electrode system. In the funnel section, a repelling force generated by the RF field prevents the ions from hitting the electrode surface and they were guided to the BGC exit. After the funnel exit, the ERs were injected either directly into the detector array or into a transport line, which was connected between the funnel exit and the detector array.

6.1 Off-line measurements with recoil-ion sources

The investigation of the characteristics of the BGC such as extraction efficiency and extraction time of ions was performed off-line with the recoil-ion sources installed inside the BGC (Fig. 6.1B). The sources replaced the the accelerator, recoil separator and entrance window compared to the setup used during on-line measurements (see Fig. 6.1A). This thin source without a protective layer enabled α -decay products to recoil out of the source. The recoil-ions were used to simulate ERs and no external ion beam was required. Using a recoil-ion source offers several additional advantages. On the one hand the number of released recoils in the stopping volume is known accurately for the first daughter in the decay chain and on the other hand due to their small size, they can be considered as a point-like sources [93, 137, 138]. They are suitable for the investigation of the extraction efficiency and the extraction time of ions from the BGC due to creation of ions in a well-defined region of the stopping

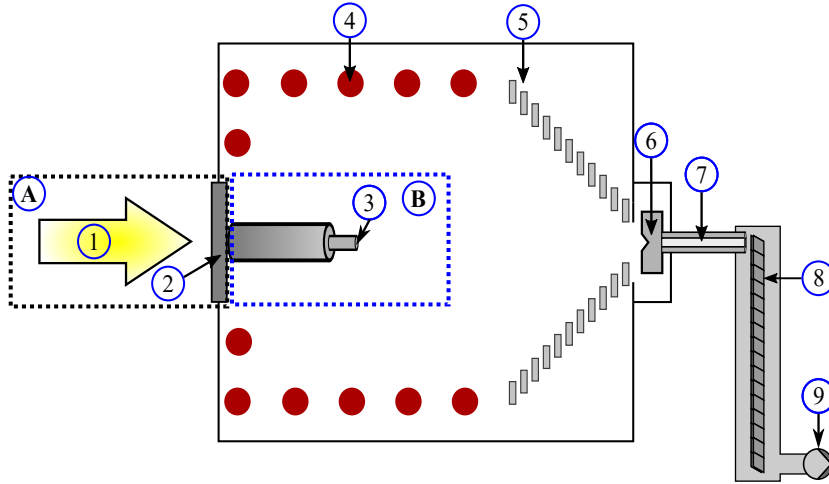


Fig. 6.1.: Schematic overview of the setup. In A) (black square) the setup for the on-line measurements is shown. The ER ions (1) passing through the entrance window (2) enter the BGC. For the off-line measurements B) (blue square), the respective recoil-ion source (3) is installed inside the BGC. Ions will be guided to the exit by a DC cage (4). In the funnel-structure (5), an RF field prevents the ions from hitting the wall. The ER ions were transferred via the transition electrode into the transport line. The α -decay was registered in the COMPACT detector array (8). The laminar gas-flow was generated by a diaphragm pump (9).

volume. In addition, they are useful tools for optimizing the BGC parameters before on-line experiments. In the following section, the ^{225}Ac and ^{223}Ra recoil-ion sources, which were used in the off-line experiments are introduced. **Tab. 6.1** summarizes the information of the two off-line recoil-ion sources, which were used in the present experiments. In addition, the branching ratio for the α -decay (b_α), activity (A) and energies (E_α) of the most intense α -lines are included.

6.1.1 ^{225}Ac recoil-ion source

The daughter ^{221}Fr ($T_{1/2} = 4.9$ min) of the α -decay of ^{225}Ac ($T_{1/2} = 10$ d, 1.6 kBq activity) is highly chemically reactive. This can be explained by the availability of one unpaired electron in its ground state configuration $7s^1$ [140–142]. The ^{225}Ac source was produced via molecular plating [143, 144] at the Department of Chemistry-TRIGA site (Johannes Gutenberg University Mainz, Germany) [145, 146]. For the molecular plating, the nitrate compound of ^{225}Ac was diluted in nitric acid and isopropanol. **Fig. 6.3** shows a schematic view of the PolyEtherEtherKetone (PEEK) cell, which was used for the molecular plating. A Ti-block serves as the anode and a metallic cylinder with a hemispherical tip was used as cathode. Only

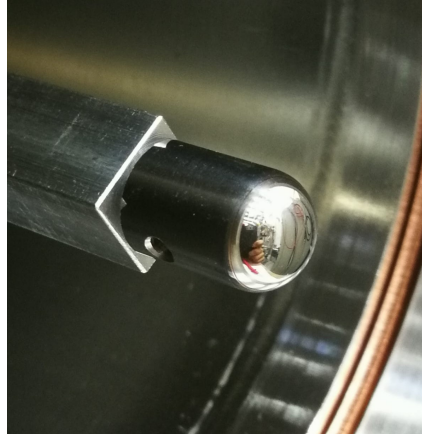


Fig. 6.2.: Photograph of the used source cone at the end of the linear-motion feedthrough. This type of source cone was used for both recoil-ion sources.

Tab. 6.1.: Parameters of the used ^{223}Ra and ^{225}Ac recoil-ion sources, which were used for the efficiency measurements. E_α is the α -particle energy and I the intensity of the corresponding line; b_α the branching ratio for alpha decay and P_{release} is the recoil release probability from the source surface. The α activity (A) and the effective release rate (\dot{N}^{tot}), which is needed for efficiency determination of both sources is given. Data were taken from [139].

Source	A (kBq)	b_α (%)	decay products	$t_{1/2}$	I (%)	E_α (keV)	P_{release} (%)	\dot{N}^{tot} ($\cdot 1000 \text{ s}^{-1}$)
^{223}Ra	8.6 ± 0.5	100	^{219}Rn	3.96 s	79.4(1)	6819.1(3)	100	8.6(5)
					12.9(6)	6552.6(10)		
					7.5(6)	6425.0(10)		
			^{215}Po	1.78 ms	100	7386.1(6)		8.6(5)
^{225}Ac	1.6 ± 0.2	100	^{221}Fr	4.9 min	83.4(8)	6341.0(13)	23(2)	0.37(5)
					15.1(2)	6126.3(15)		

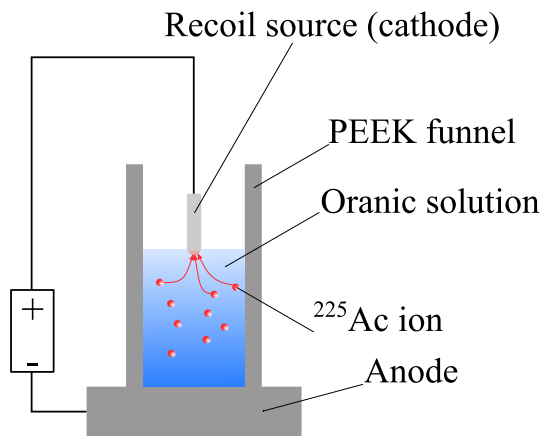


Fig. 6.3.: Experimental setup for the molecular plating of the ^{225}Ac recoil-ion source.

the tip was immersed in the organic solution reservoir, so that the activity was deposited only in this small area. A voltage of 1200 V was applied for 40 min to the metallic cylinder. The deposition yield was determined by α -particle measurements of the supernatant solution after the molecular plating. Fig. 6.4 presents the decay chain of the ^{225}Ac recoil-ion source used during the off-line measurements and the corresponding α -spectrum is shown in Fig. 6.7A.

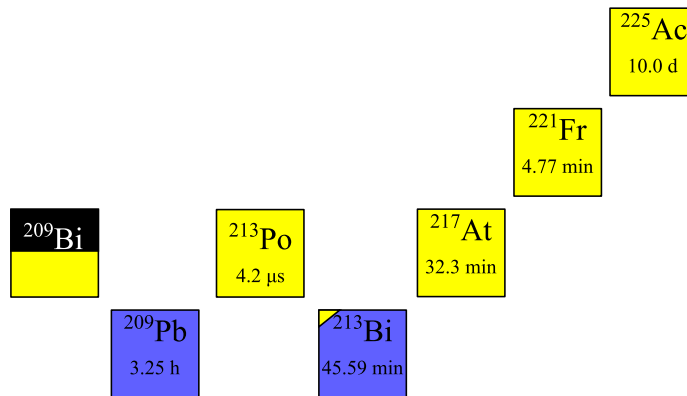


Fig. 6.4.: The ^{225}Ac decay chain for the ^{225}Ac recoil-ion source. The half-life and the decay mode (yellow: α -decay; blue: β^- -decay) is given. Data were taken from [139].

6.1.2 ^{223}Ra recoil-ion source

Short-lived ^{219}Rn ions ($T_{1/2} = 3.96\text{ s}$) were obtained as α -decay daughter products emerging from a source of the α -decay precursor ^{223}Ra ($T_{1/2} = 11.43\text{ d}$) with 8.6 kBq activity. Fig. 6.5 presents the decay chain of the ^{223}Ra recoil-ion source used during the off-line measurements. Rn is a suitable model element for the behavior of non-reactive volatile species due to its closed electron shell configuration $4f^{14}5d^{10}6s^26p^6$ [140–142]. The production of the ^{223}Ra recoil-ion source was conducted at the Department of Chemistry - TRIGA site (Johannes Gutenberg University Mainz, Germany) [137, 147]. A nitrate solution of the isotope ^{227}Ac (200 kBq activity) was electrochemically deposited on a $100\ \mu\text{m}$ -thick Ti-foil (see Fig. 6.6). ^{223}Ra ions recoil from the ^{227}Ac source after the β^- -decay into ^{227}Th . The ^{223}Ra ions were thermalized in 40 mbar He gas and $\approx 85\%$ of the recoiling Rn remained as ions after the thermalization process [138]. The ^{223}Ra ions were accelerated by an electric field (25–35 V/cm) and guided to a metallic cylinder with a hemispherical tip, which was placed 2 cm above the ^{227}Ac source. The ^{223}Ra recoil collection efficiency was about 20% [137]. The loss of ^{223}Ra recoils is explained by the influence of the thickness of the ^{227}Ac source. Not all ^{223}Ra recoil-ions emitted into the anterior hemisphere can leave the source. The source thickness is not only due to the ^{227}Ac , but in particular to metallic impurities (Pb, Th). The α -spectrum of the ^{223}Ra recoil-ion source is shown in Fig. 6.7B.

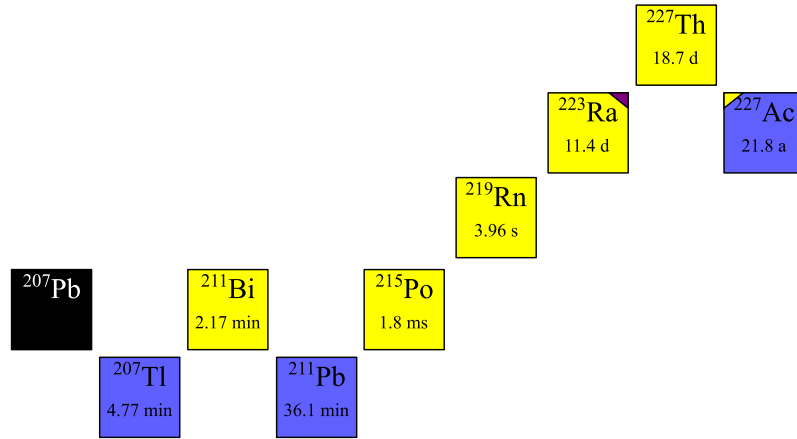


Fig. 6.5.: The ^{227}Ac decay chain for the ^{223}Ra recoil-ion source. The origin source was ^{227}Ac . The half-life and the decay mode (yellow: α -decay; blue: β^- -decay) is given. Data were taken from [139].

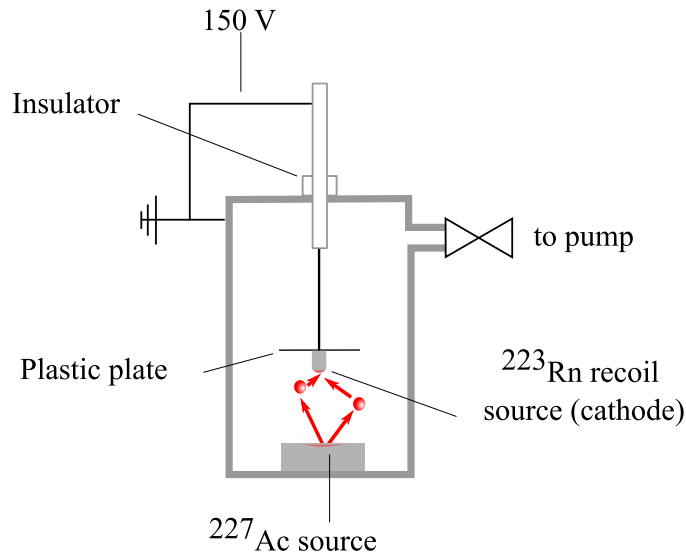


Fig. 6.6.: Experimental setup for the production of the ^{223}Ra recoil-ion source.

6.2 On-line measurements behind a recoil separator

The herein presented on-line experimental data for the extraction efficiency were collected in five individual fusion reaction experiments with accelerated ^{40}Ar - and ^{48}Ca -beams and five different solid-state lanthanide targets. The experiments with the ^{40}Ar beam were performed at Texas A&M University (USA) Cyclotron Institute at the Momentum Achromat Recoil Spectrometer (MARS) with the K500 cyclotron [148]. The ^{48}Ca induced reaction was performed at GSI Helmholtzzentrum für Schwerionenforschung in Darmstadt (Germany) at the TransActinide Separator and Chemistry Apparatus (TASCA) [149] with the UNILAC [21, 150, 151]. An overview of the principal on-line experimental setup is given in Fig. 6.1a.

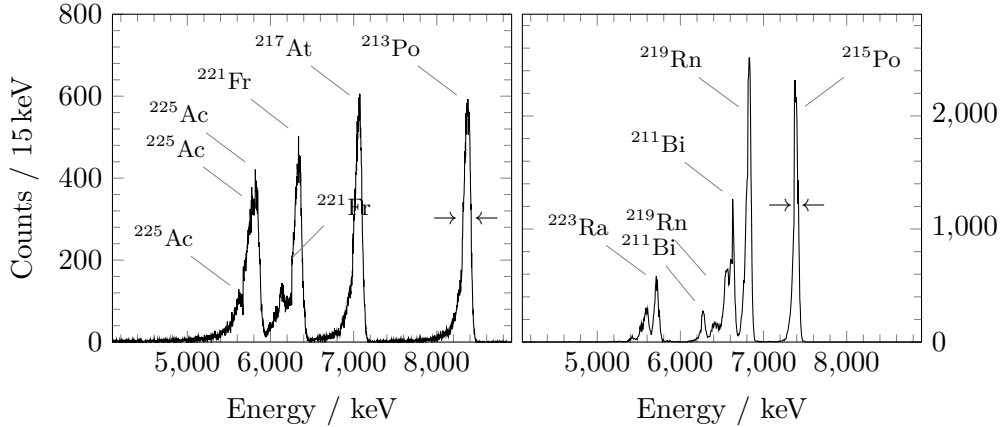


Fig. 6.7.: α -decay spectra of the extracted ^{225}Ac (A) and ^{223}Ra (B) ions and their decay products. The energy resolution in the α -spectrum was about 70 keV (FWHM) for ^{223}Ra and about 90 keV (FWHM) in the case of ^{225}Ac .

6.2.1 Beam production

The chemical studies of SHEs require neutron-rich isotopes with half-lives of a few seconds. The required neutron-rich isotopes can be produced in hot fusion reactions of actinide targets with light ion beams. For the experiments described in this dissertation lighter homologous were studied as model elements for the chemical behavior of the SHEs. These were produced in fusion-evaporation reactions with projectile energies above the Coulomb barrier [49, 82, 115, 152]. In the following paragraph the K500 cyclotron and the UNILAC are comprehensively described.

Experiments at MARS - The K500 cyclotron

To perform the fusion reactions for the studied extraction efficiency behind the MARS spectrometer, an accelerated beam of ^{40}Ar projectiles was required. Therefore ^{40}Ar was fed into an 6.4 GHz Electron Cyclotron Resonance (ECR) ion-source and here the Ar atoms were ionized in the ECR source plasma. These ions were transferred into the K500 cyclotron and accelerated to the requested energy. To eliminate unwanted contaminants, the cyclotron additionally performs an intermediate charge-to-mass Q/M selection. The charge state of ^{40}Ar projectiles used in these efficiency experiments was 5^+ . The requested 190 – 212 MeV primary beam energy at just about the Coulomb barrier was achieved by operating the K500 in 2nd harmonic mode. The beam energy for the experiment was determined experimentally by passing the accelerated ions through a $0.05 \text{ mg cm}^2 \text{ natC}$ foil and measuring the magnetic rigidities of the resultant charge states. The average beam intensity on the target was $2.5(2) \cdot 10^{10} \text{ particle s}^{-1}$. The MARS spectrometer is installed in the Heavy Ion (HI)-branch of the Cyclotron Institute facility, as shown in Fig. 6.8.

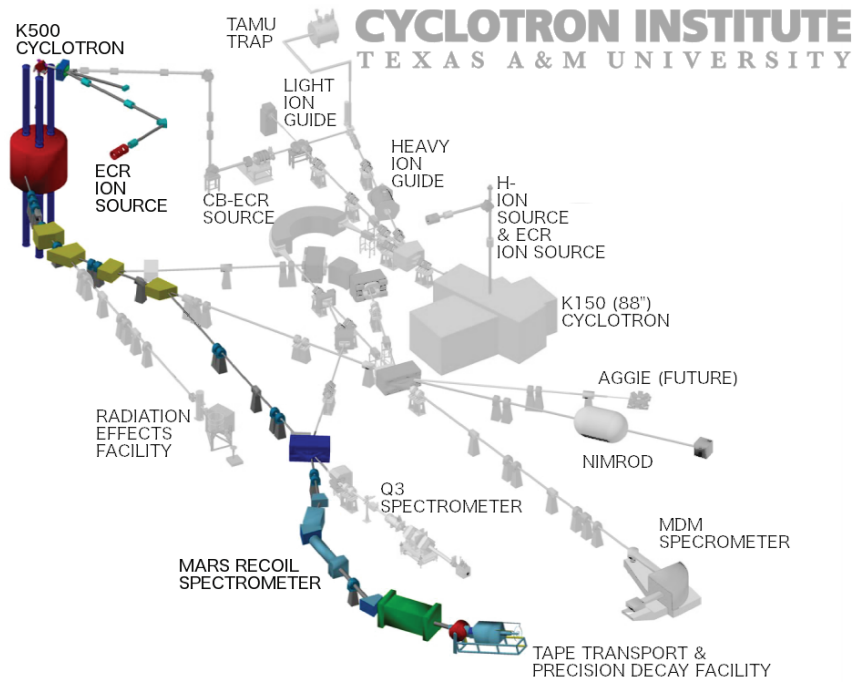


Fig. 6.8.: Schematic overview of the Cyclotron Institute facility. The beamline that was used for the experiments at the Cyclotron Institute behind the MARS spectrometer is clearly shown, while all other branches have been blurred. Figure is modified from [153].

Experiments at TASCA - The UNILAC

The required ^{48}Ca primary beam for chemical experiments at TASCA was provided from the heavy ion linac UNILAC with a duty cycle of 25% (5 ms pulse length, 50 Hz repetition rate, main beam) or 2.5% (5 ms pulse length, 5 Hz repetition rate, parasitic beam). The gas-filled separator TASCA is established in the cave X8 of the UNILAC experimental hall. A high-temperature oven was used to volatilize ^{48}Ca , which was afterwards ionized in an inductively coupled plasma of the ECR ion-source. TASCA is coupled to the UNILAC via a differential pumping station, which serves to separate the high vacuum area of the accelerator (around 10^{-7} mbar) from the low vacuum area inside the gas-filled separator (typically 0.8 mbar). The differential pumping system consists of one Roots pump and two turbo molecular pumps. The advantage of this windowless separation of the accelerator and separator is that the beam intensity can be increased without the limitation of stability of the window. The beam intensity is only limited by the stability of the used target backing and the target. Both have to withstand the highly-ionizing environment created by the beam. The extracted beam intensities were measured by passing through two transformers, one positioned near the entrance to the X-branch, and another one just upstream of the target position. The average beam intensity on the target was $1.8(2) \cdot 10^{11}$ particle s^{-1} . The present GSI accelerator complex is shown in Fig. 6.9.

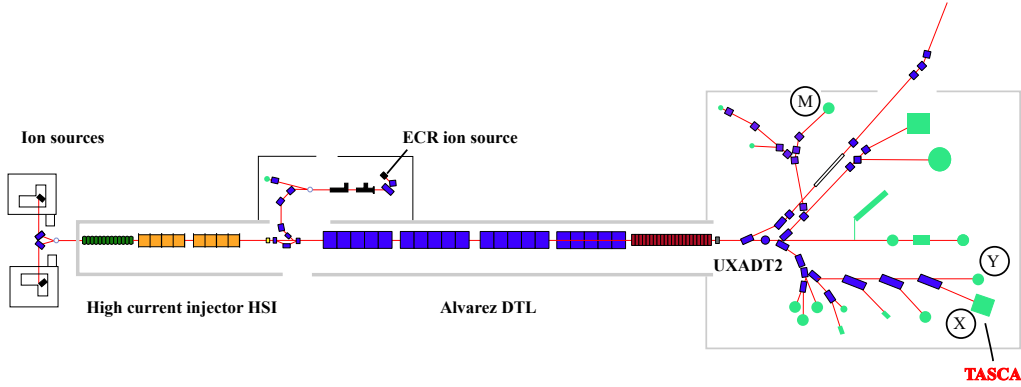


Fig. 6.9.: Schematic overview of the GSI UNILAC and ECR source [154].

6.2.2 Targets

The thin round targets foils used in the efficiency measurements behind the MARS spectrometer were made of lanthanide elements. Two different targets were irradiated: a $300\text{-}\mu\text{g}/\text{cm}^2$ -thick ^{165}Ho target (monoisotopic composition) and a $300\text{-}\mu\text{g}/\text{cm}^2$ -thick samarium target (isotopic composition: 50% ^{144}Sm ; 50% ^{147}Sm). The targets were prepared by thermal evaporation onto $2\text{-}\mu\text{m}$ -thick Ti-target backings [155]. In the extraction experiments behind TASCA were the rotating target wheel installed, which consists of four banana-shaped $395\text{ }\mu\text{g cm}^{-2}$ -thick ^{165}Ho -segments (arc-shaped, monoisotopic composition on $2\text{ }\mu\text{m}$ Ti). The target wheel were rotated synchronously with the beam-macrostructure [156]. For the preparation of lanthanide target foils, Physical Vapor Deposition (PVD) and Electrochemical Deposition (ED) were used. Both methods will be described in the following paragraphs. A summary of the used targets is given in Tab. 10.1.

Physical vapor deposition

The $^{144,147}\text{Sm}$ (for the ^{40}Ar -experiment at TAMU) and ^{165}Ho (for the ^{48}Ca -experiment at GSI) targets were prepared by vapor deposition and were made in the GSI target laboratory. For the target production natural samarium or holmium was evaporated from a Pt crucible. The Sm/Ho vapor is transported in a low vacuum region from the source to the substrate. On the substrate, the Sm/Ho vapor undergoes condensation to form a thin Sm/Ho layer on the $2\text{ }\mu\text{m}$ -thick Ti backing [145, 155, 157]. The $^{144,147}\text{Sm}$ or ^{165}Ho targets were covered with carbon layer of $5\text{ }\mu\text{m}$, which was evaporated by resistance heating [155]. The targets for the TAMU experiment were stored and transported under inert gas atmosphere.

Molecular plating

The ^{40}Ar experiments used a ^{152}Gd ($460\text{ }\mu\text{g cm}^{-2}$ $^{152}\text{Gd}_2\text{O}_3$ on $2\text{ }\mu\text{m}$ Ti) and a ^{165}Ho ($300\text{ }\mu\text{g cm}^{-2}$ $^{165}\text{Ho}_2\text{O}_3$ on $1\text{ }\mu\text{m}$ Al) targets. The targets were mounted on a "target

ladder” and inserted into the target chamber for the ion-beam irradiations. The ladder was made of Al and had the capability of holding up to 8 targets [152]. All these targets were in oxide form and were prepared by the MP technique, which is called molecular plating. The targets on the Ti-backing were produced by the staff of the the Department of Chemistry-TRIGA site (Johannes Gutenberg University Mainz, Germany) [145, 158] and the ^{165}Ho target on Al were produced at Texas A&M University [143, 159–161].

Molecular deposition was chosen because of its high deposition yields and the possibility to recover the target material. For the molecular plating, a small quantity of the Gd or Ho isotope was dissolved in 0.1 M nitric acid. 12–14 mL isopropanol was added and the solution was transferred to the PEEK electrodeposition cell. The Al and Ti foils were purchased in high purity (minimum 99.999%) and prepared by a step-by-step cold-rolling process in a laboratory roller until the desired thickness of the foil was reached. Afterwards, the rolled foils were cleaned with acetone and isopropanol before mounting on the Ti-cathode. A voltage of 150 V was applied to carry out the molecular plating with current density of 1.5 mA cm^{-2} . The ED process typically had an overall efficiency of 90%. The targets were stored and transported to the Cyclotron Institute at Texas A&M (USA) under inert gas atmosphere. Tab. 6.2 summarizes the experimental conditions for the MP of the targets used in this dissertation.

Tab. 6.2.: *Conditions for the MP of $^{144,147}\text{Sm}$ and ^{165}Ho targets.*

Isotope	Backing	Voltage (V)	Time (h)	Target density ($\mu\text{g cm}^{-2}$)
^{152}Gd	Ti	150	4	460
^{165}Ho	Al	400	1	300

6.2.3 Physical separators

The production of SHEs in fusion-evaporation reaction is a challenge and requires constant advances in efficiency. The low cross section for SHEs result in low production rates of a few atoms per day [82, 115]. This is the primary restriction for many chemical studies on a one-atom-at-a-time scale. Their identification relies on ‘clean’ background, where byproducts do not interfere with the decay chain of the SHE. The required sensitivity for the identification can be achieved with the combination of physical pre-separator and the chemical technique. The gas-filled separators TASCAs and MARS separated the contamination of lighter elements and unwanted side reactions from the ERs based on the magnetic rigidity $B\rho$. In the following paragraphs, a description of the used pre-separators TASCAs and MARS spectrometer is given.

MARS

The experiments at the Texas A&M University Cyclotron Institute were performed with the MARS spectrometer and a schematic of MARS is given in Fig. 6.10. The MARS spectrometer consists of the Wien Filter, three dipole magnets, five quadrupole magnets, and two sextupole magnets [148, 152].

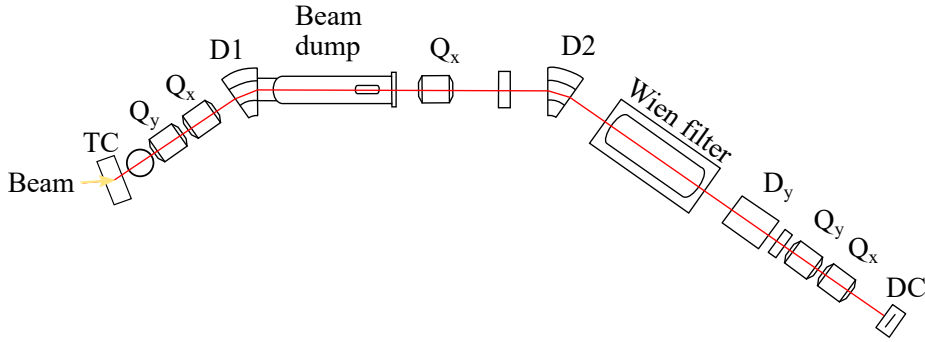


Fig. 6.10.: Schematic view of the MARS spectrometer. The subscripts on each of the quadrupole or dipole magnets indicate the focusing plane of the magnet. The incoming beam from the K500 cyclotron enters the target chamber (TC) from the left side. The flight trajectory of the ERs to the detector chamber (DC) are also shown [148, 162].

The MARS spectrometer used the magnetic rigidity dispersion in the dipoles D1 and D2 (both bend with an angle of 35°) and the velocity filter (Wien filter) to separate the primary beam from the ERs. In the first separation stage, the ions were separated in a magnetic field B in dependence of their magnetic rigidity $B\rho$ (where ρ is the radius of curvature) to their momentum (mv) to charge (q) (shown in Eq. 6.1).

$$B\rho = \frac{mv}{q} \quad (6.1)$$

In the second stage, the Wien filter selected particles based on their velocities. The employed electric field, the trajectory of the charged particle and the magnetic field were perpendicular to each other. The ERs can leave the Wien filter, if the Lorentz force (qvB) is equal to the electrical force (qE). For the velocity v of the transmitted ER in dependence to the electric E and the magnetic field B strength, Eq. 6.2 is valid [96, 163]. The dipole D3 steers the product beam up and was held at an angle of 5° .

$$v = \frac{E}{B} \quad (6.2)$$

The quadrupole magnets Q4 and Q5 provide horizontal and vertical focusing after the Wien filter into the Focal Plane (FP), where the BGC was located.

TASCA

The TASCA separator was built in the cave X8 in the UNILAC experimental hall in 2005 and successfully put into operation after a two year commission phase in 2008. TASCA was designed as a compact gas-filled separator with maximum transmission for SHEs, which are produced in hot fusion evaporation reactions. A schematic view of the TASCA setup is given in Fig. 6.11. The separator consists of a dipole with an

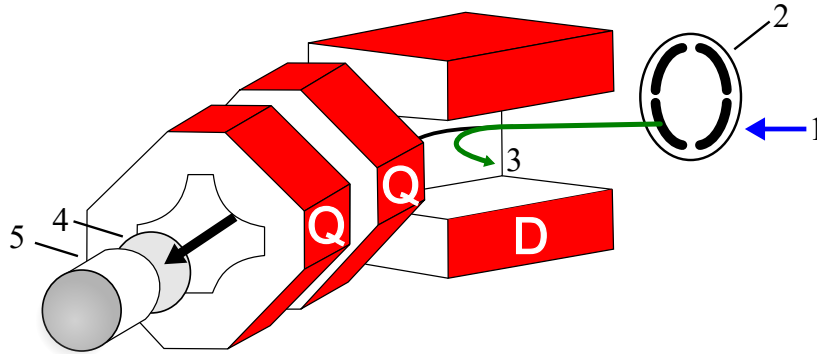


Fig. 6.11.: A schematic layout of a TASCA. The primary beam (1) from the UNILAC passes through a rotating target wheel (2). The separator TASCA consists of one dipole (D) magnet, where unwanted nuclear reaction products and unreacted primary beam (3) are separated from EVRs and subsequently focused by means of two quadrupole (Q) magnets. At the exit of TASCA, an entrance window (4) separates the low-pressure region in TASCA from the high-pressure region in the BGC (5). The figure was adopted from [68].

angle of 30° and a quadrupole doublet [149, 164]. The ^{48}Ca -beam passes a differential pumping system before entering the target station with the rotating target wheel [156]. The wheel was synchronized with the beam macrostructure to irradiate the target segments in an alternating sequence to minimize thermal stress for the target segments. Additionally, the target wheel was installed in a target cassette to prevent contamination of the UNILAC or the TASCA setup in a case of an accident. The compound nucleus ERs are formed with the momentum of the beam and recoiling through the target before they enter TASCA. The TASCA setup was operated in the DQQ (here, D = dipole magnet and Q = quadrupole magnet) configuration and were filled with 0.8 mbar He gas. The primary beam and unwanted byproducts from the fusion reaction were separated from the ERs in the dipole magnet by their magnetic rigidities $B\rho$ (see Eq. 6.1). After the dipole, the ER beam was focused by the quadrupole doublet, which was operated in the High Transmission Mode (HTM) with the DQ_hQ_v (here, the indices indicate horizontal (h) or vertical (v) focusing of the respectively quadrupole magnet) into the FP [164].

6.2.4 Focal Plane Detector

The evaporation residues produced in the ^{40}Ar and ^{48}Ca -induced reactions were separated using physical pre-separators and focused into a detection chamber. The quadrupole magnets focused the nuclear fusion products at a given position in the detection chamber, and the plane along the focusing axis is called focal plane. Inside the detection chamber, FP detector was positioned into the FP, and the EvRs implanted into this detector. The FP events were detected by a 16-strip Position-Sensitive Silicon Detector (PSSD) in case of experiments at MARS and by a Double-Sided Silicon Strip Detector (DSSD) in case of experiments at TASCA. The PSSD had an active area of 50 mm x 50 mm and was 300 μm thick. The Bias Voltage was -60 V. The α -particle detection efficiency ϵ_{Det} was calculated to be $(55\pm 3)\%$ [148, 152]. The active area of the DSSD for the TASCA experiments was 60 mm x 60 mm and was 310 μm thick. The geometrical detector efficiency ϵ_{Det} was about $(60\pm 3)\%$ for detecting an emitted α -particle. The PSSD and the DSSD was energy calibrated before the experimental series with a four line α -particle source, which contained ≈ 370 Bq each of ^{148}Gd , ^{239}Pu , ^{241}Am and ^{244}Cm . The internal calibration was conducted by using the energy of ERs from α -decay products of the respective ^{40}Ar or ^{48}Ca induced fusion evaporation reactions. The measured α energy values can be extracted from the calibration spectrum with the following equations:

$$E_{\alpha,\text{ext}} = m_{\text{ext}} \cdot \text{channel} + b_{\text{ext}} \quad (6.3)$$

$$E_{\alpha,\text{int}} = m_{\text{int}} \cdot \text{channel} + b_{\text{int}} \quad (6.4)$$

$$E_{\alpha} = m_{\text{ext}} \cdot m_{\text{int}} \cdot \text{channel} + m_{\text{int}} \cdot b_{\text{ext}} + b_{\text{int}}, \quad (6.5)$$

where m and b describe the slope and intercept and the subscripts the internal and external calibrations, respectively. Tab. 6.3 summarizes the expected α -energies E_{α} with the corresponding intensity I of the respective α -line and the branching ratio b_{α} of the α -decay.

The Focal Plane Detector (FPD) was used to determine the extraction efficiency of the produced ERs. The extraction efficiency is defined as the ratio of the number of ions which reached the subsequently detector unit to the number of the ions entering the BGC trough the entrance window. It is essential to determine the exact number of ions, which reached the stopping volume of the BGC.

For the chemistry experiments with the gas-phase chromatographic detector unit, the FPD was replaced in the FP with the BGC and the subsequent detector unit.

6.3 Buffer-gas-cell

The BGC is a device suitable for transforming fast recoil-ions into low-energy radioactive beams. For the proof-of-principle studies reported here, the former room temperature BGC, which was originally built at Ludwigs-Maximilian-Universität

Tab. 6.3.: *Decay properties of the nuclides used for the calibration of the DSSD and PSSD*

Nuclide	$T_{1/2}$ (a)	b_α (%)	I (%)	E_α (MeV)
^{241}Am	432	100	85.0(10)	5.49
			13.0(6)	5.44
^{239}Pu	24110	100	73.3(8)	5.16
			15.1(8)	5.14
			11.5(8)	5.11
^{244}Cm	18	100	76.4(2)	5.80
			23.6(2)	5.76
^{148}Gd	75	100	100.0	3.27

Munich, Germany, and has more recently been used at the Separator for Heavy-Ion reaction Products (SHIP) for high-precision mass measurements of No and Lr isotopes [93, 100] was used. The BGC has two tasks: (i) stopping of the produced ions and (ii) transport of the ions towards to BGC exit.

The reaction products of the nuclear fusion are thermalised and extracted as charged ions in a gas-cell with superimposed electric fields. The BGC is the interface, which connects the pre-separator with the gas-phase chemical experimental setup. On the basis of low production rates for the fusion reactions of SHEs, there were special requirements of the BGC. A fast and effective extraction of the produced ions towards to the detector unit is the key requirement for the BGC. For the effective extraction and guiding of the ions inside the BGC, a optimum purity of the whole setup is decisive. Already amounts of impurities can form molecules or make recombination reactions. Both together will limit the applicable electrical field strength. Therefore, the experiments with the BGC were performed in Ultra-Vigh Vacuum (UHV) conditions ($<10^{-9}$ mbar). A DC-field gradient and Radio Frequency(RF)-field generated by the BGC electrode system guide the thermalized ER ions to the exit. Gas catcher with an RF-Funnel were introduced in of the INS-RIKEN gas cell [165], the Argonne typ gas cells [166] and the SHIPTRAP gas cell [100]. The detector array behind the BGC exit was connected either directly or connected with via a transport line. The combined efficiency for stopping and extraction is of about 12% [93]. A schematic view of the two techniques, which were used in off-line and on-line experiments, is given in Fig. 6.1.

Tab. 6.4.: *Optimum parameters for the operation of the gas stop cell.*

source position related to funnel exit (d_{Pos})	260 mm
stopping gas	Helium
pressure in inside gas stop cell (p_{Cell})	30–100 mbar
pressure in inside COMPACT (p_{COM})	30–40 mbar
Surface of COMPACT	Au or SiO ₂
Operation mode COMPACT	Isothermal chromatography (IC)
Electrode (symbol)	Voltage (V)
Source Voltage (U_{Source})	245
DC cage max (U_{DCmax})	300
DC cage min (U_{DCmin})	80
Funnel max ($U_{\text{Funnelmax}}$)	75
Funnel min ($U_{\text{Funnelmin}}$)	15
Funnel amplitude (\tilde{U}_{RF})	160
Funnel frequency (f_{RF})	796 kHz

6.3.1 DC Cage

The DC cage (see Fig. 6.12) is one of the key parts of the BGC. The DC cage contains the stopping volume for the ions and consists of five cylindrical electrodes with an outer (inner) diameter of 180 mm (160 mm). The different DC electrode segments were assembled at the distance of 1 mm via five ceramic screws.

The incoming nuclear fusion products or recoil-ions were thermalized in 30-100 mbar helium gas and extracted as charged ions. The main driving force for guiding the thermalized ions towards the exit originates from the voltage gradient applied on the DC cage, which drives them towards the end of the cell. The cylindrical design of the DC cage electrodes ensures a homogeneous electric field within the enclosed stop volume. If a recoil-ion source were inserted into this field leads only to a low electric field distortion [97]. The specific voltages for the electrodes of the DC cage as well as all other important operating parameters of the gas stop cell are summarized in the Tab. 6.4. Unless otherwise stated.

6.3.2 RF funnel

The RF-Funnel (see Fig. 6.13) is a conical electrode system consisting of 40 stainless steel ring electrodes with a constant distance between two adjacent electrodes of 1 mm. The thickness of each electrode is 1 mm. There are two sets of electrodes, the first set of electrodes has an RF waveform applied to it, while the second set has a 180° phase-shifted of the same frequency compared to the first electrode set. The basic principle to focusing the ions via the RF funnel can be described by an ion in a quadrupole field (see Sec. 4.2.1). In such a field, the opposite RF waveforms cancel each other out at any significant distance away from the electrode surface, when the electrodes are relatively close together. Only near the electrode surface a

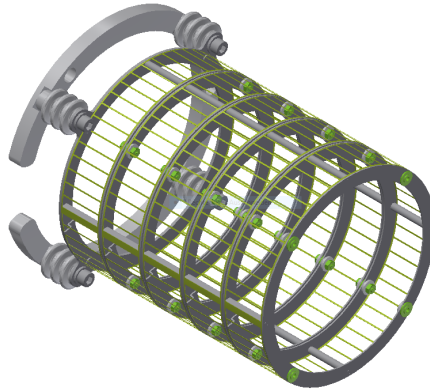


Fig. 6.12.: *The DC cage structure in a schematic view. The DC cage consists of 5 ring segments, which were connected to an RF-/DC-mixing board. The system is fixed to the entrance flange via four ceramic spacers.*

repulsive force prevents the ions from collisions with the electrodes [97, 165]. The DC gradient in the RF funnel was used as a continuation of the DC cage gradient in these experiments and therefore operated with the exact same values. Due to the resulting effective force F_{eff} (see Fig. 4.10), the ions guided through the electrode structure of the BGC. The specific voltages for the RF funnel as well as all other important operating parameters of the BGC are summarized in the Tab. 6.4. Unless otherwise stated, the voltages given there were used for all experiments described in the following sections.

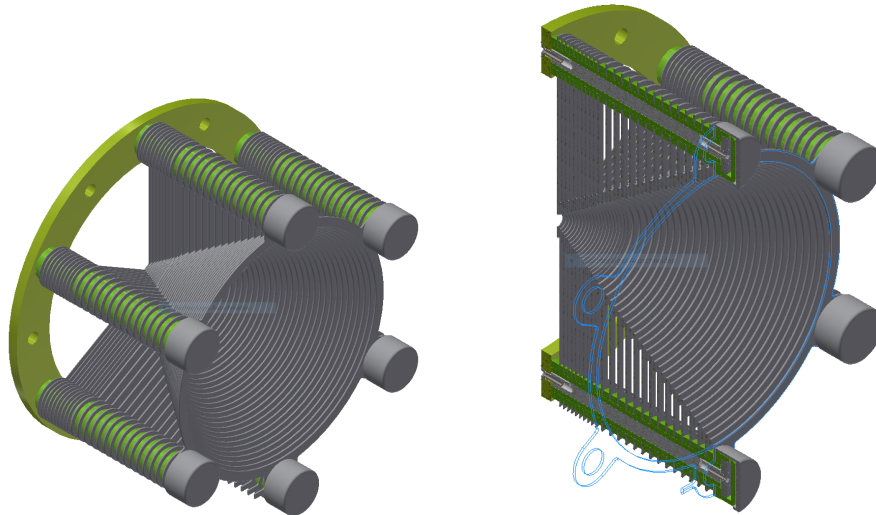


Fig. 6.13.: *The RF funnel structure in a schematic view with the 40 ring electrode plates and the ceramic spacers between adjacent plates. The left side shows the complete funnels with the ceramic spacers (green). On the right side, a half-cut of the funnel structure is shown. The contour of the last funnel ring electrode is complete shown (blue).*

6.4 COMPACT detector array

Two COMPACT arrays (see Fig. 6.14), each consisting of 2 x 32 Positive-Intrinsic-Negative (PIN) silicon photodiodes with an active area of $(9.7 \times 9.8) \text{ mm}^2$ were attached together with indium-wire sealing. In COMPACT, the chromatography column is made up from two rows of PIN diodes, which were mounted with the active areas of both rows facing each other at a distance of $600 \mu\text{m}$, thus forming a 32-cm long column with a cross section of $0.6 \times 10 \text{ mm}^2$. The surface of the diodes is covered with a 30-50 nm thick Au layer produced by vapor deposition at temperatures of around 100 to 130°C , or with SiO_2 created through oxidation of Si [167]. The respective surface of the diodes were depending on the chemical properties of the element to be investigated. The calculated geometrical efficiency for detecting, ϵ_{Det} , an α -particle emerging from an atom residing inside the COMPACT detector array is 76% [49, 65]. In the presented experiments, the COMPACT detector array was

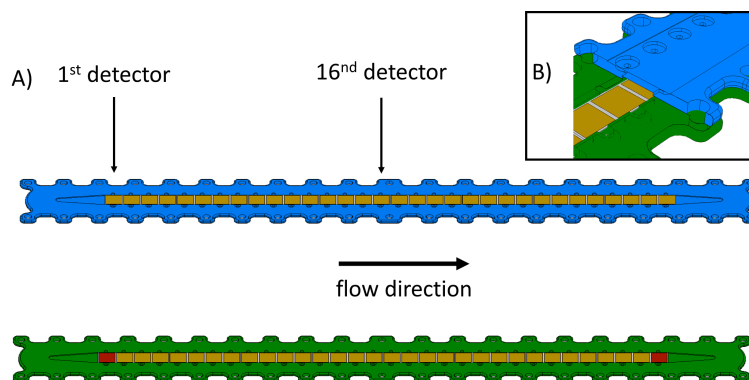


Fig. 6.14.: Schematic of the COMPACT array. The flow direction is marked. The bottom and top half-array is shown in full, including the detectors, with the 1st and 16th labeled. B) Enlarged view of the last section of the COMPACT array. Only the last part of the top half-array - containing the top detectors facing the bottom detectors and leaving a gap of 0.05 mm to form the rectangular chromatography channel - is shown towards the end of the array.

operated as Isothermal Chromatograph (IC, room temperature) unit.

6.5 COMPACT data acquisition systems

For measuring the extraction efficiency and transport time of the BGC, analog electronics for signal processing from the COMPACT's PIN diodes, read-out triggering and Data Acquisition System (DAQ) were needed. A schematic overview of the signal handling can be found in Fig. 6.15.

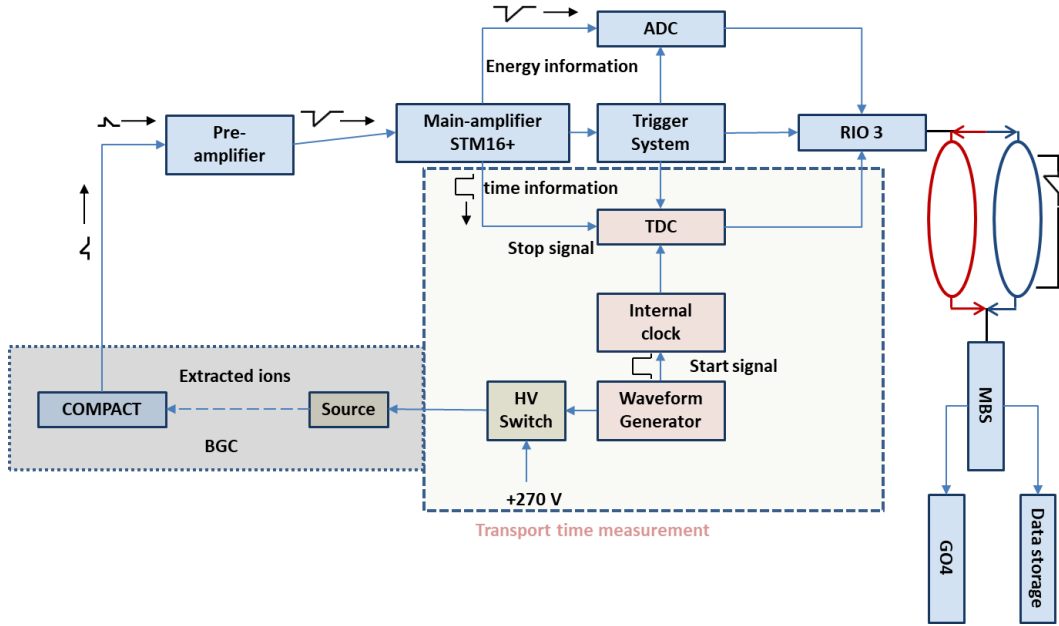


Fig. 6.15.: Schematic overview of the electronics for the efficiency and transport time measurements with the BGC is shown. On the top, the analogue signal processing is shown. For a detailed description see text. The dashed box shows the process for the extraction time measurements.

The COMPACT PIN diodes were connected with coaxial cables to four 16-channel charge sensitive preamplifier, which were developed at the IKP (Institut für Kernphysik), University of Cologne [168]. Each preamplifier has one bias for 16 channels. Here the otherwise weak negative polarized signal of the collected α is amplified and send to the main-amplifier. The main-amplifier amplifies the signal with two amplification ranges (x1 or x10) further, to shape ($2 \mu\text{s}$) it to a Gaussian pulse and change the polarity. This improves the signal to noise ratio. At the same time a strobe signal with a adjusted duration between 1 to $10 \mu\text{s}$ was created in the discriminator. The strobe signal and the logical signal were then transferred to the 12-bit ADCs (Analog-Digital-Converter).

The main amplifiers are 16-channel-NIM (Nuclear Instrumentation Standards) Mesytec STM-16+ modules [169]. In addition to the main amplifier, this module has Timing-Filter-Amplifier (TFA) und Constant-Fraction-Discriminator (CFD) for a time- and logic-output. The signal- and logic-output from the MADC-32 modules by Mesytec is used in two ways. I.e, it is passed on to two ADCs and it is also used for the trigger system. In the first step of generation of the Master trigger a logical 'OR' of all 32 channels for the PIN diodes of the COMPACT detector array is generated separately with the strobe signal. In the final step the trigger signal is validated in the VME trigger logic (TRIVA5) [170] and the Master trigger is created. This validated signal is used to starts a gate generator which determines the timeframe during which the ADCs reads out the maximum of the analog pulse and converts it to digital code, if the peak maximum was detected within the trigger time (strobe time). Finally this

Tab. 6.5.: *Main parameters for the extraction time measurement*

parameter	
U_{source} (release mode)	+245 V
U_{source} (retention mode)	+ 0
puls length	20 ms
source	^{223}Ra
measurment cycle lenght	320 ms

information is sent to the processor RIO3 for on-line visualization and storage. The PIN diodes of the COMPACT detector array were biased with high voltage via the IKP preamplifier.

For the transport time measurements a waveform generator creates a trigger signal, which is used to pulse the source and as a start signal to increment the clock cycle in the TDC (Time-to-Digital-Converter). The typical reference frequency was 100 MHz (10 ns resolution). The source voltage ($U_{\text{source}} = +245$ V, only for experiments with the recoil-ion source) is chosen such that only during the trigger pulse of 20 ms (see Tab. 6.5), recoil-ions can emanate. With an attractive voltage of 0 V, compared to the voltages (+300 V) of the surrounding first DC cage electrodes, the recoil-ions were hold back on the source. Only the recoil-ions emitted within 20 ms pulse can be extracted.

6.6 Gas handling system

He gas with a purity of 99.9999% was used and was passed through a Oxisorb[®] cartridge (Spectromol) [171] to reduce the concentration of water and oxygen to ppb levels (manufacturer specifications: $\text{H}_2\text{O} < 5$ ppb, $\text{O}_2 < 30$ ppb). All vacuum seals are made of Cu. The entire BGC and the gas inlet was baked at 100 °C for 3 d before the experiments. The gas-supply system is controlled by a custom LABVIEW[®]-based interface, where the flow conditions were controlled continuously via mass flow controllers (MKS 1179 Mass-Flo[®] controller). The gas pressure was monitored over a long-term with a capacitron (Pfeiffer Vacuum CMR 261) and the gas-flow rate was also manually adjusted in the LABVIEW[®] based Graphic User Interface (GUI)-controls. The continuous flowing of the He carrier gas was realized with a diaphragm pump (see (9) in Fig. 6.1) at the exit of the COMPACT detector array. The pressure close to the COMPACT detector array entrance was controlled by a pressure gauge and the pump capacity was adjusted with a needle valve to achieve the required flow rate of the He carrier gas. The described gas-supply system was used for all experiments reported in this thesis.

During the thesis project at hand, the room-temperature BGC previously used to thermalize ERs of heavy elements behind the velocity filter SHIP [22, 172] for Penning trap mass spectrometry investigations [173, 174] was modified such that it can be reliably and conveniently used in chemistry experiments behind the gas-filled separator TASCAs. The SHIPTRAP Penning trap mass spectrometer (mass measurements behind SHIP) BGC consists of i) the entrance window or ii) linear motion feedthrough with the recoil-ion source, the electrode system, the extraction nozzle and the gas-supply system. At the de Laval nozzle the He buffer gas expands into the extraction RFQ (10⁻¹ – 10⁻³ mbar) to perform a supersonic gas jet and dragging the extracted ions. The extraction RFQ following the nozzle is used for separating the ions from the neutral gas and for cooling the ions transversely, which is needed for highly precise Penning trap mass measurements [175–177]. For the gas-phase chemistry experiments, no transversal cooling and removing of the neutral buffer gas is needed; therefore, the de Laval nozzle [92, 97] and the RFQ was replaced by a newly designed interface. This way, the instrumental development accompanies as well as drives progress in gas-phase chemistry. The new interface, called Transition Electrode (TE), will be described in detail in Sec. 7.1. So far only volatile elements have been used in gaschromatography experiments, but in this thesis, access to non-volatile elements should be actively promoted. For this reason, the ²²⁵Ac recoil source was introduced, providing of non-volatile ²²¹Fr for further development of the COMPACT detector. The production of the source is described in Sec. 6.1.1. Due to the preparation from a organic solution, there was an unwanted dead layer on top of the activity and has to be taken into account (a detailed description for the analytical method to determine the released number of ions from the recoil-ion source is given in [178]). The consequent further development of the COMPACT detector (see Sec. 6.4) led to the design of the miniCOMPACT, which is described in detail in Sec. 7.2.

7.1 Transition electrode

The SHIPTRAP BGC used a de Laval nozzle to connect the high-pressure area of the BGC with the low-pressure area of the extraction RFQ. The convergent-divergent shape of the de Laval nozzle generates a supersonic gas-jet in the axial exit area due to the isentropic gas-flow. The gaschromatographic detector column COMPACT needs laminar gas-flows, therefore no supersonic gas-flows are required. The de Laval

nozzle was replaced by the TE in experiments, which used the COMPACT detector. In the case of chemical experiments with the miniCOMPACT (see Sec. 7.2) a different interface was used. The TE is made from stainless steel and was electrically separated from the transport line by 1-mm thick ceramic spacer ring. The transport line is a 250 mm long Teflon capillary with an inner diameter of 4 mm, which connected the TE with the entrance of the COMPACT detector array. The TE has a conical shape with the inner diameter reducing from 10 mm to 1.0 mm. A DC voltage (typical $U_{TE} = -3\text{ V}$) can be applied to the TE, which results in a gentle acceleration of the ions into the transport line. The relevant aspects concerning the Teflon tube include: (i) it connects the funnel exit with the entrance of the gas chromatography setup entrance, (ii) surface encounters of ions extracted from the BGC lead to their conversion to neutral atoms, and (iii) its inert surface ensures that loss of neutral, volatile atoms like Rn (or Cn and Fl in future studies with SHE) through adsorption processes on the wall surface are minimized.

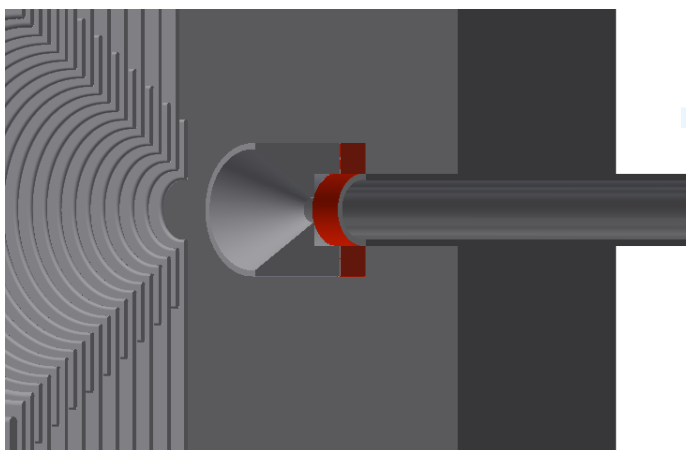


Fig. 7.1.: *Enlarged schematic view of the TE. Only the last funnel electrodes and the conical shape of the TE are shown. The TE represents the entrance into the Teflon transport line. The Teflon tube inside the metal tube is not shown.*

7.2 MiniCOMPACT

For the investigation of the value of the adsorption enthalpy, SiO_2 -, Al-, Au- or combination of SiO_2 /Au-covered COMPACT detectors were used [13, 179]. Depending on the interaction strength of the atoms with the surface, the decay of the atoms can be observed on either the Au or SiO_2 surface. The deposition of the short-lived isotopes of for example At and Fr on the Au and SiO_2 surfaces was dependent on their volatility and their interaction with the surface. On the inert surface SiO_2 no adsorption of relatively non-reactive elements like At were expected and Fr, which has an unpaired electron available in its ground-state configuration, was expected to stick on the SiO_2 surface. On the more reactive Au surface, At was expected

to have a strong interaction strength. In preliminary investigation on the 'classic' COMPACT detector array with the ^{225}Ac recoil-ion source it could be shown that Fr could not be extracted but the daughter ^{217}At reached the detector unit. In these preliminary experiments, a 250 cm-long Teflon capillary was used to connect the classic COMPACT detector with the BGC exit. The ^{221}Fr ions were lost in the transport line due to the strong interaction with the capillary walls. The main focus for the modification of the classic COMPACT array was on the elimination of a non-active area between the BGC exit nozzle and the COMPACT detector. The first wall contact shall occur on the active area of a positive intrinsic negative (PIN) diode. In the present COMPACT detector design, the transport gas is injected perpendicularly to the column axis. This configuration of the gas entrance into the classic COMPACT array is important for a vacuum tight detector, which is essential for operations as thermochromatography column. Here, a negative temperature gradient can be applied along a chromatography column down to temperatures around 113 K (-160 °C). This leads to a change in the adsorption behavior of the investigated species on the detector surface and a separation of different species from each other based on their adsorption enthalpies is possible. A vacuum tight detector array is necessary to prevent the freeze out of impurities inside the column, which leads to change in the surface nature¹ and on the long-term to a blocking of the gas channel. This configuration has the disadvantage that no PIN diodes can be placed in the entrance area of the COMPACT detector. In addition, in the entrance of the classic COMPACT array there is a 2 cm-long PTFE (Polytetrafluoroethylene) coated area, which is used to create a laminar flow regime inside the detector column. This means that the first wall contact for some atoms is not the detector surface. This does not matter for volatile elements, which will not adsorb at the first wall contact, but for non-volatile elements, the atoms which have wall collisions in this area will be lost for a potential detection. For this reason, the gas entrance into the newly built miniCOMPACT changes from perpendicular to parallel to the beam axis. With this change, the aim of the first wall contact occurring on the active area of PIN diode can be achieved. Furthermore, preliminary experiments indicate that a short version of the COMPACT array is sufficient. In Fig. 7.2 the distribution pattern of ^{217}At along an Au-covered COMPACT detector array is shown. ^{217}At shows a strong interaction strength with the Au surface and deposits only in the first five detector units. From these results, it is evident that a miniCOMPACT with 8 detector units per array is sufficient to measure the adsorption distribution pattern of non-volatile elements, while volatile species can well be transported further to a regular COMPACT detector using the well established transport by Teflon tubes and Teflon coated surfaces.

¹Results in a disturbance in the chromatogram and incorrect assessment of the adsorption enthalpy.

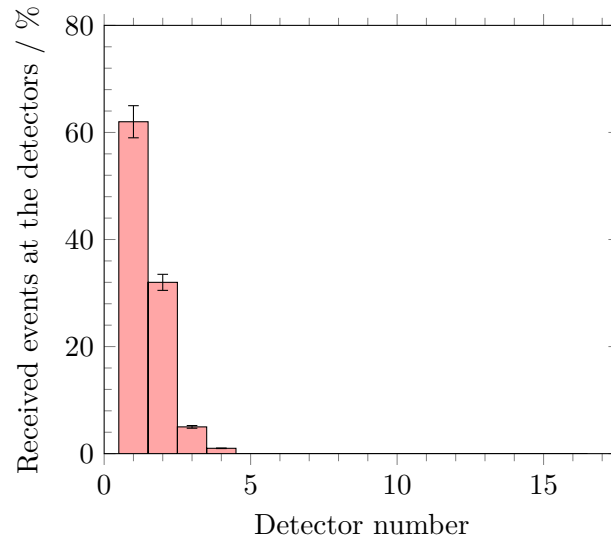


Fig. 7.2.: Measured distribution of adsorbed ^{217}At along an Au-covered COMPACT detector.

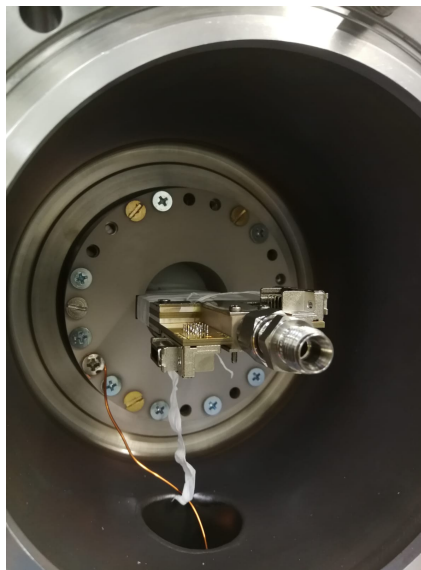


Fig. 7.3.: Photo of the miniCOMPACT in the open vacuum chamber directly behind the BGC exit. At the end of the miniCOMPACT, the Swagelok[®] connector is shown.

7.2.1 Design of the miniCOMPACT

The new detection system miniCOMPACT was developed particularly for chemical experiments with non-volatile elements like Fr as an isothermal chromatography column and is the advancement of the COMPACT detector, which is described in [Sec. 6.4](#). Two Printed Circuit Boards (PCBs) (see [Fig. 7.4 a](#)) with lateral metal spacers form a vacuum tight gas channel of 10 mm in width, 80 mm in length and 1 mm in depth. Each PCB array consists of 8 pairs of 10 mm x 10 mm PIN photodiodes. They have

an active area of 9.7 mm x 9.8 mm and an effective thickness of 150 μm . The surface of the PIN diodes was covered with a 30-50 nm thick layer of gold or SiO_2 . The bottom and top PCB array were shielded with a grounded metallic plate. The calculated geometrical efficiency ϵ_{Det} for detecting an α particle is about 76%. The elimination of a non-active area between the BGC exit nozzle and the COMPACT detector was reached with a customized flange with a milling, which presses the two miniCOMPACT panels together. The flange holds additionally the nozzle with an entrance diameter of 3 mm and a throat of 0.6 mm. With this setup, the detector surface started directly behind the nozzle. In this configuration no transport line was needed.

The miniCOMPACT detector was sealed with epoxy resin on the outside surface, and to reduce any potential leak rate, the miniCOMPACT was installed in a vacuum chamber. This vacuum chamber can be installed at the BGC exit. The vacuum chamber is relevant to ensure the UHV conditions during the baking process, because the custom-made attached holder of the miniCOMPACT was not gas tight at higher gas pressure differences between the BGC and the miniCOMPACT. The here presented miniCOMPACT can only be operated in the combination with the BGC and the new interface. With a modified version of the interface, a combination with the classic RTC is possible and was successfully used in off-line and on-line experiments. For a detailed description of this combination between the RTC and miniCOMPACT see [180]).

7.2.2 Basic characterization of the miniCOMPACT as detector unit for non-volatile elements

The miniCOMPACT detector array was compared with the 'classic' COMPACT detector array, which was described in detail in the work of Dvorak *et al.*[13], for the basic characterization. The COMPACT detector array was designed for the detection of volatile elements as a chromatography column. Both detector arrays were used under similar experimental conditions to study the functioning and performance.

Study of the signal noise

The transport line in the setup with the COMPACT detector array also has a positive side effect, because the extension increases the distance between the RF funnel and the detector. The RF funnel generates a high frequency noise, which increases with increasing of the applied amplitude (U_{RF}) on the funnel. The COMPACT detector array was a relatively good antenna for this noise. The signal-to-noise ratio (SNR) is of great importance in several respects. Short-term fluctuations have a negative impact on the detection level of α -signals, whereas, long-term fluctuation reduces the linearity of the energy calibration of the detector units as well as the reproducibility of the measured results. In the presented work, was given to special attention to the

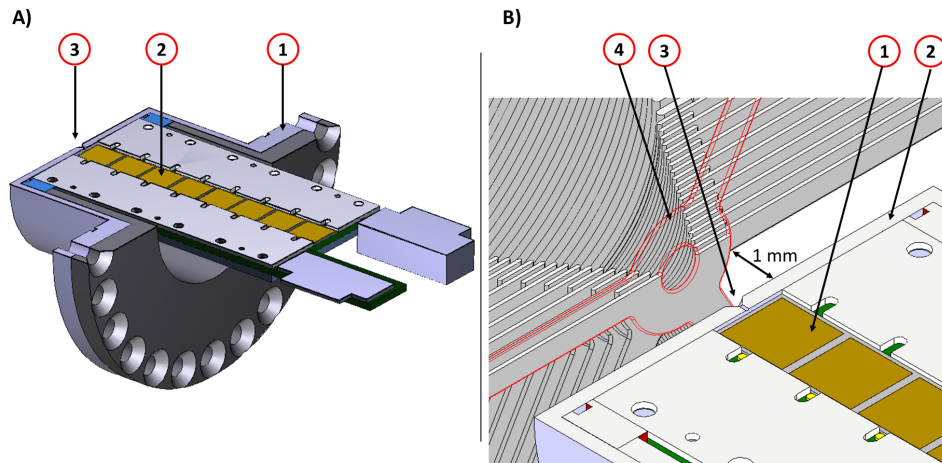


Fig. 7.4.: A) Half-section view of the miniCOMPACT in its mounting flange (1). Only the bottom of the miniCOMPACT array with the 8 PIN diodes (2) is shown. B) Schematic of the coupling section of the miniCOMPACT array to the RF-funnel. The bottom half of the mounting flange (1) with the first three PIN diodes (2), the entrance nozzle (3) and the last funnel electrode (4, red contour) are shown. The distance between the last funnel electrode and the miniCOMPACT entrance is enlarged by a factor of 10 for a better overview. The opening diameter of the nozzle is 3 mm and converging to a diameter of 0.6 mm to match the pitch between the detectors in the miniCOMPACT.

noise level. The influence of the RF noise from the RF funnel depends not only on U_{RF} but also on the distance between the RF funnel and the COMPACT detector. One aim of introducing the miniCOMPACT was to eliminate the transport line, because in the case of non-volatile elements, this is the bottle-neck. One consequence of this development was the new location of the miniCOMPACT directly at the funnel exit. For this new setup, the miniCOMPACT was electrically insulated from the funnel with ceramics (blue highlighted in Fig. 7.5) suitable for UHV conditions. Preliminary investigation showed that the noise level on the miniCOMPACT was in the same range as with the 'classic' COMPACT setup. The outer flange ((1) in Fig. 7.5) can be used as an electrode at appropriate voltages.

Fig. 7.6 shows the influence of the RF funnel on the mean signal noise on the miniCOMPACT. In the case that the RF funnel was switched off, the absolute maximum noise level was 28.1 mV with a root mean square of 8 mV. The main component of the mean signal noise was from the thermal noise and is unavoidable. In the case that the RF funnel was operated at maximum amplitude around 160 V_{PP}, the noise level was doubled. The miniCOMPACT as antenna picked up only a small amount of the RF noise. The typical noise level on the 'classic' COMPACT detector was around 50–60 mV and is in the same range as the mean noise on the miniCOMPACT with switched on RF field.

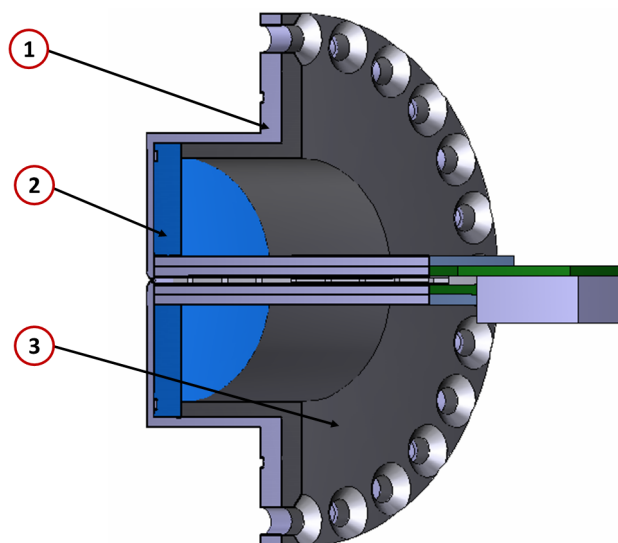


Fig. 7.5.: Schematic view of the custom made flanges with the miniCOMPACT. The outer flange (1) with the extraction nozzle connects the funnel exit with miniCOMPACT entrance. The outer flange holds the ceramic plate (2) in which the miniCOMPACT sits. The inner flange (3) is used to press the ceramic plate on the outer flange.

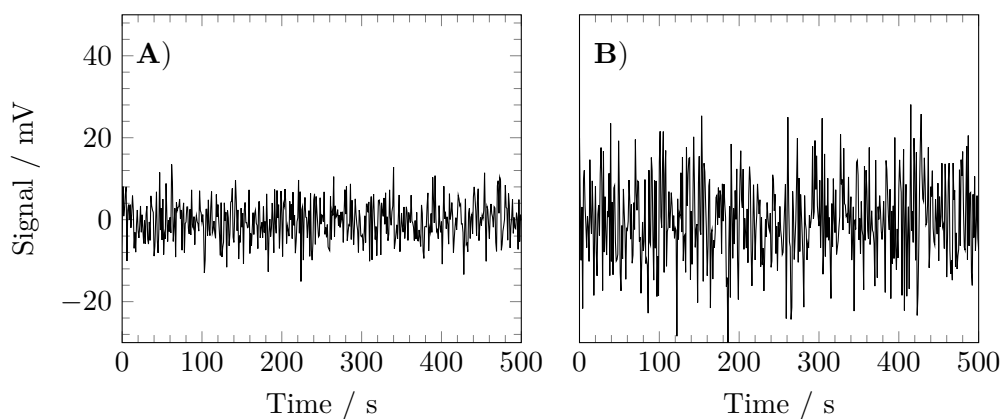


Fig. 7.6.: Achievable mean signal noise on the miniCOMPACT with the parameters from Tab. 6.4 (A) without RF from the funnel and (B) with RF on the funnel.

The BGC is an essential link between the pre-separator and the chemical experimental setup. To ensure the best possible BGC performance, different optimizations of the experimental parameters were executed to maximize the efficiency. The individual optimization steps had been completed before on-line and off-line experiments. The verification of the experimental parameters of the BGC guaranteed the flawless condition. [Sec. 8.1](#) describes fist of all the kinematic and the stopping distribution of the fusion products or recoil-ions from the ion source, respectively. The chapter is concluded by a summary of the individual parameters of the electric fields in [Sec. 8.3](#).

8.1 Simulations

A numeric simulation is a powerful tool for scientists responsible for the operation of complex processes and systems. If simulated experimental designs are available, it can help to find the combination of different factors at which the response value is optimized. Based on Stopping and Range of Ions in Matter (SRIM) simulations, the stopping efficiency of the produced ERs was calculated in the present thesis, for the example of different entrance window foils and buffer gas pressures inside the BGC. SRIM simulations [181] characterize reliably the stopping behavior of ions passing the metallic foil and their subsequent thermalization in the buffer gas volume. This method allows the determination of suitable entrance window thicknesses in conjunction with the gas pressure before an on-line experiment.

8.1.1 Estimation of the stopping distribution of fusion products inside the BGC

The simulation program SRIM calculated the penetration depth of the produced ERs in dependence of the respective nuclide ion and kinetic energy on the one side and material of the 'target' layer on the other side. For a detailed description see [Sec. A.1](#)

For the experiment, it was important that the ERs were stopped in the center of the stopping volume of the DC cage and the loss of ER ions in the entrance window foil should remain as low as possible. Therefore, the best combination of entrance foil thickness and buffer gas pressure was studied by SRIM simulations. For this purpose, the respective kinetic energy of fusion evaporation reaction products was calculated and checked with the computer program LISE++ [182, 183]. Afterwards,

the kinetic energy lost in the backing foil, target material, separator and entrance window foil was determined using SRIM.

Simulation results

In the on-line experiments behind the MARS spectrometer, short-lived α -decaying radioisotopes were produced in the nuclear fusion reactions $^{152}\text{Gd}(^{40}\text{Ar},4\text{n})^{187}\text{Pb}$, $^{165}\text{Ho}(^{40}\text{Ar},5-6\text{n})^{199,200}\text{At}$ and $^{144,147}\text{Sm}(^{40}\text{Ar},2-4\text{n})^{182,183}\text{Hg}$ using beams of ^{40}Ar with lab frame energies (E_{Lab}) of 212 MeV (^{187}Pb), 200 MeV ($^{199,200}\text{At}$) and 193 MeV ($^{182,183}\text{Hg}$) delivered by the K500 cyclotron at the Cyclotron Institute (Texas A&M University, College Station, TX, USA).

In the gas-phase chemical studies behind the gas-filled separator TASCA, radioisotopes of Fr were produced in the nuclear fusion reaction with ^{165}Ho as target at E_{Lab} of 289 MeV, using a ^{48}Ca beam delivered by the UNILAC at GSI Darmstadt (Germany). The lab frame energies and target information for both on-line experiments are summarized in [Tab. 8.1](#). Therefore, the energy loss was simulated with SRIM and

Tab. 8.1.: Target information for the experiments at MARS and TASCA.

Reaction	E_{Lab} (MeV)	backing	target thickness ($\mu\text{g cm}^{-2}$)
$^{40}\text{Ar} + ^{152}\text{Gd}$	214	2.0 μm Ti	460
$^{40}\text{Ar} + ^{165}\text{Ho}$	217	1.0 μm Al	300
$^{40}\text{Ar} + ^{144,147}\text{Sm}$	219	2.0 μm Ti	600
$^{48}\text{Ca} + ^{165}\text{Ho}$	289	2.3 μm Ti	395

the resulting energies were the start values for the calculation of the kinetic energy of the compound nucleus. The kinetic energy of the compound nucleus E_{CN} can be calculated in consideration of the reduced E_{Lab} and the masses of the projectile (P), target (T) and compound nucleus (CN). In the center-of-mass coordinate system, the kinetic energy of the CN in consideration of the laws of conservation of energy and momentum is given by [Eq. 8.1](#).

$$E_{\text{CN}} = \left(\frac{m_{\text{P}}}{m_{\text{P}} + m_{\text{T}}} \right)^2 \cdot \frac{m_{\text{P}} \cdot E_{\text{Lab}}}{m_{\text{P}}} = E_{\text{Lab}} \cdot \frac{m_{\text{P}}}{m_{\text{P}} + m_{\text{T}}} \quad (8.1)$$

For the kinetic energy of the ER (E_{ER}) the mass of the ER must also be considered, where the energy loss due to neutron evaporation has been neglected.

$$E_{\text{ER}} = \left(\frac{m_{\text{ER}}}{m_{\text{CN}}} \right) \cdot E_{\text{CN}} \quad (8.2)$$

The energy loss in the gas-filled pre-separator TASCA was estimated to be around 5 MeV. E_{BW} described the kinetic energy of the respective ER in front of entrance window for the following Transport of Ions in Matter (TRIM) simulations. The

kinetic energies for the TRIM simulations in 50 mbar He buffer gas of the used fusion reaction evaporation residues are summarized in [Tab. 8.2](#). The TRIM simulation was performed with 2000 ions of the respective nuclide and the accuracy of the energy loss calculation is proportional to the total number of projectiles ($\approx \sqrt{N_{\text{tot}}^{-1}}$); it can be improved by increasing N_{tot} . The type of TRIM damage calculation

Tab. 8.2.: *Kinetic energies of the fusion evaporation residues in front of the entrance window to the BGC.*

Reaction	CN	E_{CN} (MeV)	Exit channel	ER	E_{ER} (MeV)	E_{BW} (MeV)
$^{40}\text{Ar} + ^{152}\text{Gd}$	^{192}Pb	43.7	4n	^{188}Pb	42,8	36,2
			5n	^{187}Pb	42,6	36,0
			6n	^{186}Pb	42,3	35,8
$^{40}\text{Ar} + ^{165}\text{Ho}$	^{205}At	38.7	4n	^{201}At	37,9	32,7
			5n	^{200}At	37,8	32,5
			6n	^{199}At	37,6	32,3
$^{40}\text{Ar} + ^{144,147}\text{Sm}$	^{187}Hg	40.6	4n	^{183}Hg	39,7	31,9
			5n	^{182}Hg	39,5	31,7
			6n	^{181}Hg	39,3	31,6
$^{48}\text{Ca} + ^{165}\text{Ho}$	^{213}Fr	61.7	6n	^{207}Fr	60,0	50,0
			7n	^{206}Fr	59,7	49,8
			8n	^{205}Fr	59,4	49,6
			9n	^{204}Fr	59,1	49,3

was 'Ion Distribution and Quick Calculation of Damage'. This ignores the atom cascades and there is no sputtering process, with this context the computational time was reduced. For the simulation of the ion trajectory in the buffer gas, it should be noted that the density is proportional to the pressure of the buffer gas. TRIM uses Standard Temperature and Pressure (STP) conditions and for this reason the gas density had to be converted to the He pressure of 50 mbar in the BGC. TRIM simulated with a Monte Carlo simulation the straggling and the projected range of each ion with the related coordinates (X_{Ion} , Y_{Ion} , Z_{Ion}). For the calculation of the stopping efficiency, the number of ions which were stopped inside the BGC has to be known. The ions were released perpendicularly to the target surface and ions with an end position inside the window foil $X_{\text{Ion}} < d_{\text{Window}}$ were lost for the later extraction. Only ions with an end position inside the BGC were also available for any extraction. The stopping volume had the dimension of the electrode system. Under the assumption that the electrode system was a cylinder whose dimension was determined by the radius of the DC cage (r_{Cage}) and the length $d_{\text{Cage} + \text{Funnel}}$ given by the DC cage d_{Cage} and funnel length d_{Funnel} , the ion coordinate has to fulfill the

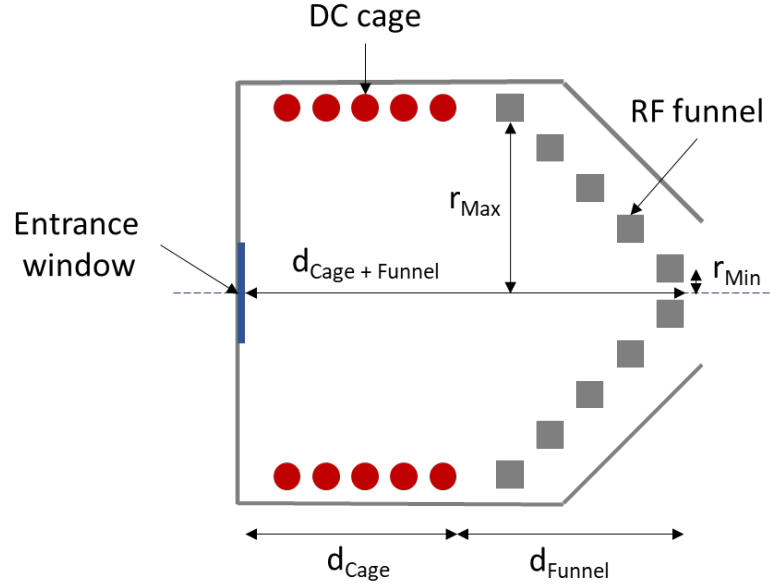


Fig. 8.1.: Schematic picture of the BGC with the used geometrical parameters for the determination of the number of ions which were stopped inside BGC.

following condition:

$$d_{\text{Window}} \leq X_{\text{Ion}} \leq d_{\text{Cage} + \text{Funnel}} \quad \text{and} \quad \sqrt{Y_{\text{Ion}}^2 + Z_{\text{Ion}}^2} \leq r_{\text{Cage}} . \quad (8.3)$$

On the basis of this number of ions, the number of ions which were stopped behind the dimension of the funnel has to be subtracted. The dimension of the funnel was described by the opening radius r_{Max} and the exit hole r_{Min} . The number of ions with the coordinates, which fulfilled the following conditions were lost by collisions with the funnel electrodes:

$$d_{\text{Cage}} \leq X_{\text{Ion}} \leq d_{\text{Cage} + \text{Funnel}} \quad \text{and} \quad (8.4)$$

$$\left(\sqrt{Y_{\text{Ion}}^2 + Z_{\text{Ion}}^2} \right) \geq \left(r_{\text{Max}} - \frac{r_{\text{Max}} - r_{\text{Min}}}{d_{\text{Funnel}}} X_{\text{Ion}} \right) . \quad (8.5)$$

Fig. 8.1 shows a schematic picture of the BGC which describes the used geometrical parameters. An example simulation for the end position of 2000 ^{205}At ions inside the BGC in consideration of $4.1 \mu\text{m}$ Ti entrance window and 50 mbar He buffer is visualized in **Fig. 8.2**.

Only ions which fulfill the **Eq. 8.3** to **Eq. 8.5** were available for a potential extraction from the BGC into the subsequent transport line or detector unit. The simulated stopping efficiency is then given by the ratio of the number of ions stopped within the electrode system to the number of ions entering the BGC through the entrance window. **Fig. 8.3** shows the dependence of the simulated stopping efficiency from

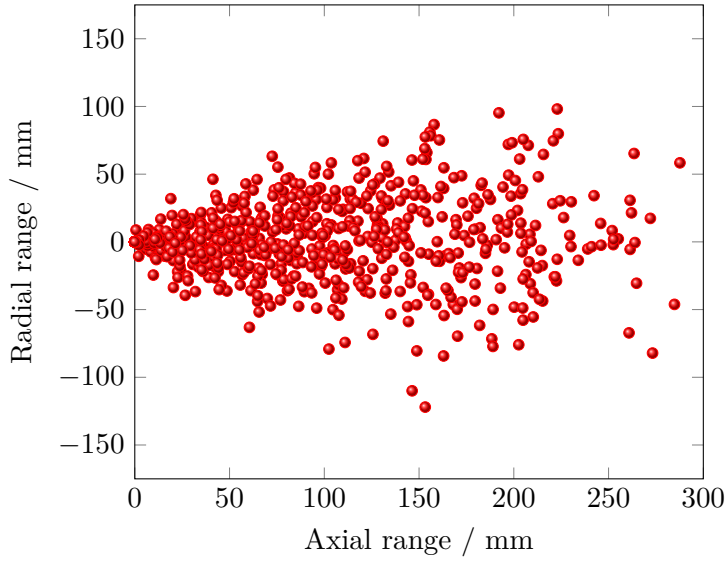


Fig. 8.2.: *Stopping positions for ^{205}At ions simulated by the computer program TRIM in consideration of a $4.1\ \mu\text{m}$ -thick Ti entrance window and 50 mbar He buffer gas.*

the entrance window thickness for At, Pb and Hg ions. The simulated stopping efficiency for At and Hg increases almost linearly in the range between $3.0\ \mu\text{m}$ and $3.4\ \mu\text{m}$ Ti foil thickness and reach the maximum of about 76% at $3.5\ \mu\text{m}$ Ti foil thickness. A further increase in the foil thickness leads then to a decreasing efficiency due to losses of ions within the window foil. In the case of Pb isotopes, the maximum stopping efficiency can not be reached in the shown range. The raising edge of the stopping efficiency is shifted to higher Ti foil thicknesses due to the larger recoil energies in this reaction. In Fig. 8.3b the stopping efficiency for Fr ions from the $^{48}\text{Ca} + ^{165}\text{Ho}$ reaction in dependence of the Ti window foil thickness is shown. The stopping efficiency increase in the range from $4.4\ \mu\text{m}$ to $5.0\ \mu\text{m}$ Ti foil thickness. The maximum stopping efficiency of about 80% is reached at $5.1\ \mu\text{m}$ Ti entrance window thickness and decreases afterwards. For these simulations, the energy spread of the incoming beam was neglected.

Discussion

The stopping efficiency inside the BGC was calculated by using the computer program TRIM. In the cases of At and Hg with a kinetic energy of 32(2) MeV, a maximum stopping efficiency of about 76% can be obtained (see Fig. 8.3a). In the case of Pb with a kinetic energy of 36(2) MeV, the maximum in stopping efficiency was probably not reached in the investigated range. In both cases, the stopping efficiency increases at lower Ti foil thicknesses before reaching the respective maximum. On the left-hand side from the maximum the stopping power of the ions is dominated by the gas pressure inside the BGC. This means, with an increasing of the gas pressure the

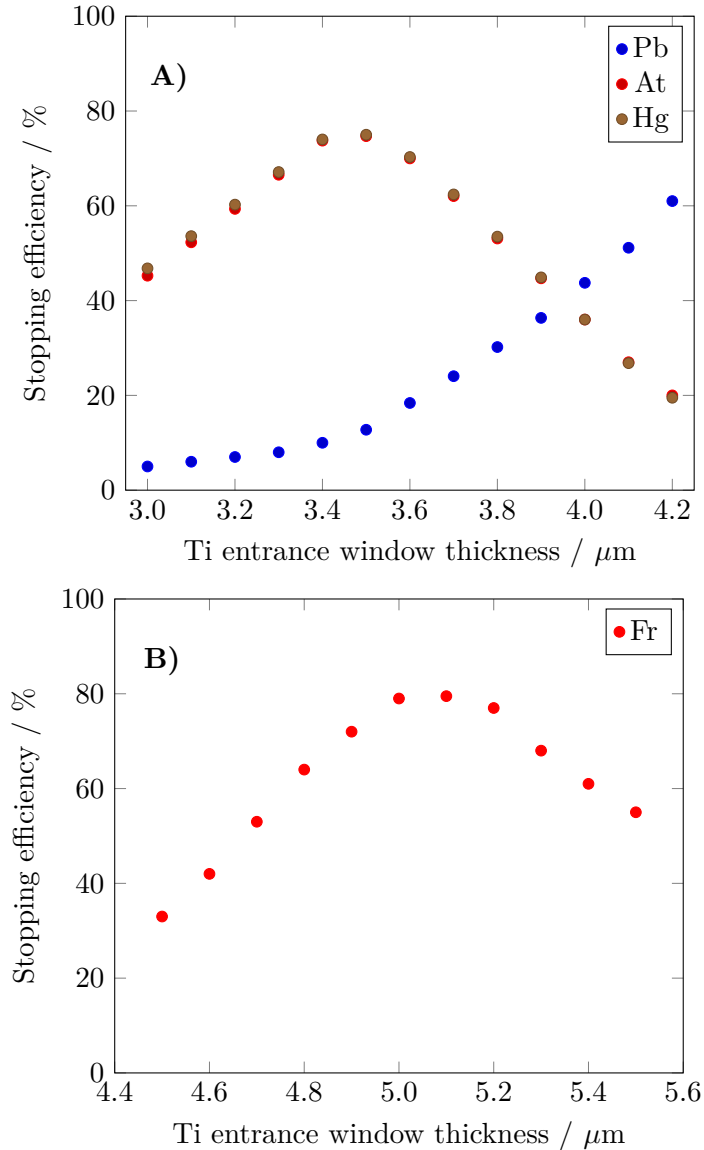


Fig. 8.3.: Dependence of the simulated stopping efficiency from the Ti entrance window thickness for (A) At, Pb and Hg and (B) for Fr ions.

maximum of the stopping efficiency can be increased and shifted to lower entrance window thicknesses [93]. With an increase of the buffer gas density in the BGC, the repulsive force that prevents ions from hitting the funnel electrode is dampened. On the right-handed side of the maximum, the continuous decrease of the stopping efficiency is due to the ion loss in the entrance window and a lower number of ions that enter the BGC. As can be seen from Fig. 8.3a, a Ti foil thickness of 3.5 μm is ideal for At and Hg. For the ^{40}Ar induced fusion reactions for At and Hg the maximum stopping efficiency can be used and only for Pb a low stopping efficiency will be expected.

In the ^{48}Ca induced fusion reaction behind TASCAs for Fr with a kinetic energy of 50(3) MeV a maximum extraction efficiency of 78% was obtained (see Fig. 8.3b).

Here, only one fusion reaction has to be considered that makes the choice of the optimal foil thickness easier. The entrance window thickness of $5.1 \mu\text{m}$ should result in the highest stopping efficiency in the TASCAs experiments.

8.2 Measurement methods

To measure and optimize the performance of the BGC a point-like recoil-ion source (see Sec. 6.1.2 and Sec. 6.1.1) is installed inside its stopping volume. In order to quantify the performance of the BGC the extraction efficiency (Sec. 8.2.1) and extraction time (Sec. 8.2.2) has to be determined, which is explained in the following sections.

8.2.1 Measurement of the extraction efficiency

The overall extraction efficiency in off-line experiments considers the probability to detect the α -decay of an recoiled ion from the respective recoil-ion source. This probability takes the in flight decay probability, the transport- and detection efficiency into account. The extraction efficiency ϵ_{extr} is given by the ratio of the number of ions reaching the COMPACT detector array $\dot{N}_{\text{Rn/Fr}}^{\text{extr}}$ to the number of ions $\dot{N}_{\text{Rn/Fr}}^{\text{recoil}}$ emitted into the stopping volume of the BGC from the recoil-ion source:

$$\epsilon_{\text{extr}} = \frac{\dot{N}_{\text{Rn/Fr}}^{\text{extr}}}{\dot{N}_{\text{Rn/Fr}}^{\text{recoil}}} . \quad (8.6)$$

For the emitted recoil-ions of the respective ion source, the time period t after the last activity measurement has to be considered. Eq. 8.7 takes all recoil losses due to α decay into consideration.

$$\dot{N}_{\text{Rn/Fr}}^{\text{recoil}} = \dot{N}^{\text{tot}} \cdot \exp\left(-\frac{\ln 2}{T_{1/2}}t\right) \quad (8.7)$$

The extracted ion rate ($\dot{N}_{\text{Rn/Fr}}^{\text{extr}}$) can be deduced from the activity measurement ($\dot{\alpha}_{\text{COM}}$) on the COMPACT detector array by

$$\dot{N}_{\text{Rn/Fr}}^{\text{extr}} = \frac{\dot{\alpha}_{\text{COM}}}{b_{\alpha} \cdot \epsilon_{\text{Det}}} \quad (8.8)$$

where $\epsilon_{\text{Det}} = 76(2)\%$ is the geometrical efficiency of the COMPACT detector array [49, 65] and b_{α} is the alpha branching ratio. The probability to detect an α -particle from a decaying nucleus inside the COMPACT array can be calculated from depositing probabilities and geometric probabilities. The deposition inside the COMPACT detector array can be separated into: (i) deposition on the active surface of the PIN diode, (ii) the atom was deposited on the nonactive detector surface or side of the gas channel. The probability of depositing on the respective surface (active or nonactive) is proportional to the surface area. The Eq. 8.8 is only valid, if all

extracted recoils were deposited inside the COMPACT detector array and none can leave the COMPACT detector array. This is only the case, if the studied element is non-volatile. In this case, the extracted species will adsorb on the detector surface and will then undergo the α decay. Rn, for example, is a noble gas and has only weak interaction strength with the respective detector surface. In this case, the extracted Rn can leave the COMPACT detector and is lost for a detection. The detection probability $P(t)$ to record an α -decay of such a nucleus is proportional to its residence time inside the COMPACT detector. The observation of an α -decay of the interested nuclei inside the active area of the detector array during its migration time is accounted by the decay probability. If the detection probability is linked to the number of ions released from the recoil-ion source, then the observable events on the COMPACT detector result. $P(t)$ of the ions as well as their decay products can be deduced from the residence time $\Delta t = t_2 - t_1$ spent in the COMPACT detector volume, where t_1 is the arrival time on detector 1 and t_2 is the arrival time on detector 16 (see [Sec. 9.2](#)) and the respective nuclear half-life $T_{1/2}$:

$$P(t) = \int_{t_1}^{t_2} \exp\left(-\frac{\ln 2 \cdot t}{T_{1/2}}\right) dt \quad . \quad (8.9)$$

The expected number of decays of the atoms of interest can be determined by using [Eq. 8.10](#).

$$\dot{N}_{\text{calc}} = \dot{N}_{\text{recoil}}^{\text{Rn}} \cdot P(t) \quad (8.10)$$

[Eq. 8.10](#) is only valid for the extraction efficiency measurement with the ^{223}Ra recoil ion source, which has an $\approx 100\%$ release probability (P_{release}) for the ^{219}Rn daughter. For the measurements with the ^{225}Ac recoil-ion source the finite P_{release} has to be taken into account instead of $P(t)$ (for details see [\[178\]](#)).

8.2.2 Measurement of the extraction time

The extraction time (source \rightarrow detector) is closely related to the survival probability of the studied isotope and hence its half-life of the investigated isotope. For this reason, the transport time is of particular importance for the successful extraction of short-lived isotopes. To measure the extraction time of ^{219}Rn recoil-ions, the ^{223}Ra source was operated in a pulsed mode. For this, the recoil-ion source could be set to different potentials V_{source} . The recoil-ion source is then repulsive for the emitted ions when V_{source} is positive (here, +250 V were applied) and the emitted recoil-ions are pushed away from the source. The recoil-ions can be extracted out of the BGC only during this 'open' phase of the source. The positive potential on the recoil source was chosen as 10 V higher than the the potential from the surrounding electric field from the DC cage electrodes. To 'close' the source to prohibit the release of recoil-ions, V_{source} was set to -10 V. In this case, the emitted ions will be attracted back to the source surface, which is attractive for the positive ions in the electric

field of the surrounding DC electrodes. A cyclic timing pattern of 20 ms open source is followed by 300 ms closed source, resulting in the release of ion beam pulses. The timing diagram of the measurement is shown in Fig. 8.4. This cycle was applied over a period of 10 hours. The released ions are thermalized and guided to the COMPACT array. The number of recoil-ions that reached the COMPACT detector array was recorded as a function of the extraction time t_{extr} of the recoil ions, which was defined as the time at which 50% of the released recoil-ions reached the COMPACT detector array. The different lifetimes of the emitted particles significantly increase the complexity of such extraction time measurements. This can be mitigated by only registering the decay-in-flight of non-adsorbed species that happen to decay during a flight over a certain detector. In this case, the radioisotopes act as indicator of gas volumes on their path through the BGC and miniCOMPACT.

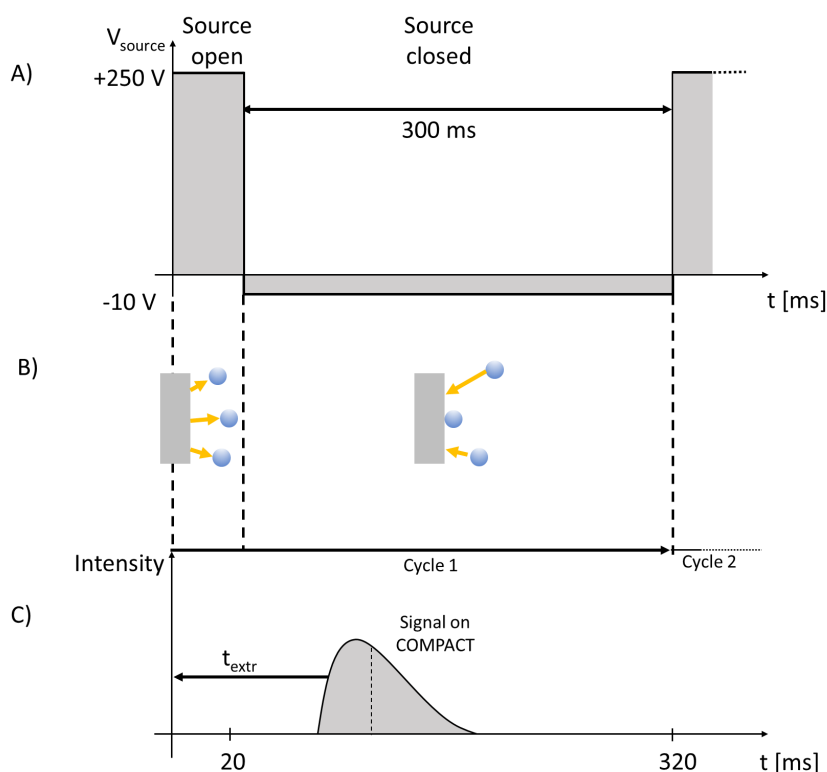


Fig. 8.4.: Timing diagram for the measurement of the extraction time t_{extr} . A) shows the applied voltage on the source in dependence of the time and B) give an overview of the trajectory of the recoil-ions. In C) the chromatogram in the COMPACT detectors is shown.

8.3 Experimental analysis of the BGC parameters

Fast and effective extractions methods are essential for gas-phase experiments with SHEs and are crucial for the chemical studies in one-atom-at-a-time experiments. The

optimization of the operating parameters, in particular the voltage difference between the last funnel electrode ($U_{\text{Funnel}_{\text{min}}}$) and the transition electrode (U_{TE}) as well as the DC gradient in the electrode system within the BGC (DC cage and funnel) together with the RF amplitude (\hat{U}_{RF}) is an important step towards a high extraction efficiency. The extraction efficiency of short-lived nuclides is closely linked to the extraction time, in particular for nuclides with half-lives in the range of the extraction time. For this reason, the extraction efficiency is of particular importance for the characterization of the BGC and is a central aspect in the preparation of experiments. An optimization of the operating parameters in view of the efficiency was performed for each of the following measurement series. In the following sections the optimization of the transition electrode (see [Sec. 8.3.3](#)), the operating RF amplitude in the funnel (see [Sec. 8.3.2](#)) and the DC gradient applied to the DC cage and funnel (see [Sec. 8.3.1](#)) will be briefly described.

8.3.1 Optimization of the DC gradient on the electrode system

In the work presented here, the gradient of the electric field ∇_{DC} along the DC cage was the same as that along the RF funnel. The electric field is thus homogeneous along the entire BGC. The recoil-ion source was inserted into the BGC at a fixed axial position 260 mm in front of the funnel exit. The pressure in the BGC was kept constant at 30 mbar at a helium gas-flow rate of $0.04 \text{ mbar L s}^{-1}$. The pressure inside the COMPACT detector was measured directly in front of the entrance into the array and was approximately 15 mbar. The funnel amplitude \hat{U}_{RF} was 130 V_{pp} peak to peak (PP). The extraction efficiency was determined with these operating parameters at different electrical field gradients (in the range of $5 - 9 \text{ V cm}^{-1}$) along the BGC. This optimization process was performed before each new series of experiments. This was used to check the reproducibility of the operating parameters and to ensure that the gas cell was operated under optimum conditions. The ^{223}Ra recoil-ion source was used and the decay products were measured with the SiO_2 -covered COMPACT.

Result

In [Fig. 8.5](#) the extraction efficiency is shown as a function of the applied DC gradient ∇_{DC} on the electrode system (DC cage and RF funnel). It can be seen that for an electric field gradient between 2.1 V cm^{-1} and 5.5 V cm^{-1} the extraction efficiency does not change significantly and is maximal at about 3.0 V cm^{-1} . The extraction efficiency decreases almost linearly as the DC gradient on the electrode system increases.

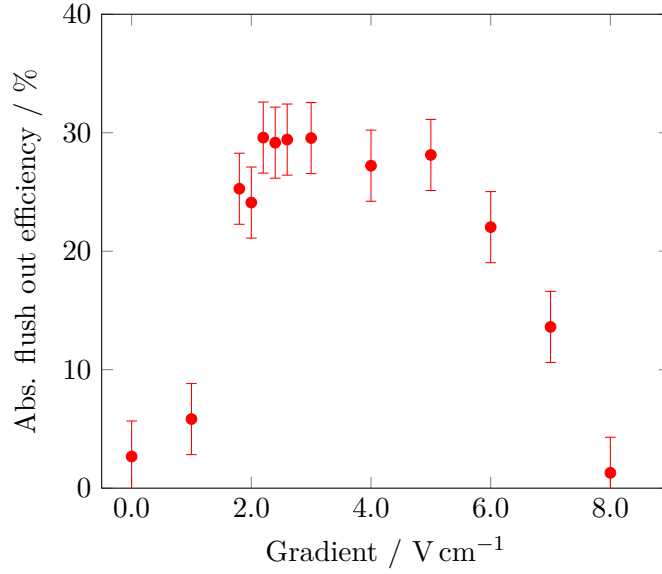


Fig. 8.5.: *Extraction efficiency of ^{219}Rn from the BGC as function of the DC gradient (∇_{DC}) applied on the electrode system.*

Discussion

In the range of 0 V cm^{-1} to 2 V cm^{-1} , the axial component of the repulsive force (F_{RF}), which was generated in the vicinity of the funnel electrodes, was greater than the accelerating force. However, that fact prevented the ions to be caught by the gas flow in the vicinity of the BGC exit so that they could be transported by the gas flow to the connected detector array. Only ions, which neutralized by collisions in the vicinity of the BGC could be extracted. For gradients larger than 2 V cm^{-1} , the superimposed effective repulsive force F_{RF} guides the ions towards funnel exit. The drop in the extraction efficiency after 5 V cm^{-1} is due to the fact that the speed of the ions through the electric field is so high that the repulsing force in the vicinity of the funnel electrode surface is no longer sufficient to avoid a collision of the ions with the electrode. This results in the drop in the extraction efficiency observed in Fig. 8.5. In principle, a larger gradient in the electric field would be possible if at the same time the repulsing force F_{RF} in the funnel is increased. The RF amplitude is limited by the increased probability of discharges (Paschen's law) between two adjacent ring electrodes [96, 109, 163], corresponding to the distance between two electrodes and the pressure inside the gas stop cell. Larger amplitudes can be reached with a change from a RF funnel system to a RF-carpet system [165, 184, 185], where spacing between two electrodes can be further decreased. Thereby, the repulsive force on the ions can be increased in presence of a higher DC gradient.

8.3.2 Optimization of the RF amplitude

The RF amplitude applied on the RF funnel was responsible for the repulsive force (F_{RF}), which was a local phenomenon in the near of the funnel electrodes. The provided repulsive force prevented ions from hitting the funnel electrodes. The effective F_{RF} led to a stable trajectory for the ions in the vicinity of the funnel electrodes. On this trajectory the ions were guided through the whole funnel to the BGC exit. The optimization of the RF amplitude was performed at three different gas pressures of 22, 39 and 60 mbar within the BGC.

Result

In Fig. 8.6 the extraction efficiency as a function of the RF amplitude is shown. A maximum extraction efficiency of 30(2)% was measured for the three different BGC pressures and a DC-field strength of 4 V cm^{-1} at the DC electrode and at the funnel electrode system, while a maximum RF amplitude of $120 \text{ V}_{\text{PP}}$ at 787 kHz was applied to the funnel electrodes.

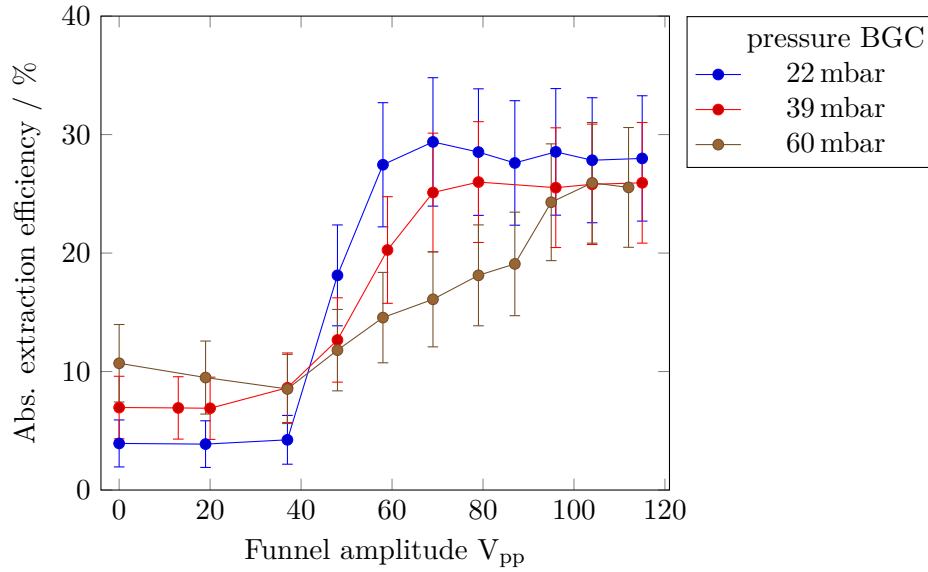


Fig. 8.6.: Extraction efficiency of ^{219}Rn from the BGC as a function RF amplitude of the RF funnel for 22, 39 and 60 mbar helium pressure inside the BGC.

The highest extraction efficiency about 30(2)% was reached for the He gas pressure of 22 mbar. In the case of 39 and 60 mbar the maximum about 25(2)% was almost identical. For lower RF amplitudes of 40 V_{PP} the higher pressure inside the BGC has the highest extraction efficiency around 10(1)%. The extraction efficiency decreased with lower pressures inside the BGC, which correspond to lower gas-flow rates. The inflection point was shifted with higher pressures to higher RF amplitudes on the funnel. Furthermore, the efficiency increased highly for lower BGC pressures and then flattened off for higher 60 mbar.

Discussion

In the range of funnel amplitudes below $40 V_{PP}$ the extraction efficiency is highest for higher pressures within the BGC. For higher gas densities in the funnel the repulsing force F_{RF} of the funnel is not sufficient to prevent collisions of the ions with the electrode surface. Accordingly, a drop in extraction efficiency would be expected for decreasing values of V_{pp} , but this is not observed. The reason for a higher extraction efficiency in the area of funnel amplitudes of less than $40 V_{PP}$ at higher gas pressures in the BGC is the fact that a larger number of neutral atoms can be extracted. The inflection point of the sigmoidal curve is shifted to higher funnel amplitudes for higher pressures because a larger repulsing force is required by a higher funnel amplitude. However, for a higher pseudo-potential close to the electrodes of the funnel, F_{RF} is sufficient to overcome the damping due to the increased gas density.

8.3.3 Influence of the voltage difference between last funnel electrode and transition electrode

The TE (see [Sec. 7.1](#)) had a unique position in the whole system, because it was responsible for the transition of the extracted ions from the ion transport inside the BGC into the gas-flow transport in the transport line. The extraction efficiency reacted sensitively on the applied voltages on the TE. Additionally, the TE has as a greater impact on the long-time stability for the transition of the ions into the transport line. The TE was only used in the combination of the BGC with the 'classic' COMPACT-array. With the introduction of the miniCOMPACT ([Sec. 7.2](#)), the TE was obsolete.

Results

The extraction efficiency of ^{219}Rn recoil-ions was measured as a function of the voltage difference $\Delta V_{\text{transition}}$ between the last funnel electrode ($U_{\text{Funnel}_{\text{min}}}$) and the TE (U_{TE}) or, in the case of the setup without TE, to the grounded Teflon transport line. The voltage on $U_{\text{Funnel}_{\text{min}}} = 5 \text{ V}$ was kept constant for the experiments with the TE.

The position of the recoil-ion source was fixed at 260 mm in front of the funnel exit. Moving the source along the central axis of the BGC has a negligible effect on the extraction efficiency [[97](#)]. This is, because the time scale of diffusion process is slower than the t_{drift} [[93](#)]. From [Fig. 8.7A](#) it can be seen that at $\Delta V_{\text{transition}} = U_{\text{TE}} - U_{\text{Funnel}_{\text{min}}}$ of 15 V to 35 V, a plateau is reached with a maximum extraction efficiency of 32(3)%. The extraction efficiency of about 30% is relatively constant over a wide voltage range. The efficiency response on the voltage difference becomes almost linear above 35 V. In [Fig. 8.7B](#) the influence of $\Delta V_{\text{transition}}$ with the TE on the extraction efficiency is investigated. Obviously, the optimum operating

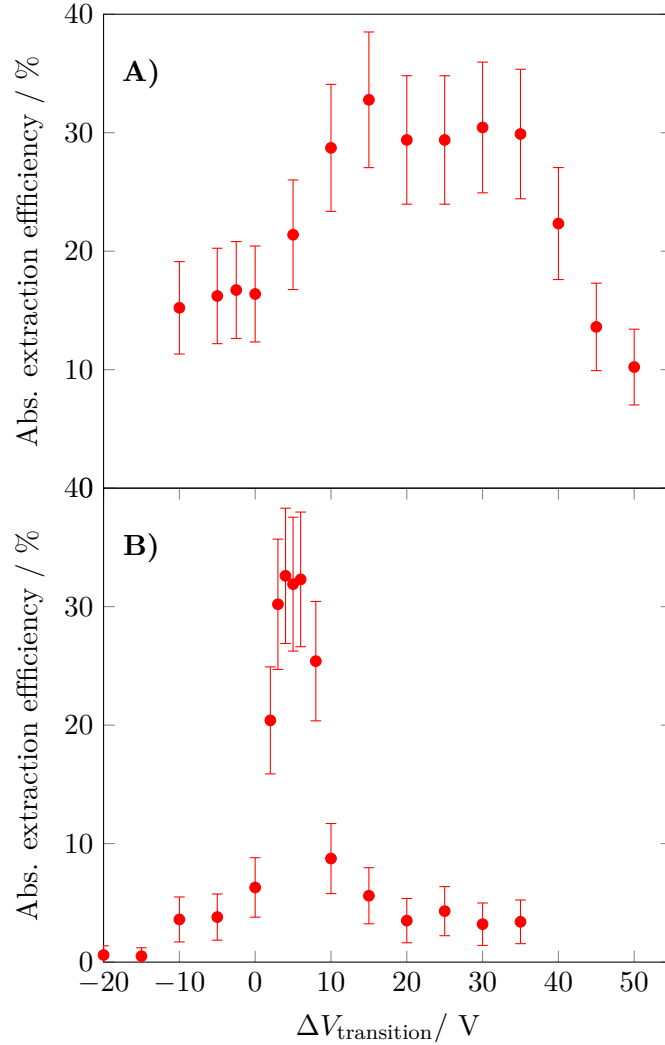


Fig. 8.7.: Investigation of the influence of $\Delta V_{\text{transition}}$ on the extraction efficiency of ^{219}Rn without TE (A) and with TE (B) for a \hat{U}_{RF} of $120V_{\text{PP}}$ at 796 kHz , $p_{\text{cell}} = 30 \text{ mbar}$ and a gradient of 8 V cm^{-1} .

range is significantly more narrow than for the transport line without the TE. The extraction efficiency shows a sharp increase around 2 V before reaching almost the same extraction efficiency of around 30%, similar to the situation shown in Fig. 8.7A. The maximum extraction efficiency is reached only between 4 V and 6 V. above 6 V the efficiency function shows a significant exponential decrease, asymptotically approaching a value of 5%. As already stated, the TE has a significant impact on the long-term stability of the used setup and is of great importance for the temporal stability of the count rate. Long-term fluctuations in the count rate reduce the reproducibility of the measured values, which has a negative impact on the determination of the BGC efficiency and on its overall performance in general. The achievable signal stability was investigated by time-resolved acquisition of the ^{219}Rn signal (see Fig. 8.8).

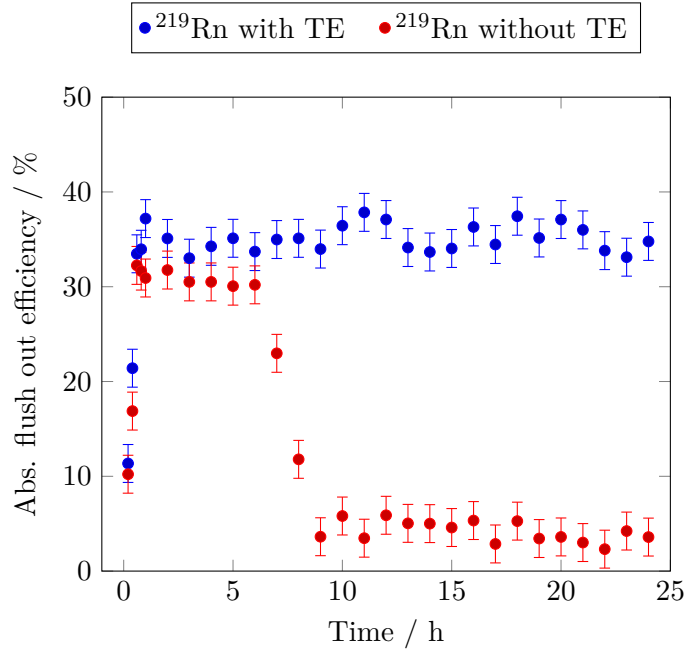


Fig. 8.8.: Long-term achievable ^{219}Rn signal stability on the COMPACT detector with TE (blue circles) or without TE (red circles).

In the setup without the TE, the extraction efficiency jumped from 22% to a maximum value of 32% during the first hour. This value was maintained for 5h, before the efficiency rapidly decreased to a stable value of 5%. The same significant increase of the extraction efficiency in the first hour was obtained in the setup with the TE (Fig. 8.8). In contrast to the setup without the TE, a relative standard deviation (RSD) of 3.7% at 35% over a period of 23 hours was achieved.

Another important parameter for the characterization of the transition electrode is the influence of the buffer gas pressure. The extraction efficiency was measured as a function of the gas pressure at a constant funnel amplitude ($U_{RF} = 130 \text{ V}_{pp}$), DC gradient ($\nabla_{DC} = 4 \text{ V cm}^{-1}$) and transition electrode potential ($U_{TE} = 5 \text{ V}$).

The relationship between the extraction efficiency and the gas pressure inside the BGC is shown in the Fig. 8.9. The influence of different buffer gas pressures on the funnel amplitude was reduced by optimizing the funnel amplitude to achieve comparable extracting efficiencies for all gas pressures tested. For gas pressures higher than 35 mbar, we see a decrease in extraction efficiency, whereas we observe a saturation in extraction efficiency of 32(7)% for gas pressures below 35 mbar.

Discussion

The voltage difference between the last funnel electrode and the transport line entrance or the TE, respectively, is responsible for a smooth transition from the BGC exit to the transport line and therefore one of the critical parameters of the setup. In the vicinity of the funnel exit the ions were handed over from the guided transport

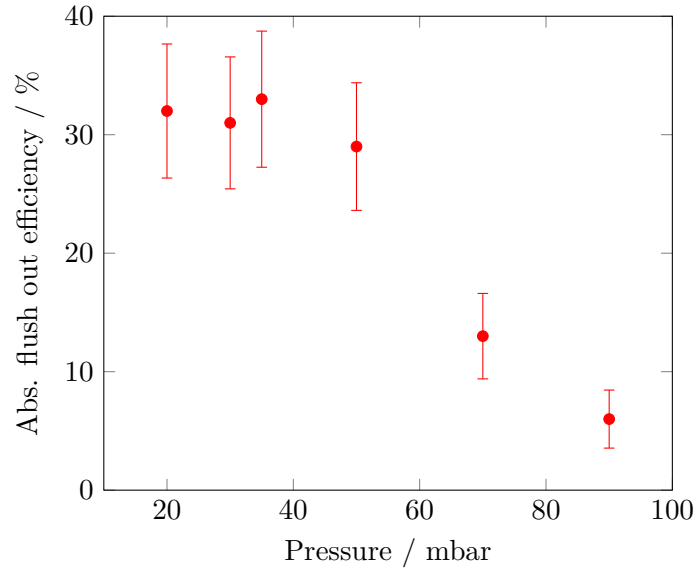


Fig. 8.9.: Investigation of the influence of the pressure on the extraction efficiency of ^{219}Rn ions on the BGC setup with TE.

via electric fields to transport via gas-flow. The ion velocity directly at the funnel exit determines the efficiency of the transition of the ion transport. In the combination of the BGC and COMPACT without the TE (see Fig. 8.7A) at voltage differences lower than 0 V, the extraction efficiency is around 15%. The passage of the ions through the funnel exit into the transport line entrance can be treated as an ion optic process. [96, 186]. The focusing mechanism relies on a delicate balance between the potential difference of the electrode together with the transport line entrance and the kinetic energy of the ions. At voltage differences lower than 0 V the potential difference exceeded the kinetic energy of the recoil-ions. In this case the ions were lost. Here, a small fraction of around 15% of the ions were transferred into the transport line. The reason for this result was that some ions could neutralize via collisions with the electrodes, and these neutral atoms were not affected by the electric field in the funnel. The used ^{219}Rn is volatile and can leave the electrode surface after the neutralization and be transferred with the gas-flow into the detector array. With an increase of the voltage difference to +10 V, the maximum extraction efficiency was reached. At the point when the ions reached the potential maximum, the electric field began to push the ions inward radially. The net effect is that the recoil-ions will slow down and spread inward radially. The degree of the inner radial force depends on the kinetic energy of the ions and the potential difference [96, 186]. If the radial force was sufficiently high, the resulting ion beam could be converged. Between +10 V and +35 V the electric field is sufficiently strong for the ions to be extracted into the entrance area of the transport line. Fig. 8.7A shows a falling extraction efficiency to higher positive voltage differences. In this voltage area, the recoil-ions are too fast to be thermalized in the gas atmosphere. Therefore, the ions will continue to

follow the electric field lines and encounter the wall at the entrance of the transport line and this leads to a loss of ions. As seen in Fig. 8.7A, the voltage difference $\Delta V_{\text{transition}}$ between 15 V to 35 V was ideal for extraction efficiency measurements without the TE. The Fig. 8.7B shows the influence of the new transition electrode on the extraction efficiency. Here, the optimum operating range is significantly narrower than for the transport line without this TE. The transition of the ions into the gas flow and transfer into the transport line is susceptible to $\Delta V_{\text{transition}}$ for this setup. This combination of funnel exit and TE result in a higher value of defocusing with an increasing voltage difference from the optimum value around 5 V. After +7 V, the extraction efficiency breaks down rapidly, because the ions are accelerated to the more negative transition electrode with respect to the last funnel electrode and adsorb there. The optimal operating range of $\Delta V_{\text{transition}}$ for the combination was between 3 and 7 V as shown in Fig. 8.7B. Since the focusing was a delicate balance between the potential difference and the kinetic energy, it should be mentioned that a kinetic energy spread of the ion beam has a negative impact. In the case of the use of recoil-ion sources, the kinetic energy spread is relatively low. The picture changes when the setup described here was used in on-line experiments. In this case the energy spread has to be considered and the optimum setting for the voltage difference has to be found for each experiment separately. The observation in Fig. 8.9 shows that for high gas velocities, the potential at the transition electrode is insufficient to guide the ions through the funnel exit into the transport line. This leads to a loss in the extraction efficiency by a factor of 6 for a gas pressure of 90 mbar. The reason for this result was that ion collisions with the buffer gas will cause changes in direction and velocity of the ions.

The introduction of the TE showed no appreciable differences in the extraction efficiency compared to the setup without the TE, except that the TE was more sensitive to the voltage difference. Seen in this light, the results show no positive impact on the extraction efficiency. But Fig. 8.8 shows that the TE has a positive influence on the long-term stability of the setup. Long-term fluctuations in the count rate reduce the reproducibility of the measured values, which has a negative impact on the determination of the BGC efficiency and on its overall performance in general. The stability and reproducibility of the BGC, in particular, is relevant in on-line experiments. Here, the beam time is often limited. The relative standard deviation (RSD) of 3.7% over a period of 23 hours is achieved after a short stabilization phase to reach standard conditions. The efficiency drop for the setup without the TE in Fig. 8.8 could be explained by a slow charging up of the Teflon tube. During the operation time, neutralization processes occurred on the Teflon tube in the entrance area of the transport line. The remaining positive charge led to a positive charging up in the entrance area of the transport line over the operating time (≈ 6 h) and to a blocking potential in front of the entrance. A similar effect was observed when a potential difference was applied on the TE and last funnel electrode, which exceeded

the kinetic energy of the ions. This effect prevented the ions from entering the transport line. Only neutral atoms, which were not affected by the blocking potential could reach the detector array through the Teflon tube.

The off-line experiments with the ^{223}Ra and ^{225}Ac recoil-ion source were performed in separate experiments starting in February 2016 and finishing in July 2019. The used recoil-ion sources are described in [Sec. 6.1](#), and in [Tab. 6.1](#) the parameters of the ^{223}Ra and ^{225}Ac recoil-ion sources are summarized. The use of the recoil-ion source has the advantage that the experiments could be performed independent from the availability of beamtime. Additionally, the recoil-ion source is a useful tool to prepare the BGC for upcoming on-line experiments. The current section presents all off-line experiments and their results. The experiments in the present thesis are subdivided into the GSI off-line experiments with the use of ^{223}Ra or ^{225}Ac recoil-ion source (this chapter), and the on-line experiments at the MARS spectrometer or the TASCA preseparator (see [Chap. 10](#)). Here, the off-line experiments at GSI Helmholtzzentrum für Schwerionenforschung GmbH (Darmstadt, Germany) are presented and show the measured extraction efficiencies in [Sec. 9.1](#) and the transport time in [Sec. 9.2](#).

9.1 Extraction efficiency measurement

The extraction efficiency measurements were performed with the ^{223}Ra and the ^{225}Ac recoil-ion sources. Before each measurement series the BGC performance was checked and the optimal settings for the maximum extraction efficiency were used. The preliminary investigation for the optimization of the BGC were described in [Chap. 8](#). The optimal settings for the BGC were summarized in [Tab. 6.4](#).

9.1.1 Result

The α -spectrum recorded in the COMPACT detector array when ^{219}Rn ions were extracted is shown in [Fig. 9.1B](#). This looks similar to that of [Fig. 6.7B](#) obtained in the calibration measurement except for the missing α -lines of the mother, ^{223}Ra , in [Fig. 9.1B](#). The ^{215}Po peak is well separated from that of ^{219}Rn , whereas, the ^{219}Rn one is not fully resolved and has an overlap with that of ^{211}Bi . Therefore, the use of ^{219}Rn for the extraction efficiency has a significantly higher inaccuracy than its daughter ^{215}Po . The half-life of only 1.8 ms is short compared to the retention time (in the order of several hundred ms) so ^{219}Po will not escape the COMPACT detector. For this reason, ^{215}Po can be used for the extraction efficiency determination for the ^{223}Ra recoil-ion source.

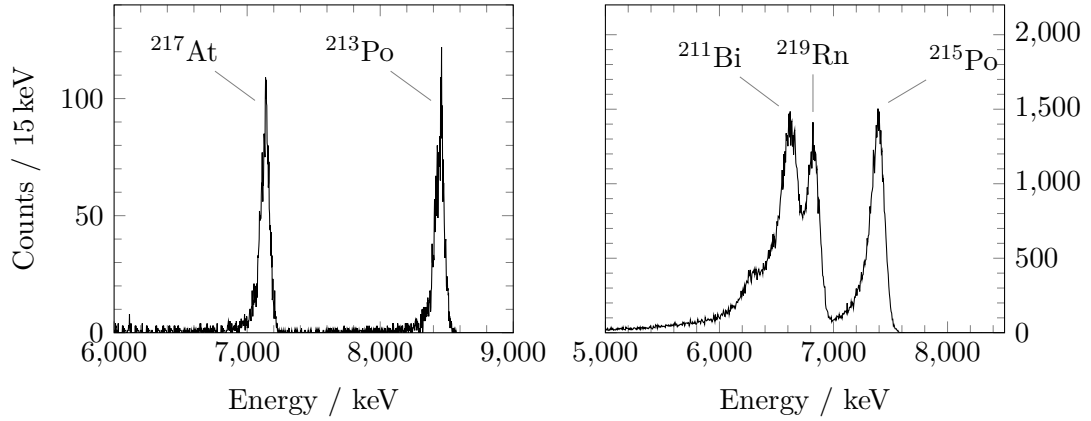


Fig. 9.1.: α -decay spectra of the extracted daughters of ^{221}Fr (A) and ^{219}Rn (B) ions and their decay products measured with COMPACT.

A typical α -spectrum obtained from extracted ^{221}Fr ions is shown in Fig. 9.1A. The spectrum is similar to that shown in Fig. 6.7A, except that the α -lines of ^{221}Fr and its mother ^{225}Ac are absent. In the spectrum of the ^{225}Ac recoil source on the COMPACT detector, only ^{217}At and ^{213}Po are present. In order to investigate this matter further, a Monte Carlo simulation (MCS) of the migration process of the species through a Teflon transport line based on the model developed by Zvara [121, 128] was performed. This procedure was repeated for different values of $-\Delta H_{\text{ads}}$, and the simulated fraction of released Fr and Rn atoms was recorded. Fig. 9.3 and Fig. 9.2 show the simulated distribution of ^{219}Rn and ^{221}Fr , respectively.

In Fig. 9.2 is the distribution patterns from the MCS of ^{221}Fr shown. The distribution pattern shows over the shown range an exponential decrease. In contrast to this result, the distribution pattern ^{219}Rn in the Teflon transport line and the COMPACT detector shows an even distribution. ΔH_{ads} for Rn was determined by using a two-column approach with MC simulations, with the first column representing the transport line (Fig. 9.3 A) and the second the COMPACT detector (Fig. 9.3 B). The starting value for the simulated atoms in the transport line is chosen based on the release rate of the recoil-ion source (see Tab. 6.1). With these boundary conditions, an MC simulation can be performed, which yields the fraction of atoms that reach the COMPACT detector as a function of ΔH_{ads} . This rate is known from the experimental measurements. The experimental data in Fig. 9.3 shows a statistical distribution. ^{219}Rn has a high survival probability inside the Teflon transport line and the COMPACT detector, since only a small fraction of the ^{219}Rn decays during the short time spent inside the COMPACT detector.

The overall extraction efficiency $\epsilon_{\text{overall}}$ can be determined for a volatile as well as for a non-volatile element, respectively. Therefore, the respective characterized recoil-ion source was used. $\epsilon_{\text{overall}}$ is the product of the extraction efficiency of the BGC ϵ_{cell}

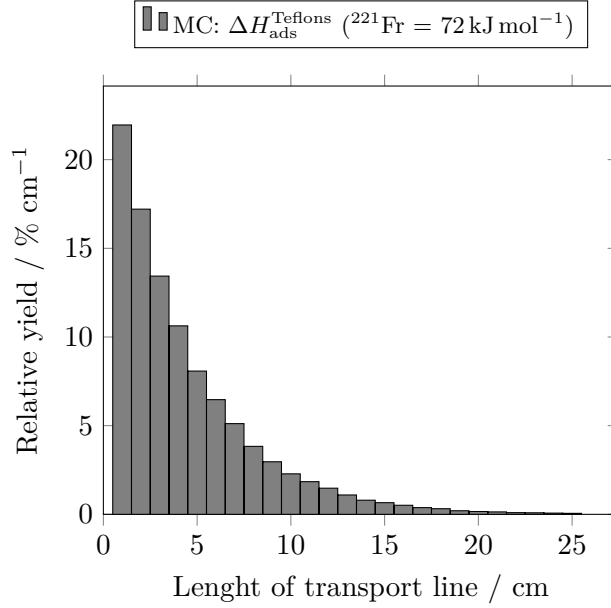


Fig. 9.2.: Distribution patterns from the MCS of ^{221}Fr in pure He gas in the Teflon transport line. The pressure inside the Teflon capillary was about 40 mbar. The value of $-\Delta H_{\text{ads}}^{\text{Teflon}}$ represents a lower limit, see text for a detailed discussion.

(source \rightarrow BGC exit), the transport efficiency ϵ_{trans} (transport line entrance \rightarrow COMPACT) through the transport line, and the detection efficiency ϵ_{det} . Here, we assume that the extraction efficiency is independent from the axial source position inside the BGC. The overall extraction efficiency can be deduced from the ratio of detected \dot{N}_{det} and emitted recoil-ions \dot{N}_{recoil}

$$\epsilon_{\text{overall}} = \frac{\dot{N}_{\text{det}}}{\dot{N}_{\text{recoil}}} \cdot b_{\alpha} = \epsilon_{\text{cell}} \epsilon_{\text{trans}} \epsilon_{\text{det}} \quad (9.1)$$

The results of the measurements of $\epsilon_{\text{overall}}$ are summarized in [Tab. 9.1](#). Because ^{221}Fr was not extracted, the α -decay daughter ^{217}At was investigated. Therefore, the ^{225}Ac source was pulsed (1 min on / 15 min off). This ensured that the increase in count rate for ^{217}At came directly from the recoil-ion source and not from the decay of daughters of ^{221}Fr adsorbed within the transport line. After the end of the 15 minute off phase (threefold half-life of ^{221}Fr) the background rate was $\approx 0.5\text{s}^{-1}$. The detection limit for ^{217}At is assured due to the low background (1σ confidence interval). The overall extraction of ^{219}Rn from the BGC as determined with the use of the ^{223}Ra recoil-ion source is 35(3)%. The ^{221}Fr ions cannot be extracted when the transport line is present; only the daughter, ^{217}At , can be extracted directly with an overall efficiency of 8(3)%.

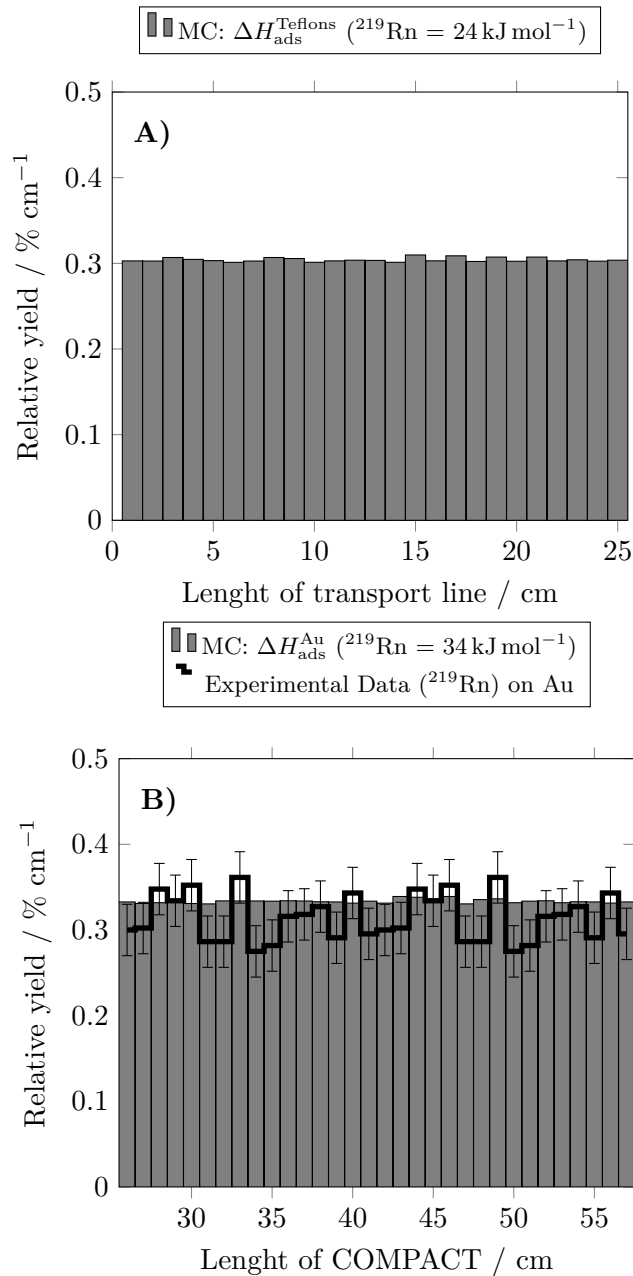


Fig. 9.3.: Distribution patterns of ^{219}Rn in pure He gas (A) in the Teflon transport line and (B) on the Au-covered COMPACT detector array. The pressure inside the Teflon transport line and inside the COMPACT detector array was about 40 mbar. The solid line in Fig. 9.3B represents experimental data. The gray bar histograms are the results of Monte Carlo simulations using the values for $\Delta H_{\text{ads}} (^{219}\text{Rn})$ indicated in the panels. For adsorption on Teflon, panel A, the value of -24 kJ/mol gives the best agreement; no substantial change is observed for values up to -30 kJ/mol . The value for adsorption on gold in panel B is taken from [187].

Tab. 9.1.: BGC efficiency studied with the recoil-ion sources ^{223}Ra and ^{225}Ac , together with the efficiencies for the extraction, transport, and detection. ϵ_{det} has been taken from [49] and ϵ_{extr} can be deduced from Eq. 9.1. \dot{N}_{det} is calculated with Eq. 8.10 and the transport times are $t_1 = 75\text{ ms}$ (detector 1) and $t_2 = 160\text{ ms}$ (detector 16). The He flow rate was $0.04\text{ mbar L s}^{-1}$ and the pressure inside the BGC was 30 mbar . The funnel amplitude was 120 V_{pp} .

	\dot{N}_{recoil}	\dot{N}_{det}	$\epsilon_{\text{overall}}$	ϵ_{cell}	ϵ_{trans}	ϵ_{det}
^{219}Rn	953 s^{-1}	334 s^{-1}	35(3)%	47(6)%	99(1)%	76(2)%
^{221}Fr	74 s^{-1}	0 s^{-1}	0%	–	0%	76(2)%
^{217}At	74 s^{-1}	6 s^{-1}	8(3)%	36(5)%	27(6)%	76(2)%

9.1.2 Discussion

The different behavior in adsorption enthalpy is due to the chemical behavior. ^{219}Rn is a noble gas and has only weak interaction strength with the Teflon or COMPACT surface, in contrast to ^{221}Fr . This fact is shown in the adsorption enthalpy of ^{219}Rn compared to ^{221}Fr . The adsorption enthalpy $-\Delta H_{\text{ads}}$ of ^{219}Rn on Teflon is $-\Delta H_{\text{ads}} = 24\text{ kJ mol}^{-1}$ and for ^{221}Fr is $-\Delta H_{\text{ads}} = 72\text{ kJ mol}^{-1}$. Apparently, Rn ions convert to volatile Rn atoms, which pass the transport line and reach the COMPACT array, whereas both, Fr ions and atoms interact strongly with any surface that is encountered prior to reaching the COMPACT detector array and are thus retained. A likely scenario is that Fr ions encounter the Teflon surface in the transport line. This prevents their extraction. The uniform distribution of ^{219}Rn along the transport line in Fig. 9.3A is caused by decay in-flight during the migration along the Teflon capillary. The simulated distribution pattern of ^{219}Rn on the Au-covered COMPACT is shown in Fig. 9.3B. Fig. 9.2 shows the simulation with the lowest value at which all the Fr atoms adsorb during the migration along the Teflon capillary, leading to a complete loss of ^{221}Fr inside the capillary. This leads to the lower limit of $-\Delta H_{\text{ads}} = 72\text{ kJ mol}^{-1}$. The absence of ^{221}Fr in Fig. 9.1, i.e., the ion emitted from the ^{225}Ac source shows that non-volatile atoms cannot be extracted with the setup described here. The MC simulations support the assumption that ^{221}Fr is lost due to the strong interaction in the Teflon capillary. The extraction of francium from the 250 mm transport line was not possible, therefore the extraction time measurement and the characterization of the BGC were performed with the ^{219}Rn recoil-ion source. The overall extraction efficiency of ^{219}Rn from the BGC as given in Tab. 9.1 is 4 times higher than for ^{217}At . The reason for this result is the low transport efficiency of only 27(6)% compared to 99(1)% for ^{219}Rn . Furthermore, ϵ_{cell} is significantly lower for At than for Rn. That result indicates that a significant number of At ions cannot reach the COMPACT detector, due to the adsorption of the mother Fr inside the BGC. From there, the half-life of the At ions ($T_{1/2} (^{217}\text{At}) = 32\text{ ms}$) is too short to reach the detector array. Therefore, only ^{217}At ions from the decay close

to the detector array entrance are able to enter the active area of the COMPACT detector. The transport losses in the Teflon transport line depend on the in flight decay probability and in the case of Fr additionally on the adsorption strength. The survival probability can be calculated from the known transport time in the gas-flow. The transport time was measured with ^{219}Rn , see [Sec. 9.2](#). For ^{217}At the half-life is significantly shorter than the transport time. The low transport efficiency shows that the transport line prevented an effective transfer of non-volatile elements. For these reason, in further experiments (see [Sec. 10.2.4](#)) with non-volatile elements, the transport line was completely removed and a new version of the COMPACT detector (miniCOMPACT) was introduced (see [Sec. 7.2](#)). Our extraction efficiency ϵ_{cell} of volatile ^{219}Rn is in agreement with the values in [\[92\]](#). The modification of the interface between the BGC and the subsequent COMPACT detector array has a negligible influence on ϵ_{cell} . The combination of the BGC with the chromatographic unit COMPACT in the current configuration is suitable for on-line experiments with volatile reaction products from fusion evaporation reactions. The situation is quite different for the extraction of non-volatile elements like ^{221}Fr , though. These are completely lost in the Teflon capillary. The less reactive daughter of Fr, the At, can be extracted in similar amounts like Rn (see [Tab. 9.1](#)).

9.2 Extraction time measurement

The extraction time was measured by the time-stamped detection of the ^{219}Rn α -decay via the non-volatile and short-lived daughter nucleus ^{215}Po on the COMPACT detector (see [Fig. 9.4](#)). The measurement methodology is described in detail in [Sec. 8.2.2](#). As already mentioned, the extraction time measurement was performed only with the ^{223}Ra recoil-ion source due to the fact that in experiments with the ^{225}Ac recoil-ion source the first daughter ^{221}Fr could not be extracted. For the extraction time measurements, the setup with the COMPACT detector and the 250 mm transport line was used.

9.2.1 Result

In [Fig. 9.4](#) is the number of ^{215}Po α decays as function of the delay between the recoil ion source and the arrival time at the PIN diodes of the first and last COMPACT detector in one array is shown. The time difference between the first and the last detector in one of the arrays will describe the retention time of the released ion package of the recoil source through the COMPACT detector array. The released ion package from the recoil-ion source reached the first PIN diode of the COMPACT detector after a delay of about 55 ms. The here shown delay time is when 50% of the respective atoms are flushed to the respective PIN diode of the COMPACT detector. The last PIN diode in one COMPACT array is reached after 125 ms after the release from the ^{223}Ra recoil-ion source. Of particular note in [Fig. 9.4](#) is that the back

tailing is increasing from the first PIN diode to the last PIN diode on the COMPACT detector array. In contrast, the rising flank of the number of decays does not show a pronounced tailing in either case. Additionally, the extraction time from the BGC

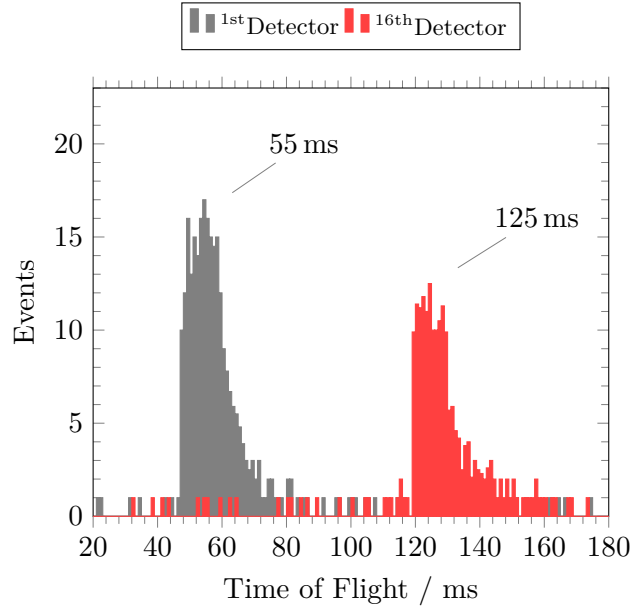


Fig. 9.4.: Number of ^{215}Po α decays as function of the delay between ion source release and the arrival at the PIN diodes of the COMPACT array.

was investigated in relation to the gas-flow rate in the BGC. The gas-flow rate has an influence on the transport time through the transport line after the ions were picked up by the gas-flow in the vicinity of the funnel exit. Fig. 9.5 shows the extraction time t_{extr} of ^{215}Po -recoil ions from the source to the first COMPACT detector as a function of the gas-flow rate.

The total extraction time from the recoil source to the first COMPACT PIN diode shows an exponential decrease with an increase of the gas-flow rate, and approaches a threshold value of around 55 ms ($t_{\text{extr}} = t_{\text{cell}} + t_{\text{trans}}$). The total extraction time t_{extr} comprises the extraction time of the BGC t_{cell} and the transport time t_{trans} via gas flow through the transport line, both of which are shown in Fig. 9.5. The threshold value of the exponential decay of t_{trans} is around 40 ms (flow rate $> 0.10 \text{ mbar L s}^{-1}$). The extraction time out of the BGC t_{cell} is increasing with raising gas-flow rate.

9.2.2 Discussion

For volatile elements such as Rn, an exact measurement of the residence times i) in the BGC (t_{extr}), ii) in the transport line (t_{trans}) and iii) in the COMPACT detector array (t_{COM}) is necessary for the efficiency determination. The sum of retention times in the BGC and transport line is the arrival time at the first COMPACT PIN diode. The transport time of the ion packet through the COMPACT detector can be determined from the difference in arrival times of the ^{219}Rn package at the positions

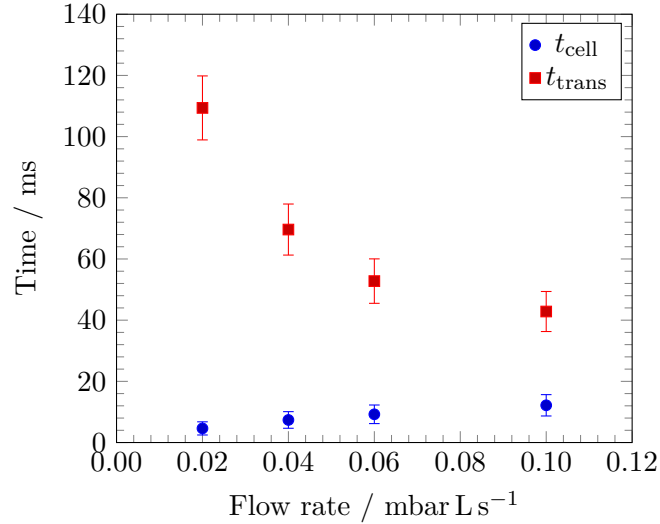


Fig. 9.5.: Extraction time t_{extr} from the BGC (source \rightarrow COMPACT detector) and transport times t_{trans} of the ion packet through the transport line. t_{cell} was calculated with Eq. 9.2.

of detectors 1 and 16 (see Fig. 9.4). The flight time t_{flight} of the ^{219}Rn at a flow rate of $0.1 \text{ mbar L s}^{-1}$ is $55(4) \text{ ms}$. The velocity \vec{v} of the ions in the BGC volume is proportional to the field strength of the electric field \vec{E} under these conditions: $\vec{v} = K \cdot \vec{E}$, with k being the ion mobility, $K = K_0 \frac{p_0 \cdot T}{p \cdot T_0}$ [97]. Then, the following equation results for the extraction time

$$t_{\text{ext,cell}} = \frac{d_{\text{pos}} T_0 p}{K_0 T p_0 E} \quad (9.2)$$

Here $d_{\text{pos}} = 250 \text{ mm}$ is the distance the ions travel through the DC-cage and DC funnel. $T_0 = 273.15 \text{ K}$ and $p_0 = 1013.25 \text{ mbar}$ are standard temperature and pressure. The reduced ion mobility of Rn ions in helium in an electrical field is taken as $K_0 = 17.37 \text{ cm}^2 \text{ V}^{-1} \text{ s}^{-1}$ from [188]. The transport time of the ion package can then be determined from the measured time difference of the mean Time-of-Flight (ToF) from the source to the first PIN diode of the COMPACT detector. This transport time is dependent on the gas-flow rate and the retention time within the transport line. The extraction time t_{extr} decreases with increasing He gas-flow rate, see Fig. 9.5, while t_{cell} of the ions from the BGC to the entrance of the transport line increases due to an increased pressure inside the BGC (Eq. 9.2). Nevertheless even at the highest gas-flow rate investigated, for which the pressure is already at the limit for a proper operation of the RF funnel, the t_{cell} contributes less than 20% to t_{extr} . The shortest measured t_{cell} with $p_{\text{cell}} = 30 \text{ mbar}$ was $9.8(7) \text{ ms}$ [92]. This is slightly longer than the calculated value of 7.3 ms . The deviation could be due to uncertainties in the K_0 or the real field strength in the RF-funnel and DC cage. The main extraction time limitation arises from the gas-flow transport and thus from the length of the capillary.

At the lowest gas-flow rate of $0.02 \text{ mbar L s}^{-1}$, a t_{extr} of about $112(8) \text{ ms}$ is reached, which is reduced to $55(4) \text{ ms}$ with an increase in gas-flow rate to $0.10 \text{ mbar L s}^{-1}$. A gas-flow rate of $0.10 \text{ mbar L s}^{-1}$ leads to a pressure of approximately $p_{\text{cell}} = 90 \text{ mbar}$ in BGC. The square diffusion coefficient $\langle r^2 \rangle$ describes the migration of the ions in a gas-filled medium and allows calculating the radial distance that the ions travel within a given time t [189], which is given by

$$\langle r^2 \rangle = 3Dt \quad (9.3)$$

where D is the diffusion coefficient. This is dependent on the ion mobility K , the Boltzmann constant k_b , the absolute temperature T , and the elementary charge e , according to

$$D = \frac{Kk_bT}{e} \quad (9.4)$$

For the diffusion of ^{219}Rn ions in He gas at a pressure of 30.5 mbar at 298 K , D is $1.5 \cdot 10^{-3} \text{ m}^2 \text{ s}^{-1}$. Within the slowest t_{cell} of 12.7 ms and the fastest $t_{\text{cell}} = 4.9 \text{ ms}$ (He flow rate of $0.10 \text{ mbar L s}^{-1}$ and $0.02 \text{ mbar L s}^{-1}$, respectively), the ions hence diffuse over a radial distance of about 8 mm (5 mm) at a gas-flow rate of $0.10 \text{ mbar L s}^{-1}$ ($0.02 \text{ mbar L s}^{-1}$). Wall collisions due to radial diffusion are therefore not expected to occur in the area of the DC cage, but may occur within the last funnel electrodes depending on the \hat{U}_{RF} . The neutralization of the ions by wall collisions is beneficial for the subsequent gas-phase chromatography process, and will ideally take place in the area of the last funnel electrodes, where the gas velocities are 900 m s^{-1} [190], so that the neutralized ^{219}Rn atoms can still be effectively extracted. The ions that have not been neutralized by this point are neutralized by the wall collisions in the Teflon capillary of the transport line, via an electron pickup on the Teflon capillary. The lowest measured transport time t_{extr} of ^{219}Rn ions is $55(4) \text{ ms}$. This is about one order of magnitude shorter than the shortest transport times achievable with RTC-based setups, and opens a perspective for chemistry studies of nuclides with half-lives of only few tens of milliseconds. A further reduction of the transport time is possible by removing the complete transport line. This will be possible, but requires a redesign of the interface between the funnel exit and the COMPACT entrance. With this improvement, the extraction time t_{extr} should only depend on t_{cell} ($t_{\text{extr}} \approx t_{\text{cell}} \approx 10 - 15 \text{ ms}$). In addition, losses of reactive species are expected to be reduced.

9.3 Summary

The BGC-COMPACT combination was characterized by extraction measurements of ions emitted by point-like recoil-ion sources installed inside the BGC. An maximum extraction efficiency of $35(3)\%$ was obtained. The extraction efficiency is 3 times higher in comparison to the off-line experiments with this BGC at SHIPTRAP [92,

93]. For volatile species, the overall efficiency is limited mainly by the poor stopping efficiency of the produced ions in the stopping volume of the BGC at lower He gas pressures. For the chemistry experiments a new interface between the funnel exit and the COMPACT detector array was implemented. With this interface a smooth transition from the ion-guided section into the laminar-flow section was possible. The voltage applied at this TE was found to be a critical parameter. The coupling of the BGC with the COMPACT detector allows an extraction time as short as 55(4) ms, which is short enough to open principal perspectives for chemical studies of SHE beyond element $Z = 114$.

In the 250 mm-long transport line, wall collisions occur. This leads to substantial losses in the case of chemically reactive species. In the current setup, this limits the chemistry experiments to studies of volatile elements.

The current section presents the experimental data obtained in the chemistry experiments with the ^{40}Ar - (see Sec. 10.1) and the ^{48}Ca -beam (see Sec. 10.2). The MARS chemistry experiments at the Cyclotron Institute at Texas A&M (College Station, USA) used the ^{40}Ar -induced reactions on ^{152}Gd , ^{165}Ho and $^{144,147}\text{Sm}$, whereas the TASCA experiments at GSI used the reaction $^{48}\text{Ca} + ^{165}\text{Ho}$. In the experiments described in this section, a high extraction efficiency and sensitivity is the key to get access to experiments with the heaviest elements of the PTE.

The production and separation of the element of interest is performed by using MARS or TASCA as a pre-separator. The recoiling ERs from the separator are thermalized in 30–70 mbar gas volume, the BGC, and guided to the exit by a DC-field gradient (see Fig. 6.1). An RF funnel, which produces a repelling force to prevent the ions from hitting the surface, is installed at the end of the BGC to focus the ions towards the exit hole. The BGC is described in Sec. 6.3. After the funnel exit, the ERs are injected into COMPACT-type detector arrays (see Sec. 7.2). The BGC-COMPACT setup is flushed with He gas, kept at a pressure of 30–70 mbar to ensure viscous flow.

Tab. 10.1.: List of the used ^{152}Gd , ^{165}Ho , and $^{144,147}\text{Sm}$ targets. The target composition and thickness as well as the backing thickness are given. The targets were prepared by Thermal Evaporation (TE) [155] or Molecular Plating (MP) [191].

Target	Isotope composition	Backing thickness (μm)	Target density ($\mu\text{g} / \text{cm}^2$)	Prep. method	Exp.
^{152}Gd	(35% ^{152}Gd , 16% ^{158}Gd , 13% ^{156}Gd , 14% ^{160}Gd , 10% ^{157}Gd , 10% ^{155}Gd)	2	460	MP	MARS
^{165}Ho	(100% ^{165}Ho)	1	300	TE	MARS
$^{144,147}\text{Sm}$	(50% ^{144}Sm , 50% ^{147}Sm)	2	600	TE	MARS
^{165}Ho	(100% ^{165}Ho)	2.3 or 7.3 ¹	395	TE	TASCA

¹2.3 μm -thick Ti-backing and 5 μm -thick Ti-degrader

10.1 On-line chemistry experiments behind the MARS spectrometer

A first exploratory experiment was performed at the Cyclotron Institute at Texas A&M University (College Station, TX, USA) behind the MARS spectrometer [148, 162]. The reactions using the ^{40}Ar projectile were performed during a six-day irradiation in May of 2017. The first two days were typically used for beam adjustments and calibrations. The remainder of the beamtime was reserved for extraction efficiency experiments with the COMPACT detector in combination with the transport line. On this occasion, the ^{152}Gd , ^{165}Ho and $^{144,147}\text{Sm}$ targets were irradiated to measure the extraction efficiency of the BGC presented in this work. A summary of the used targets is given in Tab. 10.1.

10.1.1 Experiments behind MARS

The BGC was mounted in the focal plane (FP) of MARS [148, 162] with the COMPACT array connected to the outlet of the BGC. Short-lived α -decaying radionuclides were produced in the nuclear reactions $^{165}\text{Ho}(^{40}\text{Ar}, 4-6\text{n})^{199-201}\text{At}$, $^{144}\text{Sm}(^{40}\text{Ar}, 4\text{n})^{180}\text{Hg}$ and $^{147}\text{Sm}(^{40}\text{Ar}, 4-5\text{n})^{182,183}\text{Hg}$. A continuous $^{40}\text{Ar}^{5+}$ ion-beam was accelerated with the K-500 cyclotron at the Cyclotron Institute at Texas A&M University to beam energies (E_{Lab}) of 217 MeV and 219 MeV. Beams at 219 MeV passed a $4.5\ \mu\text{m}$ Al degrader, leaving this at an energy of 203 MeV, and were used to induce the $^{40}\text{Ar} + ^{144,147}\text{Sm}$ nuclear fusion reactions for the production of Hg isotopes. Beams of $E_{\text{Lab}} = 217\text{ MeV}$ were used to induce the $^{40}\text{Ar} + ^{165}\text{Ho}$ nuclear fusion reaction leading to the production of At isotopes. The ^{165}Ho target (average target thickness: $300\ \mu\text{g}/\text{cm}^2$ of $^{\text{nat}}\text{Ho}$) was prepared by molecular plating [192] onto $1.1(1)\ \mu\text{m}$ Al foil. The samarium target (average target thickness: $600\ \mu\text{g}/\text{cm}^2$ of $^{144,147}\text{Sm}$; isotopic composition: 50% ^{144}Sm ; 50% ^{147}Sm) was prepared by thermal evaporation [155] onto $2.2(1)\ \mu\text{m}$ Ti foil. The beams first penetrated the backings before entering the target material. All energy losses in this work were calculated with SRIM2013 [193]. The target thinning upon a heavy-ion irradiation was not taken into account [194]. A summary of the beam parameters and ER properties can be found in Tab. 10.2. For each projectile-target combination only the highest cross sections σ_{HIVAP} according to HIVAP calculations [41, 195] at the given E_{COT} are listed in Tab. 10.2. In addition, the energy of the CN (E_{CN}), the relative α -decay probability (b_{α}) and most intense α -lines ($E_{\alpha 1}$) are included. The information presented in Tab. 10.2 are of importance for the data analysis. The ion-beam intensity on the targets was $2.5(2) \cdot 10^{10}$ particle \cdot s $^{-1}$ ($4.0(4)\ \text{nA}_{\text{part}}$). The Rutherford scattering was used to monitor the number of ion-beam particles bombarding the target with two Si-detectors mounted at $\pm 30^\circ$ relative to the beam axis. The reaction products were separated from the primary ion beam based on their magnetic rigidity and velocity. A retractable 16-strip position-sensitive Si-detector with an active area of $50 \times 50\ \text{mm}^2$ was mounted

Tab. 10.2.: List of experiments with ^{40}Ar ion beams as described in this thesis. The cross sections σ_{HIVAP} were calculated with HIVAP [41, 195], at the lab-frame ion beam energy in the center of the target E_{COT} . The E_{CN} is the kinetic energy of the CN if formed at ion beam energy E_{COT} . The three right-most columns indicate nuclear properties of the produced EVRs: energy of the most intense α -line ($E_{\alpha 1}$) [196], branching for α -decay (b_{α}) [196], and half-life $T_{1/2}$ [196]. The energy loss was calculated with SRIM-2013 [193]

Reaction	Exit CH	Product	E_{COT} (MeV)	E_{CN} (MeV)	σ_{HIVAP} (mb)	E_{α} (keV)	b_{α} (%)	$T_{1/2}$
$^{40}\text{Ar} + ^{165}\text{Ho}$	5n	^{200}At	212	41.4	0.037	6464	57(6)	43(1) s
	6n	^{199}At	212	41.4	0.500	6643	90(5)	7.2(5) s
$^{40}\text{Ar} + ^{147}\text{Sm}$	4n	^{183}Hg	190	40.7	6.811	5904	11.7(20)	9.4(7) s
	5n	^{182}Hg	190	40.7	4.242	5867	15.2(8)	10.8(1) s
$^{40}\text{Ar} + ^{144}\text{Sm}$	4n	^{180}Hg	190	40.7	2.411	6120	48(4)	2.8(2) s

25 cm upstream of the BGC in the MARS focal plane to measure absolute ER rates. The signals from this detector were amplified with a gain of 7–8 mV/MeV and shaped by CAEN amplifiers. The shaped signals from each amplifier were passed into its own 32-channel Analog-to-Digital Converter (ADC). The ADCs transmitted the digital output signal through the PCI bus to the data acquisition computer, where the energy and position values were stored. The typical energy resolution of the obtained α -spectra was around 90 keV.

The detector was retracted for the efficiency measurements with the BGC. The ER focal-plane image size (FWHM, Full Width at Half Maximum) was 32 mm in the horizontal direction and 24 mm in the vertical direction. The transmission efficiency of MARS depends on the mass asymmetry of the fusion reaction. For the used reactions, this efficiency was between 2 and 4% [192]. An external energy calibration was performed by using a four-line α -source, consisting of ^{148}Gd , ^{239}Pu , ^{241}Am , and ^{244}Cm . The geometric efficiency of the FP detector to register α -particles of implanted ERs was estimated to be 55(3)%.

A 3.5(1) μm Ti foil with a diameter of 60 mm was mounted inside a CF-flange to separate the buffer-gas volume from the beamline vacuum. It was sealed with a gold wire, and supported by a grid with a geometrical transparency of 95% [197]. The entrance window and the back of the DC cage were kept at a potential of typically +250 V in order to optimize the electric field inside the BGC. The BGC was filled with high-purity (99.9999%) helium gas. The ERs, extracted from the BGC, entered a 25 cm-long Teflon transport line (inner diameter 4 mm), establishing the connection to COMPACT.

10.1.2 Focal plane measurements behind MARS

For chemistry experiments with SHEs, the extraction efficiency and the extraction time is the key, since the SHEs have low production rates and short half-lives. In order to determine the extraction efficiency in on-line experiments, the rates of incoming ERs into the FP must first be determined from α -spectra from the FP-measurements. This information is needed for the calculation of the overall extraction efficiency of the BGC. The rates of incoming ERs were identified based on their known α -decay energies. The implanting ERs were detected with a 16-strip position-sensitive silicon detector (PSSD). The α -decaying ERs from the $^{40}\text{Ar} + ^{165}\text{Ho}$ reaction were used to correct for the recoiling daughter energy to obtain an internal calibration.

Result

The $^{40}\text{Ar} + ^{152}\text{Gd}$, ^{165}Ho , and $^{144,147}\text{Sm}$ reactions were studied in the experiments behind the MARS spectrometer. The beam energies result in CN excitation energies, which populated the evaporation channels 4n, 5n, and 6n. Not all xn exit channel were observed for all of the presented reactions. In addition to the xn deexcitation channels, the channels that involved the emission of a proton or α -particle plus few neutrons from the CN could not be observed in the respective α -spectra. Fig. 10.1 shows typical α -spectra of implanted fusion products of the three ^{40}Ar -induced reactions. The beam dose for the measurement series was between $(4.1\text{--}5.6)\cdot 10^{10}$ particles. For the reaction $^{152}\text{Gd} + ^{40}\text{Ar}$ to synthesize the CN $^{182}\text{Pb}^*$, the production rate was relatively low, since the HIVAP predicted cross section σ_{HIVAP} for this reaction is two orders of magnitude lower than σ_{HIVAP} for the other two ^{40}Ar -induced reactions.

Discussion

The products of the 4-6n evaporation channels have high production cross sections and are, thus, the most prominent. The observed α -particle energies are in agreement with the literature values given in Tab. 10.2. In all spectra, xn -evaporation products dominate; no products of charged-particle evaporation are visible. The low production rates for Pb nuclei (see Fig. 10.1 A) and the not ideal Ti-window thickness for these nuclear fusion reaction (see Sec. 8.1) led to insufficient statistics below the determination limit of the used setup (3σ [198]). In the $^{40}\text{Ar} + ^{144,147}\text{Sm}$ reaction, the peaks of ^{182}Hg and ^{183}Hg could not be resolved (Fig. 10.1 C). Therefore, for $^{182,183}\text{Hg}$ only a sum of the 5n and 6n channel is reported and used for the determination of the overall extraction efficiency of the BGC (in Sec. 10.1.3). In the nuclear fusion reaction $^{40}\text{Ar} + ^{165}\text{Ho}$, the $^{199,200}\text{At}$ are well separated and can be used for the efficiency evaluation of the BGC.

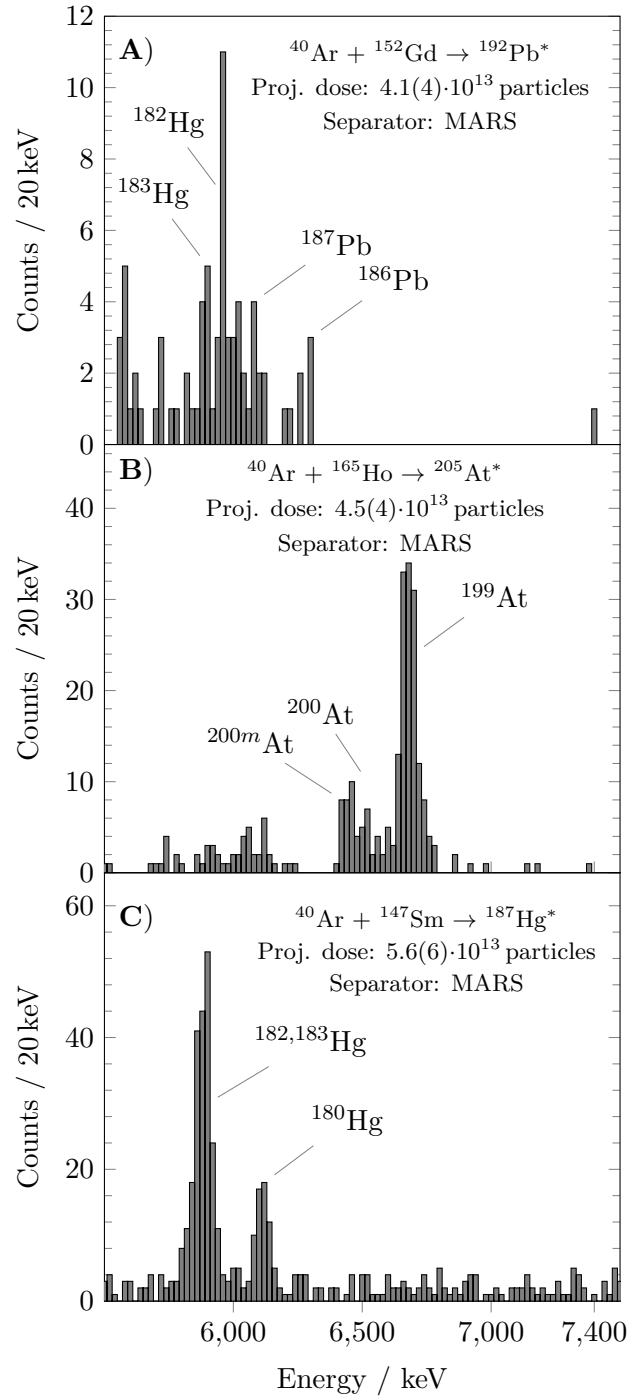


Fig. 10.1.: Typical α -spectra measured with the FP-detector for fusion products in ^{40}Ar -induced reactions on (A) ^{152}Gd , (B) ^{165}Ho and (C) ^{147}Sm . The respective particle dose is shown in each of the figures.

10.1.3 Extraction efficiency measurements behind the MARS separator

The extraction efficiency ϵ_{exp} is given by the ratio of the number of ions reaching the COMPACT array to the number of ions entering the BGC, both normalized to

the ion-beam intensity. The latter number is obtained from the FP measurements, taking into account the efficiency of 55(3)% to register α -particles emitted by ERs implanted into the FP-detector and the entrance-window-grid transmission of 95%. The extraction efficiency was determined for ^{199}At , $^{200,200m}\text{At}$ and $^{182,183}\text{Hg}$.

Result

Fig. 10.2 shows two typical α -spectra collected with COMPACT. Both α -spectra are

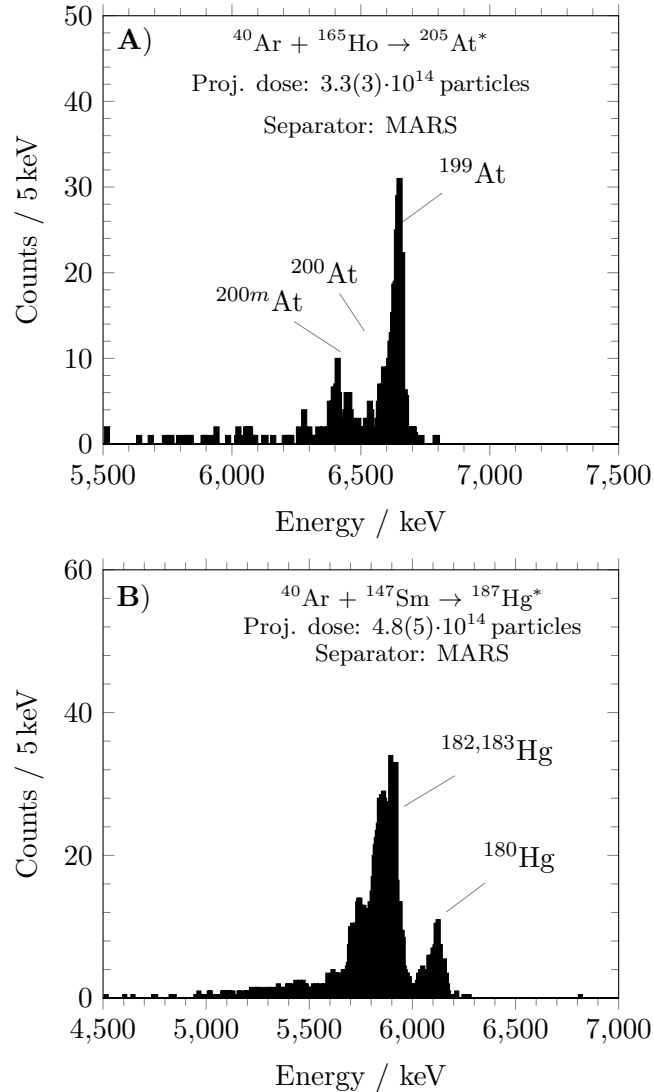


Fig. 10.2.: Typical α spectra with COMPACT-detector for fusion products in ^{40}Ar -induced reactions on (A) ^{165}Ho and (B) ^{147}Sm .

similar to the corresponding FP-spectra given in Fig. 10.1. The peak of ^{199}At is well resolved in Fig. 10.2 A, in contrast to the situation in Fig. 10.2 B, where the α -lines of ^{182}Hg and ^{183}Hg overlap almost completely. In the latter case, increased noise due to an increased RF-amplitude on the RF-funnel led to a reduced resolution. Therefore, the unresolved sum spectrum has had to be used to calculate the extraction efficiency.

The measured extraction efficiencies ϵ_{exp} for the ^{40}Ar -induced reactions on ^{165}Ho and ^{147}Sm are shown in **Tab. 10.3**, where the detected decays of ERs in the FP and in COMPACT are normalized to the ion-beam dose.

Discussion

The evaluated efficiencies in **Tab. 10.3** are slightly lower than the value of 35(3)% measured off-line with a ^{223}Ra α -decay recoil-ion source. This may be due to a larger spatial distribution and a wider range of recoil energies under which the ERs enter the BGC compared to the off-line experiments. Thus, a larger fraction collides with the funnel electrodes before thermalization in the case of the herein presented on-line experiments. In addition, some of the ions counted in the FP-detector are too slow to penetrate the entrance window ($E_{\text{kin}} < 30\text{ MeV}$) or they are too fast for thermalization in the BGC ($E_{\text{kin}} > 48\text{ MeV}$), thus implanting into the back wall. The stopping efficiency inside the BGC depends on the gas pressure inside the BGC and the thickness of the entrance window and was determined by using the SRIM code [193]. For the latter, the ion trajectories of 10,000 ^{199}At or ^{182}Hg ions with kinetic energies of $E_{\text{kin}} = 40\text{ MeV}$ were simulated. Ions with simulated endpoint coordinates inside the $3.5\text{ }\mu\text{m}$ -thick entrance window foil were lost for a subsequent extraction out of the BGC. The fraction of ions passing the entrance window foil (N_{win}), is given in **Tab. 10.3**. The fraction of ions with simulated end point positions inside the electrode system structure was taken as that stopped inside the BGC (ϵ_{stop}) was available for a later extraction out of the BGC. **Tab. 10.3** shows that the

Tab. 10.3.: *Measured experimental efficiency ϵ_{exp} for the given astatine and mercury radionuclides in comparison to the calculated extraction efficiency, ϵ_{calc} . N_{win} is the fraction of ions that passes through the entrance window, and ϵ_{stop} is the stopping efficiency for these ions inside the BGC as calculated with SRIM for ^{199}At and ^{182}Hg ions with kinetic energies of 40 MeV impinging on a $3.5\text{ }\mu\text{m}$ -thick titanium foil. ϵ_{BGC} is the extraction efficiency of the BGC as measured in the off-line studies. ϵ_{calc} is the product of ϵ_{BGC} , N_{win} and ϵ_{stop} , which is in good agreement with ϵ_{exp} .*

Nuclide	N_{win} (%)	ϵ_{stop} (%)	ϵ_{BGC} (%)	ϵ_{calc} (%)	ϵ_{exp} (%)	norm. events FP	norm. events COMPACT
^{199}At	86(9)	83(8)	35(3)	25(4)	24(4)	4.88(50)	1.18(11)
$^{200,200\text{m}}\text{At}$	86(9)	83(8)	35(3)	25(4)	24(4)	1.22(20)	0.30(10)
$^{182,183}\text{Hg}$	82(8)	94(8)	35(3)	27(3)	26(3)	7.99(80)	2.06(20)

calculated stopping efficiency ϵ_{calc} , which takes into account N_{win} , ϵ_{BGC} and ϵ_{stop} , is in agreement with the experimental values ϵ_{exp} .

10.2 On-line chemistry experiments behind the gas-filled separator TASCA

Based on the first results from Sec. 10.1, the setup was further improved with the introduction of the new miniCOMPACT (see Sec. 7.2), and the main experimental run was then performed at TASCA at GSI Helmholtzzentrum für Schwerionenforschung GmbH, Darmstadt. The COMPACT array, which was used in the off-line experiments at GSI (see Sec. 8.2.1) and on-line experiments behind the MARS spectrometer (see Sec. 10.1), in combination with a Teflon transfer line hampered the investigation of non-volatile species. In order to gain access to non-volatile elements and also to speed up the transport to the detector, an improved version of the COMPACT detector array was developed for the experimental campaign at TASCA (see Sec. 7.2). The main focus was on the elimination of any non-detector surfaces between the BGC exit nozzle and the detector. The experiment with ^{48}Ca was performed during a five-day irradiation in March 2019. The ^{165}Ho target was irradiated at two different beam energies, $E_{\text{COT}} = 273\text{ MeV}$ and 244 MeV in the middle of the target. The formal process was similar to the ^{40}Ar irradiations.

10.2.1 Experiments behind TASCA

A pulsed ion-beam (5 Hz, 5 ms on, 195 ms off) of $^{48}\text{Ca}^{10+}$, provided by an Electron Cyclotron Resonance ion source, was accelerated by the UNiVersal Linear ACcelerator (UNILAC) at the GSI Helmholtzzentrum für Schwerionenforschung GmbH to an energy of $E_{\text{Lab}} = 289\text{ MeV}$. Typical ion-beam intensities were $1.8(2)\cdot 10^{11}\text{ particles}\cdot\text{s}^{-1}$ ($29(3)\text{ nA}_{\text{part}}$). The ion-beam energy was degraded for portions of the run by passing the ion beam through a $5.0(1)\text{ }\mu\text{m}$ Ti degrader foil mounted on a rotating wheel upstream of the targets [193, 199]. Four $395\text{ }\mu\text{g}/\text{cm}^2$ -thick ^{165}Ho target segments (arc-shaped, monoisotopic composition) were mounted on a second wheel and rotated together with the degrader wheel, synchronously with the macro structure of the ion beam [156]. With E_{Lab} of 289 MeV , the energies (E_{COT}) were 273 MeV and 244 MeV for $2.3\text{ }\mu\text{m}$ and $7.3\text{ }\mu\text{m}$ ($2.3\text{ }\mu\text{m} + 5.0\text{ }\mu\text{m}$) Ti-foil thicknesses, respectively. The target backing with the target material was mounted on the downstream side (in beam direction) of the target frame. This allowed a small fraction of projectiles to scatter off the surface of the target frame into the backing and subsequently the target material layer. These scattering processes led to a small fraction of projectiles having substantially (tens of MeV) smaller energies than the nominal ion-beam energy (E_{Lab}), which led to the population of exit channels that are only expected at much lower beam energies, but feature large cross sections at such low energies (cf. Fig. 10.6). The ^{165}Ho targets were prepared by thermal evaporation onto $2.3(1)\text{-}\mu\text{m}$ -thick Ti-target backings [155].

The compound nuclei, with the momentum of the ion beam, recoiled through the

remaining target material before entering the gas-filled separator TASCAs. In the experiments with $E_{\text{COT}} = 273 \text{ MeV}$, the ER energy was degraded by adding a $100\text{-}\mu\text{g}/\text{cm}^2$ carbon-foil wheel behind the target. The ERs were separated from the primary ion-beam and unwanted nuclear reaction by-products by their different magnetic rigidities in 0.8 mbar helium in the TASCAs separator. The ERs with a magnetic rigidity of $1.7 \text{ T}\cdot\text{m}$, were directed to the focal plane of TASCAs, which was operated in its High Transmission Mode (HTM) [200]. For the reference of the transmission measurement, the ERs entered the TAsISpec set-up [201] in the configuration used for a subsequent flerovium decay spectroscopy experiment [202]. The TAsISpec implantation detector was a double-sided silicon-strip detector (DSSD) with 32 strips in horizontal and vertical direction, respectively, and an active area of $58 \times 58 \text{ mm}^2$. The geometric efficiency for detecting the α -decay of implanted ERs with the DSSD was $\approx 50\%$ [203]. The energy calibration of the DSSD was obtained using α -decay spectra from implanted ^{252}No , produced in the nuclear reaction of the same ion-beam with $^{206,207}\text{Pb}$ -targets [204]. The energy resolution (FWHM) of the DSSD for α -decay lines in the range $E_\alpha = 6\text{--}12 \text{ MeV}$ increased from 31 to 42 keV. After preamplification, the DSSD signals were directly digitized by 50-MHz, 14-bit sampling Analog to Digital Converters (ADC). The focal-plane image size was 48 mm in the horizontal direction and 20 mm in the vertical direction (FWHM). For the main part of the TASCAs experiment, TAsISpec was replaced by the BGC. The latter was separated from TASCAs by a $5.1(1)\text{-}\mu\text{m}$ -thick titanium foil with a diameter of 60 mm. This entrance window was supported by a grid with a geometrical transparency of 95%. The BGC (see Sec. 6.3) was filled with high-purity (99.9999%) helium gas. The ERs, extracted from the BGC, entered the miniCOMPACT detector array (see Sec. 7.2), which was connected directly to the BGC.

10.2.2 Analyses of the obtained experimental data

Because of the relatively high excitation energies of the CN, a large number of xn and pxn deexcitation channels was observed. The α -particle energies of these short-lived reaction products were located close together in the obtained α -spectrum, so that the individual α -peaks cannot be fully resolved. In this case, only the sum of overlapping peaks can be obtained from the α -spectra in the miniCOMPACT detector. Fig. 10.3 shows the α -spectrum measured with the miniCOMPACT when the products at $E_{\text{COT}} 273 \text{ MeV}$ of the $^{165}\text{Ho}(^{48}\text{Ca}, xn)$ reaction were collected on the first three miniCOMPACT detector pairs. On the remaining detectors, only signals from At and Rn isotopes decaying-in-flight were observed. All Fr isotopes adsorbed quantitatively on the first three detector pairs PIN diodes. Due to the reduced resolution of 175 keV (FWHM), individual α -lines are unresolved. The peak broadening is attributed to (i) the electronic noise caused by the RF and beam operation, and (ii) the anisotropic path of α -particles through the gas and

Tab. 10.4.: List of experiments with ^{48}Ca beams as described in this paper. The cross sections σ_{HIVAP} were calculated with HIVAP [41, 195], at the given E_{COT} . The data for E_{α} , b_{α} and $T_{1/2}$ are taken from the Evaluated Nuclear Structure File (ENSDF) database [196]. The energy loss was calculated with SRIM-2013 [193].

Reaction	Exit CH	Product	E_{COT} (MeV)	E_{CN} (MeV)	σ_{HIVAP} (mb)	E_{α} (keV)	b_{α} (%)	$T_{1/2}$	
$^{48}\text{Ca} + ^{165}\text{Ho}$	4n	^{209}Fr	273	62	< 0.001	6646	89(3)	50.0(3) s	
	5n	^{208}Fr	273	62	< 0.001	6641	90(4)	59.1(3) s	
	6n	^{207}Fr	273	62	0.006	6768	95(2)	14.8(1) s	
	7n	^{206}Fr	273	62	0.272	6790	84(2)	15.9(2) s	
	8n	^{205}Fr	273	62	2.612	6915	99(1)	3.9(1) s	
	9n	^{204}Fr	273	62	2.424	7013	80(1)	1.7(3) s	
	p4n	^{208}Rn	273	62	< 0.001	6143	62(7)	24.3(1) min	
	p5n	^{207}Rn	273	62	0.004	6131	21(3)	9.3(2) min	
	p6n	^{206}Rn	273	62	0.204	6260	63(3)	5.7(2) min	
	p7n	^{205}Rn	273	62	1.997	6262	23(4)	2.8(1) min	
	p8n	^{204}Rn	273	62	2.826	6419	73(1)	1.2(1) min	
	α 7n	^{202}At	273	62	2.153	6228	18(3)	3.1(1) min	
	$^{48}\text{Ca} + ^{165}\text{Ho}$	4n	^{209}Fr	244	55	< 0.001	6646	89(3)	50.0(3) s
		5n	^{208}Fr	244	55	< 0.113	6641	90(4)	59.1(3) s
6n		^{207}Fr	244	55	4.282	6768	95(2)	14.8(1) s	
7n		^{206}Fr	244	55	13.408	6790	84(2)	15.9(2) s	
8n		^{205}Fr	244	55	2.345	6915	99(1)	3.9(1) s	
p5n		^{207}Rn	244	55	1.146	6131	21(3)	9.3(2) min	
p6n		^{206}Rn	244	55	4.052	6260	63(3)	5.7(2) min	
α 8n		^{201}At	244	55	2.491	6344	71(7)	1.48(3) min	

detector dead-layer. To obtain information on the contribution of individual α -lines a multiple-peak fit approach was used.

Theoretical multiple-peak fit functions are a suitable tool in the case of largely overlapping α -lines. A variety of functions is available for a multiple-peak analysis, and by choosing suitable boundary conditions, it is possible to decompose the sum spectrum into its single components. As the α -decay lines in our α -spectra have non-Gaussian shapes, they were fitted with an asymmetric function. The asymmetric double sigmoidal-function is given by:

$$y = y_0 + A \frac{1}{1 + e^{-\frac{x-x_c+\omega_1/2}{\omega_2}}} \cdot \left(1 - \frac{1}{1 + e^{-\frac{x-x_c-\omega_1/2}{\omega_3}}} \right) \quad (10.1)$$

This function has six parameters: the vertical offset given by $y_0 = 0$ (baseline correction), the amplitude A , the centroid x_c , and three width values ω_1 , ω_2 , and ω_3 which determine the asymmetry of the peak. The three width parameters were

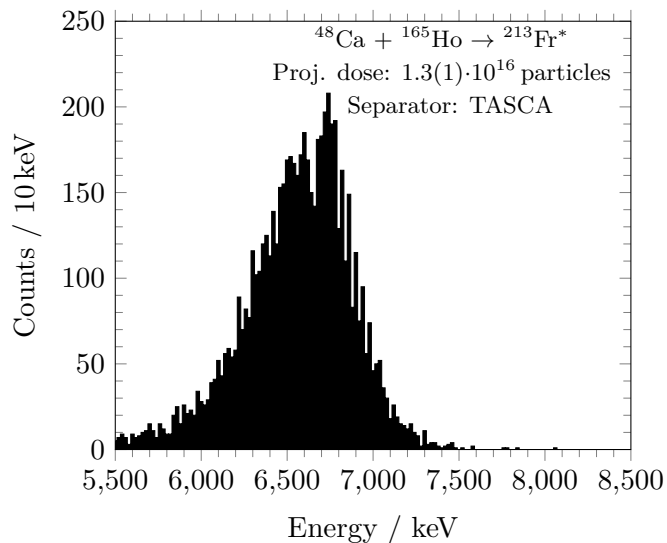


Fig. 10.3.: *Sum α -spectrum on the first three miniCOMPACT detector pairs of the $^{48}\text{Ca} + ^{165}\text{Ho}$ reaction at $E_{\text{COT}} = 273\text{ MeV}$. The measurement time was 60 min.*

determined from the calibration spectrum of ^{221}Fr , ^{217}At , and ^{213}Po , amounting to $\omega_1 = 25\text{ keV}$, $\omega_2 = 125\text{ keV}$, and $\omega_3 = 25\text{ keV}$ (cf. Fig. 10.5). The influence of the ω_2 value in the description of the low energy tailing of a α -signal is shown in Fig. 10.4 (For ω_3 it is analogous to ω_2 with the difference it describes the high energy tailing). ω_1 represent the FWHM of the base peak. Meanwhile, the values for x_c can be retrieved from literature, i.e., in the form of listed energies for the individual α -lines of the radionuclides in question. The values of the width parameters, as determined from a dependent fit of the well-separated α -lines in the calibration spectrum (see Fig. 10.5), in combination with the values for the centroids allow for the multiple-peak fit analysis of complex spectra with largely overlapping α -lines. This approach leaves the amplitudes of individual fit functions of single α -lines as the only free parameter. The multiple-fit analysis was performed in Origin[®] from OriginLab[®]

10.2.3 Focal plane measurements behind TASCA

For the gas-chromatographic studies at TASCA, the novel detector miniCOMPACT was connected directly to the BGC. To perform chemistry experiments with the heaviest elements, efficiency and sensitivity is a key factor. For the determination of the miniCOMPACT efficiency, the incoming particle rate on the FP-detector was measured. In addition, the FP-detector allows the mapping of the ion-beam profile. The number of incoming ERs and their subsequent decays into the FP were determined in measurements with 32 strips in horizontal and vertical direction,

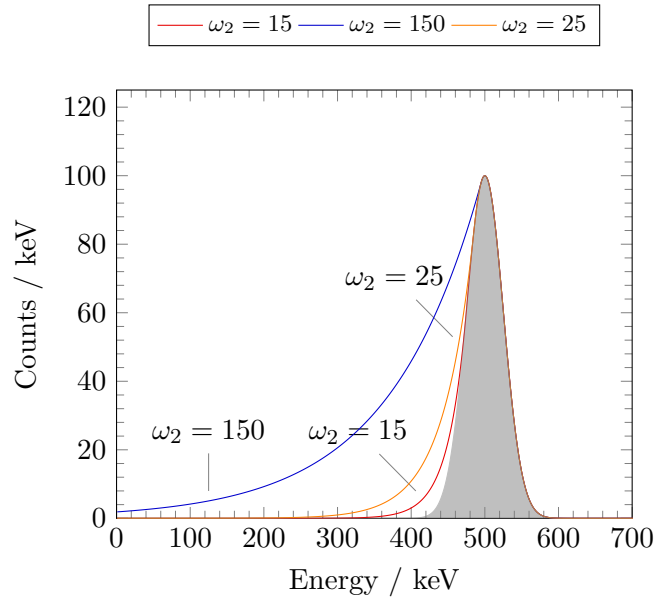


Fig. 10.4.: Influence of the different variance ω_2 values on the low energy tailing of a simulated α -peak.

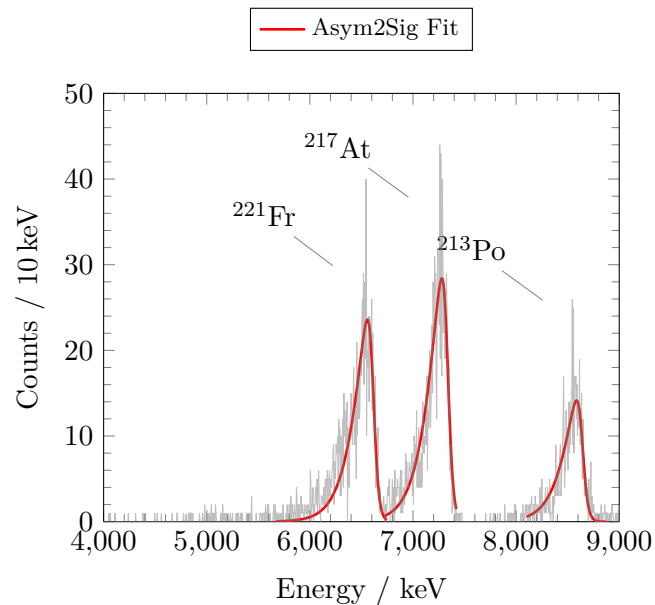


Fig. 10.5.: Calibration spectrum of the miniCOMPACT with an ^{225}Ac recoil-ion source. The peaks were fitted with an asymmetric double sigmoidal (*Asym2Sig*) function from Eq. 10.1.

respectively, and an active area of $58 \times 58 \text{ mm}^2$. The geometric efficiency for detecting the α -decay of implanted ERs with the DSSD was $\approx 50\%$ [203]. The ^{48}Ca -induced experiments used two excitation energy settings: (i) $E_{\text{COT}} = 273 \text{ MeV}$ and (ii) $E_{\text{COT}} = 244 \text{ MeV}$. For the latter E_{COT} the beam energy was reduced by a $5.0(1) \mu\text{m}$ Ti degrader foil, which was mounted on a separate rotating target wheel upstream of the targets. The kinematic setting for both experiments which include the use of

^{165}Ho targets are shown in [Tab. 10.4](#).

Results

The typical α -decay spectra measured in the FP for the decay of implanted ERs in each ^{48}Ca -induced reaction are shown in [Fig. 10.6A](#) and [Fig. 10.6B](#). The observed fusion-evaporation products were identified according to their known α -decay energies. To ensure all ER decay events were collected after the end of irradiation of the ^{165}Ho target, the data acquisition was continued for several half-lives of the longest-lived fusion-evaporation product. The peak fitting of each decay product was performed with the multi-peak-fit approach in OriginLab. In the low energy part of both α -spectra, the characteristic α -decays of the $p\alpha n$ (Rn) and the αxn (At) exit channel products were observed. The nearly identical $T_{1/2}$ and/or α -energies of these deexcitation channels in the reaction $^{165}\text{Ho} + ^{48}\text{Ca}$ make their individual α -lines unresolved. In the high energy part of the α -spectra, the xn residues (Fr) synthesized in the ^{48}Ca -induced reaction with ^{165}Ho were obtained. From [Fig. 10.6](#), it is directly clear that a decrease of the excitation energy leads to a reduced number of evaporated neutrons. The determined rate entering the BGC for each nuclide is used for the chemical yield determination of short-lived isotopes in the miniCOMPACT measurements. In [Tab. 10.5](#) the number of counts for each nuclide seen in [Fig. 10.6](#) is shown.

Tab. 10.5.: *Summary of the measured number of counts in the $^{48}\text{Ca} + ^{165}\text{Ho}$ reaction in the TASCFA FP at $E_{\text{COT}} = 273\text{ MeV}$ and 244 MeV . The projectile dose was $1.3(1) \cdot 10^{14}$ for $E_{\text{COT}} = 273\text{ MeV}$ and $1.2(2) \cdot 10^{14}$ for $E_{\text{COT}} = 244\text{ MeV}$.*

Nuclide	$E_{\text{COT}} = 273\text{ MeV}$	$E_{\text{COT}} = 244\text{ MeV}$
	cts	cts
^{204}Fr	5(2)	-
^{205}Fr	16(5)	65(6)
$^{206+207}\text{Fr}$	39(4)	560(45)
$^{208+209}\text{Fr}$	188(15)	209(17)
^{204}Rn	156(13)	-
^{201}At	160(13)	31(5)
^{205}Rn	72(8)	-
^{202}At	26(5)	-

Discussion

Production cross sections σ_{HIVAP} , as calculated by a statistical evaporation model of the nuclear reaction $^{165}\text{Ho}(^{48}\text{Ca}, xn)$, are given in [Tab. 10.4](#). The largest σ_{HIVAP} at $E_{\text{COT}} = 273\text{ MeV}$ result in the 8n-, 9n-, p7n-, p8n- and α 7n-channels, where σ_{HIVAP}

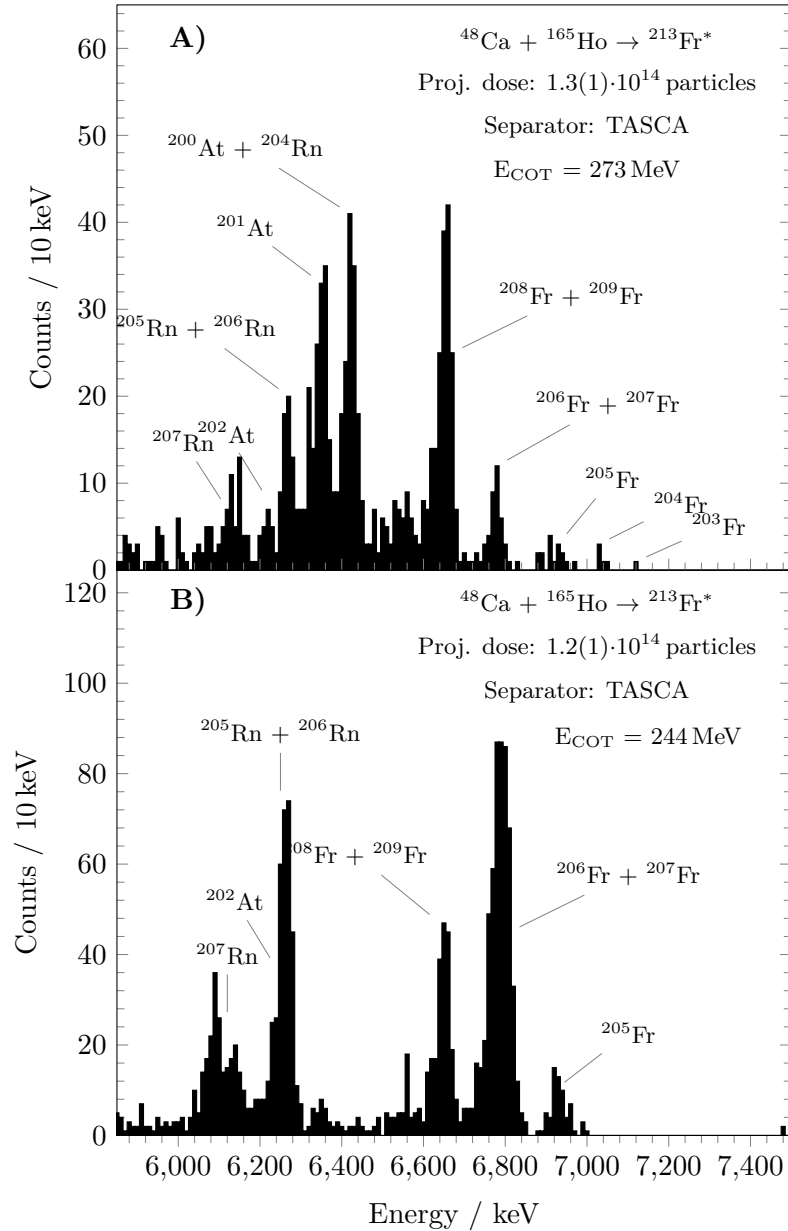


Fig. 10.6.: Alpha spectra recorded in the FP measurement at TASCA (A) at $E_{\text{COT}} = 273$ MeV and (B) at $E_{\text{COT}} = 244$ MeV. Dominant lines are labeled.

is in the range of several mb. The other nuclear reaction products have cross sections below 1 mb. With the shift to $E_{\text{COT}} = 244$ MeV the maximum σ_{HIVAP} is predicted for the 7n channel. Indeed, the α -spectra shown in Fig. 10.6 reveal that all expected ERs can be found. The α -spectra also exhibit α -lines of products from channels with fewer evaporated neutrons than expected from the HIVAP calculations. These were formed by the small fraction of ion-beam scattered to lower energies, where these channels dominate and exhibit larger cross sections than those nominally expected at the E_{Lab} , cf. the results of HIVAP calculations provided in Sec. A.2.

10.2.4 Extraction efficiency measurement behind the gas-filled separator TASCA

The overall extraction efficiency of the BGC was determined with the transmission efficiency from the previous FP measurements (see Sec. 10.2.3), which corresponds to the number of ions which enters the BGC trough the entrance window. The bar graph in Fig. 10.3 shows the summed spectrum of the first three miniCOMPACT-detector pairs obtained at $E_{\text{COT}} = 273 \text{ MeV}$ of the $^{165}\text{Ho}(^{48}\text{Ca},x\text{n})$ reaction. All francium radioisotopes are adsorbed on the first three detector pairs. On the remaining detectors, mainly signals from $^{204,205}\text{Rn}$, decaying in-flight, were observed. Due to the reduced energy resolution of 175 keV (FWHM), individual α -lines could not be resolved. To obtain information on the contribution of individual α -lines a multiple-peak-fit approach was used (see Sec. 10.2.2). In Eq. 10.1 three width values occur and were set to $\omega_1 = 25$, $\omega_2 = 125$ and $\omega_3 = 25$ as determined from a calibration spectrum, cf. Fig. 10.5. There, each α -peak is well separated and can be used to determine the ω values for the multiple-peak-fit approach. In the calibration spectrum the three width values lead to a proper description of ^{221}Fr , ^{217}At and ^{213}Po (see Fig. 10.5). The multi-peak fit approach allowed the analysis of complex spectra with largely overlapping α -lines. In this approach, the amplitudes of the individual fit functions of the respective α -peak were the only free parameter.

Result

Production cross sections σ_{HIVAP} , as calculated by a statistical evaporation model of the nuclear reaction $^{165}\text{Ho}(^{48}\text{Ca},x\text{n})$, are given in Tab. 10.4. The largest σ_{HIVAP} at $E_{\text{COT}} = 273 \text{ MeV}$ result in the 8n-, 9n-, p7n-, p8n- and α 7n-channels, where σ_{HIVAP} is in the range of several mb. The other nuclear reaction products have cross sections below 1 mb. With the shift to $E_{\text{COT}} = 244 \text{ MeV}$ the maximum σ_{HIVAP} is predicted for the 7n channel.

To obtain information on the contribution of individual α -lines a multiple-peak fit approach was used (see Sec. 10.2.2) with shared/fixed widths parameters, fixed energy positions and free areas for the individual peaks. The fitting result of experimental data from the multi-peak fit approach is shown in Fig. 10.7. This procedure is able to describe the experimental data and Tab. 10.6 summarizes the multiple-peak analysis for the experimental data.

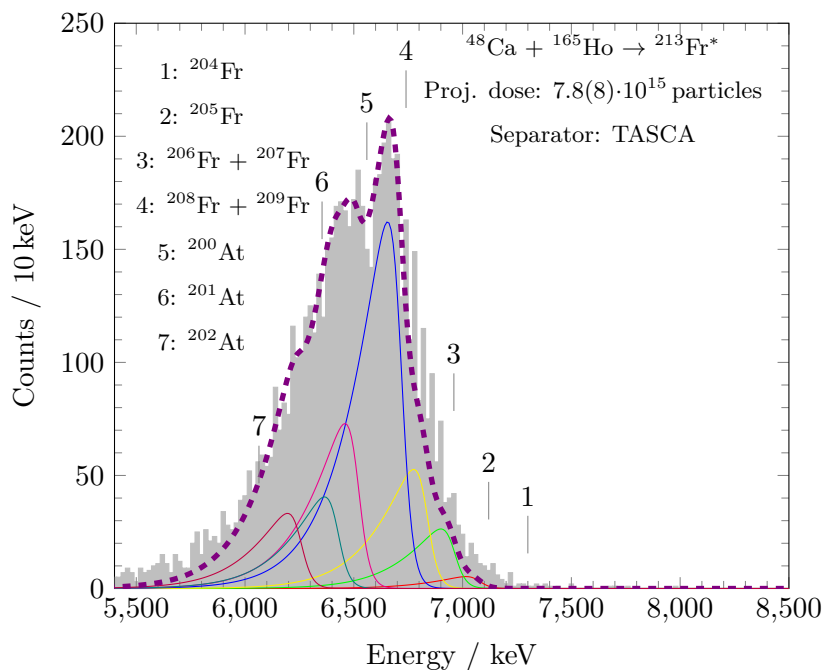


Fig. 10.7.: *Experimental data (sum α spectrum, see Fig. 10.3) simulated with multiple asymmetric double sigmoidal fits. The enveloping curve around the experimental data is the sum of the individual simulated peaks from the multiple fit analysis for the respective nuclides.*

Discussion

Indeed, the α -spectra shown in Fig. 10.6 reveal that all expected ERs can be found. The α -spectra also exhibit lines of products from channels with fewer evaporated neutrons than expected from the HIVAP calculations. These were formed by the small fraction of ion-beam scattered to lower energies, where these channels dominate and exhibit larger cross sections than those nominally expected at the E_{Lab} , cf. the results of HIVAP calculations provided in Sec. A.2. In Fig. 10.8 the relative peak areas from the FP spectra (see Tab. 10.6) compared to the relative peak areas as determined by the multiple-fit analysis (see Tab. 10.6) is shown. The ratios of the individual peak areas of different pairs of radionuclides (see Tab. 10.6), as derived from the FP- and miniCOMPACT-spectra are in good agreement. Thus, the applied multi-peak-fit analysis indeed allows for the determination of the correct relative peak areas of the investigated radioisotopes of francium in comparably complex spectra with inferior resolution. Furthermore, it shows that the peak area of all At isotopes were reduced by the same factor. We ascribe this to the fact that elemental At is volatile (similar to Hg) and does not adsorb on the SiO_2 -surface of the detector array, due to its low adsorption enthalphy on SiO_2 [205]. This is further substantiated by the fact that on the remaining miniCOMPACT detectors only decay-in-flight is observable.

The weighted average value of ϵ_{exp} for all five francium radioisotopes, as determined

Tab. 10.6.: Calculated extraction efficiencies using the multiple-peak fit analysis from *Sec. 10.2.2* for the data obtained with the miniCOMPACT for A) $E_{COT} = 244$ MeV and B) $E_{COT} = 273$ MeV. The overall efficiencies ϵ_{exp} of the BGC-miniCOMPACT system for the respective Fr radioisotopes are compared to the theoretically expected efficiencies ϵ_{calc} (for further details see *Sec. 10.1.3*).

A)					
Nuclide	N_{win} (%)	ϵ_{stop} (%)	ϵ_{BGC} (%)	ϵ_{calc} (%)	ϵ_{exp} (%)
^{205}Fr	86(4)	94(4)	35(2)	28(3)	21(3)
$^{206+207}\text{Fr}$	86(4)	94(4)	35(2)	28(3)	22(2)
$^{208+209}\text{Fr}$	86(4)	94(4)	35(2)	28(3)	21(2)
B)					
^{204}Fr	94(4)	84(4)	35(2)	27(3)	23(7)
^{205}Fr	94(4)	84(4)	35(2)	27(3)	21(5)
$^{206+207}\text{Fr}$	94(4)	84(4)	35(2)	27(3)	20(2)
$^{208+209}\text{Fr}$	94(4)	84(4)	35(2)	27(3)	21(2)

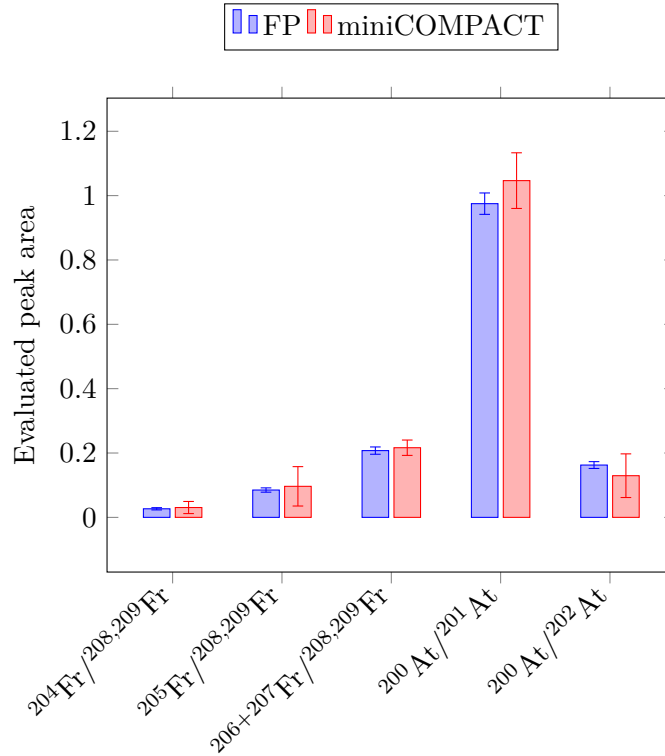


Fig. 10.8.: The relative peak areas from the FP spectra (see *Tab. 10.6*) compared to the relative peak area as determined by the multiple fit analysis.

by the multi-peak-fit analysis, was 21(3)% for both energies. If ϵ_{stop} , ϵ_{BGC} and N_{win} are taken into account (see *Sec. 10.1.3*), the resulting ϵ_{calc} agrees quite well with the value of ϵ_{exp} . The remaining difference can be explained by the difference in angular spread of products emitted from an α -recoil-ion source and ERs entering the BGC in a much wider distribution.

In the off-line measurements with a ^{225}Ac recoil-ion source, it was not possible to

detect Fr in the COMPACT. This was attributed to Fr adsorption in the Teflon tube used in that work to connect COMPACT to the BGC. The new interface between the funnel exit and the new miniCOMPACT has almost eliminated this distance, where the ions are no longer guided by electric fields. In the present setup, first contact of extracted ions no longer occurs on a Teflon tube, but on the active detector surface of the miniCOMPACT. This therefore allows registration also of a substantial fraction of 23(4)% of non-volatile, reactive elements like Fr.

10.2.5 Summary

The fusion-evaporation reactions of ^{40}Ar - or ^{48}Ca -beams with ^{165}Ho - and $^{144,147}\text{Sm}$ -targets were used to characterize a new setup for fast transactinide chemistry experiments. α -decaying radioisotopes of mercury, francium, and astatine were produced and isolated in the MARS or TASCA recoil separators and guided into the BGC. The BGC-COMPACT setup has been successfully tested in on-line experiments behind the MARS spectrometer at Texas A&M University. The measured extraction efficiencies for ^{199}At , $^{200,200m}\text{At}$ and $^{182,183}\text{Hg}$, as determined with the COMPACT detector after a 25 cm-long Teflon transport line, were 24(4) % and 26(3) %, respectively. The good agreement between the experimental and calculated efficiency (see Tab. 10.3) shows that the characterization of the BGC is well understood. These efficiencies are slightly lower than the obtained value of 35(3) % during the off-line experiments with ^{219}Rn ions from a ^{223}Ra recoil-ion source mounted within the BGC. The difference in efficiency between the off-line and on-line experiments is based on losses in the entrance window of the BGC as well as its limited stopping efficiency and the larger angular spread of the ERs [93]. The long transport line in this setup suppressed the extraction of non-volatile elements. These elements adsorbed on their way through the transport line and did not reach the COMPACT detector array.

For the present study at TASCA, the novel miniCOMPACT was developed. The new detector array was tailored to experiments with short-lived radioisotopes of relatively less volatile elements and was successfully coupled to the BGC. The elimination of any transport line by means of a new interface to the miniCOMPACT allowed for the detection of non-volatile chemical elements. In the experiments behind TASCA, an extraction efficiency of 21(3) % for the investigated radioisotopes of francium was reached. This extraction efficiency is similar to the values obtained for the more volatile elements astatine and mercury adsorbing on the Au-covered detectors in COMPACT. These experimental results show that the setup presented here is suitable for the extraction of both volatile and non-volatile elements. Furthermore, the miniCOMPACT is not limited to the application in experiments with the BGC, but it can also be used behind a classic RTC [59]. First promising preliminary studies with this coupling type were performed at GSI [180].

The BGC and miniCOMPACT setup enables experiments with, in comparison,

short-lived radioisotopes ($T_{1/2} > 50$ ms), also of non-volatile elements. Our obtained results also show weaknesses of the used setup, mainly connected with the finite thermalization capabilities of the BGC. Based on our results, the design of a next-generation BGC was developed [206], which is expected to provide higher thermalization efficiency and yet shorter extraction times, as desirable for studies of the superheavy elements.

11.1 Chemical experiments of superheavy nuclei

Beside the GSI Helmholtzzentrum für Schwerionenforschung there are several facilities at which chemical investigations of the properties of SHEs are performed. For example, Fl was also characterized via gas-phase chromatography in the reaction $^{48}\text{Ca} + ^{242,244}\text{Pu}$ at the Flerov Laboratory for Nuclear Reactions (FLNR), Dubna, Russia. In these experiments, the adsorption behavior of Fl on gold was investigated [83]. The gas-phase chromatography is used for studies of Nh, which was produced in the heavy-ion-induced nuclear fusion reaction of $^{48}\text{Ca} + ^{243}\text{Am}$ [180]. The isotopes $^{284,285}\text{Nh}$ from the α -decay of the precursor $^{288,289}\text{Mc}$ were in the focus of interest in these experiments. So far it has not yet been possible to extract Nh after the separation at the Dubna Gas-Filled Recoil Separator due to larger retention of elemental Nh in the Teflon capillary [80]. Another approach to understand the atomic structure of SHEs is by mass spectrometry of superheavy elements. The first direct measurement of the mass numbers for Nh and Mc was performed at FIONA (For the Identification of Nuclide A) at the Lawrence Berkeley National Laboratory (USA) behind the Berkeley gas-filled separator [207]. The new facility SHEF (superheavy element factory) at the FLNR institute Dubna, Russia, aims to discover new superheavy nuclides and to study those already synthesized in more detail. The SHEF enables a tenfold increase in beam intensity by using the DC-280 cyclotron up to $10\text{ p}\mu\text{A}$ for ions with masses of 50-60 u; such an increase in beam intensity enables the study of reactions with lower cross sections that would otherwise be inaccessible [208].

11.2 Chemistry beyond Fl

To get access to shorter-lived isotopes and thus eventually to Mc and beyond, a faster extraction technique for chemical experiments, which can be connected to the well established gas-phase chromatography is needed. The successful fast extraction of ^{219}Rn with 55(4) ms and with an extraction efficiency of 35(3)% has shown the capability of the TASCA-BGC system to investigate short-lived isotopes. The extraction time of 55 ms from the BGC demonstrated in this thesis is by a factor of 7 to 9 shorter than for the RTC. In response to these extraction time and on the basis of the current production rates of SHEs, the element Nh and Mc are directly in reach for chemical studies with gas-phase chromatography. To proceed

to even heavier elements or exotic nuclei, either the overall efficiency of the setup has to be further increased or the amount of produced nuclei has to be increased. The overall efficiency of 35% is one of the limiting factors. A highly efficient (up to 100%) extraction method will improve the sensitivity for gas-phase chemistry experiments. With a highly efficient and fast extraction method, the isotopes with half-lives of several milliseconds should be accessible at the one-atom-at-the-time scale. The overall efficiency is not the only key to gas-phase experiments with SHEs since it strongly depends on the half-life of the heaviest elements [45]. Furthermore, the chemical study in the gas-phase needs a volatility of atoms or molecules in the presence of a Teflon transport line to transport the in-situ produced ERs. This is the reason why the chemical studies are limited to elements, which are volatile or form volatile compounds. The heavier elements Mc till Og are predicted to be chemically reactive and their isotopes are in the 100 ms-range. The experiments at Dubna with Nh show [80] that Nh for example is very reactive and has a strong interaction with Teflon and cannot be successfully extracted to the chemical setup. The same behavior is observable for the non-volatile ^{221}Fr . With the introduction of the novel RTC-miniCOMPACT system, the extraction of non-volatile elements could be achieved. The overall extraction efficiency for the non-volatile ^{221}Fr was in the same range like the volatile elements. A further improvement for a fast and efficient transfer of the fusion products can be achieved by the implementation of a high-density BGC and an RF-only ejector interface directly behind the funnel exit, which is tightly connected to the entrance of the COMPACT detector. In this configuration, the gas-jet out of the funnel can be efficiently transferred into the COMPACT detector and an extraction efficiency up to 100% can be reached [206]. A first generation of a high-density BGC is currently under development. The simulated extraction time of this high-density BGC is as short as 2 ms. In the case that this extraction time and efficiency can be confirmed, studies of the elements up to Ts are no longer limited by the half-life but only by the production rate (see Fig. 11.1).

The successful extraction of non-volatile elements in this work goes hand in hand with the further development of the detector since the non-volatile and highly reactive elements will adsorb on the first detector PIN diodes. To improve the resolution in the chromatography column, a logarithmically scaled PIN diode surface is developed. Here the number of detectors in the entrance area is increased. The higher resolution in the adsorption behavior allows a more detailed insight of the adsorption enthalpy for non-volatile elements.

As a next step, chemical studies of Nh, which is expected to be more reactive than Cn and Fl, are in the focus of chemical investigations at TASCA. Due to similar production cross-sections as for $^{288,289}\text{Fl}$ and a half-life of 0.94 s, studies of ^{284}Nh will be carried out in the next years. First attempts on Nh chemistry were performed at the JINR (Joint Institute for Nuclear Research), Dubna, Russia to determine the

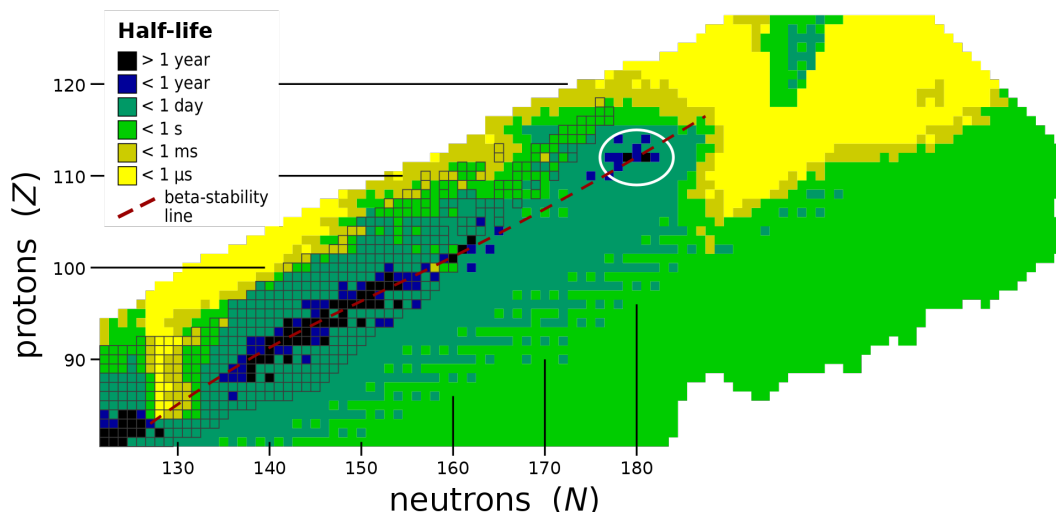


Fig. 11.1.: *Estimated half-lives of isotopes in the region of the heaviest elements. Based on data from [209, 210]. Figure taken from [211].*

volatility of Nh in 2014. The isotope ^{284}Nh was synthesized as the daughter of ^{288}Mc produced in the $^{243}\text{Am} + ^{48}\text{Ca}$ reaction with a cross section about 8 pb. The ^{288}Mc decays to ^{284}Nh with a half-life of 164 ms. The ^{284}Nh is long-lived enough to perform gas-phase chromatography with this isotope, but none of these atoms were registered in the COLD detectors [81]. In theoretical calculations it was shown that Nh has a higher predicted reactivity in comparison to Fl or Cn and the use of a long transfer capillary from the separator to the COLD detector prevents the Nh extraction [212]. For this reason, prior to the Nh studies, further optimization experiments with the short-lived Tl isotopes were performed at GSI to increase the overall chemical yield. In future, chemical studies on the even heavier transactinide Nh and Lv ($Z = 116$) are planned, which are predicted to be relatively reactive. With the combination of the high-density BGC with the miniCOMPACT, it can be investigated due to the fact that the predicted transportation time of around 2 ms is lower than the half-life ($T_{1/2} < 60$ ms) [206].

11.3 Summary

The gas-phase chromatography behind a preseparator is in many ways the most powerful technique for chemical studies of SHEs. RTCs, which were conventionally used as an interface between the preseparator and the chemical setup, have a limitation in terms of their extraction time around 0.5 s. In view of the short half-lives as well as the low production rates of the heaviest elements, this leads to a drastic loss of the required statistics in the investigation of the chemical properties of these short-lived isotopes.

The present work deals with the development and characterization of a novel system based on the combination of a BGC with a DC field superimposed on a RF signal in

order to drag ions towards the exit of the cell and a novel interface with a modified COMPACT detector. These gas cells work no longer only with gas-flow to flush out the ions and should thus overcome the limitation in the extraction time.

Within the scope of this work, a BGC with superimposed electric fields was coupled as an interface between the existing preseparator TASCA and the chemistry setup COMPACT. Its performance with respect to efficiency and extraction time has been investigated with recoil-ion sources in off-line experiments and in two separate on-line experiments behind the MARS spectrometer and TASCA. The modification of the classic COMPACT detector to the so called miniCOMPACT allows in addition the extraction of non-volatile elements like Fr. These improvements increased the the extraction time from more than 400 ms down to 55 ms with an overall efficiency of about 35%. This paves the way for chemical investigations of Nh and elements beyond Fl without being dependent on volatile elements or the formation of volatile compounds, as they are otherwise needed for gas-phase chromatography [45, 49, 115]. Prior to this work, it could be shown that ions can reach the subsequent miniCOMPACT detector and neutralize on the first wall collision on the detector surface. These ions are still available for chromatographic studies in the COMPACT detector and are therefore not lost. The extraction of elements in the ionic charge state does not represent a disadvantage of this method. On the other hand, this method opens up the window for carrying out chemical studies with reactive and non-volatile elements that were previously inaccessible by using this method. In previous studies [80], the non-volatile compounds were lost in the transfer capillary from the separator to the chemical setup.

The performance of this new coupling of a BGC with superimposed electric field with the chemistry setup could be transferred from the test conditions with recoil-ions sources (off-line measurements) to real on-line experiments within the framework of the presented work. The extraction efficiency of about 35% of the offline experiments could be confirmed in both on-line experiments at the Cyclotron Institute and the GSI. Both on-line experiments have contributed to a continuous further development of the presented interface. In addition, the robustness and reproducibility of these coupling for the investigation of SHEs could be confirmed.

A.1 Stopping Distribution Simulations

The interaction of traveling ions through matter is complex as it depends upon the atomic number, the charge state (distribution), the electron configuration, polarizabilities and the relative velocity of the involved atoms and ions. THE SRIM software package is dedicated to simulate these complex interactions of moving ions through matter. SRIM is able to reproduce the stopping power of 25.000 experimental data within a 95% confidence interval [181]. In binary collision approximations Monte Carlo simulation with random impact parameters for the next collision, the distribution of the ER ions inside the BGC is simulated [213, 214]. While traveling through solids or gas, particles transfers kinetic energy to orbital electrons and nuclei. Due to this energy transfer, the ions lose energy along their path. The amount of energy transfer is not linear and depends on collisions and the kinetic energy of the particle. The stopping power was introduced to characterize the energy loss of the ions during the interaction with material. The stopping power $S(E)$ is defined as:

$$S(E) = -\frac{dE}{dx} . \quad (\text{A.1})$$

The stopping power is separated into two terms: the electronic stopping power $S_{\text{ele.}}(E)$ and the nuclear stopping power $S_{\text{nuc.}}(E)$. The energy lost via electronic interaction is described by the further development of the Bethe-Bloch equation [215, 216], the so called LSS (Lindhard-Scharff-Schiott)-Theory [217]. The additional work results in Eq. A.2.

$$S_{\text{ele.}}(E) = 8\pi e^2 a_0 \frac{Z_1^{7/6} Z_2}{\left(Z_1^{2/3} + T_2^{2/3}\right)} \sqrt{\frac{2E_{\text{kin}}}{M}} \quad (\text{A.2})$$

where M , a_0 , v , E , Z are respectively the mass of the ion, the Bohr radius, the velocity, the energy and the charge of the particle; c is the speed of light. The nuclear stopping power can be described by the energy transfer after a nuclear collision on the basis of calculations from J.F Ziegler, J.P. Biersack and U. Littmark [218] in units of eV/(atom/cm²):

$$S_{\text{nuc.}}(E) = \frac{8.462 \cdot 10^{-15} \cdot Z_1 \cdot Z_2 \cdot M_1}{(M_1 + M_2) \cdot (Z_1^{0.23} + Z_2^{0.23})} \quad (\text{A.3})$$

where $M_{1,2}$ is the mass of the incident ion and its collision partner. The program SRIM version 2011 has an average accuracy of about 4.6% in comparison with experimental data for stopping power and approximately 69% (86%) of all measured data is in variation of 5% (10%) in comparison to SRIM calculations as it is reported in [104].

A.2 HIVAP: MARS experimente

The theoretical coss sections σ_{HIVAP} were calculated with the HIVAP code [41, 195]. This code is based on the conventional two step process of complete fusion and the subsequent statistical de-excitation of the compound nucleus. HIVAP calculations for the complete fusion evaporation reactions $^{152}\text{Gd}(^{40}\text{Ar}, 4-6\text{n})^{188}\text{Pb}$, $^{165}\text{Ho}(^{40}\text{Ar}, 5-6\text{n})^{199,200}\text{At}$ and $^{147}\text{Sm}(^{40}\text{Ar}, 2-4\text{n})^{182,183}\text{Hg}$, have been performed. The result for the exit channels for the $^{152}\text{Gd}(^{40}\text{Ar}, xn)^{192-x}\text{Pb}$ reaction is shown in Fig. A.1. In

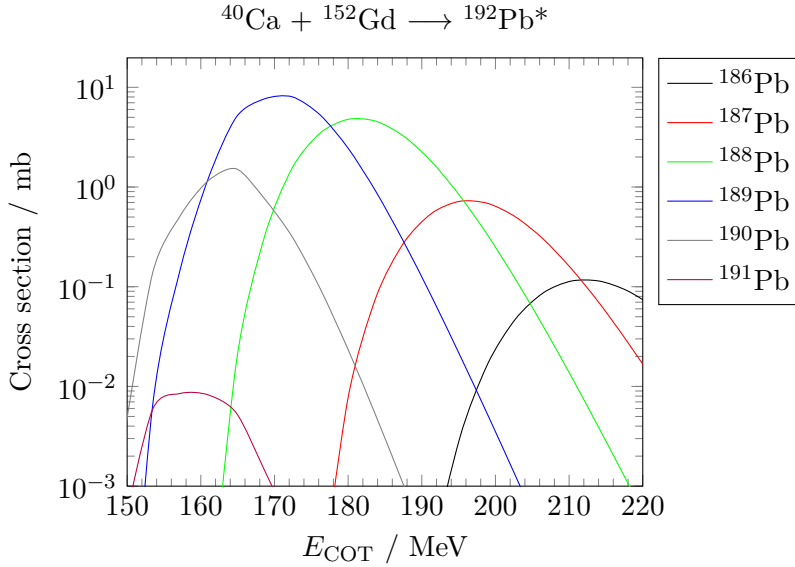


Fig. A.1.: HIVAP predictions for the excitation functions for the $^{152}\text{Gd}(^{40}\text{Ar}, xn)^{192-x}\text{Pb}$ reaction. Data was taken from [219].

hot fusion reactions, the 3n and 4n evaporation channels typically have the largest cross section. The excitation of these channels are of predominate interest for the later efficiency measurements of the BGC, due to larger production rates of these fusion evaporation residues. In most instances 3n–5n channel products were detected. For the $^{152}\text{Gd}(^{40}\text{Ar}, xn)^{192-x}\text{Pb}$ reaction, HIVAP predicts the 3n channel to be the dominant deexcitation channel with a maximum cross section of about 8 mb at an E_{COT} of about 170 MeV. The 4n and 5n channel are predicted to have maximum cross sections of about 5 mb or 0.7 mb at 180 MeV and 195 MeV, respectively. The HIVAP predictions for the excitation functions for the $^{147}\text{Sm}(^{40}\text{Ar}, xn)^{187-x}\text{Hg}$ reaction are displayed in Fig. A.2. In these HIVAP predictions, the 3n deexcitation channel at E_{COT} of about 170 MeV has the largest cross section of about 24 mb.

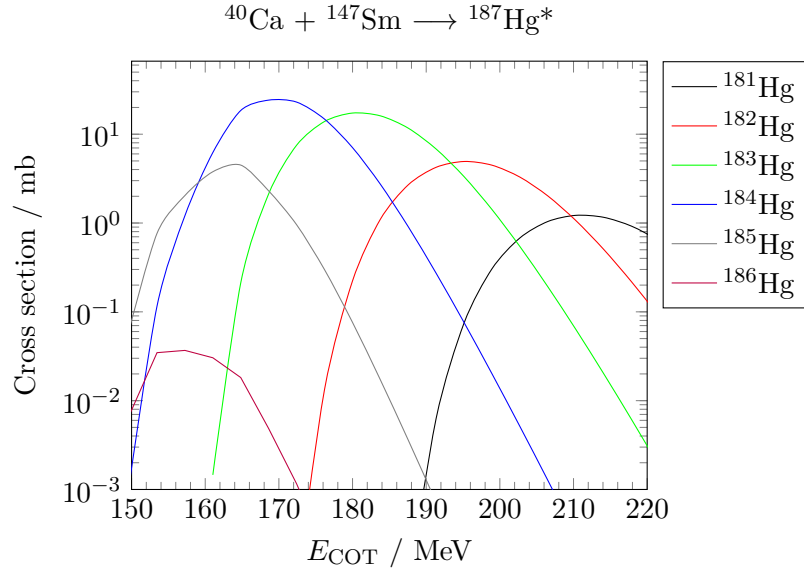


Fig. A.2.: *HIVAP* predictions for the excitation functions for the $^{147}\text{Sm}(^{40}\text{Ar}, xn)^{187-x}\text{Hg}$ reaction. Data was taken from [219].

In this case, the 3n channel is around three times larger than for the $^{152}\text{Gd}(^{40}\text{Ar}, xn)^{192-x}\text{Pb}$ reaction. For the 4n channel the predicted cross section is around 17 mb at a laboratory energy of around 180 MeV. At 195 MeV, *HIVAP* also predicts a maximum cross section of about 5 mb for the 5n deexcitation channel. This is in the same order than the most dominant 3n channel for the $^{152}\text{Gd}(^{40}\text{Ar}, xn)^{192-x}\text{Pb}$ reaction.

The *HIVAP* calculation result for the exit channels for the $^{165}\text{Ho}(^{40}\text{Ar}, xn)^{205-x}\text{At}$ reaction is shown in Fig. A.3. Here, *HIVAP* predicts the 4n channel to be the dominant deexcitation channel with a maximum cross section of about 14 mb at an E_{COT} of about 180 MeV. The maximum cross section for the 6n is about 7 mb at E_{COT} of about 190 MeV, The 6n and 3n channel are predicted to have maximum cross sections of about 3 mb at 170 MeV and 200 MeV, respectively.

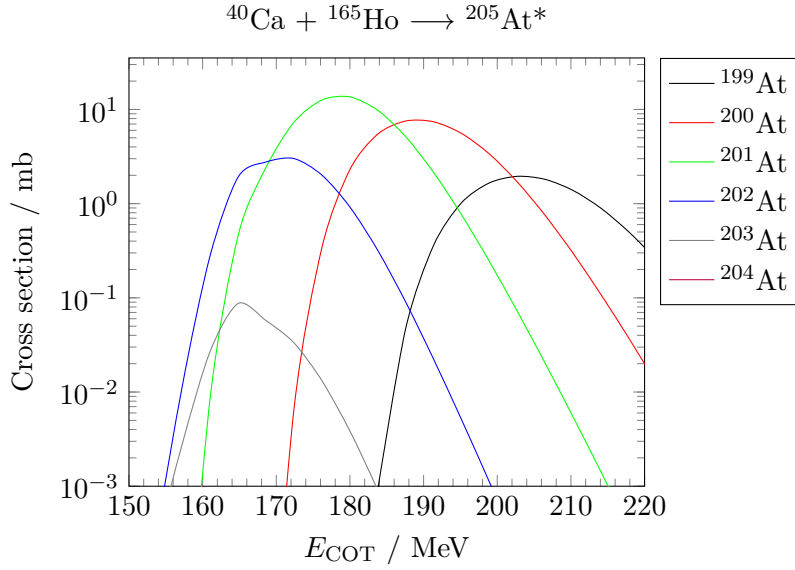


Fig. A.3.: HIVAP predictions for the excitation functions for the ${}^{165}\text{Ho}({}^{40}\text{Ar}, xn){}^{205-x}\text{At}$ reaction. Data was taken from [219].

A.3 HIVAP: TASCA experimente

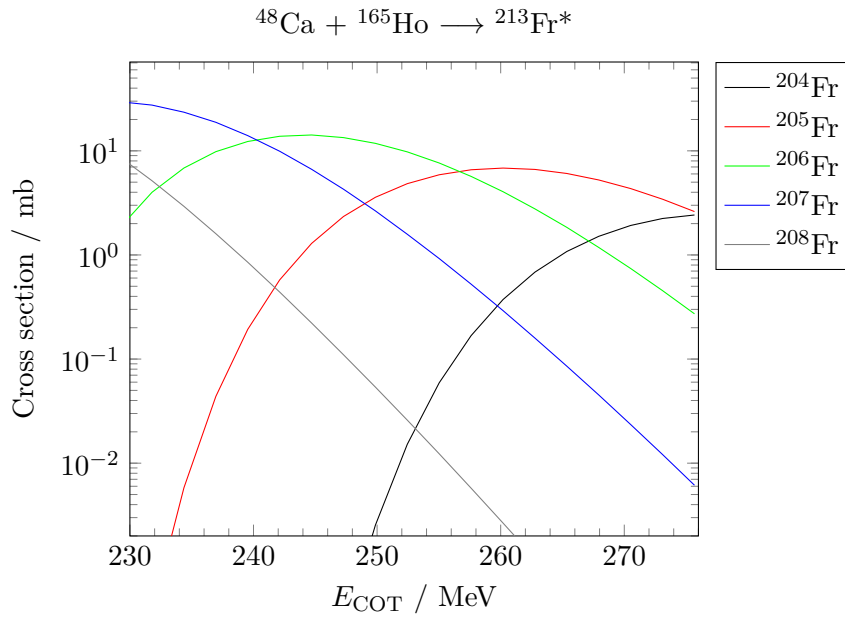


Fig. A.4.: HIVAP predictions for 5n- to 9n-evaporation channels of the fusion reaction ${}^{165}\text{Ho} + {}^{48}\text{Ca}$. Data was taken from [219].

The HIVAP predictions for the excitation functions for the ${}^{165}\text{Ho}({}^{48}\text{Ca}, xn){}^{213-x}\text{Fr}$ reaction at both center of target energies are displayed in Fig. A.4. In these HIVAP predictions, the 8n deexcitation channel at E_{COT} of 276 MeV has the largest predicted cross section of about 2.6 mb, which decrease slightly for $E_{\text{COT}} = 246$ with a cross section around 2.3 mb. The 9n deexcitation channel at $E_{\text{COT}} = 276$ MeV is in the

same order of magnitude as the 8n channel. The number of evaporated neutrons is shifted to lower numbers with the decrease of the excitation energy. The 7n deexcitation channel has the largest cross section at $E_{\text{COT}} = 246$ MeV with 14.2 mb, which drops two orders of magnitude at E_{COT} of 276 MeV. The predicted cross section of the 6n channel is comparable with that of the 8n channel, both about 2–4 mb. The HIVAP prediction for the pxn deexcitation channels are shown in Fig. A.5.

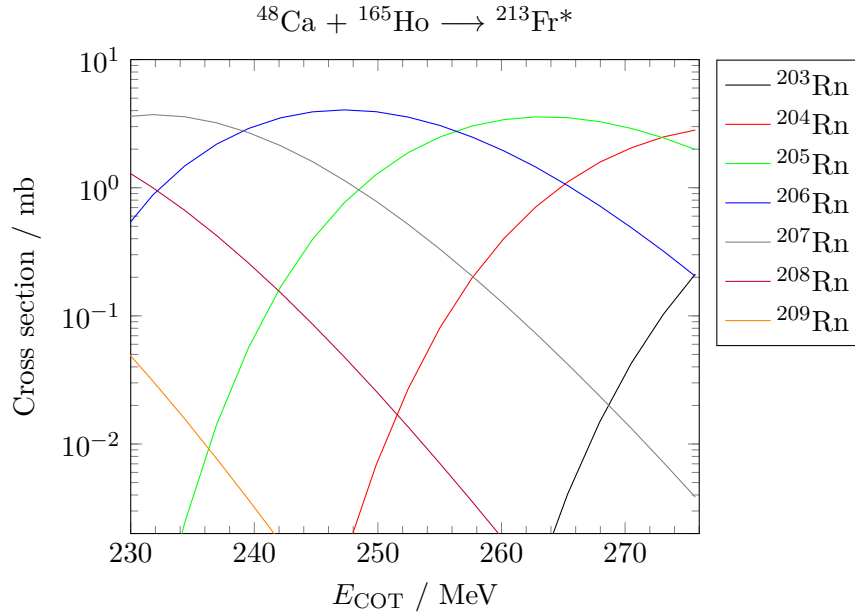


Fig. A.5.: HIVAP predictions for pxn -evaporation channels of the fusion reaction $^{165}\text{Ho} + ^{48}\text{Ca}$. Data was taken from [219].

In general, the predicted cross sections are one order of magnitude lower than the corresponding xn channels. The maximum cross section at $E_{\text{COT}} = 276$ MeV is peaked at the p9n and p8n channels with around 2 mb. With a shift to the lower excitation energy, the maximum cross section is shifted to the p7n deexcitation channel, which is the dominating deexcitation mode. The p6n and p5n channels have a small contribution with around 1 mb to the production rate for Rn. The HIVAP predictions for the αxn channel for the $^{165}\text{Ho} + ^{48}\text{Ca}$ reaction is displayed in Fig. A.6. The αxn deexcitation channel have only a small contribution to the total deexcitation modes. The maximum cross section at $E_{\text{COT}} = 276$ MeV is located at the $\alpha 7n$ channel with a maximum cross section of 2 mb. With a shift to the lower excitation energy at E_{COT} , the $\alpha 7n$ cross section drops two orders of magnitude and the $\alpha 7n$ deexcitation channel is the most dominant deexcitation mode.

A.4 Study of the recoil release probability

In off-line measurements with recoil-ion sources, the overall efficiency of the BGC is studied by determining the α particles measured on the detector array from the

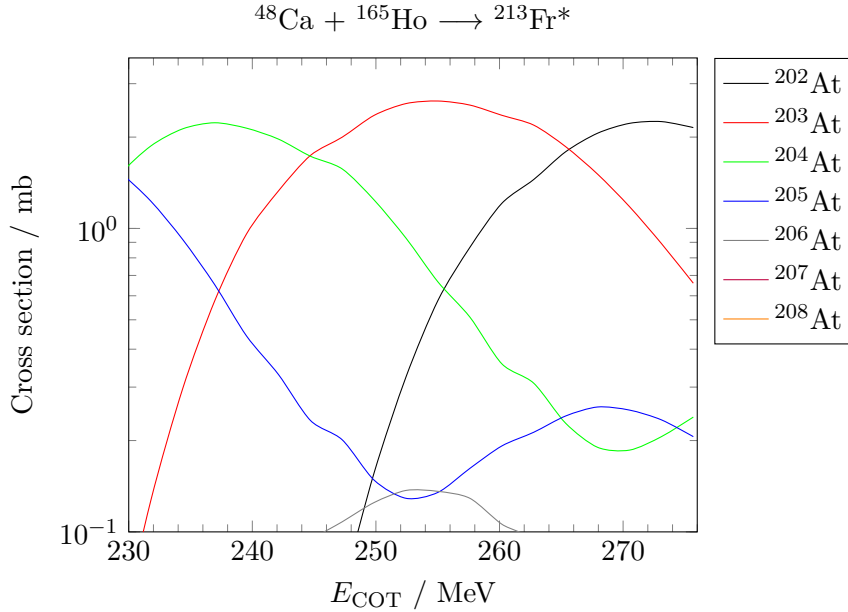


Fig. A.6.: *HIVAP predictions for αn -evaporation channels of the fusion reaction $^{165}\text{Ho} + ^{48}\text{Ca}$. Data was taken from [219].*

α -decay of the respective recoil-ions in comparison to the number of particles released from the recoil-ion source. In the case of the ^{223}Ra the release probability was extensively studied. The source was produced under vacuum condition by using electrical fields to deposit the ^{223}Ra on a metallic cylinder. This process produces relatively thin sources ($< 0.15 \mu\text{g}/\text{cm}^2$) [220]. With a recoil energy of 109 keV for ^{219}Rn and an energy loss of 4.5 keV in ^{223}Ra [181], the release probability of ^{219}Rn from the ^{223}Ra recoil-ion source is nearly 100% [137, 138, 221]. In the case of the ^{225}Ac recoil-ion source there was a deadlayer due to the molecular plating from a organic solution (see Fig. A.7). This deadlayer of unwanted layers on top of the source sample, which were deposited during the molecular plating time, is usually present [146, 158, 191]. The presence of this deadlayer can already be seen in Fig. 6.7a, where the α peaks are broadened due to the energy loss of the α particles passing through the deadlayer. Due to the higher stopping power of the unwanted layer on top of the source sample, a fraction of ^{219}Rn recoils was stopped inside the deadlayer. This stopped fraction of recoil-ions is lost for the extraction measurements and thus distorts or threatens to distort the efficiency of the BGC. For reliable efficiency determinations by using of recoil-ion sources the number of released recoil ions is crucial and therefore also the release probability P_{release} has to be measured precisely. The measurement principle for the determination of P_{release} of ^{221}Fr is shown in Fig. A.8. P_{release} was investigated with the same setup like in the source calibration measurements. At the beginning of the analysis period the α -activity of the mother ^{225}Ac was measured, while the recoils were implanted into the detector surface. After reaching the radioactive equilibrium between ^{225}Ac and its decay

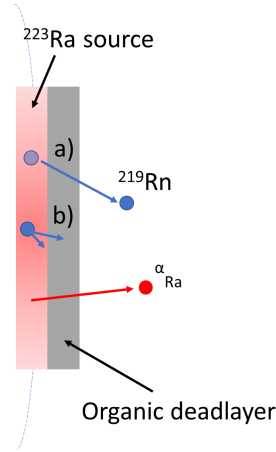


Fig. A.7.: Schematic view of the organic deadlayer on the ^{225}Ac recoil-ion source. In a) the kinetic energy of ^{219}Rn is high enough to penetrate the deadlayer and ^{219}Rn can leave the recoil-ion source. In the case that the kinetic energy is not high enough (b)) only the α -particle can leave the recoil-ion source.

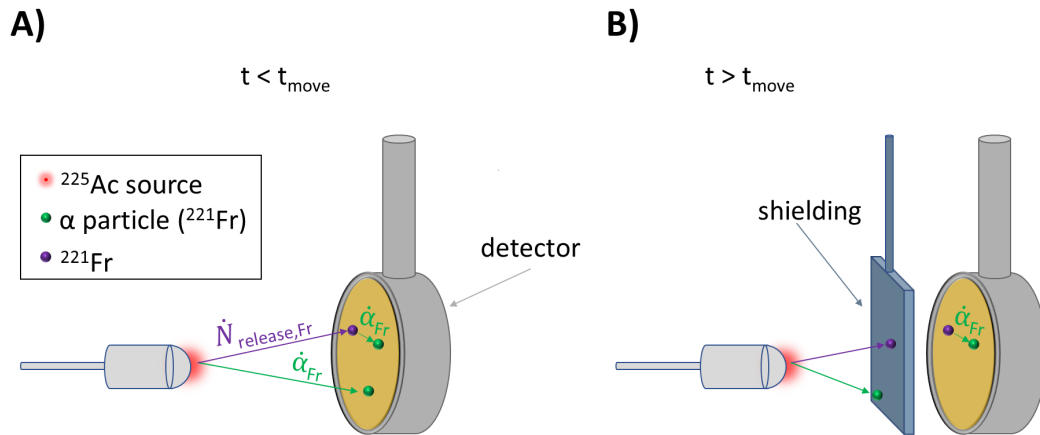


Fig. A.8.: Setup (schematic) for the determination of P_{release} of ^{221}Fr .

products (t_{move}), the detector was shielded from the ^{225}Ac source. This shielding is necessary, thus allowing the measurement of just the α -decays of the ^{221}Fr recoils, which were implanted into the detector and not α -particles which came directly from the ^{225}Ac recoil-ion source. To deduce P_{release} the ^{221}Fr α -decay rate was measured as a function of time (see Fig. A.9). The actual implanted activity at the point in time when the source was shielded was extrapolated from the data of the measured ^{221}Fr α -decay. This implanted activity was then compared to the total activity of ^{225}Ac . This provided access to the value of P_{release} . Typical release probabilities of ^{221}Fr were found to be between 10% and 25%.

With the knowledge of P_{release} , the effective release rate of both recoil-ion sources,

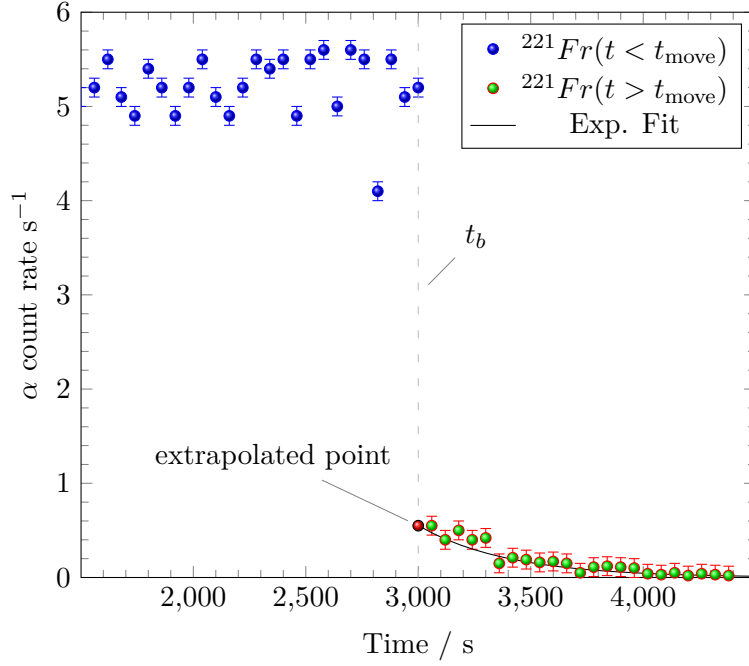


Fig. A.9.: Detected alpha rates for ^{221}Fr with 'open' and shielded detector. The rates were determined by successive measurements with measurement times of 30 s. The detector was shielded at the time t_{move} . The ^{221}Fr α -rate from the implanted recoils on the detector has to be extrapolated from the exponential fit.

taking into account the detector efficiency $\epsilon_{\text{Det}} \approx 100\%$, is given by

$$\dot{N}_{\text{Ra/Ac}}^{\text{tot}} = P_{\text{release}} \cdot \epsilon_{\text{em}} \cdot A_{\text{Ra/Ac}} \cdot \epsilon_{\text{Det}} \cdot b_{\alpha} \quad [\text{in s}^{-1}], \quad (\text{A.4})$$

where ϵ_{em} is the fraction of recoils emitted by the source to be available inside the gas volume of the BGC. The ions, which were emitted backwards into the source, were implanted into the source material. This fraction of recoil-ions is lost for further measurements, which reduces the available number of recoils for efficiency measurements. Therefore, one hemisphere is available for the further efficiency measurements leading to $\epsilon_{\text{em}} = 0.50$ in Eq. A.4. With the recoil energy of ^{221}Fr of 107.4 keV and the release probability for these recoil-ions the organic deadlayer can be simulated with the program SRIM-2010 [181]. The experimental values for P_{release} can be described with a simulation based on a organic layer (isopropanol) on top of the source with an thickness between 0.09 and 0.11 μm .

- [1] T. C. L. Chanda, Globalization and interdependence: science, technology and innovation for development, United Nations - General Assembly, **2017**, Chapter A/72/422/Add.2, p. 10.
- [2] L. Soby, The International Year of the Periodic Table, A Common Language for Science, (Eds.: N. Tarasova, J. Reedijk, C. Brett, C. Ober, L. Öhrström, M.-H. Chiu), UNESCO, **2019**, <https://iypt2019.org/>.
- [3] D. I. Mendeleev, "Sootnoshenie svoystv s atomnym vesom elementov", *Journal of Russian Physical Chemistry Society* **1869**, *1*, 60–77.
- [4] P. Y. Jackson, "General Chemistry: An Elementary Survey Emphasizing Industrial Applications and Fundamental Principles. Fifth edition, rewritten and revised (Deming, Horace G.)", *Journal of Chemical Education* **1945**, *22*, 570, DOI [10.1021/ed022p570.3](https://doi.org/10.1021/ed022p570.3).
- [5] G. T. SEABORG, "The Chemical and Radioactive Properties of the Heavy Elements", *Chemical & Engineering News* **1945**, *23*, 2190–2193, DOI [10.1021/cen-v023n023.p2190](https://doi.org/10.1021/cen-v023n023.p2190).
- [6] P. J. Karol, R. C. Barber, B. M. Sherrill, E. Vardaci, T. Yamazaki, "Discovery of the element with atomic number $Z = 118$ completing the 7th row of the periodic table", *Pure and Applied Chemistry* **2016**, *88*, 139–153, DOI [10.1515/pac-2015-0501](https://doi.org/10.1515/pac-2015-0501).
- [7] P. J. Karol, R. C. Barber, B. M. Sherrill, E. Vardaci, T. Yamazaki, "Discovery of the element with atomic number $Z = 118$ completing the 7th row of the periodic table", *Pure and Applied Chemistry* **2016**, *88*, 155–160, DOI [10.1515/pac-2015-0501](https://doi.org/10.1515/pac-2015-0501).
- [8] L. Öhrström, J. Reedijk, "Names and symbols of the elements with atomic numbers 113, 115, 117 and 118 (IUPAC Recommendations 2016)", *Pure and Applied Chemistry* **2016**, *88*, 1225–1229, DOI [10.1515/pac-2016-0501](https://doi.org/10.1515/pac-2016-0501).
- [9] D. C. HOFFMAN, F. O. LAWRENCE, J. L. MEWHERTER, F. M. ROURKE, "Detection of Plutonium-244 in Nature", *Nature* **1971**, *234*, 132–134, DOI [10.1038/234132a0](https://doi.org/10.1038/234132a0).
- [10] G. Gamow, "Mass defect curve and nuclear constitution", *Proceedings of the Royal Society A* **1930**, *126*, 632–644, DOI [10.1098/rspa.1930.0032](https://doi.org/10.1098/rspa.1930.0032).
- [11] C. F. von Weizsäcker, "Zur Theorie der Kernmassen", *Zeitschrift für Physik* **1935**, *96*, 431–458, DOI [10.1007/bf01337700](https://doi.org/10.1007/bf01337700).
- [12] A. Sobczewski, Z. Patyk, S. Cwiok, "Do the superheavy nuclei really form an island?", *Physics Letters B* **1987**, *186*, 6–8, DOI [10.1016/0370-2693\(87\)90502-8](https://doi.org/10.1016/0370-2693(87)90502-8).
- [13] J. Dvorak, W. Bröchle, M. Chelnokov, R. Dressler, Ch. E. Düllmann, K. Eberhardt, V. Gorshkov, E. Jäger, R. Krücken, A. Kuznetsov, Y. Nagame, F. Nebel, Z. Novackova, Z. Qin, M. Schädel, B. Schausten, E. Schimpf, A. Semchenkov, P. Thörle, A. Türler, M. Wegrzecki, B. Wierczinski, A. Yakushev, A. Yeremin, "Doubly Magic Hs", *Physical Review Letters* **2006**, *97*, DOI [10.1103/physrevlett.97.242501](https://doi.org/10.1103/physrevlett.97.242501).
- [14] S. Hofmann, G. Münzenberg, "The discovery of the heaviest elements", *Reviews of Modern Physics* **2000**, *72*, 733–767, DOI [10.1103/revmodphys.72.733](https://doi.org/10.1103/revmodphys.72.733).
- [15] S. Hofmann, "Synthesis of superheavy elements by cold fusion", *Russian Chemical Reviews* **2009**, *78*, 1123–1138, DOI [10.1070/rc2009v078n12abeh004076](https://doi.org/10.1070/rc2009v078n12abeh004076).

- [16] F. P. Heßberger, G. Münzenberg, S. Hofmann, W. Reisdorf, K. H. Schmidt, H. J. Schött, P. Armbruster, R. Hingmann, B. Thuma, D. Vermeulen, “Study of evaporation residues produced in reactions of $^{207,208}\text{Pb}$ with ^{50}Ti ”, *Zeitschrift für Physik A Atoms and Nuclei* **1985**, *321*, 317–327, DOI [10.1007/bf01493453](https://doi.org/10.1007/bf01493453).
- [17] K. Morita, K. Morimoto, D. Kaji, H. Haba, K. Ozeki, Y. Kudou, T. Sumita, Y. Wakabayashi, A. Yoneda, K. Tanaka, S. Yamaki, R. Sakai, T. Akiyama, S.-i. Goto, H. Hasebe, M. Huang, T. Huang, E. Ideguchi, Y. Kasamatsu, K. Katori, Y. Kariya, H. Kikunaga, H. Koura, H. Kudo, A. Mashiko, K. Mayama, S.-i. Mitsuoka, T. Moriya, M. Murakami, H. Murayama, S. Namai, A. Ozawa, N. Sato, K. Sueki, M. Takeyama, F. Tokanai, T. Yamaguchi, A. Yoshida, “New Result in the Production and Decay of an Isotope, $^{278}113$, of the 113th Element”, *Journal of the Physical Society of Japan* **2012**, *81*, 103201, DOI [10.1143/jpsj.81.103201](https://doi.org/10.1143/jpsj.81.103201).
- [18] A. Türler, V. Pershina, “Advances in the Production and Chemistry of the Heaviest Elements”, *Chemical Reviews* **2013**, *113*, 1237–1312, DOI [10.1021/cr3002438](https://doi.org/10.1021/cr3002438).
- [19] Y. Oganessian, “Heaviest nuclei from ^{48}Ca -induced reactions”, *Journal of Physics G: Nuclear and Particle Physics* **2007**, *34*, R165–R242, DOI [10.1088/0954-3899/34/4/r01](https://doi.org/10.1088/0954-3899/34/4/r01).
- [20] Y. T. Oganessian, V. K. Utyonkov, Y. V. Lobanov, F. S. Abdullin, A. N. Polyakov, R. N. Sagaidak, I. V. Shirokovsky, Y. S. Tsyganov, A. A. Voinov, G. G. Gulbekian, S. L. Bogomolov, B. N. Gikal, A. N. Mezentsev, S. Iliev, V. G. Subbotin, A. M. Sukhov, K. Subotic, V. I. Zagrebaev, G. K. Vostokin, M. G. Itkis, K. J. Moody, J. B. Patin, D. A. Shaughnessy, M. A. Stoyer, N. J. Stoyer, P. A. Wilk, J. M. Kenneally, J. H. Landrum, J. F. Wild, R. W. Lougheed, “Synthesis of the isotopes of elements 118 and 116 in the $\text{Cf}249$ and $\text{Cm}245 + \text{Ca}48$ fusion reactions”, *Physical Review C* **2006**, *74*, DOI [10.1103/physrevc.74.044602](https://doi.org/10.1103/physrevc.74.044602).
- [21] M. Schädel, “Chemie superschwerer Elemente”, *Angewandte Chemie* **2006**, *118*, 378–414, DOI [10.1002/ange.200461072](https://doi.org/10.1002/ange.200461072).
- [22] D. C. Hoffman, D. M. Lee, “Chemistry of the Heaviest Elements- One Atom at a Time”, *Journal of Chemical Education* **1999**, *76*, 331, DOI [10.1021/ed076p331](https://doi.org/10.1021/ed076p331).
- [23] M. Schädel, D. Shaughnessy, *The Chemistry of Superheavy Elements*, Springer-Verlag GmbH, **2013**.
- [24] P. Pyykko, J. P. Desclaux, “Relativity and the periodic system of elements”, *Accounts of Chemical Research* **1979**, *12*, 276–281, DOI [10.1021/ar50140a002](https://doi.org/10.1021/ar50140a002).
- [25] B. Fricke in *Recent Impact of Physics on Inorganic Chemistry*, Springer Berlin Heidelberg, **1974**, pp. 89–144, DOI [10.1007/bfb0116498](https://doi.org/10.1007/bfb0116498).
- [26] P. Pyykkö, “A suggested periodic table up to $Z \leq 172$, based on Dirac–Fock calculations on atoms and ions”, *Phys. Chem. Chem. Phys.* **2011**, *13*, 161–168, DOI [10.1039/c0cp01575j](https://doi.org/10.1039/c0cp01575j).
- [27] P. Indelicato, J. Bieroń, P. Jönsson, “Are MCDF calculations 101% correct in the super-heavy elements range?”, *Theoretical Chemistry Accounts* **2011**, *129*, 495–505, DOI [10.1007/s00214-010-0887-3](https://doi.org/10.1007/s00214-010-0887-3).
- [28] B. Fricke, W. Greiner, J. T. Waber, “The continuation of the periodic table up to $Z = 172$. The chemistry of superheavy elements”, *Theoretica Chimica Acta* **1971**, *21*, 235–260, DOI [10.1007/bf01172015](https://doi.org/10.1007/bf01172015).
- [29] M. G. Mayer, “On Closed Shells in Nuclei. II”, *Physical Review* **1949**, *75*, 1969–1970, DOI [10.1103/physrev.75.1969](https://doi.org/10.1103/physrev.75.1969).
- [30] T. Mayer-Kuckuk, *Kernphysik*, Vieweg+Teubner Verlag, **2002**, 372 pp.
- [31] N. Bohr, J. A. Wheeler, “The Mechanism of Nuclear Fission”, *Physical Review* **1939**, *56*, 426–450, DOI [10.1103/physrev.56.426](https://doi.org/10.1103/physrev.56.426).

- [32] G. Audi, O. Bersillon, J. Blachot, A. Wapstra, “The Nubase evaluation of nuclear and decay properties”, *Nuclear Physics A* **2003**, 729, 3–128, DOI [10.1016/j.nuclphysa.2003.11.001](https://doi.org/10.1016/j.nuclphysa.2003.11.001).
- [33] M. G. Mayer, “Nuclear Configurations in the Spin-Orbit Coupling Model. I. Empirical Evidence”, *Physical Review* **1950**, 78, 16–21, DOI [10.1103/physrev.78.16](https://doi.org/10.1103/physrev.78.16).
- [34] M. G. Mayer, “Nuclear Configurations in the Spin-Orbit Coupling Model. II. Theoretical Considerations”, *Physical Review* **1950**, 78, 22–23, DOI [10.1103/physrev.78.22](https://doi.org/10.1103/physrev.78.22).
- [35] *The Nobel Prize in Physics 1963*. NobelPrize.org. Nobel Media AB 2020, **2020**.
- [36] S. Nilsson, “Binding states of individual nucleons in strongly deformed nuclei”, *Kong. Dan. Vid. Sel. Mat. Fys. Med.* **1955**, 29N16, 1–69.
- [37] J. R. Nix, “Calculation of Fission Barriers for Heavy and Superheavy Nuclei”, *Annual Review of Nuclear Science* **1972**, 22, 65–120, DOI [10.1146/annurev.ns.22.120172.000433](https://doi.org/10.1146/annurev.ns.22.120172.000433).
- [38] A. Ghiorso, S. G. Thompson, G. H. Higgins, G. T. Seaborg, M. H. Studier, P. R. Fields, S. M. Fried, H. Diamond, J. F. Mech, G. L. Pyle, J. R. Huizenga, A. Hirsch, W. M. Manning, C. I. Browne, H. L. Smith, R. W. Spence, “New Elements Einsteinium and Fermium, Atomic Numbers 99 and 100”, *Physical Review* **1955**, 99, 1048–1049, DOI [10.1103/physrev.99.1048](https://doi.org/10.1103/physrev.99.1048).
- [39] N. Bohr, “Neutron Capture and Nuclear Constitution”, *Nature* **1936**, 137, 344–348, DOI [10.1038/137344a0](https://doi.org/10.1038/137344a0).
- [40] R. Bass, “Fusion of heavy nuclei in a classical model”, *Nuclear Physics A* **1974**, 231, 45–63, DOI [10.1016/0375-9474\(74\)90292-9](https://doi.org/10.1016/0375-9474(74)90292-9).
- [41] W. Reisdorf, M. Schädel, “How well do we understand the synthesis of heavy elements by heavy-ion induced fusion?”, *Zeitschrift für Physik A Hadrons and Nuclei* **1992**, 343, 47–57, DOI [10.1007/bf01291597](https://doi.org/10.1007/bf01291597).
- [42] *The Chemistry of Superheavy Elements*, (Eds.: M. Schädel, D. Shaughnessy), Springer Berlin Heidelberg, **2014**, DOI [10.1007/978-3-642-37466-1](https://doi.org/10.1007/978-3-642-37466-1).
- [43] W. J. Świątecki, K. Siwek-Wilczyńska, J. Wilczyński, “Fusion by diffusion. II. Synthesis of transfermium elements in cold fusion reactions”, *Physical Review C* **2005**, 71, DOI [10.1103/physrevc.71.014602](https://doi.org/10.1103/physrevc.71.014602).
- [44] E. K. HYDE, D. C. HOFFMAN, O. L. KELLER, “A History and Analysis of the Discovery of Elements 104 and 105”, *Radiochimica Acta* **1987**, 42, DOI [10.1524/ract.1987.42.2.57](https://doi.org/10.1524/ract.1987.42.2.57).
- [45] A. Türler, R. Eichler, A. Yakushev, “Chemical studies of elements with $Z \geq 104$ in gas phase”, *Nuclear Physics A* **2015**, 944, Special Issue on Superheavy Elements, 640–689, DOI <https://doi.org/10.1016/j.nuclphysa.2015.09.012>.
- [46] L. MEYER, *Modernen theorien der chemie und ihre bedeutung fur die chemische mechanik*, VERO Verlag, Place of publication not identified, **2016**.
- [47] H. Haba, “A new period in superheavy-element hunting”, *Nature Chemistry* **2018**, 11, 10–13, DOI [10.1038/s41557-018-0191-8](https://doi.org/10.1038/s41557-018-0191-8).
- [48] P. Pyykkö, “Relativistic Effects in Chemistry: More Common Than You Thought”, *Annual Review of Physical Chemistry* **2012**, 63, 45–64, DOI [10.1146/annurev-physchem-032511-143755](https://doi.org/10.1146/annurev-physchem-032511-143755).

- [49] A. Yakushev, J. M. Gates, A. Türler, M. Schädel, Ch. E. Düllmann, D. Ackermann, L.-L. Andersson, M. Block, W. Bröchle, J. Dvorak, K. Eberhardt, H. G. Essel, J. Even, U. Forsberg, A. Gorshkov, R. Graeger, K. E. Gregorich, W. Hartmann, R.-D. Herzberg, F. P. Heßberger, D. Hild, A. Hübner, E. Jäger, J. Khuyagbaatar, B. Kindler, J. V. Kratz, J. Krier, N. Kurz, B. Lommel, L. J. Niewisch, H. Nitsche, J. P. Omtvedt, E. Parr, Z. Qin, D. Rudolph, J. Runke, B. Schausten, E. Schimpf, A. Semchenkov, J. Steiner, P. Thörle-Pospiech, J. Uusitalo, M. Wegrzecki, N. Wiehl, "Superheavy Element Flerovium (Element 114) Is a Volatile Metal", *Inorganic Chemistry* **2014**, *53*, PMID: 24456007, 1624–1629, DOI [10.1021/ic4026766](https://doi.org/10.1021/ic4026766).
- [50] R. Eichler, N. Aksenov, A. Belozerov, G. Bozhikov, V. Chepigina, S. Dmitriev, R. Dressler, H. Gäggeler, A. Gorshkov, M. Itkis, F. Haenssler, A. Laube, V. Lebedev, O. Malyshev, Y. Oganessian, O. Petrushkin, D. Piguet, A. Popeko, P. Rasmussen, S. Shishkin, A. Serov, A. Shutov, A. Svirikhin, E. Tereshatov, G. Vostokin, M. Wegrzecki, A. Yerein, "Thermochemical and Physical Properties of Element 112", *Angewandte Chemie International Edition* **2008**, *47*, 3262–3266, DOI [10.1002/anie.200705019](https://doi.org/10.1002/anie.200705019).
- [51] J. V. Kratz, "Critical evaluation of the chemical properties of the transactinide elements (IUPAC Technical Report)", *Pure and Applied Chemistry* **2003**, *75*, 103–108, DOI [10.1351/pac200375010103](https://doi.org/10.1351/pac200375010103).
- [52] Y. Nagame, K. Tsukada, M. Asai, A. Toyoshima, K. Akiyama, Y. Ishii, T. Kaneko-Sato, M. Hirata, I. Nishinaka, S. Ichikawa, H. Haba, S. Enomoto, "Chemical studies on rutherfordium (Rf) at JAERI", *Radiochimica Acta* **2005**, *93*, DOI [10.1524/ract.2005.93.9-10.519](https://doi.org/10.1524/ract.2005.93.9-10.519).
- [53] K. R. Czerwinski, K. E. Gregorich, N. J. Hannink, C. D. Kacher, B. A. Kadkhodayan, S. A. Kreek, D. M. Lee, M. J. Nurmi, A. Türler, G. T. Seaborg, D. C. Hoffman, "Solution Chemistry of Element 104: Part I. Liquid-Liquid Extractions with Triisooctylamine", *Radiochimica Acta* **1994**, *64*, DOI [10.1524/ract.1994.64.1.23](https://doi.org/10.1524/ract.1994.64.1.23).
- [54] K. E. GREGORICH, R. A. HENDERSON, D. M. LEE, M. J. NURMIA, R. M. CHASTELER, H. L. HALL, D. A. BENNETT, C. M. GANNETT, R. B. CHADWICK, J. D. LEYBA, D. C. HOFFMAN, G. HERRMANN, "Aqueous Chemistry of Element 105", *Radiochimica Acta* **1988**, *43*, DOI [10.1524/ract.1988.43.4.223](https://doi.org/10.1524/ract.1988.43.4.223).
- [55] M. Schädel, W. Bröchle, E. Jäger, E. Schimpf, J. V. Kratz, U. W. Scherer, H. P. Zimmermann, "ARCA II – A New Apparatus for Fast, Repetitive HPLC Separations", *Radiochimica Acta* **1989**, *48*, DOI [10.1524/ract.1989.48.34.171](https://doi.org/10.1524/ract.1989.48.34.171).
- [56] H. Haba, D. Kaji, Y. Kudou, K. Morimoto, K. Morita, K. Ozeki, R. Sakai, T. Sumita, A. Yoneda, Y. Kasamatsu, Y. Komori, A. Shinohara, H. Kikunaga, H. Kudo, K. Nishio, K. Ooe, N. Sato, K. Tsukada, "Production of ^{265}Sg in the $^{248}\text{Cm} (^{22}\text{Ne}, 5n)^{265}\text{Sg}$ reaction and decay properties of two isomeric states in ^{265}Sg ", *Physical Review C* **2012**, *85*, DOI [10.1103/physrevc.85.024611](https://doi.org/10.1103/physrevc.85.024611).
- [57] M. Schädel, W. Bröchle, R. Dressler, B. Eichler, H. W. Gäggeler, R. Günther, K. E. Gregorich, D. C. Hoffman, S. Hübener, D. T. Jost, J. V. Kratz, W. Paulus, D. Schumann, S. Timokhin, N. Trautmann, A. Türler, G. Wirth, A. Yakushev, "Chemical properties of element 106 (seaborgium)", *Nature* **1997**, *388*, 55–57, DOI [10.1038/40375](https://doi.org/10.1038/40375).
- [58] M. Schädel, "First aqueous chemistry with seaborgium (element 106)", *Journal of Alloys and Compounds* **1998**, *271-273*, 312–315, DOI [10.1016/s0925-8388\(98\)00078-4](https://doi.org/10.1016/s0925-8388(98)00078-4).
- [59] J. Even, J. Ballof, W. Bröchle, R. Buda, Ch. E. Düllmann, K. Eberhardt, A. Gorshkov, E. Gromm, D. Hild, E. Jäger, J. Khuyagbaatar, J. Kratz, J. Krier, D. Liebe, M. Mendel, D. Nayak, K. Opel, J. Omtvedt, P. Reichert, J. Runke, A. Sabelnikov, F. Samadani, M. Schädel, B. Schausten, N. Scheid, E. Schimpf, A. Semchenkov, P. Thörle-Pospiech, A. Toyoshima, A. Türler, V. V. Vilas, N. Wiehl, T. Wunderlich, A. Yakushev, "The recoil transfer chamber—An interface to connect the physical

- preseparator TASCAs with chemistry and counting setups”, *Nuclear Instruments and Methods in Physics Research Section A: Accelerators Spectrometers Detectors and Associated Equipment* **2011**, *638*, 157–164, DOI [10.1016/j.nima.2011.02.053](https://doi.org/10.1016/j.nima.2011.02.053).
- [60] I. Zvara, Y. Chuburkov, R. Caletka, T. Zvarova, M. Shalaevskii, B. Shilov, “The chemical properties of element 104”, *Journal of Nuclear Energy* **1967**, *21*, 601–603, DOI [10.1016/0022-3107\(67\)90075-5](https://doi.org/10.1016/0022-3107(67)90075-5).
- [61] I. Zvara, Y. Chuburkov, V. Belov, G. Buklanov, B. Zakhvataev, T. Zvarova, O. Maslov, R. Caletka, M. Shalaevsky, “Experiments on chemistry of element 104—kurchatovium—V”, *Journal of Inorganic and Nuclear Chemistry* **1970**, *32*, 1885–1894, DOI [10.1016/0022-1902\(70\)80598-x](https://doi.org/10.1016/0022-1902(70)80598-x).
- [62] H. Gäggeler, D. Jost, U. Baltensperger, A. Weber, A. Kovacs, D. Vermeulen, A. Türler, “OLGA II, an on-line gas chemistry apparatus for applications in heavy element research”, *Nuclear Instruments and Methods in Physics Research Section A: Accelerators Spectrometers Detectors and Associated Equipment* **1991**, *309*, 201–208, DOI [10.1016/0168-9002\(91\)90103-w](https://doi.org/10.1016/0168-9002(91)90103-w).
- [63] B. Kadkhodayan, A. Türler, K. Gregorich, M. Nurmia, D. Lee, D. Hoffman, “The heavy element volatility instrument (HEVI)”, *Nuclear Instruments and Methods in Physics Research Section A: Accelerators Spectrometers Detectors and Associated Equipment* **1992**, *317*, 254–261, DOI [10.1016/0168-9002\(92\)90616-c](https://doi.org/10.1016/0168-9002(92)90616-c).
- [64] Ch. E. Düllmann, W. Bröchle, R. Dressler, K. Eberhardt, B. Eichler, R. Eichler, H. W. Gäggeler, T. N. Ginter, F. Glaus, K. E. Gregorich, D. C. Hoffman, E. Jäger, D. T. Jost, U. W. Kirbach, D. M. Lee, H. Nitsche, J. B. Patin, V. Pershina, D. Piguet, Z. Qin, M. Schädel, B. Schausten, E. Schimpf, H.-J. Schött, S. Soverna, R. Sudowe, P. Thörle, S. N. Timokhin, N. Trautmann, A. Türler, A. Vahle, G. Wirth, A. B. Yakushev, P. M. Zielinski, “Chemical investigation of hassium (element 108)”, *Nature* **2002**, *418*, 859–862, DOI [10.1038/nature00980](https://doi.org/10.1038/nature00980).
- [65] J. Even, A. Yakushev, Ch. E. Düllmann, H. Haba, M. Asai, T. K. Sato, H. Brand, A. Di Nitto, R. Eichler, F. L. Fan, W. Hartmann, M. Huang, E. Jäger, D. Kaji, J. Kanaya, Y. Kaneya, J. Khuyagbaatar, B. Kindler, J. V. Kratz, J. Krier, Y. Kudou, N. Kurz, B. Lommel, S. Miyashita, K. Morimoto, K. Morita, M. Murakami, Y. Nagame, H. Nitsche, K. Ooe, Z. Qin, M. Schädel, J. Steiner, T. Sumita, M. Takeyama, K. Tanaka, A. Toyoshima, K. Tsukada, A. Türler, I. Usoltsev, Y. Wakabayashi, Y. Wang, N. Wiehl, S. Yamaki, “Synthesis and detection of a seaborgium carbonyl complex”, *Science* **2014**, *345*, 1491–1493, DOI [10.1126/science.1255720](https://doi.org/10.1126/science.1255720).
- [66] M. Götz, S. Götz, J.-V. Kratz, J. Ballof, C. E. Düllmann, K. Eberhardt, C. Mokry, D. Renisch, J. Runke, T. K. Sato, P. Thörle-Pospiech, N. Trautmann, A. Yakushev, “Gas phase synthesis of 4d transition metal carbonyl complexes with thermalized fission fragments in single-atom reactions”, *Radiochimica Acta* **2021**, *109*, 153–165, DOI [10.1515/ract-2020-0052](https://doi.org/10.1515/ract-2020-0052).
- [67] K. Morita, K. Morimoto, D. Kaji, T. Akiyama, S.-i. Goto, H. Haba, E. Ideguchi, R. Kanungo, K. Katori, H. Koura, H. Kudo, T. Ohnishi, A. Ozawa, T. Suda, K. Sueki, H. Xu, T. Yamaguchi, A. Yoneda, A. Yoshida, Y. Zhao, “Experiment on the Synthesis of Element 113 in the Reaction $^{209}\text{Bi}(^{70}\text{Zn},n)^{278}113$ ”, *Journal of the Physical Society of Japan* **2004**, *73*, 2593–2596, DOI [10.1143/JPSJ.73.2593](https://doi.org/10.1143/JPSJ.73.2593).
- [68] L. Lens, PhD thesis, Fachbereich Chemie der Johannes Gutenberg-Universität Mainz, **2018**.
- [69] Y. T. Oganessian, V. K. Utyonkov, “Super-heavy element research”, *Reports on Progress in Physics* **2015**, *78*, 036301, DOI [10.1088/0034-4885/78/3/036301](https://doi.org/10.1088/0034-4885/78/3/036301).
- [70] E. Sylwester, K. Gregorich, D. Lee, B. Kadkhodayan, A. Türler, J. Adams, C. Kacher, M. Lane, C. Laue, C. McGrath, “On-line gas chromatographic studies of Rf, Zr, and Hf bromides”, *Radiochimica Acta* **2000**, *88*, DOI [10.1524/ract.2000.88.12.837](https://doi.org/10.1524/ract.2000.88.12.837).

- [71] A. Türler, G. Buklanov, B. Eichler, H. Gäggeler, M. Grantz, S. Hübener, D. Jost, V. Lebedev, D. Piguet, S. Timokhin, A. Yakushev, I. Zvara, "Evidence for relativistic effects in the chemistry of element 104", *Journal of Alloys and Compounds* **1998**, *271-273*, 287–291, DOI [10.1016/s0925-8388\(98\)00072-3](https://doi.org/10.1016/s0925-8388(98)00072-3).
- [72] M.-S. Lin, F.-L. Fan, W. X. Huang, X. L. Yan, J. Bai, X. L. Wu, F. A. Lei, H. J. Ding, F. Ma, G. S. Li, H. B. Zhou, J.-S. Guo, "On-line gas chromatographic studies of Nb, Ta, and Db bromides", *Radiochimica Acta* **2012**, *100*, 285–289, DOI [10.1524/ract.2012.1924](https://doi.org/10.1524/ract.2012.1924).
- [73] A. Türler, H. W. Gäggeler, K. E. Gregorich, H. Barth, W. Bröchle, K. R. Czerwinski, M. K. Gober, N. J. Hannink, R. A. Henderson, D. C. Hoffman, D. T. Jost, C. D. Kacher, B. Kadkhodayan, J. Kovacs, J. V. Kratz, S. A. Kreek, D. M. Lee, J. D. Leyba, M. J. Nurmi, M. Schädel, U. W. Scherer, Schimpf, D. Vermeulen, A. Weber, H. P. Zimmermann, I. Zvara, "Gas phase chromatography of halides of elements 104 and 105", *Journal of Radioanalytical and Nuclear Chemistry Articles* **1992**, *160*, 327–339, DOI [10.1007/bf02037108](https://doi.org/10.1007/bf02037108).
- [74] I. Zvara, A. B. Yakushev, S. N. Timokhin, X. Honggui, V. P. Perelygin, Y. T. Chuburkov, "Chemical Identification of Element 106 (Thermochromatography of Oxochlorides)", *Radiochimica Acta* **1998**, *81*, DOI [10.1524/ract.1998.81.4.179](https://doi.org/10.1524/ract.1998.81.4.179).
- [75] S. Hübener, S. Taut, A. Vahle, R. Dressler, B. Eichler, H. W. Gäggeler, D. Jost, D. Piguet, A. Türler, W. Bröchle, "Physico-chemical characterization of seaborgium as oxide hydroxide", *Radiochimica Acta* **2001**, *89*, DOI [10.1524/ract.2001.89.11-12.737](https://doi.org/10.1524/ract.2001.89.11-12.737).
- [76] A. Türler, W. Bröchle, R. Dressler, B. Eichler, R. Eichler, H. W. Gäggeler, M. Gärtner, J.-P. Glatz, K. E. Gregorich, S. Hübener, D. T. Jost, V. Y. Lebedev, V. G. Pershina, M. Schädel, S. Taut, S. N. Timokhin, N. Trautmann, A. Vahle, A. B. Yakushev, "First Measurement of a Thermochemical Property of a Seaborgium Compound", *Angewandte Chemie International Edition* **1999**, *38*, 2212–2213, DOI [10.1002/\(sici\)1521-3773\(19990802\)38:15<2212::aid-anie2212>3.0.co;2-6](https://doi.org/10.1002/(sici)1521-3773(19990802)38:15<2212::aid-anie2212>3.0.co;2-6).
- [77] R. Eichler, W. Bröchle, R. Dressler, C. Düllmann, B. Eichler, H. W. Gäggeler, K. E. Gregorich, D. C. Hoffman, S. Hübener, D. T. Jost, U. W. Kirbach, C. A. Laue, V. M. Lavanchy, H. Nitsche, J. B. Patin, D. Piguet, M. Schädel, D. A. Shaughnessy, D. A. Strellis, S. Taut, L. Tobler, Y. S. Tsyganov, A. Türler, A. Vahle, P. A. Wilk, A. B. Yakushev, "Chemical characterization of bohrium (element 107)", *Nature* **2000**, *407*, 63–65, DOI [10.1038/35024044](https://doi.org/10.1038/35024044).
- [78] R. Eichler, W. Bröchle, R. Buda, S. Bürger, R. Dressler, Ch. E. Düllmann, J. Dvorak, K. Eberhardt, B. Eichler, C. M. Folden, H. W. Gäggeler, K. E. Gregorich, F. Haenssler, D. C. Hoffman, H. Hummrich, E. Jäger, J. V. Kratz, B. Kuczewski, D. Liebe, D. Nayak, H. Nitsche, D. Piguet, Z. Qin, U. Rieth, M. Schädel, B. Schausten, E. Schimpf, A. Semchenkov, S. Soverna, R. Sudowe, N. Trautmann, P. Thörle, A. Türler, B. Wierczinski, N. Wiehl, P. A. Wilk, G. Wirth, A. B. Yakushev, A. von Zweidorf, "Attempts to chemically investigate element 112", *Radiochimica Acta* **2006**, *94*, DOI [10.1524/ract.2006.94.4.181](https://doi.org/10.1524/ract.2006.94.4.181).
- [79] R. Eichler, N. V. Aksenov, A. V. Belozerov, G. A. Bozhikov, V. I. Chepigin, S. N. Dmitriev, R. Dressler, H. W. Gäggeler, V. A. Gorshkov, F. Haenssler, M. G. Itkis, A. Laube, V. Y. Lebedev, O. N. Malyshev, Y. T. Oganessian, O. V. Petrushkin, D. Piguet, P. Rasmussen, S. V. Shishkin, A. V. Shutov, A. I. Svirikhin, E. E. Tereshatov, G. K. Vostokin, M. Wegrzecki, A. V. Yeregin, "Chemical characterization of element 112", *Nature* **2007**, *447*, 72–75, DOI [10.1038/nature05761](https://doi.org/10.1038/nature05761).
- [80] N. V. Aksenov, P. Steinegger, F. S. Abdullin, Y. V. Albin, G. A. Bozhikov, V. I. Chepigin, R. Eichler, V. Y. Lebedev, A. S. Madumarov, O. N. Malyshev, O. V. Petrushkin, A. N. Polyakov, Y. A. Popov, A. V. Sabel'nikov, R. N. Sagaidak, I. V. Shirokovsky, M. V. Shumeiko, G. Y. Starodub, Y. S. Tsyganov, V. K. Utyonkov, A. A. Voinov, G. K. Vostokin, A. V. Yeregin, S. N. Dmitriev, "On the volatility

- of nihonium (Nh, $Z = 113$)”, *The European Physical Journal A* **2017**, *53*, DOI [10.1140/epja/i2017-12348-8](https://doi.org/10.1140/epja/i2017-12348-8).
- [81] S. N. Dmitriev, N. V. Aksenov, Y. V. Albin, G. A. Bozhikov, M. L. Chelnokov, V. I. Chepygin, R. Eichler, A. V. Isaev, D. E. Katrasev, V. Y. Lebedev, O. N. Malyshev, O. V. Petrushkin, L. S. Porobanuk, M. A. Ryabinin, A. V. Sabel’nikov, E. A. Sokol, A. V. Svirikhin, G. Y. Starodub, I. Usoltsev, G. K. Vostokin, A. V. Yeremin, “Pioneering experiments on the chemical properties of element 113”, *Mendeleev Communications* **2014**, *24*, 253–256, DOI [10.1016/j.mencom.2014.09.001](https://doi.org/10.1016/j.mencom.2014.09.001).
- [82] A. Yakushev, R. Eichler, “Gas-phase chemistry of element 114, flerovium”, *EPJ Web of Conferences* **2016**, *131*, (Ed.: D. Rudolph), 07003, DOI [10.1051/epjconf/201613107003](https://doi.org/10.1051/epjconf/201613107003).
- [83] R. Eichler, N. V. Aksenov, Y. V. Albin, A. V. Belozerov, G. A. Bozhikov, V. I. Chepigin, S. N. Dmitriev, R. Dressler, H. W. Gäggeler, V. A. Gorshkov, G. Henderson, et al., “Indication for a volatile element 114”, *Radiochimica Acta* **2010**, *98*, DOI [10.1524/ract.2010.1705](https://doi.org/10.1524/ract.2010.1705).
- [84] H. Wollnik, “Principles behind a He-jet system and its application for isotope separation”, *Nuclear Instruments and Methods* **1976**, *139*, 311–318, DOI [10.1016/0029-554x\(76\)90691-1](https://doi.org/10.1016/0029-554x(76)90691-1).
- [85] Ch. E. Düllmann, C.M. Folden, K. Gregorich, D.C. Hoffman, D. Leitner, G.K. Pang, R. Sudowe, P.M. Zielinski, H. Nitsche, “Heavy-ion-induced production and physical pre-separation of short-lived isotopes for chemistry experiments”, *Nuclear Instruments and Methods in Physics Research Section A: Accelerators Spectrometers Detectors and Associated Equipment* **2005**, *551*, 528–539, DOI [10.1016/j.nima.2005.05.077](https://doi.org/10.1016/j.nima.2005.05.077).
- [86] Ch. E. Düllmann, “Physical pre-separation: A powerful new method for transactinide chemists”, *The European Physical Journal D* **2007**, *45*, 75–80, DOI [10.1140/epjd/e2007-00033-9](https://doi.org/10.1140/epjd/e2007-00033-9).
- [87] V. Ninov, K. E. Gregorich, C. A. McGrath in ASCE, **1998**, DOI [10.1063/1.57362](https://doi.org/10.1063/1.57362).
- [88] U. Kirbach, C. F. III, T. Ginter, K. Gregorich, D. Lee, V. Ninov, J. Omtvedt, J. Patin, N. Seward, D. Strellis, R. Sudowe, A. Türler, P. Wilk, P. Zielinski, D. Hoffman, H. Nitsche, “The Cryo-Thermochromatographic Separator (CTS):” *Nuclear Instruments and Methods in Physics Research Section A: Accelerators Spectrometers Detectors and Associated Equipment* **2002**, *484*, 587–594, DOI [10.1016/s0168-9002\(01\)01990-8](https://doi.org/10.1016/s0168-9002(01)01990-8).
- [89] P. Steinegger, R. Dressler, R. Eichler, D. Piguet, S. Streuli, A. Türler, “Diamond detectors for high-temperature transactinide chemistry experiments”, *Nuclear Instruments and Methods in Physics Research Section A: Accelerators Spectrometers Detectors and Associated Equipment* **2017**, *850*, 61–67, DOI [10.1016/j.nima.2016.12.014](https://doi.org/10.1016/j.nima.2016.12.014).
- [90] P. Steinegger, M. Asai, R. Dressler, R. Eichler, Y. Kaneya, A. Mitsukai, Y. Nagame, D. Piguet, T. K. Sato, M. Schädel, S. Takeda, A. Toyoshima, K. Tsukada, A. Türler, A. Vascon, “Vacuum Chromatography of Tl on SiO₂ at the Single-Atom Level”, *The Journal of Physical Chemistry C* **2016**, *120*, 7122–7132, DOI [10.1021/acs.jpcc.5b12033](https://doi.org/10.1021/acs.jpcc.5b12033).
- [91] M. Wada in AIP Conference Proceedings, AIP, **2002**, DOI [10.1063/1.1454340](https://doi.org/10.1063/1.1454340).
- [92] J. Neumayr, L. Beck, D. Habs, S. Heinz, J. Szerypo, P. Thierolf, V. Varentsov, F. Voit, D. Ackermann, D. Beck, M. Block, Z. Di, S. Eliseev, H. Geissel, F. Herfurth, F. Heßberger, S. Hofmann, H.-J. Kluge, M. Mukherjee, G. Münzenberg, M. Petrick, W. Quint, S. Rahaman, C. Rauth, D. Rodríguez, C. Scheidenberger, G. Sikler, Z. Wang, C. Weber, W. Plaß, M. Breitenfeldt, A. Chaudhuri, G. Marx, L. Schweikhard, A. Dodonov, Y. Novikov, M. Suhonen, “The ion-catcher device for SHIPTRAP”, *Nuclear Instruments and Methods in Physics Research Section B: Beam Interactions with Materials and Atoms* **2006**, *244*, 489–500, DOI <https://doi.org/10.1016/j.nimb.2005.10.017>.

- [93] S. Eliseev, M. Block, A. Chaudhuri, Z. Di, D. Habs, F. Herfurth, H.-J. Kluge, J. Neumayr, W. Plaß, C. Rauth, P. Thierolf, G. Vorobjev, Z. Wang, “Extraction efficiency and extraction time of the SHIPTRAP gas-filled stopping cell”, *Nuclear Instruments and Methods in Physics Research Section B: Beam Interactions with Materials and Atoms* **2007**, *258*, 479–484, DOI <https://doi.org/10.1016/j.nimb.2007.01.291>.
- [94] Y. T. Oganessian, A. Sobiczewski, G. M. Ter-Akopian, “Superheavy nuclei: from predictions to discovery”, *Physica Scripta* **2017**, *92*, 023003, DOI [10.1088/1402-4896/aa53c1](https://doi.org/10.1088/1402-4896/aa53c1).
- [95] J. Ärje, K. Valli, “Helium-jet ion guide for an on-line isotope separator”, *Nuclear Instruments and Methods* **1981**, *179*, 533–539, DOI [10.1016/0029-554x\(81\)90179-8](https://doi.org/10.1016/0029-554x(81)90179-8).
- [96] P. A. Tipler, G. Mosca, *Physik*, (Eds.: P. Kersten, J. Wagner), Springer Berlin Heidelberg, **2019**, DOI [10.1007/978-3-662-58281-7](https://doi.org/10.1007/978-3-662-58281-7).
- [97] C. Droese, S. Eliseev, K. Blaum, M. Block, F. Herfurth, M. Laatiaoui, F. Lautenschläger, E. M. Ramirez, L. Schweikhard, V. Simon, P. Thierolf, “The cryogenic gas stopping cell of SHIPTRAP”, *Nuclear Instruments and Methods in Physics Research Section B: Beam Interactions with Materials and Atoms* **2014**, *338*, 126–138, DOI <https://doi.org/10.1016/j.nimb.2014.08.004>.
- [98] J. Ärje, J. Äystö, H. Hyvönen, P. Taskinen, V. Koponen, J. Honkanen, A. Hautojärvi, K. Vierinen, “Submillisecond On-Line Mass Separation of Nonvolatile Radioactive Elements: An Application of Charge Exchange and Thermalization Processes of Primary Recoil Ions in Helium”, *Physical Review Letters* **1985**, *54*, 99–101, DOI [10.1103/physrevlett.54.99](https://doi.org/10.1103/physrevlett.54.99).
- [99] M. Huysse, M. Facina, Y. Kudryavtsev, P. V. Duppen, I. collaboration, “Intensity limitations of a gas cell for stopping, storing and guiding of radioactive ions”, *Nuclear Instruments and Methods in Physics Research Section B: Beam Interactions with Materials and Atoms* **2002**, *187*, 535–547, DOI [10.1016/s0168-583x\(01\)01152-1](https://doi.org/10.1016/s0168-583x(01)01152-1).
- [100] J. B. Neumayr, P. G. Thierolf, D. Habs, S. Heinz, V. S. Kolhinen, M. Sewtz, J. Szerypo, “Performance of the MLL-IonCatcher”, *Review of Scientific Instruments* **2006**, *77*, 065109, DOI [10.1063/1.2213154](https://doi.org/10.1063/1.2213154).
- [101] Y. Kudryavtsev, B. Bruyneel, M. Huysse, J. Gentens, P. V. den Bergh, P. V. Duppen, L. Vermeeren, “A gas cell for thermalizing, storing and transporting radioactive ions and atoms. Part I: Off-line studies with a laser ion source”, *Nuclear Instruments and Methods in Physics Research Section B: Beam Interactions with Materials and Atoms* **2001**, *179*, 412–435, DOI [10.1016/s0168-583x\(01\)00575-4](https://doi.org/10.1016/s0168-583x(01)00575-4).
- [102] M. Facina, C. Bachelet, M. Block, G. Bollen, D. Davies, C. Folden, C. Guenaut, J. Huikari, E. Kwan, D. Morrissey, G. Pang, A. Prinke, R. Ringle, J. Savory, P. Schury, S. Schwarz, C. Sumithrarachchi, T. Sun, “Charged particle transport and extraction studies in the NSCL gas cell for stopping radioactive fragments”, *Nuclear Instruments and Methods in Physics Research Section B: Beam Interactions with Materials and Atoms* **2008**, *266*, Proceedings of the XVth International Conference on Electromagnetic Isotope Separators and Techniques Related to their Applications, 4471–4474, DOI <https://doi.org/10.1016/j.nimb.2008.05.052>.
- [103] F. Bloch, “Bremsvermögen von Atomen mit mehreren Elektronen”, *Zeitschrift für Physik* **1933**, *81*, 363–376, DOI [10.1007/bf01344553](https://doi.org/10.1007/bf01344553).
- [104] J. F. Ziegler, M. Ziegler, J. Biersack, “SRIM – The stopping and range of ions in matter (2010)”, *Nuclear Instruments and Methods in Physics Research Section B: Beam Interactions with Materials and Atoms* **2010**, *268*, 1818–1823, DOI [10.1016/j.nimb.2010.02.091](https://doi.org/10.1016/j.nimb.2010.02.091).
- [105] J. Äystö, “Overview of recent highlights at ISOL facilities”, *Nuclear Physics A* **2008**, *805*, 162c–171c, DOI [10.1016/j.nuclphysa.2008.02.237](https://doi.org/10.1016/j.nuclphysa.2008.02.237).

- [106] D. Morrissey, G. Bollen, M. Facina, S. Schwarz, “Pulsed extraction of ionization from helium buffer gas”, *Nuclear Instruments and Methods in Physics Research Section B: Beam Interactions with Materials and Atoms* **2008**, *266*, 4822–4828, DOI [10.1016/j.nimb.2008.07.018](https://doi.org/10.1016/j.nimb.2008.07.018).
- [107] B. H. Mahan, “Mechanism for Ion—Neutral Association Reactions”, *The Journal of Chemical Physics* **1965**, *43*, 3080–3082, DOI [10.1063/1.1697280](https://doi.org/10.1063/1.1697280).
- [108] M. Wada, “Genealogy of gas cells for low-energy RI-beam production”, *Nuclear Instruments and Methods in Physics Research Section B: Beam Interactions with Materials and Atoms* **2013**, *317*, 450–456, DOI [10.1016/j.nimb.2013.08.062](https://doi.org/10.1016/j.nimb.2013.08.062).
- [109] F. Paschen, “Ueber die zum Funkenübergang in Luft, Wasserstoff und Kohlensäure bei verschiedenen Drucken erforderliche Potentialdifferenz”, *Annalen der Physik* **1889**, *273*, 69–96, DOI [10.1002/andp.18892730505](https://doi.org/10.1002/andp.18892730505).
- [110] L. Weissman, D. Morrissey, G. Bollen, D. Davies, E. Kwan, P. Lofy, P. Schury, S. Schwarz, C. Sumithrarachchi, T. Sun, R. Ringle, “Conversion of $^{38}\text{Ca}/^{37}\text{K}$ projectile fragments into thermalized ion beams”, *Nuclear Instruments and Methods in Physics Research Section A: Accelerators Spectrometers Detectors and Associated Equipment* **2005**, *540*, 245–258, DOI [10.1016/j.nima.2004.11.048](https://doi.org/10.1016/j.nima.2004.11.048).
- [111] W. Paul, H. Steinwedel, “Notizen: Ein neues Massenspektrometer ohne Magnetfeld”, *Zeitschrift für Naturforschung A* **1953**, *8*, 448–450, DOI [10.1515/zna-1953-0710](https://doi.org/10.1515/zna-1953-0710).
- [112] S. Masuda, T. Kamimura, “Approximate methods for calculating a non-uniform travelling field”, *Journal of Electrostatics* **1975**, *1*, 351–370, DOI [10.1016/0304-3886\(75\)90030-3](https://doi.org/10.1016/0304-3886(75)90030-3).
- [113] G. Savard, “Large radio-frequency gas catchers and the production of radioactive nuclear beams”, *Journal of Physics: Conference Series* **2011**, *312*, 052004, DOI [10.1088/1742-6596/312/5/052004](https://doi.org/10.1088/1742-6596/312/5/052004).
- [114] P. G. Thirolf in Euroschool on Exotic Beams, FLNR Dubna, Russia, **2013**.
- [115] L. Lens, A. Yakushev, Ch. E. Düllmann, M. Asai, J. Ballof, M. Block, H. M. David, J. Despotopoulos, A. D. Nitto, K. Eberhardt, J. Even, M. Götz, S. Götz, H. Haba, L. Harkness-Brennan, F. P. Heßberger, R. D. Herzberg, J. Hoffmann, A. Hübner, E. Jäger, D. Judson, J. Khuyagbaatar, B. Kindler, Y. Komori, J. Konki, J. V. Kratz, J. Krier, N. Kurz, M. Laatiaoui, S. Lahiri, B. Lommel, M. Maiti, A. K. Mistry, C. Mokry, K. Moody, Y. Nagame, J. P. Omtvedt, P. Papadakis, V. Pershina, J. Runke, M. Schädel, P. Scharrer, T. Sato, D. Shaughnessy, B. Schausten, P. Thörle-Pospiech, N. Trautmann, K. Tsukada, J. Uusitalo, A. Ward, M. Wegrzecki, N. Wiehl, V. Yakusheva, “Online chemical adsorption studies of Hg, Tl, and Pb on SiO_2 and Au surfaces in preparation for chemical investigations on Cn, Nh, and Fl at TASCA”, *Radiochimica Acta* **2018**, *106*, 949–962, DOI [10.1515/ract-2017-2914](https://doi.org/10.1515/ract-2017-2914).
- [116] P. W. Atkins, J. de Paula, *Physikalische Chemie*, Wiley-VCH GmbH, **2013**.
- [117] G. Wedler, H.-J. Freund, *Lehr- und Arbeitsbuch Physikalische Chemie*, Wiley-VCH GmbH, **2018**.
- [118] D. C. Harris, *Lehrbuch der Quantitativen Analyse*, (Eds.: G. Werner, T. Werner), Springer Berlin Heidelberg, **2014**, DOI [10.1007/978-3-642-37788-4](https://doi.org/10.1007/978-3-642-37788-4).
- [119] D. A. Skoog, J. J. Leary, *Instrumentelle Analytik*, Springer Berlin Heidelberg, **1996**, DOI [10.1007/978-3-662-07916-4](https://doi.org/10.1007/978-3-662-07916-4).
- [120] H. Thiele, “The Dynamical Character of Adsorption, von H. J. de Boer. Oxford University Press, 1953. 1. Aufl. X V, 239 S., 45 Abb. gebd. s. 30.—”, *Angewandte Chemie* **1953**, *65*, 431–431, DOI [10.1002/ange.19530651619](https://doi.org/10.1002/ange.19530651619).
- [121] I. Zvára, “Simulation of Thermo chromatographic Processes by the Monte Carlo Method”, *Radiochimica Acta* **1985**, *38*, DOI [10.1524/ract.1985.38.2.95](https://doi.org/10.1524/ract.1985.38.2.95).
- [122] A. Türler, “Gas Phase Chemistry Experiments with Transactinide Elements”, *Radiochimica Acta* **1996**, *72*, DOI [10.1524/ract.1996.72.1.7](https://doi.org/10.1524/ract.1996.72.1.7).

- [123] I. Zvara, “Thermochromatographic Method of Separation of Chemical Elements in Nuclear and Radiochemistry”, *Isotopenpraxis Isotopes in Environmental and Health Studies* **1990**, *26*, 251–258, DOI [10.1080/10256019008624294](https://doi.org/10.1080/10256019008624294).
- [124] I. Zvara, “Problems in thermochromatographic separation of radioelements”, *Journal of Radioanalytical and Nuclear Chemistry Articles* **1996**, *204*, 123–134, DOI [10.1007/bf02060873](https://doi.org/10.1007/bf02060873).
- [125] A. Vahle, S. Hübener, R. Dressler, B. Eichler, A. Türler, “Reaction Gas Chromatography of Oxide and Hydroxide Species of Molybdenum - Simulation and Experiment”, *Radiochimica Acta* **1997**, *78*, DOI [10.1524/ract.1997.78.special-issue.53](https://doi.org/10.1524/ract.1997.78.special-issue.53).
- [126] P. Debye, “Zur Theorie der spezifischen Wärmen”, *Annalen der Physik* **1912**, *344*, 789–839, DOI [10.1002/andp.19123441404](https://doi.org/10.1002/andp.19123441404).
- [127] E. R. Gilliland, “Diffusion Coefficients in Gaseous Systems”, *Industrial & Engineering Chemistry* **1934**, *26*, 681–685, DOI [10.1021/ie50294a020](https://doi.org/10.1021/ie50294a020).
- [128] I. Zvara, *The Inorganic Radiochemistry of Heavy Elements*, Springer-Verlag GmbH, **2008**.
- [129] O. Reynolds, “III. An experimental investigation of the circumstances which determine whether the motion of water shall be direct or sinuous, and of the law of resistance in parallel channels”, *Proceedings of the Royal Society of London* **1883**, *35*, 84–99, DOI [10.1098/rsp1.1883.0018](https://doi.org/10.1098/rsp1.1883.0018).
- [130] B. R. Munson, A. P. Rothmayer, T. H. Okiishi, *Fundamentals of Fluid Mechanics*, WILEY, **2012**, 747 pp.
- [131] R. B. Bird, W. E. Stewart, E. N. Lightfoot, *Transport Phenomena*, John Wiley & Sons Inc, **2006**, 928 pp.
- [132] W. Haynes, *CRC handbook of chemistry and physics : a ready-reference book of chemical and physical data*, CRC Press, Boca Raton, Florida, **2017**.
- [133] R. Eichler, N. V. Aksenov, A. V. Belozerov, G. A. Bozhikov, V. I. Chepigin, S. N. Dmitriev, R. Dressler, H. W. Gäggeler, A. V. Gorshkov, M. G. Itkis, F. Haenssler, A. Laube, V. Y. Lebedev, O. N. Malyshev, Y. T. Oganessian, O. V. Petrushkin, D. Piguet, A. G. Popeko, P. Rasmussen, S. V. Shishkin, A. A. Serov, A. V. Shutov, A. I. Svirikhin, E. E. Tereshatov, G. K. Vostokin, M. Wegrzecki, A. V. Yerebin, “Thermochemische und physikalische Eigenschaften von Element 112”, *Angewandte Chemie* **2008**, *120*, 3306–3310, DOI [10.1002/ange.200705019](https://doi.org/10.1002/ange.200705019).
- [134] V. Pershina, A. Borschevsky, J. Anton, T. Jacob, “Theoretical predictions of trends in spectroscopic properties of homonuclear dimers and volatility of the 7p elements”, *The Journal of Chemical Physics* **2010**, *132*, 194314, DOI [10.1063/1.3425996](https://doi.org/10.1063/1.3425996).
- [135] V. Pershina in *Handbook of Relativistic Quantum Chemistry*, Springer Berlin Heidelberg, **2016**, pp. 857–899, DOI [10.1007/978-3-642-40766-6_35](https://doi.org/10.1007/978-3-642-40766-6_35).
- [136] V. Pershina, “A relativistic periodic DFT study on interaction of superheavy elements 112 (Cn) and 114 (Fl) and their homologs Hg and Pb, respectively, with a quartz surface”, *Physical Chemistry Chemical Physics* **2016**, *18*, 17750–17756, DOI [10.1039/c6cp02253g](https://doi.org/10.1039/c6cp02253g).
- [137] M. Ranjan, S. Purushothaman, T. Dickel, H. Geissel, W. R. Plass, D. Schäfer, C. Scheidenberger, J. V. de Walle, H. Weick, P. Dendooven, “New stopping cell capabilities: RF carpet performance at high gas density and cryogenic operation”, *EPL (Europhysics Letters)* **2011**, *96*, 52001, DOI [10.1209/0295-5075/96/52001](https://doi.org/10.1209/0295-5075/96/52001).
- [138] P. Dendooven, “The development and status of the IGISOL technique”, *Nuclear Instruments and Methods in Physics Research Section B: Beam Interactions with Materials and Atoms* **1997**, *126*, International Conference on Electromagnetic Isotope Separators and Techniques Related to Their Applications, 182–189, DOI [https://doi.org/10.1016/S0168-583X\(96\)01010-5](https://doi.org/10.1016/S0168-583X(96)01010-5).

- [139] National Nuclear Data Center, available at <http://www.nndc.bnl.gov/>, (accessed on March 8, 2021).
- [140] A. F. Holleman, E. Wiberg, N. Wiberg, *Lehrbuch der Anorganischen Chemie*. Gruyter, 1995.
- [141] C. Housecroft, A. G. Sharpe, *Anorganische Chemie*, Pearson Studium, München, 2006.
- [142] E. Riedel, C. Janiak, *Anorganische Chemie*, DE GRUYTER, 2010, DOI [10.1515/9783110225679](https://doi.org/10.1515/9783110225679).
- [143] W. Parker, R. Falk, “Molecular plating: A method for the electrolytic formation of thin inorganic films”, *Nuclear Instruments and Methods* **1962**, *16*, 355–357, DOI [https://doi.org/10.1016/0029-554X\(62\)90142-8](https://doi.org/10.1016/0029-554X(62)90142-8).
- [144] N. Getoff, H. Bildstein, E. Proksch, “Molecular plating, V. The influence of some experimental factors on the deposition yield”, *Nuclear Instruments and Methods* **1967**, *46*, 305–308, DOI [10.1016/0029-554x\(67\)90088-2](https://doi.org/10.1016/0029-554x(67)90088-2).
- [145] K. Eberhardt, W. Bröchle, Ch. E. Düllmann, K. Gregorich, W. Hartmann, A. Hübner, E. Jäger, B. Kindler, J. Kratz, D. Liebe, B. Lommel, H.-J. Maier, M. Schädel, B. Schausten, E. Schimpf, A. Semchenkov, J. Steiner, J. Szerypo, P. Thörle, A. Türler, A. Yakushev, “Preparation of targets for the gas-filled recoil separator TASCA by electrochemical deposition and design of the TASCA target wheel assembly”, *Nuclear Instruments and Methods in Physics Research Section A: Accelerators Spectrometers Detectors and Associated Equipment* **2008**, *590*, 134–140, DOI [10.1016/j.nima.2008.02.069](https://doi.org/10.1016/j.nima.2008.02.069).
- [146] A. Vascon, S. Santi, A. Isse, T. Reich, J. Drebert, H. Christ, Ch. E. Düllmann, K. Eberhardt, “Elucidation of constant current density molecular plating”, *Nuclear Instruments and Methods in Physics Research Section A: Accelerators Spectrometers Detectors and Associated Equipment* **2012**, *696*, 180–191, DOI [10.1016/j.nima.2012.08.072](https://doi.org/10.1016/j.nima.2012.08.072).
- [147] P. Schwamb, Dissertation, Institute for Physic, University Mainz, 1996.
- [148] R. Tribble, R. Burch, C. Gagliardi, “MARS: A momentum achromat recoil spectrometer”, *Nuclear Instruments and Methods in Physics Research Section A: Accelerators Spectrometers Detectors and Associated Equipment* **1989**, *285*, 441–446, DOI [10.1016/0168-9002\(89\)90215-5](https://doi.org/10.1016/0168-9002(89)90215-5).
- [149] J. M. Gates, Ch. E. Düllmann, M. Schädel, A. Yakushev, A. Türler, K. Eberhardt, J. V. Kratz, D. Ackermann, L.-L. Andersson, M. Block, W. Bröchle, J. Dvorak, H. G. Essel, P. A. Ellison, J. Even, U. Forsberg, J. Gellanki, A. Gorshkov, R. Graeger, K. E. Gregorich, W. Hartmann, R.-D. Herzberg, F. P. Heßberger, D. Hild, A. Hübner, E. Jäger, J. Khuyagbaatar, B. Kindler, J. Krier, N. Kurz, S. Lahiri, D. Liebe, B. Lommel, M. Maiti, H. Nitsche, J. P. Omtvedt, E. Parr, D. Rudolph, J. Runke, H. Schaffner, B. Schausten, E. Schimpf, A. Semchenkov, J. Steiner, P. Thörle-Pospiech, J. Uusitalo, M. Wegrzecki, N. Wiehl, “First superheavy element experiments at the GSI recoil separator TASCA: The production and decay of element 114 in the $^{244}\text{Pu}(^{48}\text{Ca},3-4n)$ reaction”, *Phys. Rev. C* **2011**, *83*, 054618, DOI [10.1103/PhysRevC.83.054618](https://doi.org/10.1103/PhysRevC.83.054618).
- [150] W. Barth, W. Bayer, L. Dahl, L. Groening, S. Richter, S. Yaramyshev, “Upgrade program of the high current heavy ion UNILAC as an injector for FAIR”, *Nuclear Instruments and Methods in Physics Research Section A: Accelerators Spectrometers Detectors and Associated Equipment* **2007**, *577*, 211–214, DOI [10.1016/j.nima.2007.02.054](https://doi.org/10.1016/j.nima.2007.02.054).
- [151] M. Schädel, “Superheavy element chemistry at GSI – status and perspectives”, *The European Physical Journal D* **2007**, *45*, 67–74, DOI [10.1140/epjd/e2007-00036-6](https://doi.org/10.1140/epjd/e2007-00036-6).

- [152] C. Folden, M. Alfonso, D. Mayorov, K. Lawrence, A. Alharbi, E. Berdugo, P. Cammarata, A. Raphelt, B. Roeder, T. Werke, “Development of the MARS separator for heavy element studies”, *Nuclear Instruments and Methods in Physics Research Section A: Accelerators Spectrometers Detectors and Associated Equipment* **2012**, 678, 1–7, DOI [10.1016/j.nima.2012.02.035](https://doi.org/10.1016/j.nima.2012.02.035).
- [153] G. Christian, C. M. Folden, J. Hardy, Y.-W. Lui, D. May, D. Melconian, J. Natowitz, R. Rapp, G. Rogachev, R. Tribble, S. Yennello, “The Cyclotron Institute at Texas A&M University”, *Nuclear Physics News* **2017**, 27, 5–13, DOI [10.1080/10619127.2017.1315281](https://doi.org/10.1080/10619127.2017.1315281).
- [154] P. Scharrer, PhD thesis, Fachbereich Physik der Johannes Gutenberg-Universität Mainz, **2017**, Dissertation zur Erlangung des Grades ”Doktor der Naturwissenschaften”.
- [155] B. Lommel, W. Bröchle, K. Eberhardt, W. Hartmann, A. Hübner, B. Kindler, J. V. Kratz, D. Liebe, M. Schädel, J. Steiner, “Backings and targets for chemical and nuclear studies of transactinides with TASCAs”, *Nuclear Instruments and Methods in Physics Research Section A: Accelerators Spectrometers Detectors and Associated Equipment* **2008**, 590, 141–144, DOI [10.1016/j.nima.2008.02.045](https://doi.org/10.1016/j.nima.2008.02.045).
- [156] E. Jäger, H. Brand, C. E. Düllmann, J. Khuyagbaatar, J. Krier, M. Schädel, T. Torres, A. Yakushev, “High intensity target wheel at TASCAs: target wheel control system and target monitoring”, *Journal of Radioanalytical and Nuclear Chemistry* **2013**, 299, 1073–1079, DOI [10.1007/s10967-013-2645-1](https://doi.org/10.1007/s10967-013-2645-1).
- [157] M. Ohring in *Materials Science of Thin Films*, Elsevier, **2002**, pp. 95–144, DOI [10.1016/b978-012524975-1/50006-9](https://doi.org/10.1016/b978-012524975-1/50006-9).
- [158] J. Runke, C. E. Düllmann, K. Eberhardt, P. A. Ellison, K. E. Gregorich, S. Hofmann, E. Jäger, B. Kindler, J. V. Kratz, J. Krier, B. Lommel, C. Mokry, H. Nitsche, J. B. Roberto, K. P. Rykaczewski, M. Schädel, P. Thörle-Pospiech, N. Trautmann, A. Yakushev, “Preparation of actinide targets for the synthesis of the heaviest elements”, *Journal of Radioanalytical and Nuclear Chemistry* **2013**, 299, 1081–1084, DOI [10.1007/s10967-013-2616-6](https://doi.org/10.1007/s10967-013-2616-6).
- [159] W. Parker, H. Bildstein, N. Getoff, H. Fischer-Colbrie, H. Regal, “Molecular plating II a rapid and quantitative method for the electrodeposition of the rare-earth elements”, *Nuclear Instruments and Methods* **1964**, 26, 61–65, DOI [10.1016/0029-554x\(64\)90050-3](https://doi.org/10.1016/0029-554x(64)90050-3).
- [160] N. Getoff, H. Bildstein, “Molecular plating, IV a rapid method for the electrodeposition of plutonium”, *Nuclear Instruments and Methods* **1965**, 36, 173–175, DOI [10.1016/0029-554x\(65\)90420-9](https://doi.org/10.1016/0029-554x(65)90420-9).
- [161] B. W. Filippone, M. Wahlgren, “Preparation of a ^7Be target via the molecular plating method”, *Nuclear Instruments and Methods in Physics Research Section A: Accelerators Spectrometers Detectors and Associated Equipment* **1986**, 243, 41–44, DOI [10.1016/0168-9002\(86\)90819-3](https://doi.org/10.1016/0168-9002(86)90819-3).
- [162] R. Tribble, C. Gagliardi, W. Liu, “MARS: a status report”, *Nuclear Instruments and Methods in Physics Research Section B: Beam Interactions with Materials and Atoms* **1991**, 56-57, 956–959, DOI [10.1016/0168-583x\(91\)95070-t](https://doi.org/10.1016/0168-583x(91)95070-t).
- [163] D. J. Griffiths, *Introduction to Electrodynamics*, Cambridge University Press, **2017**, DOI [10.1017/9781108333511](https://doi.org/10.1017/9781108333511).
- [164] A. Semchenkov, W. Bröchle, E. Jäger, E. Schimpf, M. Schädel, C. Mühle, F. Klos, A. Türler, A. Yakushev, A. Belov, T. Belyakova, M. Kaparkova, V. Kukhtin, E. Lamzin, S. Sytchevsky, “The TransActinide Separator and Chemistry Apparatus (TASCAs) at GSI – Optimization of ion-optical structures and magnet designs”, *Nuclear Instruments and Methods in Physics Research Section B: Beam Interactions with Materials and Atoms* **2008**, 266, 4153–4161, DOI [10.1016/j.nimb.2008.05.132](https://doi.org/10.1016/j.nimb.2008.05.132).

- [165] M. Wada, Y. Ishida, T. Nakamura, Y. Yamazaki, T. Kambara, H. Ohyama, Y. Kanai, T. M. Kojima, Y. Nakai, N. Ohshima, A. Yoshida, T. Kubo, Y. Matsuo, Y. Fukuyama, K. Okada, T. Sonoda, S. Ohtani, K. Noda, H. Kawakami, I. Katayama, “Slow RI-beams from projectile fragment separators”, *Nuclear Instruments and Methods in Physics Research Section B: Beam Interactions with Materials and Atoms* **2003**, *204*, 14th International Conference on Electromagnetic Isotope Separators and Techniques Related to their Applications, 570–581, DOI [https://doi.org/10.1016/S0168-583X\(02\)02151-1](https://doi.org/10.1016/S0168-583X(02)02151-1).
- [166] G. Savard, J. Clark, C. Boudreau, F. Buchinger, J. Crawford, H. Geissel, J. Greene, S. Gulick, A. Heinz, J. Lee, A. Levand, M. Maier, G. Münzenberg, C. Scheidenberger, D. Seweryniak, K. Sharma, G. Sprouse, J. Vaz, J. Wang, B. Zabransky, Z. Zhou, “Development and operation of gas catchers to thermalize fusion evaporation and fragmentation products”, *Nuclear Instruments and Methods in Physics Research Section B: Beam Interactions with Materials and Atoms* **2003**, *204*, 14th International Conference on Electromagnetic Isotope Separators and Techniques Related to their Applications, 582–586, DOI [https://doi.org/10.1016/S0168-583X\(02\)02134-1](https://doi.org/10.1016/S0168-583X(02)02134-1).
- [167] M. Węgrzecki, J. Bar, T. Budzyński, M. Cież, P. Grabiec, R. Kozłowski, J. Kulawik, A. Panas, J. Sarnecki, W. Słysz, D. Szmigiel, I. Węgrzecka, M. Wielunski, K. Witek, A. Yakushev, M. Zaborowski in Electron Technology Conference 2013, (Eds.: P. Szczepanski, R. Kisiel, R. S. Romaniuk), SPIE, **2013**, DOI [10.1117/12.2031041](https://doi.org/10.1117/12.2031041).
- [168] C. Görden, Elektronik für kernphysikalische Experimente, Institute for nuclear physics at cologne university, <https://www.ikp.uni-koeln.de/institut/einrichtungen/elektronikwerkstatt/>.
- [169] www.mesytec.com - Detector Readout Systems, available at <https://www.mesytec.com>, (accessed on March 21, 2021).
- [170] J.Hoffmann, N.Kurz, M.Richter, TRIVA 5, VME Trigger Module, **2009**.
- [171] Oxisorb[®] Nachreinigungspatronen, **2020**.
- [172] F. P. Heßberger, “Discovery of the Heaviest Elements”, *ChemPhysChem* **2013**, *14*, 483–489, DOI [10.1002/cphc.201201011](https://doi.org/10.1002/cphc.201201011).
- [173] M. Block, D. Ackermann, K. Blaum, C. Droese, M. Dworschak, S. Eliseev, T. Fleckenstein, E. Haettner, F. Herfurth, F. P. Heßberger, S. Hofmann, J. Ketelaer, J. Ketter, H.-J. Kluge, G. Marx, M. Mazzocco, Y. N. Novikov, W. R. Plaß, A. Popeko, S. Rahaman, D. Rodríguez, C. Scheidenberger, L. Schweikhard, P. G. Thirolf, G. K. Vorobyev, C. Weber, “Direct mass measurements above uranium bridge the gap to the island of stability”, *Nature* **2010**, *463*, 785–788, DOI [10.1038/nature08774](https://doi.org/10.1038/nature08774).
- [174] E. M. Ramirez, D. Ackermann, K. Blaum, M. Block, C. Droese, Ch. E. Düllmann, M. Dworschak, M. Eibach, S. Eliseev, E. Haettner, F. Herfurth, F. P. Heßberger, S. Hofmann, J. Ketelaer, G. Marx, M. Mazzocco, D. Nesterenko, Y. N. Novikov, W. R. Plass, D. Rodriguez, C. Scheidenberger, L. Schweikhard, P. G. Thirolf, C. Weber, “Direct Mapping of Nuclear Shell Effects in the Heaviest Elements”, *Science* **2012**, *337*, 1207–1210, DOI [10.1126/science.1225636](https://doi.org/10.1126/science.1225636).
- [175] F. Penning, “Die glimmentladung bei niedrigem druck zwischen koaxialen zylindern in einem axialen magnetfeld”, *Physica* **1936**, *3*, 873–894, DOI [10.1016/s0031-8914\(36\)80313-9](https://doi.org/10.1016/s0031-8914(36)80313-9).
- [176] L. S. Brown, G. Gabrielse, “Geonium theory: Physics of a single electron or ion in a Penning trap”, *Reviews of Modern Physics* **1986**, *58*, 233–311, DOI [10.1103/revmodphys.58.233](https://doi.org/10.1103/revmodphys.58.233).
- [177] K. Blaum, F. Herfurth, A. Kellerbauer, “Eine Waage für exotische Kerne: Massenbestimmung von Atomkernen mit Isoltrap”, *Physik in unserer Zeit* **2005**, *36*, 222–228, DOI [10.1002/piuz.200501074](https://doi.org/10.1002/piuz.200501074).
- [178] O. T. Kaleja, PhD thesis, Fachbereich Chemie der Johannes Gutenberg-Universität Mainz, **2020**, DOI [10.25358/OPENSOURCE-5111](https://doi.org/10.25358/OPENSOURCE-5111).

- [179] J. Dvorak, PhD thesis, Fachbereich Physik der Technischen Universität München, **2006**.
- [180] A. Yakushev, L. Lens, C. E. Düllmann, M. Block, H. Brand, T. Calverly, M. Dasgupta, A. D. Nitto, M. Götz, S. Götz, H. Haba, L. Harkness-Brennan, R.-D. Herzberg, F. Heßberger, D. Hinde, A. Hübner, E. Jäger, D. Judson, J. Khuyagbaatar, B. Kindler, Y. Komori, J. Konki, J. Kratz, J. Krier, N. Kurz, M. Laatiaoui, B. Lommel, C. Lorenz, M. Maiti, A. Mistry, C. Mokry, Y. Nagame, P. Papadakis, A. Roth, D. Rudolph, J. Runke, L. Samiento, T. Sato, M. Schädel, P. Scharrer, B. Schausten, J. Steiner, P. Thörle-Pospiech, A. Toyoshima, N. Trautmann, J. Uusitalo, A. Ward, M. Wegrzecki, V. Yakusheva, “First attempt to study nihonium (Nh, $Z = 113$) chemically at TASCA”, *in preparation for submission to Frontiers in Chemistry* **2020**.
- [181] J. Ziegler, Computer Code SRIM-2010, **2018**.
- [182] O. Tarasov, D. Bazin, “LISE++: Radioactive beam production with in-flight separators”, *Nuclear Instruments and Methods in Physics Research Section B: Beam Interactions with Materials and Atoms* **2008**, 266, 4657–4664, DOI [10.1016/j.nimb.2008.05.110](https://doi.org/10.1016/j.nimb.2008.05.110).
- [183] D. Bazin, O. Tarasov, M. Lewitowicz, O. Sorlin, “The program LISE: a simulation of fragment separators”, *Nuclear Instruments and Methods in Physics Research Section A: Accelerators Spectrometers Detectors and Associated Equipment* **2002**, 482, 307–327, DOI [10.1016/s0168-9002\(01\)01504-2](https://doi.org/10.1016/s0168-9002(01)01504-2).
- [184] S. Schwarz, “RF ion carpets: The electric field, the effective potential, operational parameters and an analysis of stability”, *International Journal of Mass Spectrometry* **2011**, 299, 71–77, DOI [10.1016/j.ijms.2010.09.021](https://doi.org/10.1016/j.ijms.2010.09.021).
- [185] G. Bollen, ““Ion surfing” with radiofrequency carpets”, *International Journal of Mass Spectrometry* **2011**, 299, 131–138, DOI [10.1016/j.ijms.2010.09.032](https://doi.org/10.1016/j.ijms.2010.09.032).
- [186] F. Hinterberger, *Physik der Teilchenbeschleuniger und Ionenoptik*, Springer Berlin Heidelberg Imprint Springer, Berlin, Heidelberg, **1997**.
- [187] R. Eichler, M. Schädel, “Adsorption of Radon on Metal Surfaces: A Model Study for Chemical Investigations of Elements 112 and 114”, *The Journal of Physical Chemistry B* **2002**, 106, 5413–5420, DOI [10.1021/jp015553q](https://doi.org/10.1021/jp015553q).
- [188] L. Viehland, “Zero-field mobilities in helium: highly accurate values for use in ion mobility spectrometry”, *Int. J. Ion Mobil. Spec.* **2012**, 15, 21–29, DOI <https://doi.org/10.1007/s12127-011-0079-4>.
- [189] C. Czeslik, H. Seemann, R. Winter, *Basiswissen Physikalische Chemie*, Vieweg+Teubner Verlag, **2010**, DOI [10.1007/978-3-8348-9359-8](https://doi.org/10.1007/978-3-8348-9359-8).
- [190] V. Varentsov, A. Ignatiev, “Numerical investigations of internal supersonic jet targets formation for storage rings”, *Nuclear Instruments and Methods in Physics Research Section A: Accelerators Spectrometers Detectors and Associated Equipment* **1998**, 413, 447–456, DOI [10.1016/s0168-9002\(98\)00354-4](https://doi.org/10.1016/s0168-9002(98)00354-4).
- [191] K. Eberhardt, W. Bröchle, Ch. E. Düllmann, K. Gregorich, W. Hartmann, A. Hübner, E. Jäger, B. Kindler, J. Kratz, D. Liebe, B. Lommel, H.-J. Maier, M. Schädel, B. Schausten, E. Schimpf, A. Semchenkov, J. Steiner, J. Szerypo, P. Thörle, A. Türler, A. Yakushev, “Preparation of targets for the gas-filled recoil separator TASCA by electrochemical deposition and design of the TASCA target wheel assembly”, *Nuclear Instruments and Methods in Physics Research Section A: Accelerators Spectrometers Detectors and Associated Equipment* **2008**, 590, Toward the Realization of Target and Stripper Foil Technologies for High-Power Proton and Radioactive Ion Accelerators, 134–140, DOI <https://doi.org/10.1016/j.nima.2008.02.069>.
- [192] D. A. Mayorov, T. A. Werke, M. C. Alfonso, M. E. Bennett, C. M. Folden, “Production cross sections of elements near the $N=126$ shell in Ca48-induced reactions with Gd-154, Tb-159, Dy-162, and Ho-165 targets”, *Physical Review C* **2014**, 90, DOI [10.1103/physrevc.90.024602](https://doi.org/10.1103/physrevc.90.024602).

- [193] J. F. Ziegler, Computer Code SRIM-2013, available at <http://www.srim.org>, (accessed on March 8, 2021).
- [194] D. Mayorov, E. Tereshatov, T. Werke, M. Frey, C. Folden, “Heavy-ion beam induced effects in enriched gadolinium target films prepared by molecular plating”, *Nuclear Instruments and Methods in Physics Research Section B: Beam Interactions with Materials and Atoms* **2017**, 407, 256–264, DOI [10.1016/j.nimb.2017.07.012](https://doi.org/10.1016/j.nimb.2017.07.012).
- [195] W. Reisdorf, “Analysis of fissionability data at high excitation energies”, *Zeitschrift für Physik A: Atoms and Nuclei* **1981**, 300, 227–238, DOI [10.1007/bf01412298](https://doi.org/10.1007/bf01412298).
- [196] ENSDF database (Evaluated Nuclear Structure Data File), **2020**, www.nndc.bnl.gov/ensdf.
- [197] F. Lautenschläger, P. Chhetri, D. Ackermann, H. Backe, M. Block, B. Cheal, A. Clark, C. Droese, R. Ferrer, F. Giacoppo, S. Götz, F. Heßberger, O. Kaleja, J. Khuyagbaatar, P. Kunz, A. Mistry, M. Laatiaoui, W. Lauth, S. Raeder, T. Walther, C. Wraith, “Developments for resonance ionization laser spectroscopy of the heaviest elements at SHIP”, *Nuclear Instruments and Methods in Physics Research Section B: Beam Interactions with Materials and Atoms* **2016**, 383, 115–122, DOI [10.1016/j.nimb.2016.06.001](https://doi.org/10.1016/j.nimb.2016.06.001).
- [198] D. MacDougall, W. B. Crummett, . et al., “Guidelines for data acquisition and data quality evaluation in environmental chemistry”, *Analytical Chemistry* **1980**, 52, 2242–2249, DOI [10.1021/ac50064a004](https://doi.org/10.1021/ac50064a004).
- [199] P. Sigmund, *Particle Penetration and Radiation Effects*, Springer Berlin Heidelberg, **2006**.
- [200] A. Semchenkov, W. Brüchle, E. Jäger, E. Schimpf, M. Schädel, C. Mühle, F. Klos, A. Türler, A. Yakushev, A. Belov, T. Belyakova, M. Kaparkova, V. Kukhtin, E. Lamzin, S. Sytchevsky, “The TransActinide Separator and Chemistry Apparatus (TASCA) at GSI - Optimization of ion-optical structures and magnet designs”, *Nucl. Instrum. Methods Phys. Res. B* **2008**, 266, 4153–4161, DOI [10.1016/j.nimb.2008.05.132](https://doi.org/10.1016/j.nimb.2008.05.132).
- [201] L.-L. Andersson, D. Rudolph, P. Golubev, R.-D. Herzberg, R. Hoischen, E. Merchán, D. Ackermann, C. Düllmann, K. Eberhardt, J. Even, J. Gerl, F. Heßberger, E. Jäger, J. Khuyagbaatar, I. Kojouharov, J. Kratz, J. Krier, N. Kurz, W. Prokopowicz, M. Schädel, H. Schaffner, B. Schausten, E. Schimpf, A. Semchenkov, A. Türler, H.-J. Wollersheim, A. Yakushev, P. Thörle-Pospiech, W. Hartmann, A. Hübner, B. Lommel, B. Kindler, J. Steiner, “TASISpec—A highly efficient multi-coincidence spectrometer for nuclear structure investigations of the heaviest nuclei”, *Nuclear Instruments and Methods in Physics Research Section A: Accelerators Spectrometers Detectors and Associated Equipment* **2010**, 622, 164–170, DOI [10.1016/j.nima.2010.06.243](https://doi.org/10.1016/j.nima.2010.06.243).
- [202] A. Sămark-Roth, D. M. Cox, D. Rudolph, L. G. Sarmiento, B. G. Carlsson, J. L. Egido, P. Golubev, J. Heery, A. Yakushev, S. Åberg, H. M. Albers, M. Albertsson, M. Block, H. Brand, T. Calverley, R. Cantemir, R. M. Clark, C. E. Düllmann, J. Eberth, C. Fahlander, U. Forsberg, J. M. Gates, F. Giacoppo, M. Götz, S. Götz, R.-D. Herzberg, Y. Hrabar, E. Jäger, D. Judson, J. Khuyagbaatar, B. Kindler, I. Kojouharov, J. V. Kratz, J. Krier, N. Kurz, L. Lens, J. Ljungberg, B. Lommel, J. Louko, C.-C. Meyer, A. K. Mistry, C. Mokry, P. Papadakis, E. Parr, J. L. Pore, I. Ragnarsson, J. Runke, M. Schädel, H. Schaffner, B. Schausten, D. A. Shaughnessy, P. Thörle-Pospiech, N. Trautmann, J. Uusitalo, “Spectroscopy along Flerovium Decay Chains: Discovery of ^{280}Ds and an Excited State in ^{282}Cn ”, *Phys. Rev. Lett.* **2021**, 126, 032503, DOI [10.1103/physrevlett.126.032503](https://doi.org/10.1103/physrevlett.126.032503).
- [203] K. Gregorich, “Simulation of recoil trajectories in gas-filled magnetic separators”, *Nuclear Instruments and Methods in Physics Research Section A: Accelerators Spectrometers Detectors and Associated Equipment* **2013**, 711, 47–59, DOI [10.1016/j.nima.2013.01.020](https://doi.org/10.1016/j.nima.2013.01.020).

- [204] D. M. Cox, A. Sårmark-Roth, D. Rudolph, L. Sarmiento, C. Fahlander, U. Forsberg, P. Golubev, J. Heery, A. Yakushev, H. M. Albers, M. Block, H. Brand, R. Clark, C. E. Düllmann, J. Eberth, J. Gates, F. Giacoppo, M. Götz, S. Götz, R.-D. Herzberg, E. Jäger, B. Kindler, J. Khuyagbaatar, I. Kojouharov, J. V. Kratz, J. Krier, N. Kurz, L. Lens, B. Lommel, A. Mistry, C.-C. Meyer, C. Mokry, P. Papadakis, J. L. Pore, J. Runke, P. Thörle-Pospiech, N. Trautmann, H. Schaffner, B. Schausten, J. Uusitalo, “Spectroscopic Tools Applied to Flerovium Decay Chains”, *J. Phys. Conf. Ser.* **2020**, *1643*, 012125, DOI [10.1088/1742-6596/1643/1/012125](https://doi.org/10.1088/1742-6596/1643/1/012125).
- [205] A. Serov, N. V. Aksenov, G. A. Bozhikov, R. Eichler, R. Dressler, V. Y. Lebedev, O. Petrushkin, D. Piguet, S. Shishkin, E. Tereshatov, A. Türler, “Adsorption interaction of astatine species with quartz and gold surfaces”, *Radiochimica Acta* **2011**, *99*, 593–600, DOI [10.1524/ract.2011.1850](https://doi.org/10.1524/ract.2011.1850).
- [206] V. Varentsov, A. Yakushev, “Concept of a new Universal High-Density Gas Stopping Cell Setup for study of gas-phase chemistry and nuclear properties of Super Heavy Elements (UniCell)”, *Nuclear Instruments and Methods in Physics Research Section A: Accelerators Spectrometers Detectors and Associated Equipment* **2019**, *940*, 206–214, DOI [10.1016/j.nima.2019.06.032](https://doi.org/10.1016/j.nima.2019.06.032).
- [207] J. Gates, G. Pang, J. Pore, K. Gregorich, J. Kwarsick, G. Savard, N. Esker, M. K. Covo, M. Mogannam, J. Batchelder, D. Bleuel, R. Clark, H. Crawford, P. Fallon, K. Hubbard, A. Hurst, I. Kolaja, A. Macchiavelli, C. Morse, R. Orford, L. Phair, M. Stoyer, “First Direct Measurements of Superheavy-Element Mass Numbers”, *Physical Review Letters* **2018**, *121*, DOI [10.1103/physrevlett.121.222501](https://doi.org/10.1103/physrevlett.121.222501).
- [208] S. Dmitriev, M. Itkis, Y. Oganessian, “Status and perspectives of the Dubna superheavy element factory”, *EPJ Web of Conferences* **2016**, *131*, (Ed.: D. Rudolph), 08001, DOI [10.1051/epjconf/201613108001](https://doi.org/10.1051/epjconf/201613108001).
- [209] A. V. Kaprov, V. I. Zagrebaev, Y. M. Palenzuela, L. F. Ruiz, W. Greiner, “Decay Properties and Stability of Heaviest Elements”, *International Journal of Modern Physics E* **2012**, *21*, 1250013, DOI [10.1142/s0218301312500139](https://doi.org/10.1142/s0218301312500139).
- [210] V. Zagrebaev in 11th International Conference on Nucleus-Nucleus Collisions (NN2012). San Antonio, Texas, US, **2012**.
- [211] Wikipedia contributors, Island of stability — Wikipedia, The Free Encyclopedia, https://en.wikipedia.org/w/index.php?title=Island_of_stability&oldid=986095396, [Online; accessed 15-November-2020], **2020**.
- [212] V. Pershina, “A Theoretical Study on the Adsorption Behavior of Element 113 and Its Homologue Tl on a Quartz Surface: Relativistic Periodic DFT Calculations”, *The Journal of Physical Chemistry C* **2016**, *120*, 20232–20238, DOI [10.1021/acs.jpcc.6b07834](https://doi.org/10.1021/acs.jpcc.6b07834).
- [213] M. Robinson, I. Torrens, “Computer simulation of atomic-displacement cascades in solids in the binary-collision approximation”, *Physical Review B* **1974**, *9*, 5008–5024, DOI [10.1103/physrevb.9.5008](https://doi.org/10.1103/physrevb.9.5008).
- [214] R. Smith, *Atomic and Ion Collisions in Solids and at Surfaces*, Cambridge University Press, **2012**, 320 pp.
- [215] H. Bethe, “Zur Theorie des Durchgangs schneller Korpuskularstrahlen durch Materie”, *Annalen der Physik* **1930**, *397*, 325–400, DOI [10.1002/andp.19303970303](https://doi.org/10.1002/andp.19303970303).
- [216] F. Bloch, “Zur Bremsung rasch bewegter Teilchen beim Durchgang durch Materie”, *Annalen der Physik* **1933**, *408*, 285–320, DOI [10.1002/andp.19334080303](https://doi.org/10.1002/andp.19334080303).
- [217] J. Lindhard, M. Scharff, “Energy Dissipation by Ions in the kev Region”, *Physical Review* **1961**, *124*, 128–130, DOI [10.1103/physrev.124.128](https://doi.org/10.1103/physrev.124.128).
- [218] J. F. Ziegler, J. P. Biersack in *Treatise on Heavy-Ion Science*, Springer US, **1985**, pp. 93–129, DOI [10.1007/978-1-4615-8103-1_3](https://doi.org/10.1007/978-1-4615-8103-1_3).
- [219] F. P. Heßberger, Private communication, GSI, **2019**.

- [220] S. Purushothaman, Dissertation, University of Groningen, **2008**.
- [221] J. Huikari, P. Dendooven, A. Jokinen, A. Nieminen, H. Penttilä, K. Peräjärvi, A. Popov, S. Rinta-Antila, J. Äystö, “Production of neutron deficient rare isotope beams at IGISOL; on-line and off-line studies”, *Nuclear Instruments and Methods in Physics Research Section B: Beam Interactions with Materials and Atoms* **2004**, *222*, 632–652, DOI <https://doi.org/10.1016/j.nimb.2004.04.164>.

Curriculum vitae



Stefan Alexander William Götz

13.10.1984 in Wiesbaden-Dotzheim

Education

- Since 03/2015 **Phd**, *Institut für Kernchemie, Johannes Gutenberg-Universität Mainz, DE*,
Titel: Characterization and modification of a buffer gas cell for rapid extraction of short-lived isotopes for use in gas-phase chemistry experiments at TASCA
- 10/2006 – 03/2015 **Diploma**, *Johannes Gutenberg-Universität, Mainz, DE*,
Titel: Separations of Actinides and Lanthanides by ion exchange chromatography
Grade: good
- 08/2002–06/2005 **Abitur**, *Friedrich-List-Schule Wiesbaden, DE*
Grade: 1,8

Experience abroad

- 05/2017 **Experiment**, *Cyclotron Institute at Texas A&M University, College Station, TX, USA*
- 03/2018 **Experiment**, *RIKEN Nishina Center, Tokai-mura, JP*

Oral presentations and posters

- 11/2018 **Presentations**, *4th International Conference on Application of RadiotraCers and Energetic Beams in Sciences (ARCEBS-2018)*, Ffort Raichak, India, “Speeding up gas-phase chemistry to access elements beyond Fl“
- 10/2017 **Presentations**, *9th Workshop on the Chemistry of the Heaviest Elements*, Ascona, Switzerland, “Speeding up gas-phase chemistry to access elements beyond Fl“
- 09/2017 **Poster**, *Wissenschaftsforum 2017*, Berlin, Germany, “Speeding up gas-phase chemistry to access elements beyond Fl“
- 09/2017 **Presentations**, *TASCA Workshop 2017*, Darmstadt, Germany, “Speeding up gas-phase chemistry to access elements beyond Fl“
- 11/2016 **Presentations**, *TASCA Workshop 2016*, Darmstadt, Germany, “Speeding up gas-phase chemistry to access elements beyond Fl“
- 09/2016 **Poster**, *9th international conference on nuclear and radiochemistry*, Helsinki, Finland, “Speeding up gas-phase chemistry to access elements beyond Fl“
- 09/2015 **Presentations**, *Wissenschaftsforum 2015*, Berlin, Germany, “ Radiochemische Untersuchung der Kinematik von Multinukleon-Transfer in $^{48}\text{Ca} + ^{248}\text{Cm}$ Kollisionen 10% oberhalb der Coulomb-barriere “

Publications

- 02/2021 **Rapid extraction of short-lived isotopes from a buffer gas cell for use in gas-phase chemistry experiments. Part I: off-line studies with ^{219}Rn and ^{221}Fr** , S. Götz *et al.*, Nuclear Physics A, Volume 995, 165090 (2021)
- 09/2021 **Rapid extraction of short-lived isotopes from a buffer gas cell for use in gas-phase chemistry experiments. Part II: on-line studies with short-lived radionuclides**, S. Götz *et al.*, Nuclear Physics B, Volume 507, Pages 27-35 (2022)